THESE DE DOCTORAT DE
L'UNIVERSITE DE LILLE 1

Spécialité:

Molécules et Matière Condensée

Présentée par

M. Stavros A. SKARLIS

Pour obtenir le grade de
DOCTEUR de l'UNIVERSITE DE LILLE 1

IR spectroscopy based kinetic modeling of NH₃-SCR on Fe-zeolites: Application for diesel engines aftertreatment system simulation

Soutenance prévu le 20 Septembre 2013

devant le jury composé de:

Mme Louise Olsson	Professeur – Chalmers University, Swede	**Rapporteur**
M. Marco Daturi	Professeur – Université de Caen, Caen	**Rapporteur**
M. Gerard Delahay	Directeur de recherche, CNRS – ENSC Montpellier	**Président**
Mme Séverine Rousseau	Ingénieur, PSA– Peugeot Citroën; Vélizy-Villacoublay	**Examinateur**
M. Pascal Granger	Professeur – Université de Lille 1, Lille, Directeur de thèse	**Examinateur**
M. Christophe Dujardin	Maitre de conférences – Université de Lille 1, Lille	**Examinateur**
M. David Berthout	Ingénieur, IFP Energies nouvelles, Rueil Malmaison	**Examinateur**
M. André Nicolle	Ingénieur, IFP Energies nouvelles, Rueil Malmaison	**Examinateur**

Paris, Septembre 2013

ΕΙΣ ΤΟΥΣ ΓΟΝΕΙΣ ΜΟΥ ΟΦΕΙΛΩ ΤΟ ΖΗΝ, ΕΙΣ ΤΟΝ ΔΙΔΑΣΚΑΛΟΝ ΜΟΥ ΤΟ ΕΥ ΖΗΝ

Μέγας Αλέξανδρος (336-323 π.Χ.)

Dedicated to my brother Michalis

Acknowledgements

Completing this PhD dissertation, was one of the most constructive and pleasant experiences of my life. Looking back to the moments of this journey, I recall the people that supported and helped me along this three year road.

First of all, I would like to kindly acknowledge IFP Energies Nouvelles, Université Lille 1 and the 7th ITN framework project VECOM for providing financial support for this research. Thanks to these parties, I had the unique opportunity to complete my PhD thesis in a highly competitive and professional environment, as well as to experience life abroad.

Many people have significantly contributed to the outcome of the present work and should be warmly acknowledged. First, I would like to thank my advisors, Dr. André Nicolle and David Berthout from IFP EN and Dr. Christophe Dujardin and Professor Pascal Granger from Université Lille 1 for their excellent guidance and support throughout the three years of this doctoral thesis. Their dedicated supervision and constructive advice allowed me not only to complete my PhD dissertation in time, but to get deep insight into fundamental aspects of heterogeneous catalysis, which was so far, a completely new field to me. Moreover, several collegues should be greatly acknowledged for their valuable contribution to the epxeriemental part of this work and for fruitful scientific discussion and guidance. I would like to warmly thank Olivier Gardol, Jean Charles Morin, Eric Capet, Dr. Sonia Carre and Professor Pascal Roussel from the Université Lille 1, for their crucial contribution to the experimental investigation presented in the frame of this study. Dr. Nikola Batch, from IFP EN is also thanked for providing the H-BEA zeolite, for testing in the laboratory.

I would also like to thank my great collegues and friends Nikola, Kirsten, Betty, Nicolas, Damien, Anthony, Stéphane, Jean Baptiste, Emre, Oguz, Lama, Haifa, Adam, Sophie, Elias, Benjamin, Carlo and Felippe. I will never forget the wonderful moments we shared together and their great support during this three years work and stay in France. I am grateful I had the opportunity to get to know them. Last but not least, I would like to tank my family, my parents Antonis and Maria, my brother Michalis and my cousins Valerie, Christophe and Alexandre, as well as my love and companion in life Margarita for their great support and help during this journey.

Remerciements

Fin de cette thèse de doctorat, a était l'une des expériences les plus constructives et agréables de ma vie. En regardant en arrière sur les moments de ce voyage, je me souviens des gens qui m'ont soutenu et aidé sur ce chemin de trois ans.

Tout d'abord, je voudrais remercier beaucoup IFP Energies Nouvelles, Université Lille 1 et le 7th ITN framework project VECOM pour avoir financé cette recherche. Grace à ces parties, j'ai eu l'occasion unique de compléter ma thèse doctoral dans un environnement très concurrentiel et professionnel, ainsi que de découvrir la vie à l'étranger.

Beaucoup de gens ont contribué de manière significative à l'issue de ce travail et doivent être chaleureusement reconnu. Tout d'abord, je tiens à remercier mes encadrants, Dr André Nicolle et David Berthout de l'IFP EN et Dr Christophe Dujardin et le Professeur Pascal Granger de l'Université Lille 1 pour leur orientation et soutien excellentes pendant les trois ans de thèse. Leur conseil et surveillance constructives m'a permis pas seulement de compléter ma thèse à l'heure, mais d'obtenir un aperçu aprofondi sur les aspects fondamentaux de la catalyse hétérogène, qui était jusqu'à présent un domaine complètement nouveau pour moi. En outre, plusieurs collègues devraient être grandement reconnus pour leur précieuse contribution à la partie epxeriemental de ce travail et pour des discussions scientifiques fructueuses. Je tiens à remercier chaleureusement Olivier Gardol, Jean Charles Morin, Eric Capet, Dr Sonia Carré et le Professeur Pascal Roussel de l'Université Lille 1 pour leur contribution essentielle à l'étude expérimentale présentée dans le cadre de cette étude. Dr Nikola Batch, de l'IFP EN est également remercié pour avoir fourni la zéolithe H-BEA, pour les tests en laboratoire.

Je tiens également à remercier de facon tres chalereuse mes collègues et amis Nikola, Kirsten, Betty, Nicolas, Damien, Anthony, Stéphane, Jean Baptiste, Emre, Oguz, Lama, Haïfa, Adam, Sophie, Elias, Benjamin, Carlo et Felippe. Je n'oublierai jamais les moments merveilleux qu'on a passé ensemble et leur grand soutien durant cette période de trois ans de travail et de séjour en France. Je suis reconnaissante d'avoir eu l'occasion de faire leur connaissance. Finalement, je voudrais dire un grand merci à ma famille, mes parents Antonis et Maria, mon frère Michalis et mes cousins Valérie, Christophe et Alexandre, ainsi que mon amour et compagnon dans la vie Margarita pour leur soutien et leur aide pendant ce voyage.

IR spectroscopy based kinetic modeling of NH₃-SCR on Fe-zeolites: Application for diesel engines aftertreatment system simulation

Abstract

Selective Catalytic Reduction of nitrogen oxides through urea or ammonia is a well established technique for the efficient abatement of NO_x, from mobile diesel engines exhaust stream. Among catalytic formulations proposed, Fe-exchanged zeolites are considered as promising SCR catalysts, due to their enhanced $deNO_x$ performance over a broad range of engine operating temperatures, as well as significant resistance to hydrothermal ageing. In the present work, detailed experimental investigation of the NH₃-SCR reactions network over Fe zeolites was performed in order to develop a phenomenological macro-kinetic model oriented to diesel engines aftertreatment system simulation. Dedicated experiments, including IR spectroscopy measurements were initially performed over lab-synthesized H- and Fe-BEA catalysts in order to unravel mechanistic aspects related to the formation and interactions of ammonia and nitrogen oxides adspecies (namely nitrate and nitrites) on acidic and redox catalytic sites. Focusing on low-temperature SCR, formation and decomposition of NH_4NO_3 was of particular concern. Based on experimental results a multi-site kinetic model was developed, which was able to account for surface acidity variation, interactions of gaseous NH_3 and NO_x species with iron sites, as well as low temperature physisorption phenomena. Special care was taken for kinetic parameters calibration, where structural properties of the studied samples and namely the Si/Al and Fe/Al rations were taken into consideration. The model was successfully validated through simulation of experiments performed over the lab-synthesized as well as commercial Fe-zeolite samples, applying a broad range of operating conditions, which showed the interest of the followed approach.

Modélisation de la SCR au NH₃ sur zéolithes au fer, basée sur spectroscopie IR: Application pour la simulation des systèmes de post-traitement des moteurs Diesel

Résumé

La réduction catalytique sélective des oxydes d'azote au moyen de l'urée ou de l'ammoniac est une technique bien connue, pour une conversion efficace des NO_x, qui existent dans le gaz d'échappement des moteurs Diesel mobiles. Parmi les formulations catalytiques proposés, les zéolithes échangées au fer sont considérés comme des catalyseurs SCR prometteuse, grâce à leur performance deNO_x élevée, sur une large gamme des températures de fonctionnement du moteur, ainsi qu'une résistance importante au vieillissement hydrothermique. Dans le cadre de cette thèse, une étude expérimentale détaillée des voies réactionnelles de la SCR sur les zéolithes au fer a été réalisée de façon à développer un modèle phénoménologique et macro-cinétique, appliqué pour la simulation des systèmes de post-traitement des moteurs Diesel. Des expériences dédiées qui comprenaient des mesures de spectroscopie IR ont initialement été réalisées sur les catalyseurs H- et Fe-BEA, synthétisés en laboratoire pour élucider les aspects mécanistiques liées à la formation et aux interactions de l'ammoniac et d'oxydes d'azote (notamment des espèces nitrates et nitrites) sur des sites catalytiques acides et redox. En se focalisant sur la SCR à basse température, la formation et la décomposition de NH_4NO_3 ont été particulièrement préoccupantes. Basé sur des résultats expérimentaux un modèle cinétique multi-site a été développé. Le modèle a été capable de prendre en compte la variation de l'acidité de surface, les interactions des espèces gazeux du NH_3 et des NO_x avec des sites métalliques, ainsi que des phénomènes de physisorption à basse température. Un soin particulier a été pris pour la calibration des paramètres cinétiques, où les propriétés structurelles des échantillons étudiés et notamment les rations Si/Al et Fe/Al ont été prises en considération. Le modèle a été validé avec succès par la simulation des expériences réalisées sur les échantillons synthèse en laboratoire, ainsi que des échantillons de zéolithe au fer commerciales, en appliquant une large variété de conditions de fonctionnement. Donc l'intérêt de l'approche suivie a été souligné.

Mots clés: catalyseurs SCR, NO_x, zéolithes échangées au Fe, H BEA, Fe BEA, spectroscopie IR, modélisation cinétique, approche multi site, NH_3 TPD, NO_2 TPD, NH_4NO_3, acidité

Nomenclature list

$A_{ads.}$: pre-exponential factor of NH_3 adsorption [m^3/s·kg$_{zeolite}$]

$A_{des.}$: pre-exponential factor of NH_3 adsorption [mol/s·kg$_{zeolite}$]

A_{open} : reactor open surface area [m^2]

Bi_m : Biot number for mass transfer phenomena [-]

CAD/CAE: computer aided design/engineering

CAO: Conception Assistée par Ordinateur

$\dot{c}_{g,i\_in}$, $\dot{c}_{g,i\_out}$: inlet and outlet concentration flow rate of species [mol/(m^3·s)]

$c_{g,i}$, $c_{s,i}$: concentration of the i species in the gas and the solid phase respectively [mol/m^3]

C_{NH_3} : concentration of ammonia in the gas phase [mol/m^3]

Cp_s : monolith' s thermal capacity [W/(kg·K)]

CPSI: channels density expressed in channels per square inch [cpsi]

D_{ax} : axial diffusion coefficient [m^2/s]

D$_{ch.}$: channel internal diameter [m]

D_e : effective diffusion coefficient, computed through the Bosanquet equation

D_i : diffusivity of gaseous species i [m^2/s]

D$_{inj.}$: external diameter of NH_3 injector attached on the single wafer reactor [m]

d_h : channel's hydraulic diameter [m]

D$_{mono.}$: monolith internal diameter [m]

DOC: Diesel Oxidation Catalyst

D$_{pel.}$ diameter of the self supported wafer [m]

DPF: Diesel Particulate Filter

D$_{reac.}$: fixed bed reactor inlet diameter [m]

DSC: Differential Scanning Calorimetry

e : characteristic length of the washcoat [m]

$E_{ads.}$: activation energy of NH_3 adsorption [J/mol]

$E_{des.}$: activation energy of NH_3 desorption [J/mol]

EfAl:	exra-framework aluminium
EGR:	Exhaust Gas Recirculation
E_o:	activation energy of NH_3 desorption for surface coverage equal to zero [J/mol]
FAl	framework aluminium
h_s:	convection's coefficient for the heat transfer (due to convection) between the gas and the solid phase [W/(m²·K)]
$k(T_s)$:	reaction rate constant [1/s]
$k_{ads}(T_s)$:	rate constant for NH_3 adsorption [m³/(s·kg$_{zeolite}$)]
$k_{des}(\theta_j, T_s)$:	rate constant for NH_3 desorption [mol/(s·kg$_{zeolite}$)]
$k_{m,i}$:	mass transfer coefficient for the external diffusion, of i-species [m/s]
L$_{cl.}$:	single wafer reactor clearance [m]
L$_{mono.}$:	monolith length [m]
LNT:	Lean NO$_x$ Trap
L$_{reac.}$:	reactor length [m]
$\dot{m}_g$:	flow rate of carrier gas [m³/s]
M_i:	molar weight of i species [kg/mol]
MS:	Mass Spectrometry
m$_{zeolite}$:	mass of zeolite [kg]
N_{acidic}:	NH_3 storage capacity over acidic sites of bare ZSM5 [mol/kg$_{zeolite}$]
$N_{acidic\_exch.}$:	NH_3 storage capacity over acidic sites of Fe-ZSM5 [mol/kg$_{zeolite}$]
N_j:	storage capacity over j surface site (j=S1, S2, S3, S4, S5) [mol/kg$_{zeolite}$]
$N_{metallic}$:	NH_3 storage capacity over iron-metallic sites of Fe-ZSM5 [mol/kg$_{zeolite}$]
NMR:	Nuclear Magnetic Resonance
N_{tot}:	NH_3 total storage capacity over bare ZSM5 [mol/kg$_{zeolite}$]
N_{weak}:	NH_3 storage capacity over weak sites of bare ZSM5 [mol/kg$_{zeolite}$]
P$_{ch.}$:	channel perimeter [m]
P$_{in}$, P$_{out}$:	gas absolute pressure at the inlet and outlet of the single wafer reactor [Pa]
q:	partition functions
R:	global gas constant [8.314 J/(mol·K)]

R_g :	gas mixture's constant [kg/(mol $\cdot$K)]
R_j :	reaction rate of [J/mol]
$R_{NH_3\_ads}, R_{NH_3\_des}$	reaction rate of the NH_3 adsorption and desorption respectively [mol/(s$\cdot$kg$_{zeolite}$)]
S:	entropy [J]
s :	surface area to volume ratio [1/m]
SCR:	Selective Catalytic Reduction
S$_f$:	shape factor [-]
S_{geom} :	geometrical catalytic surface based on the open section ratio of the catalyst [m^2]
Sh :	Sherwood number [-]
S$_{open}$:	open surface area [m^2]
STPD:	Stepwise Temperature Programmed Desorption
T_g, T_s :	temperatures of the gas and the solid phase respectively [K]
TGA:	Thermogravimetric Analysis
TPD:	Temperature Programmed Desorption
TRM:	Transient Response Method
u :	gas velocity [m/s]
V$_{mono.}$:	monolith volume [m^3]
V$_{reac.}$:	reactor volume [m^3]
V_s :	volume of the solid phase [m^3]
V_{wash} :	volume of the washcoat [m^3]
WSCR:	Wall flow filter combined with a SCR layer in a single aftertreatment device
W$_{th.}$:	monolith wall thickness [m]
XRD:	X-ray Diffraction

Greek symbols

α:	constant for the description of the dependence of the activation energy of desorption from the surface coverage [-]
Δh_i :	specific enthalpy of ith-species formation [W/kg]
ε:	reactor void fraction [-]
η_{exch} :	percentage of the ion exchange degree [-]

$\eta_i :$ effectiveness factor for mass transport phenomena in the gas and the solid phase [-]

$\theta_j :$ surface coverage of j surface site (j = S1, S2, S3, S4, S5) [-]

μ: dynamic viscosity [(N·s)/m^2]

$\rho_g :$ density of gas mixture [kg/m^3]

$\rho_s :$ density of the solid phase [kg/m^3]

$\phi :$ Thiele modulus [-]

$\phi_{film} :$ chemical source term due to ammonia's adsorption and desorption, including mass transfer phenomena in both gas and solid phase [mol/(m^3·s)]

$\Phi_{w\_ext} :$ global external heat transfers [W]

$v_j :$ stoichiometric coefficient of NH$_3$ adsorption and desorption over each site [-]

$\dot{\omega}_i :$ chemical source term due to the chemical reactions for the species i [mol/s]

Table of contents

Extended Summary

Transportation is one of the most important sources of worldwide nitrogen oxide (NO_x) emissions. NO and NO_2 existing in mobile diesel engines exhaust stream are related to severe environmental and public health impacts and hence they are subjected to increasingly stringent restrictions. To meet forthcoming diesel engines NO_x emissions legislation, sophisticated engine calibration and/or advanced aftertreatment systems are required. Regarding the latter, the Selective Catalytic Reduction of nitrogen oxides through urea or ammonia is a well established technique, enabling an efficient abatement of NO_x, produced by mobile diesel sources. So far, different catalytic formulations have been proposed for SCR catalytic systems, including noble metal and vanadium/tungsten based catalysts. Recently, transition metal exchanged zeolites have been introduced in the automotive sector, since they exhibit increased $deNO_x$ performance over a broad range of engine operating temperatures, as well as significant resistance to hydrothermal ageing.

Modeling and simulation could be a very useful tool, towards the development of highly efficient exhaust aftertreatment systems. Computer aided engineering (CAE) can enable automotive OEMs and suppliers to optimize the design and properties of individual catalytic devices as well as the exhaust aftertreatment systems layout. In this context, kinetic concept modeling may provide particular opportunities, since it could facilitate to unravel complicated reaction pathways, determine optimized catalytic properties and study poisoning and ageing issues. As far as the modeling of chemical reactions is concerned, several approaches are reported in the recent literature, involving different levels of complexity. Kinetic models may range from molecular dynamics to global kinetic models, based on the mean field approximation, hence providing different levels of understanding and simulation precision.

In the frame of the present work, experimental studies were performed in order to develop a phenomenological macro-kinetic model of NH_3-SCR over Fe-zeolite based catalysts, oriented to diesel engines aftertreatment system simulation. A correlation between Fe-zeolite structural properties and a phenomenological macro-kinetic model constitutes the actual thesis innovation. At a first stage, dedicated experimental analysis was performed over lab-synthesized H- and Fe-exchanged zeolites in order to unravel mechanistic aspects related to the NH_3-SCR reactions network. Employing in-situ IR spectroscopy, interactions of NH_3 and NO_x with different surface sites were characterized and respective reaction pathways were identified. Based on this analysis, a multi-site kinetic model was subsequently developed, which could account for NH_3-SCR reactions occurrence over acidic and redox sites. The kinetic model was finally calibrated and validated by simulating experiments performed over lab-synthesized H- and Fe-BEA samples as well as commercial Fe-zeolites.

The methodology followed is based on a two parallel axes analysis, which includes detailed kinetic modeling and experimental studies. Regarding the former, a 0D SCR catalytic converter model was developed and a multi-site kinetic model was implemented. The latter was developed on the basis of NH_3 adsorption and desorption experiments over H- and Fe-ZSM5 catalysts reported in the recent literature. Thus, a "skeleton" of a detailed kinetic model was determined, which could be further capitalized in order to include reactions of the NH_3-SCR network. In parallel, a Fe-exchanged BEA

zeolite was synthesized in the laboratory under well controlled conditions and characterized, employing various optical techniques. Hence, a reference catalytic sample was obtained, which enable to perform well targeted experiments for depicting mechanistic aspects related to NH_3-SCR over Fe-zeolites.

Once having prepared the reference kinetic model and the Fe-BEA catalytic sample, the actual reaction pathways related to the SCR of NO_x through NH_3 were experimentally investigated and modeled. The first step of the NH_3-SCR process is the storage of ammonia. Therefore, NH_3 adsorption and TPD experiments were coupled with IR spectroscopic measurements in order to identify ammonia interactions with Lewis and Brønsted acidic sites, as well as iron, redox sites. Utilizing obtained experimental results the reference multi-site kinetic model was further capitalized by drawing correlations between model and Fe-zeolite surface sites. The updated kinetic model was then calibrated employing data reported in the literature, as well as structural properties obtained through catalyst characterization (namely Si/Al and Fe/Al ratios). Finally, using a single set of kinetic parameters the proposed multi-site kinetic model was validated by simulating NH_3 adsorption and TPD experiments performed over the H- and the Fe-BEA lab-synthesized samples, applying a broad range of operating conditions.

Another group of reactions related to the SCR process is the storage of NO_x and NO oxidation, which are related to formation of nitrite and nitrate adspecies. Therefore, adsorption and desorption of NO and NO_2 in the presence and absence of oxygen were experimentally studied over the same samples. Employing IR spectroscopy, NO_2 adsorption and disproportionation (towards nitrates/nitrites), as well as NO storage and oxidation, over acidic and redox surface sites were depicted. Based on obtained results a respective multi-site kinetic model was developed accounting for NO_x storage and nitrates/nitrites formation and decomposition on different catalytic positions. In analogy with the kinetic model of NH_3 storage, the proposed kinetic model was calibrated utilizing data reported in literature and structural properties of the studied samples. Finally, it was validated through simulation of NO_2 adsorption and TPD as well as NO/O_2 STPD experiments performed on the studied samples and on lab-synthesized and commercial Fe-BEA catalysts reported in the recent bibliography.

Finally, reactivity between NH_3 and NO_x, under lean conditions was experimentally investigated. Performing NO_x-NH_3 TRM and TPD runs, coupled with IR spectroscopy, interactions between ammonia and nitrogen oxides adspecies on different surface sites were identified. Focusing on low temperature SCR conditions, formation and decomposition of ammonium nitrate was of particular concern, since this intermediate species control catalyst activity at this temperature regime. In order to further investigate the effect of acidic and redox sites of H- and Fe-BEA on NH_4NO_3 decomposition, additional experiments were performed (TGA, DSC, thermo-XRD), using powder NH_4NO_3. Obtained results were compared with respective observations made during TRM-TPD experiments, enable to elucidate the mechanisms related to the thermal decomposition of ammonium nitrate.

Compiling information obtained from the latter section, a deep understanding of interactions between NH_3 and NO_x, with respect to Fe-zeolite structural properties was gained. Therefore, using the respective experimental results detailed multi-site kinetic models of NH_3 and NO_x storage and NO

oxidation could be coupled, leading to a complete phenomenological macro-kinetic model of NH_3-SCR over Fe-zeolite catalysts, oriented to diesel engines aftertreatment system simulation.

Résumé étendu

    Le secteur des transports est l'une des plus importantes sources mondiales d'émissions d'oxydes d'azote (NO_x). Les NO et NO_2 existants à l'échappement des moteurs Diesel mobiles sont la cause d'impacts environnementaux et de santé publique graves et sont donc sujets à des régulations de plus en plus sévères. Pour atteindre la future norme sur les émissions de NO_x des moteurs Diesel, une calibration moteur raffinée et/ou des systèmes de post-traitement avancés sont requis. Concernant ce dernier point, la réduction catalytique sélective des oxydes d'azote au moyen de l'urée ou de l'ammoniac est une technique bien connue, permettant une conversion efficace des NO_x, produits par les sources mobiles Diesel. Jusqu'à maintenant, différentes formulations catalytiques ont été proposées pour les systèmes catalytiques SCR, incluant des catalyseurs basés sur des métaux nobles et du vanadium/tungstène. Récemment, les zéolithes échangées aux métaux de transition ont été introduites dans le secteur automobile, puisqu'ils montrent une performance accrue du traitement des NO_x sur une large gamme de température de fonctionnement du moteur ainsi qu'une résistance significative au vieillissement hydrothermique.

    La modélisation et la simulation peuvent être un moyen très utile, vers le développement de systèmes de post-traitement hautement efficaces. Le "Computer-Aided Engineering" (CAE) peut permettre aux OEMs et aux fournisseurs d'optimiser la conception et les propriétés des catalyseurs ainsi que celles de la ligne d'échappement complète. Dans ce contexte, le concept de la modélisation cinétique peut fournir des opportunités particulières, car il peut faciliter l'analyse des voies réactionnelles complexes, la détermination des propriétés optimales catalytiques et l'étude des problèmes liés à l'empoisonnement et au vieillissement. En ce qui concerne la modélisation des réactions chimiques, plusieurs approches existent dans la littérature récente, impliquant différents niveaux de complexité. Les modèles cinétiques s'échelonnent de la dynamique moléculaire aux modèles cinétiques globaux, basés sur l'approximation de champ moyen, fournissant donc différents niveaux de compréhension et de précision.

    Dans le cadre de ce travail, des études expérimentales ont été réalisées de façon à développer un modèle phénoménologique macro-cinétique des catalyseurs SCR à l'urée basés sur les zéolithes au fer, appliqués à la simulation des systèmes de post-traitement des moteurs Diesel. La corrélation entre les propriétés structurelles des zéolithes au fer et le modèle phénoménologique macro-cinétique constitue l'innovation apportée par la thèse. Dans un premier temps, une analyse expérimentale détaillée a été réalisée sur des zéolithes échangées au fer et des zéolithes protonées, synthétisées en laboratoire, afin d'étudier les aspects mécanistiques liés aux réactions SCR. En utilisant la spectroscopie IR, en conditions in-situ, les interactions entre les espèces NH_3 et NO_x et les différents sites de surface ont été caractérisées et les voies réactionnelles respectives ont été identifiées. Sur la base de cette analyse, un modèle cinétique multi-site a été ensuite développé, prenant en compte la réalisation des réactions SCR sur des sites acides et redox. Le modèle cinétique a finalement été calibré et validé en simulant les expériences réalisées sur les échantillons H- et Fe-BEA synthétisés au laboratoire ainsi que sur des zéolithes échangées au fer commerciales.

La méthodologie suivie est basée sur deux axes parallèles d'analyse, qui incluent une modélisation cinétique détaillée et des études expérimentales. Concernant la modélisation, un modèle de catalyseur SCR 0D a été développé et un modèle cinétique multi-site a été implémenté. Ce dernier a été conçu sur la base des essais d'adsorption et de désorption du NH_3 sur des catalyseurs H- et Fe-ZSM5 présentés dans la littérature. De cette façon, un squelette de modèle cinétique détaillé a été déterminé, et pourra par la suite être capitalisé pour inclure les réactions du processus SCR. En parallèle, une zéolithe de type BEA échangée au fer a été synthétisée au laboratoire en conditions contrôlées et caractérisée en employant plusieurs techniques optiques. Un échantillon catalytique de référence a donc été obtenu, ce qui permet de réaliser des essais ciblés afin de comprendre les aspects mécanistiques liés à la SCR sur les zéolithes au fer.

Une fois que le modèle cinétique de référence et l'échantillon catalytique Fe-BEA, les voies réactionnelles liées à la SCR des NO_x par NH_3 ont été expérimentalement étudiées et modélisées. La première étape du processus NH_3-SCR est le stockage d'ammoniac. Les expériences d'adsorption et de TPD du NH_3 ont été combinés avec les mesures spectroscopiques IR de façon à identifier les interactions entre l'ammoniac et les sites acides de type Lewis et Bronsted, ainsi qu'avec des sites fer, redox. En utilisant les résultats expérimentaux obtenus, le modèle cinétique multi-site de référence a ensuite été capitalisé en faisant le lien entre le modèle et les sites de surface Fe-zéolithe. Le modèle cinétique mis à jour a ensuite été calibré en utilisant des données de la littérature, ainsi que des propriétés structurelles obtenues par la caractérisation du catalyseur (notamment les rapports Si/Al et Fe/Al). Finalement, en utilisant un ensemble de paramètres cinétique unique, le modèle multi-site proposé a été validé en simulant les essais d'adsorption et de TPD réalisés sur des échantillons H- et Fe-BEA synthétisés au laboratoire. Une large gamme de conditions de fonctionnement a été appliquée.

Un autre groupe de réactions associées au processus SCR est le stockage des NO_x et l'oxydation du NO qui sont reliées à la formation des espèces de surface nitrite et nitrate. L'adsorption et la désorption de NO et de NO_2 en présence et en l'absence d'oxygène a ensuite été étudié expérimentalement sur les mêmes échantillons. Les mesures par spectroscopie IR ont été réalisées afin d'étudier l'adsorption et la disproportionation (vers les nitrates et nitrites), ainsi que le stockage et l'oxydation du NO sur des sites de surface acides et redox. Basé sur les résultats obtenus, un modèle cinétique multi-site dédié a été développé en prenant en compte le stockage des NO_x et la formation et décomposition des nitrates/nitrites sur différentes positions catalytiques. Par analogie avec le modèle cinétique du stockage du NH_3, le modèle cinétique proposé a été calibré avec des données de la littérature et avec les propriétés structurelles des échantillons utilisés. Finalement, il a été validé par la simulation des expériences d'adsorption et TPD du NO_2 ainsi celle des expériences STPD NO/O_2 réalisées sur les échantillons étudiés et sur les catalyseurs synthétisés au laboratoire et les catalyseurs commerciaux Fe-BEA décrits dans la littérature récente.

Finalement, la réactivité entre NH_3 et NO_x en conditions pauvres a été expérimentalement étudiée. En réalisant des essais NO_x-NH_3 TRM et TPD, couplés avec la spectroscopie IR, les interactions entre les espèces de surface ammoniac et oxydes d'azote sur différents sites de surface ont pu être identifiées. En se focalisant sur les conditions SCR basse température, la formation et la décomposition du nitrate d'ammoniac a été mis en avant puisque cette espèce intermédiaire contrôle l'activité du catalyseur dans cet intervalle de température. De façon à étudier par la suite l'effet des

sites acides et redox des catalyseurs H- et Fe-BEA sur la décomposition du NH_4NO_3, des essais supplémentaires ont été réalisés (ATG, DSC, thermo-DRX) en utilisant une poudre de NH_4NO_3. Les résultats obtenus ont été comparés avec les observations faites pendant les expériences TRM-TPD, et ont permis d'élucider les mécanismes relatifs à la décomposition thermique du nitrate d'ammonium.

En compilant les informations obtenues dans la section précédente, une profonde compréhension des interactions entre NH_3 et NO_x du point de vue des propriétés structurelles des zéolithes au fer a été acquise. En utilisant les résultats expérimentaux, les modèles cinétiques multi-sites détaillés portant sur le stockage du NH_3, sur le stockage des NO_x et sur l'oxydation du NO peuvent ainsi être couplés. Ceci résultant en un modèle macro-cinétique phénoménologique complet de la SCR à l'ammoniac sur catalyseurs zéolithe au fer, appliqué à la simulation des systèmes de post-traitement des moteurs Diesel.

Chapter 1

General Introduction and Bibliography Review

1 General Introduction and Bibliography Review

Abstract

An extensive overview of the Selective Catalytic Reduction of nitrogen oxides (NO_x) through urea/ammonia (Urea/NH_3-SCR), over Fe-exchanged zeolites is presented in this chapter. The review, which is oriented to diesel engine vehicles, aftertreatment applications, covers a great variety of topics, ranging from the state of the art of Urea-SCR automotive catalysts to detailed chemical aspects of the selective catalytic reduction process over Fe-zeolites. Considering the forthcoming stringent legislation related to NO_x emissions from diesel engines, a comprehensive review of modern deNO$_x$ technologies is given, namely focusing on the concept of Urea-SCR over Fe-exchanged zeolites. The chemistry of the SCR of NO_x as well as the respective kinetic concept modeling are of major concern.

Regarding the understanding of the SCR network over iron based zeolites, global and semi-detailed kinetic schemes available in literature are presented. Moreover, results from experiments are discussed in order to get more insight into mechanistic aspects related to the SCR chemistry. Thus, an attempt is made to bridge the gap between micro- and macro-scale phenomena of the NH_3-SCR process. Particular attention is paid for low temperature operating conditions, where formation of ammonium nitrate (NH_4NO_3) is considered, inhibiting temporarily catalyst deNO$_x$ activity.

As far as the kinetic modeling of the NH_3-SCR is concerned, semi-detailed and global models are mainly under consideration due to the well balanced trade off between complexity and accuracy, with respect to model calibration and computational time. Reported approaches are analyzed and compared so as to identify the level of complexity and accuracy of different models, depicting reactions of the SCR process.

Based on the abovementioned results the objectives of this work are discussed and the contribution of the respective results to existing bibliography is highlighted. Finally, the methodology followed is analyzed.

Résumé

Un panorama exhaustif de la réduction catalytique sélective des oxydes d'azote (NO_x) par l'urée/ammoniac (Urea/NH_3-SCR), sur les zéolithes échangées au fer est présenté dans ce chapitre. Cette révision, qui est orientée vers les applications de post-traitement véhicules à moteur Diesel, couvre une grande variété de sujets, allant de l'état de l'art des catalyseurs SCR à l'urée automobiles et les aspects chimiques détaillés de la réduction catalytique sélective sur zéolites au Fe. Compte tenu de réglementations futures strictes concernant les émissions de NO_x des moteurs Diesel, un examen complet des technologies modernes de post-traitement des NO_x est donnée, à savoir en se concentrant sur le concept de l'urée-SCR sur les zéolithes échangées au fer. La chimie du SCR des NO_x ainsi que la modélisation des concepts respectifs cinétiques sont une préoccupation majeure.

En ce qui concerne la compréhension des voies réactionnelles SCR sur les zéolithes échangées au fer, les schémas cinétiques globaux et semi-détaillés rapportés dans la littérature sont présentés. En outre, les résultats expérimentaux sont présentés dans le but d'obtenir un meilleur aperçu des aspects mécanistiques concernant la chimie SCR. Ainsi, une tentative est faite pour combler le fossé entre les phénomènes micro-et macro-échelle du processus de la SCR. Une attention particulière est accordée aux conditions de fonctionnement à basse température, où la formation du nitrate d'ammonium (NH_4NO_3) est considérée, en inhibant temporairement l'activité du catalyseur.

En ce qui concerne la modélisation cinétique de la SCR par le NH_3, les modèles semi-détaillés et globaux sont principalement à l'étude en raison d'un compromis bien équilibré entre la complexité et la précision, à l'égard de la calibration du modèle et du temps de calcul. Les approches rapportées sont analysées et comparées afin d'identifier le niveau de la complexité et de la précision des différents modèles, représentant les réactions du procédé SCR.

D'après les résultats mentionnés ci-dessus les objectifs de la thèse doctorale présentée sont discutés et la contribution des résultats respectifs à la bibliographie existante est mise en avant. Enfin, la méthodologie suivie est analysée.

1.1 NO$_x$ emissions and standards for diesel vehicles

Nitrogen oxides (NO$_x$) are one of the major atmospheric pollutants existing in the exhaust gas of internal combustion diesel engines. Formed in the engine cylinder due to reactions between N$_2$ and O$_2$ at high temperature, they include nitrogen monoxide, (or nitric oxide) NO and nitrogen dioxide, NO$_2$ [1]. NO is a colorless, odorless and tasteless gas, which can be slowly oxidized to nitrogen dioxide in the atmosphere, whereas NO$_2$ is a poisonous reddish-brown gas with a penetrating odor [2]. Besides NO and NO$_2$, nitrous oxide (N$_2$O) can be also formed in diesel engines aftertreatment system, as it is going to be discussed later. Typical NO$_x$ concentrations in diesel exhaust stream range from 50 to 100 ppm at idle and 600 to 2000 ppm at full load, with NO being in abundance (approximately 70% - 90%), under typical engine operating conditions [2].

The control of NO$_x$ emissions is of great importance because of their harmful environmental [3,4] and health [5,6] effects. Regarding public health issues, NO$_x$ and especially NO$_2$ can easily react with ammonia, moisture and other compounds to form small particles that can penetrate deeply into lungs sensitive parts, causing adverse respiratory and aggravated cardiologic diseases. Exposure to NO$_x$ is proved to cause airway inflammation and respiratory symptoms such as asthma, emphysema and bronchitis. As far as environmental effects are concerned, NO and NO$_2$ are noxious, contributing directly to the formation of acid rain. Furthermore, the photochemical reaction of NO$_x$ with volatile organic compounds (VOC) in the atmosphere leads to the formation of ground-level ozone (smog) and particulates. These phenomena result in impaired air quality, acidification of streams and coastal and/or forest ecosystems, as well as accelerated decay of materials, cultural artifacts paints etc. Besides NO and NO$_2$, N$_2$O has both environmental and health impacts, exhibiting narcotic activity on humans [7], whereas it is also considered to be a potent greenhouse gas contributing to global warming [8].

The contribution of cars and heavy duty vehicles to severe air pollution, due to gaseous emissions and particulate matters, is already known and well documented. Since around 48% of NO$_x$ emissions in European countries are produced by transportation (Figure 1.1) [9], NO$_x$ deriving from diesel engines are subjected to significant restrictions. Forthcoming Euro 6 regulations (by 9/2014) [10] impose a limit of 0.08 g/km NO$_x$ and 0.17 g/km of combined NO$_x$ and hydrocarbon (HC) emissions, which corresponds to a 55% and a 26% reduction respectively compared to the Euro 5 standards, currently being in force (Table 1.1). Similar trends appear in the USA [11], where ULEV II or SULEV II Californian standards and low-bin Federal Tier 2 standards restrict NO$_x$ emissions up to 0.02 g/mile. Even though NO and NO$_2$ emissions are regulated, N$_2$O emissions are not [12]. The main source of nitrous oxide emissions is the agricultural sector, whereas the respective contribution of transportation remains limited [13].
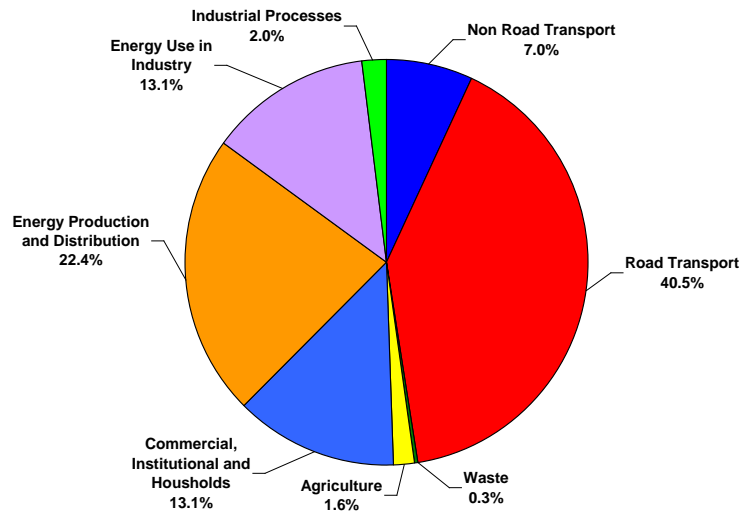
Figure 1.1 Sector share of nitrogen oxides emissions: data collected during 2010 (EEA member countries) [9].

Table 1.1 Evolution of European Union emission standards for passenger cars (data extracted from reference [14]).

Emission standards[1]	Gasoline Engines				Diesel Engines			
	CO	HC	NO_x	$HC+NO_x$	CO	NO_x	$HC+NO_x$	PM
Euro 1 (1993)	2.72	-	-	0.97	2.72	-	0.97	0.14
Euro 2 (1996)	2.20	-	-	0.5	1.00	-	0.90	0.10
Euro 3 (2000)	2.30	0.20	0.15	-	0.64	0.50	0.56	0.05
Euro 4 (2005)	1.00	0.10	0.08	-	0.50	0.25	0.30	0.025
Euro 5 (2009)	1.00	0.10	0.06	-	0.50	0.18	0.25	0.005
Euro 6 (2014)	1.00	0.10	0.06	-	0.50	0.08	0.17	0.005

[1] Emissions in (g/km).

1.2 Diesel engine de-NO_x technologies – Overview

The abatement of NO_x (deNO_x) from diesel exhaust gas can be accomplished nowadays thanks to the dramatic technological development in the fields of engine design and management as well as exhaust aftertreatment systems. A detailed review of modern methodologies applied for the limitation of nitrogen oxide emissions is presented elsewhere [15,16].

Concerning in-cylinder NO_x formation restriction, proper engine design and calibration aim mainly to control the combustion temperature and the air-to-fuel ratio so as to limit NO_x formation in engine combustion chamber. Towards this direction, various techniques can be implimented, notably the Exhaust Gas Recirculation (EGR), which includes the introduction of exhaust gas directly inside the chamber lowering the combustion temperature [17]. Other techniques include the throttling of the air

flow in the inlet manifold, resulting in a richer air-fuel mixture [18] or the increase of the air humidity upstream the cylinder, leading to a significant decrease in combustion temperature [19].

Regarding the application of aftertreatment devices, two technologies are mainly applied: (i) NO_x absorbers or Lean NO_x Traps (LNT) [20,21] and (ii) the Urea or NH_3 Selective Catalytic Reduction (Urea- or NH_3-SCR) catalysts [22,23]. The LNT was initially introduced in the automotive sector by Toyota [24,25]. According to this technology, NOx chemisorbs on the catalytic surface during engine lean operation [26]. By running the engine periodically in rich mode, unburned hydrocarbons are emitted in the exhaust manifold, reducing selectively stored NO_x. Even though LNT conversion efficiency of nitrogen oxides exceeds 90% within a temperature range of 200 – 400 °C, it is significantly limited at higher ones [27]. Moreover, the fuel penalty, linked with its performance [28], as well as thermal ageing [29] and sulphur poisoning [30] issues are not to be neglected.

The alternative to this method is the Urea or NH_3–SCR catalyst, which enables the reduction of NO_x through ammonia. The Urea-SCR concept was initially applied for NO_x abatement from stationary engines and particularly from coal fired boilers in Japanese power plants (late 1970s) [31]. SCR introduction, for the reduction of NO_x from the exhaust stream of mobile sources was launched with marine engines, when the first SCR systems were installed in 1989 and 1990 on two Korean carriers [32]. Only after 2000, SCR was applied to passenger cars and heavy duty vehicles, starting with Mercedes-Benz, the first manufacturer, which utilized an urea SCR catalyst on a passenger car named E320 BlueTEC, in October 2006 [33]. According to this technology a standardized 32.5% aqueous urea solution ($(NH_2)_2CO + H_2O$), which is well known with the commercial name AdBlue, is directly injected inside the exhaust stream, upstream the converter, reducing selectively and continuously NO_x on the catalytic surface [34]. New materials ensure high SCR performance over a wide range of operating conditions. Nevertheless, system complexity as well as the storage and management of urea and/or NH_3 are important limitations to be tackled.

1.3 The Urea-SCR catalyst

A typical configuration of a Urea-SCR system is described elsewhere [35]. As shown in Figure 1.2 A, the urea solution, which is stored in a special on board tank, is injected directly in the exhaust pipe, upstream the SCR catalyst. Once mixing with the exhaust gas through a static mixing device, urea undergoes hydrolysis and thermal decomposition leading to the formation of ammonia (optionally within a hydrolysis catalyst). Then, ammonia can selectively reduce NO_x leading to the formation of nitrogen and water. Since the SCR process is incomplete, part of ammonia is not consumed within the catalyst and escapes to environment. The latter, which is called "ammonia slip" is often tackled through the use of an additional oxidation catalyst placed downstream the SCR catalyst (ammonia slip catalyst), converting NH_3 to molar nitrogen as well as N_2O or NO.

The complexity of the Urea-SCR system, in particular the urea management and the SCR system control calls for on board electronic management. Concerning the urea management, two main issues are to be emphasized, including, the onboard urea storage and/or supply as well as the urea injection. Regarding the former, Adblue freezes at temperatures lower than -11 °C, which can completely block

urea supply during low ambient temperature winter conditions. Heating of urea supply lines as well as by-pass ducts for emptying the dosing system when the engine is turned off can minimize the risk of urea injection problems guarantying the SCR system safety [36]. As far as urea injection issues are concerned, undesirable urea byproducts deposits are of major concern. Solid urea deposits originate from the incomplete decomposition of urea at low temperatures (<152 °C), resulting in the formation of solid biuret and cyanuric acid [37]. These compounds can accumulate on several surfaces of the Urea-SCR system (including tube walls, injector, mixer surfaces and even the inlet cross-section of the actual SCR catalyst) and lead to an increase of exhaust aftertreatment system backpressure and materials erosion [37]. Optimized positioning of the urea injector in order to enhance SCR catalyst dosing and ensure the urea-SCR system durability has been reported in numerous studies [38,39].

As far as the management of the Urea-SCR system is concerned, a closed - loop architecture is generally preferred where a pre-programmed map of engine NO_x emissions is used to control the urea injection rate [40]. Thus, not only a NO_x conversion efficiency up to 98% can be accomplished but the converter can be protected from ageing or poisoning as well. Finally, due to stringent forthcoming legislation for both NO_x and particulate matters (PM) emissions, the combined use of diesel particulate filters (DPF) and Urea–SCR catalysts is required. The arrangement of these two devices in the same exhaust line, which represents a great challenge, is discussed elsewhere [41] (Figure 1.2 B). Recently, a new technology has been introduced, suggesting the utilization of a single SCR/DPF device, which is composed of a wall-flow filter coated with a SCR catalytic layer in a single substrate [42,43]. Finally, a combined LNT – Urea-SCR catalyst is also possible, according to which NH_3 produced within the LNT is then employed by the Urea-SCR catalyst for additional NO_x conversion [44,45].

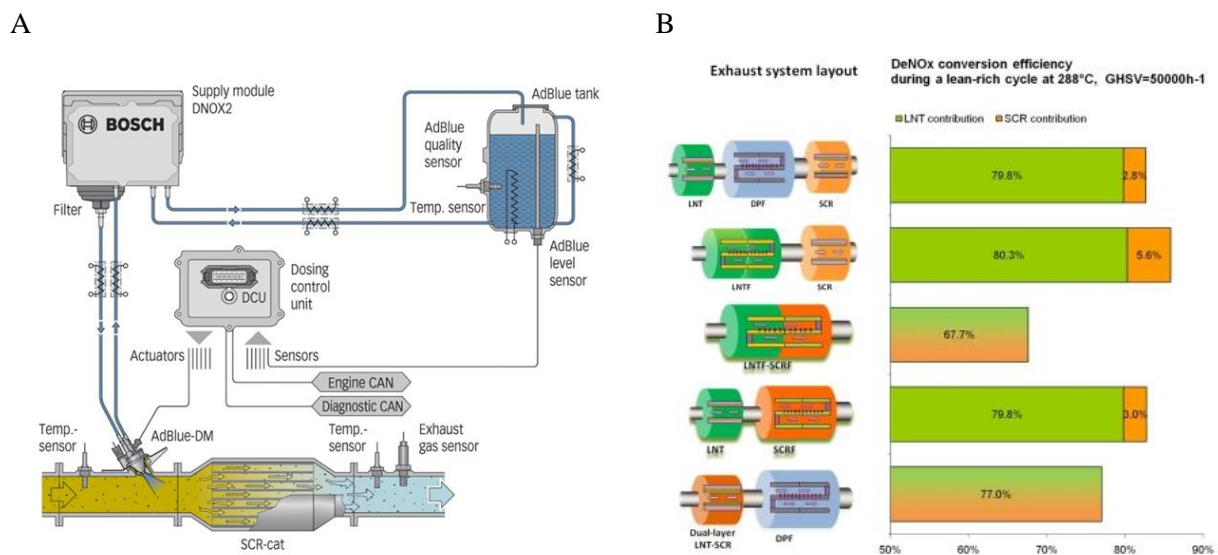A   B

Figure 1.2 A) Urea-SCR system configuration [35], B) Model based comparison of deNO$_x$ systems [46].

NH_3-SCR has been tested over various catalytic formulations. Precious metals, vanadium and transition metal exchanged zeolites are mainly reported for mobile applications and can be classified

on the basis of their maximum activity [9] (Figure 1.3 A). Baik et al. have reported that Pt-based catalysts (Pt/Al$_2$O$_3$) exhibit high performance within a temperature range of 150 – 230 °C, whereas further temperature increase leads to a deterioration of NO conversion due to the catalytic oxidation of ammonia to NO and/or N$_2$ [47]. In order to achieve high deNO$_x$ efficiency at elevated temperatures, vanadium-based catalysts were introduced [48]. These catalysts constitute homogeneous mixtures of titanium dioxide (TiO$_2$), tungsten trioxide (WO$_3$) (or molybdenum trioxide - MO$_3$) and divanadium pentoxide (V$_2$O$_5$), formulated in honeycomb shapes. SCR activity of such catalysts becomes limited however above 450 °C because of deactivation, which is related to a phase transformation of TiO$_2$ anatase into TiO$_2$ rutile with simultaneous vanadia species release in the atmosphere [49]. Vanadium pentoxide is considered to be toxic and thus, respective emissions may have raise public health issues.
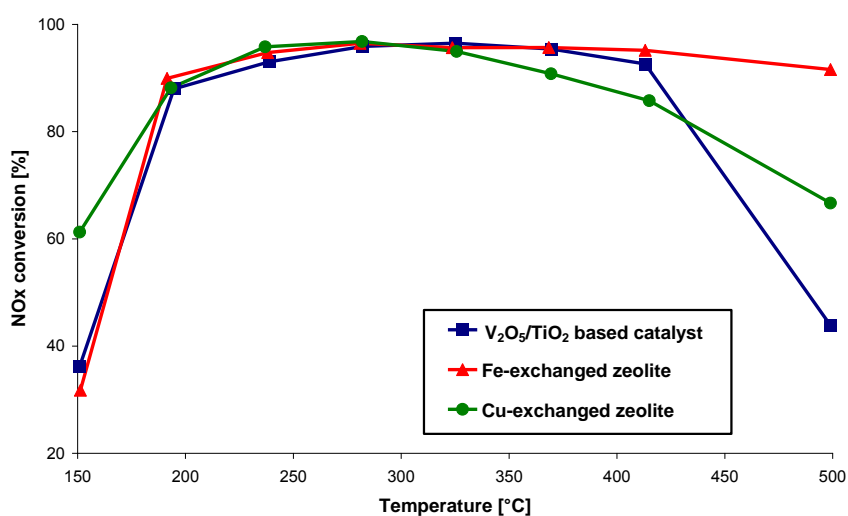
Figure 1.3 Operating temperatures of different types of urea SCR catalysts for vehicle applications. Data extracted from reference [50].

Modern aftertreatment system configurations may include a diesel particulate filter, placed in most cases, upstream the SCR catalyst. Hence, a Urea-SCR converter can experience temperatures more than 700 °C during DPF's regeneration [51]. Zeolite based catalysts were proposed as an alternative to vanadium-based ones, since they exhibit enhanced performance over a broad range of temperatures, as well as significant resistance to hydrothermal ageing. Cu- Fe- and Mn zeolite based catalysts have already been tested, showing very satisfactory performance [52,53,54]. Regarding Fe-zeolites they are considered to exhibit high NO$_x$ conversion at a temperature range of 150 – 550 °C, being also resistant to elevated hydrothermal temperatures [55,56]. At low temperatures their activity is based on their high NO$_x$ selectivity, whereas at high ones it is limited due to durability. At temperatures higher than 600 °C and in the presence of water (steam), ion exchanged zeolites are deactivated due to de-alumination, according to which Al^{3+} ions in the silica framework migrates out of the zeolite's structure leading to the irreversible catalyst deactivation [57]. Finally, as far as sulphur poisoning is concerned, temporary deactivation has been reported over Fe-zeolites due to exposure to SO$_2$ and/or SO$_3$ and the catalyst can be regenerated by heating it up to 650 °C in excess of oxygen [22]. Finally, it

has to be pointed out that Fe based zeolites sulphur tolerance is also affected by the catalyst ageing status [22].

1.4 Zeolites as SCR catalysts

1.4.1 General overview

Zeolites are crystalline, microporous alumina-silicate minerals with well defined crystalline structure and pore sizes [58]. The term "zeolite" originates from a combination of the Greek words "ζέω" (zeo) and "λίθος" (lithos), literally meaning "a boiling stone", because of zeolites tendency to release water when being heated [59]. They can be either natural or synthetic and are used in many industrial applications, including petroleum refining, sewage treatment, odor control, soil conditioning and water softening for household water treatment units [60]. Among these applications the use of zeolites for Fuel Catalytic Cracking (FCC) of heavy petroleum distillation (1962) is to be emphasized, since it led to an outstanding gasoline yield enhancement in the order of magnitude of several billion US dollars per year, reducing simultaneously refining costs by at least 10 US dollars per year [61].

The ideal zeolite structure (Figure 1.4) includes [62]:

➢ a three dimensional framework formed by TO_4 tetrahedra (T = Si,Al), where each oxygen atom is bonded to two neighboring T elements

➢ channels and cavities of molecular size, where charged compensating cations as well as other molecules are located.

The existence of the negative charged $[AlO_4]^-$ must be compensated by a cation, in order to maintain the overall electroneutrality of the zeolite and thus, structure stability. Such cations may be alkali, alkaline earth or R_4N^+ cations (R=H, alkyl, aryl) [62]. The generic chemical formula is shown below:

$$x_1 M_1^{n1}; x_2 M_2^{n2}; y_1 T_1; y_2 T_2)O_2(y_1 + y_2)^{x-}$$
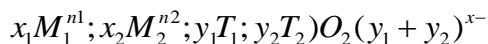
where T stands for the Si and Al elements in tetrahedral coordination, Mi corresponds to cations with charge n_i for framework negative charge compensation. Finally, the sum $\Sigma x_i n_i$ must be equal to x.

As far as synthetic zeolites are concerned, depending on the zeolite type, the synthesis method and the post-synthesis treatment the zeolitic framework may exhibit defective sites, which correspond to non bridging oxygen and vacant sites [62] and which can be charged or neutral [63]. Typically the size of a synthetic crystal is in the order of magnitude of 1 up to several μm, whereas, channels diameter ranges between 0.3 and 1.3 nm [62]. Moreover, zeolites channels network results in high internal surface areas of maximum 800 m^2/g and pore volumes of 0.35 cm^3/g [62]. Based on the structure topology different structure types of zeolites are identified. A complete review can be found in the atlas of zeolite framework type [64]. According to it, different zeolites are classified based on their framework density, which is expressed as the number of TO_4 tetrahedra contained in a volume of 1000 $Å^3$.

I) TO$_4$ tetrahedra (T = Si,Al)

Si   Al   O
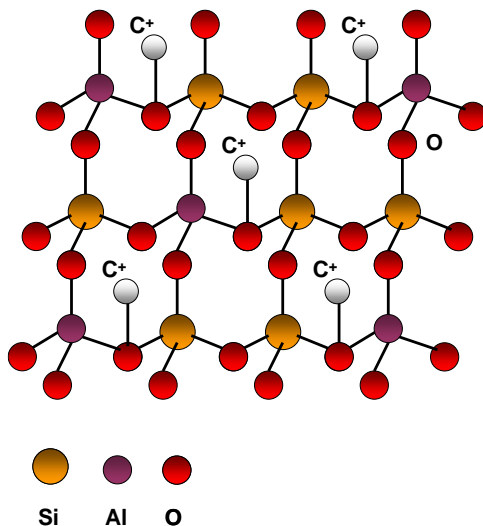
II) Arrangement of TO$_4$ tetrahedra (T = Si,Al) in a zeolite framework
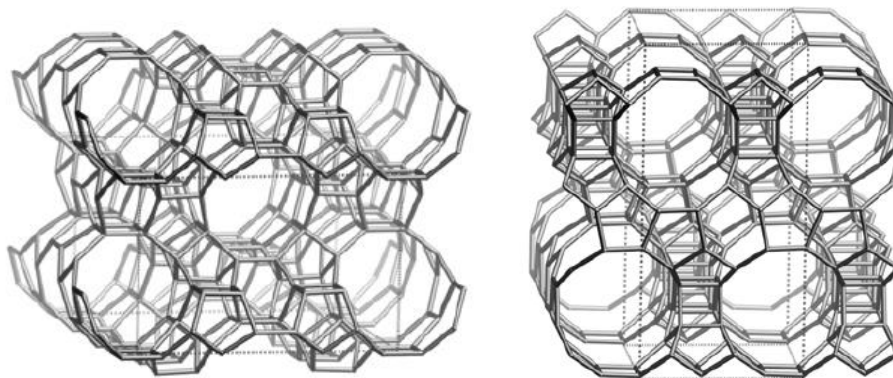
III) Channels network of a ZSM5 (left) and BEA (right) zeolites (figures obtained from [64])

Figure 1.4 Schematic representation of a zeolite ideal structure.

1.4.2. Zeolite properties

The most important zeolite property, being associated with catalytic applications is acidity. According to classical acido-basicity theories of Brønsted-Lowry (1923) and Lewis (1923) two different definitions of an acid exist [65]. Based on the former, an acid-base reaction includes a proton transfer from the acid to the base, thus, the acid behaves as a proton donor, leading to the protonation

of the interacting base. On the other hand, in Lewis theory, an acid is represented as an electron pair acceptor, aiming to complete its own valence ring, adopting a stable electron configuration.

Based on these definitions, both Brønsted and Lewis type acidic sites have been identified in the framework of several zeolites. Simon-Masseron et al. [63] have suggested the existence of three different types of acidic sites, based on the Al location in the zeolitic structure: a) framework Al atoms, that form Si, Al hydroxyl bridged groups (Si-OH-Al) and hence Brønsted type acidic sites, b) partially coordinated Al atoms that correspond to Lewis acidic sites and finally c) extra-framework Al sites that can be either polymeric or monomeric, charged or neutral.

Overall zeolitic acidity is modulated by two parameters including acidic sites density and strength. Regarding the former, acidic sites concentration is proportional to zeolite Si/Al ratio. Interestingly, NH_3 temperature programmed desorption (NH_3-TPD) studies over H-ZSM5 zeolites of different Si/Al ratios, reported by Costa et al. [66] showed that H^+ cations density and thus, Brønsted sites decrease linearly by increasing the Si/Al ratio. On the other hand acidity strength and particularly that of Brønsted sites is related to structural properties of the $Si-OH^+$-Al sites, as well as the chemical composition of the zeolitic cavities [59]. OH^+ acidity strength increases when the $O-H^+$ bond is elongated and the Si-O and/or Al-O bond lengths decrease. Finally, regarding the composition of the zeolitic cavity, an increased number of neighboring Al tetrahedra leads to a degradation of the local electronegativity of the framework and thus to low acidity strength. An overview of the acidity strength of different zeolites is reported elsewhere [67] and results are summarized in Figure 1.5.
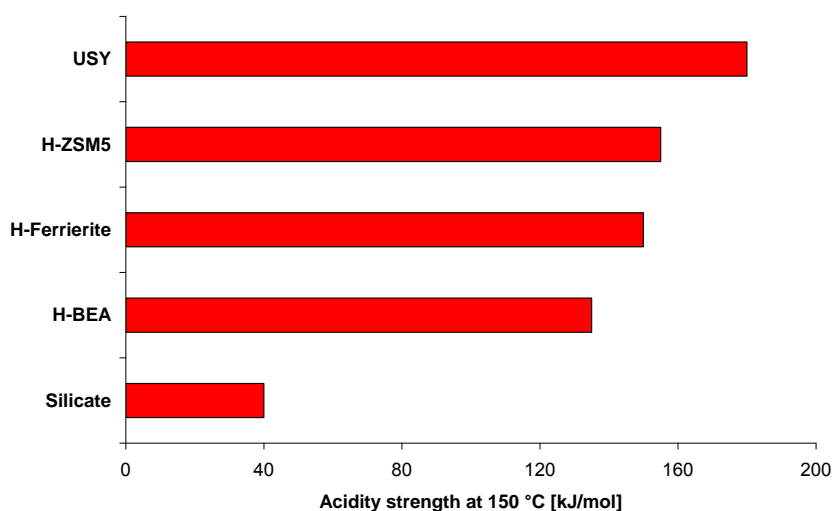
Figure 1.5 Acidity of various zeolites. Data extracted from [67].

Besides acidity, zeolites selectivity for certain reactions is highly affected by porosity. Generally speaking, heterogeneous catalysis involves reactants bulk diffusion in gas phase, followed by pore diffusion before accessing an active site. Subsequently, the surface reaction occurs and products diffuse through the porous media, back to the gaseous mixture. In this context, zeolites porosity

introduces diffusion limitations of reactants and products and/or locally influences the space availability around an active site.

Zeolites pore diameter and length significantly control reactions by decelerating reactants transfer to active sites and determining the catalytic process residence time in case of high active sites density [59]. Moreover the porous structure influences the molecules diffusion inside the porous network through the cage effect and the molecular traffic control [59]. The former is related to a selective diffusion inhibition of certain molecular chains in the structure of certain zeolites (for example erionite zeolite inhibits the diffusion of n-paraffin molecules in the range of C_7 to C_9) [68]. The traffic control mainly concerns zeolites that include cages of different dimensions (such as ZSM5) and it imposes a restricted diffusion of small molecules through small channels, whereas broader channels are used for larger molecules transfer.

Zeolites pore diffusivity is determined by the crystalographic pore dimensions and thus by the actual type of zeolite. Nevertheless, modification of zeolitic porosity is also feasible, either by changing conditions during synthesis and/or through post-synthesis techniques. Regarding the former, controlling factors such as synthesis temperature, duration and mixture alkalinity can enable the preparation of targeted crystal shapes [69]. On the other hand post-treatment methods include deposition of organic or inorganic materials, which results in changes in pore openings, as well as introduction of bulky compounds inside zeolitic cavities so as to restrict the available space in the vicinity of an active site [70].

1.4.3. Iron based zeolites for the SCR of NO$_x$

The charge compensating cations discussed in section 1.4.1 can be further exchanged by transition metals such as Fe, Cu, Mn etc.. Metal exchanged, zeolite based catalysts exhibit reduction and oxidation properties (redox), which explains why these formulations are considered suitable for selective catalytic reduction applications. A typical ion exchange is performed by physically contacting the bare zeolite with a metal precursor at ambient or elevated temperature if an accelerated exchange is desired [62]. In recent literature various ion exchange techniques have been reported. Indicatively some of the most conventional ones are briefly described below [71,72,73,74]:

Wet ion exchange: Wet ion exchange is considered as one of the most conventional preparation methods. According to it an iron precursor and the zeolite powder are diluted in a solution, and stirred for a specific period of time. Synthesis of Fe-ZSM5 in a $Fe(NO_3)_3$ aqueous solution and a $Fe(acac)_3$ (acetyl acetonate) toluene solution are reported elsewhere [74]. Then, the mixture is filtered and the catalyst is dried and calcined at high temperature.

Solid state, ion exchange: According to this preparation method, a solid iron salt (e.g. $FeSO_4$) is mechanically mixed with the zeolite powder and subsequently heated in an oven.

Sublimation: Based on this method an iron salt (e.g. $Fe(Cl)_3$) is evaporated and reacts with an H-form zeolite. In more details, a H-type zeolite and the iron precursor are heated slowly under Ar up to the sublimation temperature. Then, the solids are maintained at the sublimation temperature for a certain

period before being cooled to room temperature. Finally, the catalyst is washed with water, dried and calcined.

The preparation method is very critical for catalyst properties, determining the sample SCR activity (Figure 1.6). It is widely reported that introduction of iron into the zeolite leads to the formation of different iron species, including isolated iron atoms, oligomeric species as well as Fe_2O_3 clusters [75,76]. Brandenberger et al. experimentally proved that all the abovementioned iron species in Fe-ZSM-5, are active for SCR of NO and that the respective conversion rates are temperature dependent [75]. In particular, nonomeric species are SCR active up to 300 °C, whereas the contribution of oligomeric Fe species and Fe_2O_3 particles is evidenced at higher temperatures. Moreover, it has to be considered that the type of Fe species also controls SCR reactions selectivity. For example, NH_3 undesirable oxidation occurs mainly over Fe binuclear species as it is going to be discussed in more details in the next section.
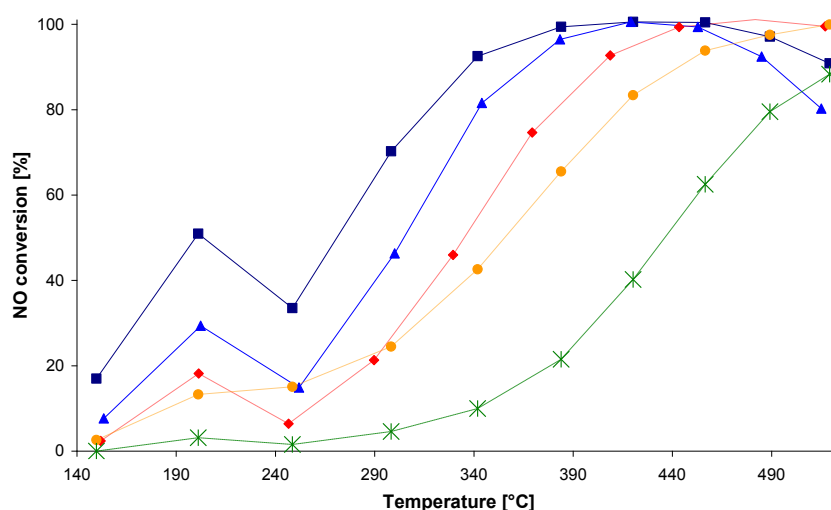
Figure 1.6 SCR of NO by NH_3 over Fe-ZSM5 catalysts, prepared by different methods: ■ 0.83 wt.% Fe-ZSM5/FeCl$_3$ sublimation, ▲ 0.49 wt.% Fe-ZSM5/FeCl$_3$ sublimation, ◆ 0.96 wt.% Fe-ZSM5/Fe(acac)$_3$ wet ion exchange, ● 0.21 wt.% Fe-ZSM5/Fe(acac)$_3$ wet ion exchange, ✳ 0.35 wt.% Fe-ZSM5/Fe(NO$_3$)$_3$ wet ion exchange. Data extracted from reference [74].

Regarding commercial Urea/NH_3-SCR Fe zeolite based catalysts various types of zeolites have been proposed, namely MFI, BEA, ferrierite, faujasite and chabazite as well as mixtures of them [22,55,77]. Finally, it is worth mentioning the application of bimetallic zeolite SCR catalysts composed of Cu and Fe in order to accomplish high deNO$_x$ performance at both low and high temperature regimes respectively [78].

1.5 SCR Chemistry over Fe-exchanged zeolites

1.5.1 SCR reactions scheme

The description of the NH_3-SCR chemistry can be carried out at many levels of complexity ranging from fundamental to very global approaches. In order to bridge the gap between macro- and micro-scale phenomena a "top-down" analysis is attempted according to which global reaction schemes are further analyzed by unraveling detailed mechanistic aspects.

The initial step of the Urea-SCR global reaction scheme (Table 1.2) includes the decomposition of the aqueous 32.5 %w urea solution to gaseous NH_3 and isocyanic acid (HNCO), which occurs at ca. 132 °C (reactions 1.1 and 1.2) [79,80,81]. NH_3 is then stored on the catalytic surface, before reacting with NO_x. Since NO is in excess in the diesel exhaust stream, the Standard SCR reaction (reaction 1.3) predominantly occurs. When equimolar amounts of NO and NO_2 are contained in the exhaust gas, the reaction 1.4 takes place. This reaction is characterized by a much higher reaction rate than the Standard-SCR and hence it is named as Fast-SCR. Moreover, in case NO_2/NO_x ratio is higher than 50%, NH_3 reacts mainly with NO_2 according to the NO_2-SCR (reaction 1.5). Finally, a very slow NO reduction by NH_3 in the absence of O_2 can also occur (reaction 1.6). The effect of NO/NO_2 ratio on the SCR activity of a commercial iron exchanged zeolite is illustrated in Figure 1.7. At this stage it has to be emphasized that the NO/NO_2 ratio can be controlled by a diesel oxidation catalyst being systematically close coupled with the internal combustion engine, upstream the SCR catalytic converter.

Table 1.2 NH_3-SCR global reaction scheme over Fe-exchanged zeolites.

SCR reactions	
$\left(NH_2\right)_2 CO_{(aq)} \;=\; \left(NH_2\right)_2 CO_{(s\,or\,l)} \;+\; m\, H_2O_{(g)}$	**reac. 1.1**
$(NH_2)_2 CO_{(s\,or\,l)} \;=\; NH_{3\;(g)} + HNCO_{(g)}$	**reac. 1.2**
$4\,NH_3 + 4\,NO + O_2 \;=\; 4\,N_2 + 6\,H_2O$	**reac. 1.3**
$4\,NH_3 + 2\,NO + 2\,NO_2 \;=\; 4\,N_2 + 6\,H_2O$	**reac. 1.4**
$8\,NH_3 + 6\,NO_2 \;=\; 7\,N_2 + 12\,H_2O$	**reac. 1.5**
$4\,NH_3 + 6\,NO \;=\; 5\,N_2 + 6\,H_2O$	**reac. 1.6**
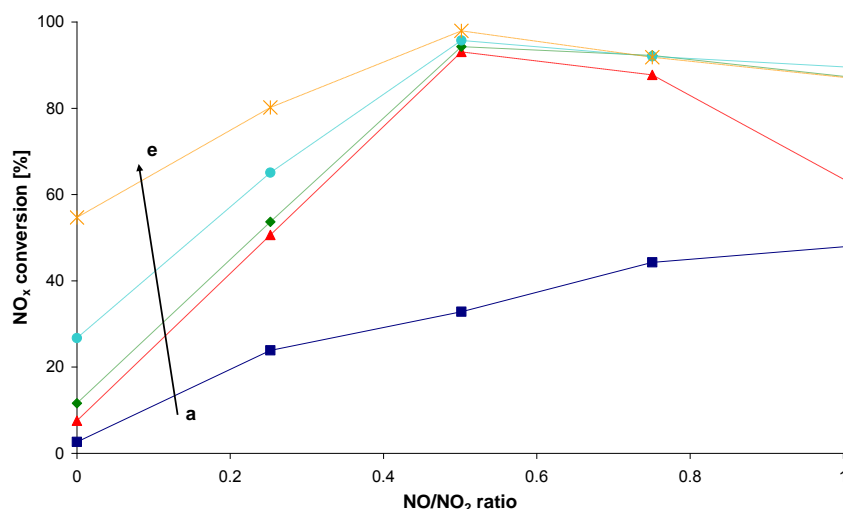
Figure 1.7 Effect of NO/NO$_2$ ratio on NO$_x$ conversion over a commercial Fe-exchanged zeolite at a) 185 °C, b) 235 °C, c) 285 °C, d) 335 °C and 385 °C. Data extracted from [82].

Further analyzing experimental data as well as results from theoretical studies reported in literature a detailed description of the SCR process over Fe-exchanged zeolites was attempted, focusing on the interaction of gaseous species (particularly NH$_3$ and NO$_x$) with surface sites, namely acidic and metallic, redox ones.

Starting from the storage of NH$_3$ on Fe-zeolites (the detailed analysis of the urea decomposition is out of the scope of this review), gaseous ammonia is reported to be physisorbed or weakly adsorbed, as well as chemisorbed over acidic and metallic sites. Three types of metallic sites were observed by Chmielarz et al. associated with (i) Fe^{3+} cations, mainly in tetrahedral coordination, (ii) FeO$_x$ species and (iii) Fe$_2$O$_3$ bulky clusters [83]. Moreover, these authors have proven, by means of Fourier Transform Infrared Spectroscopy measurements (FTIR spectroscopy), that Fe addition leads to the formation of Lewis type acid sites, with acidic strength depending on the type of iron oxide. Concerning the NH$_3$ adsorption over acid sites, ammonia is assumed to be stored on Lewis sites, which are substantiated through the identification of coordinated NH$_3$ in the 3H form on the catalytic surface [84]. Ammonia can also be chemisorbed on Brønsted acid sites forming ammonium ions (NH$_4^+$) located in AlO$_4$ tetrahedra, in a 3H structure at high temperatures (300–400 °C) and a 2H structure at lower temperatures [85]. Castoldi et al. [86] have identified the abovementioned ammonia adspecies on a Fe-ZSM5 (1 wt.% Fe, SiO$_2$/Al$_2$O$_3$ = 23.3) catalyst, employing IR spectroscopic measurements (Figure 1.8). In conclusion, the storage of NH$_3$ over Fe-zeolites can be described through reactions 1.7 to 1.10.

$$NH_3 + HO - Si - Z \rightleftharpoons NH_3 - HO - Si - Z \qquad \textbf{reac. 1.7}$$

$$NH_3 + H^+ - OZ \rightleftharpoons NH_4^+ - OZ \qquad \textbf{reac. 1.8}$$

$$NH_3 + Al^- - Z \rightleftharpoons [NH_3 - Al]^- - Z \qquad \textbf{reac. 1.9}$$

$$NH_3 + Fe^{n+} - Z \rightleftharpoons [NH_3 - Fe]^{n+} - Z \qquad \textbf{reac. 1.10}$$
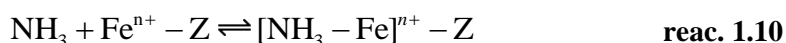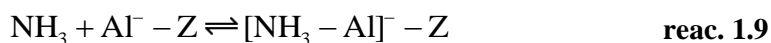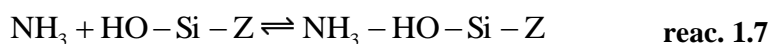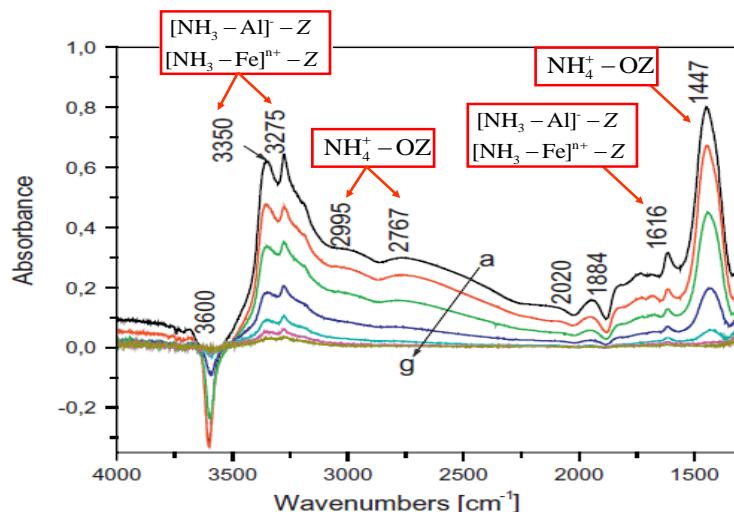
Figure 1.8 FTIR spectra recorded upon admission of NH_3 (5 mbar) at 250 °C over a Fe-ZSM5 catalyst (curve a) and subsequent evacuation at b) 250 °C, c) 300 °C, d) 350 °C, e) 400 °C, f) 450 °C and g) 500 °C. IR spectra are reported in [86].

NO and NO_2 adsorption and desorption are much more complicated compared to ammonia storage described above. Focusing on nitrogen monoxide, detailed IR spectroscopy measurements [87] showed that NO can interact with Brønsted acidic sites forming nitrosium ions (NO^+) and water (reaction 1.11). Adsorption of nitrogen monoxide has also been observed on Fe^{2+} isolated species (rection 1.12), which results in the formation of mononitrosyl or dinitrosyl complexes ($[Fe-NO]^{2+}$ and $[Fe(NO)_2]^{2+}$ respectively) [88,89]. Interestingly, iron monomeric ions in the oxidized state (Fe^{3+}) are not favorable for adsorption of nitrogen monoxide, which results in negligible NO storage [82].

$$NO + 2^+ HO - Z \rightleftharpoons NO^+ - Z + H_2O - Z \qquad \textbf{reac. 1.11}$$

$$NO + Fe^{2+} - Z \rightleftharpoons [NO - Fe]^{2+} - Z \qquad \textbf{reac. 1.12}$$
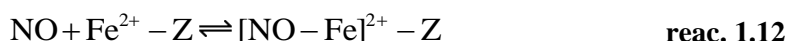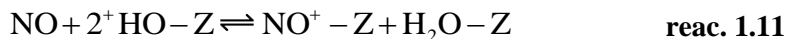
Grossale et al. have elucidated the storage of nitrogen dioxide by performing dedicated experimental studies over a commercial Fe-zeolite catalyst [90,91,92]. These authors showed that under excess of oxygen NO_2 is initially stored on the catalytic surface and dimerized to form N_2O_4 (reaction 1.13). Subsequently the NO_2 dimer disproportionates towards nitrite (NO_2^-) and nitrate (NO_3^-) ions with a simultaneous release of gaseous nitrogen monoxide (reactions 1.18 to 1.20). Nitrites can further react with NO_2 yielding additional amounts of nitrate adspecies. Under typical engine operating conditions water exist also in the feed. H_2O can also interact with N_2O_4 yielding nitrous (HNO_2) and nitric (HNO_3) acid, as well as gaseous NO (reactions 1.15 to 1.17). The overall NO_2 adsorption mechanism under presence of water and oxygen is illustrated through reactions 1.14 to 1.21. Interestingly, the ratio between the consumed amount of NO_2 and the generated amount of NO is 3/1, thus the stoichiometry of reactions 1.17 and 1.20 is followed.

$$2NO_2 \rightleftharpoons N_2O_4 \qquad \textbf{reac. 1.13}$$

$$N_2O_4 \rightleftharpoons NO_3^- + NO^+ \qquad \textbf{reac. 1.14}$$

$$N_2O_4 + H_2O \rightleftharpoons HNO_2 + HNO_3 \qquad \textbf{reac. 1.15}$$

$$NO_2 + HNO_2 \rightleftharpoons HNO_3 + NO_{(g)} \qquad \textbf{reac. 1.16}$$

$$3NO_2 + H_2O \rightleftharpoons 2HNO_3 + NO_{(g)} \qquad \textbf{reac. 1.17}$$

$$N_2O_4 \rightleftharpoons NO_3^- + NO \qquad \textbf{reac. 1.18}$$

$$2NO_2 + O^{2-} \rightleftharpoons NO_3^- + NO_{(g)} \qquad \textbf{reac. 1.19}$$

$$3NO_2 + \tfrac{1}{2}O_2 \rightleftharpoons 2NO_3 + NO_{(g)} \qquad \textbf{reac. 1.20}$$
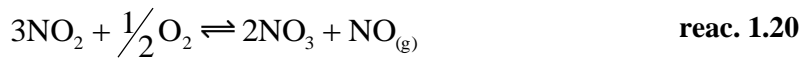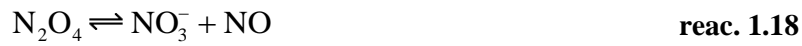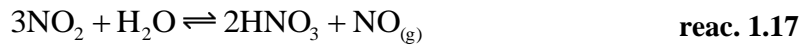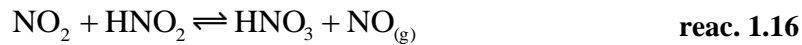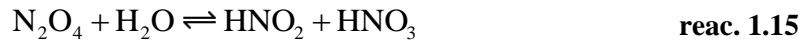
Surface sites of Fe-exchanged zeolites contributing to NO_2 adsorption and disproportionation have been reported in several experimental and DFT studies. Results suggest the existence of physisorbed N_2O_4 adspecies, possibly formed on terminal, non acidic silanols (reaction 1.21), as well as NO_2 disproportionation on Brønsted or Lewis acidic sites (reactions 1.22 and 1.23 respectively) [93] and iron sites. The latter could be either Fe^{n+} monomeric [94] and/or binuclear Fe species [95] (reactions 1.24 and 1.25 respectively).

$$2NO_2 + HO - Si - Z \rightleftharpoons N_2O_4 - HO - Si - Z \qquad \textbf{reac. 1.21}$$

$$3NO_2 + [HO]^- - Z \rightleftharpoons 2[NO_3 - H]^- - Z + NO_{(g)} \qquad \textbf{reac. 1.22}$$

$$3NO_2 + [AlO]^- - Z \rightleftharpoons 2[NO_3 - Al]^- - Z + NO_{(g)} \qquad \textbf{reac. 1.23}$$

$$3NO_2 + [FeO]^{3+} - Z \rightleftharpoons 2[NO_3 - Fe]^{3+} - Z + NO_{(g)} \qquad \textbf{reac. 1.24}$$

$$3NO_2 + [Fe\text{-}O\text{-}Fe]^{3+} - Z \rightleftharpoons 2[Fe - NO_3 - Fe]^{3+} - Z + NO_{(g)} \qquad \textbf{reac. 1.25}$$
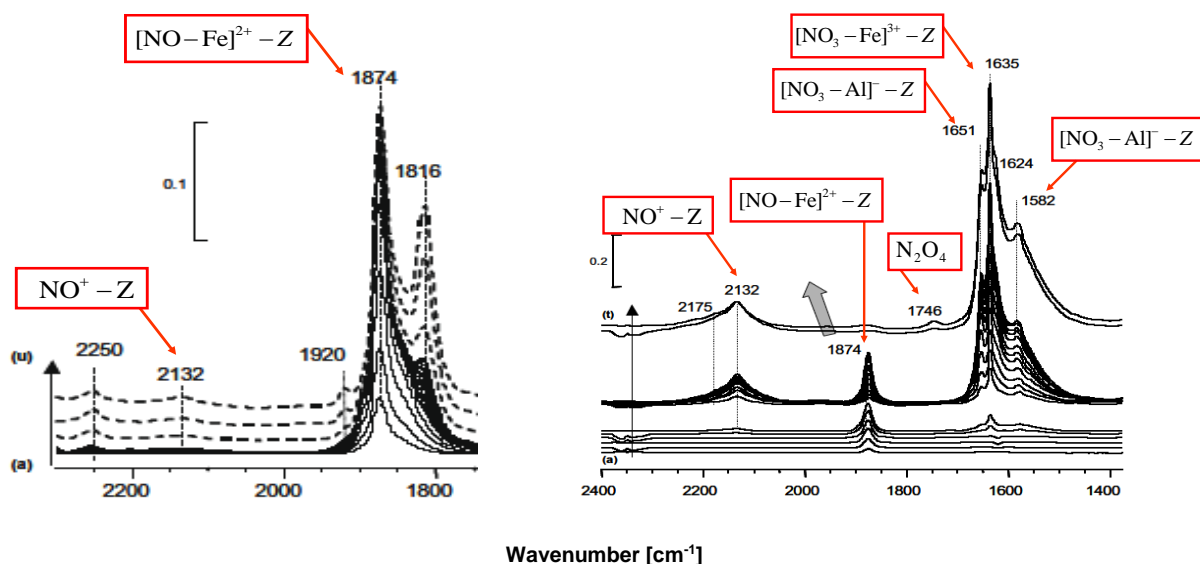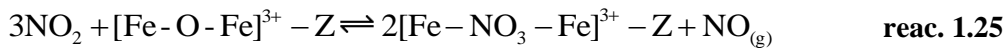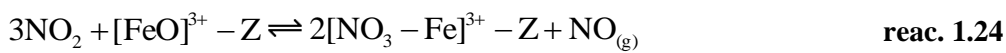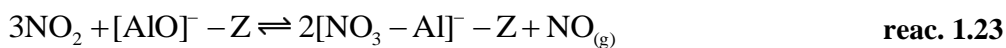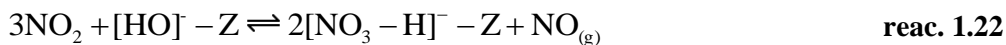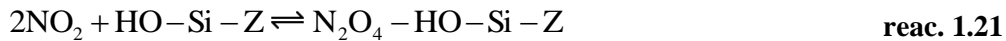
Figure 1.9 IR spectra of NOx adspecies formed on a Fe-BEA catalyst upon NO (on the left) and NO_2 adsorption (on the right). IR spectra are reported in [96].

Ahrens et al. [96] have performed dedicated experimental studies of NO and NO_2 adsorption over a Fe-BEA catalyst (0.76 wt.% Fe, Si/Al = 40) followed by IR spectroscopy. IR spectra corresponding to the NO_x adspescies, discussed in this section are presented Figure 1.9.

As Brandenberger et al. highlight in a recent review [97], the uniqueness of the SCR process over zeolites lies in the fact that NO first has to be oxidized to NO_2, before reacting with ammonia. Tronconi et al. proposed a redox cycle of iron ions, which is summarized through reactions 1.27 to 1.29 [98]. This oxidation process is supposed to be the rate-determining step of the SCR mechanism, hence fast SCR reaction is considered as the actual and general SCR reaction over zeolites. The capability of iron to oxidize NO to NO_2 is experimentally confirmed for Fe-ZSM5 catalysts [99]. However, Schwidder et al. raise serious doubt that NO oxidation is the rate determining step of the SCR, suggesting that even though NO_x adspecies exist as intermediates, the participation of free NO_2 in the standard SCR reaction should be ruled out [100].

$$NO + Fe^{3+} OH \rightleftharpoons Fe^{2+} + HONO \qquad \textbf{reac.1. 26}$$

$$HONO + Fe^{3+}OH \rightleftharpoons Fe^{3+}ONO + H_2O \qquad \textbf{reac. 1.27}$$

$$Fe^{3+}ONO \rightleftharpoons Fe^{2+} + NO_2 \qquad \textbf{reac. 1.28}$$

$$2Fe^{2+} + 1/2O_2 + H_2O \rightleftharpoons 2Fe^{3+}OH \qquad \textbf{reac. 1.29}$$
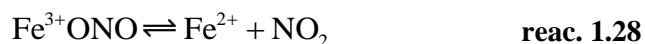
Nitrites, nitrates and ammonia adspecies finally interact with each other yielding intermediate surface species including ammonium nitrite (NH_4NO_2) and ammonium nitrate (NH_4NO_3) (reactions 1.30 and 1.31 respectively). NH_4NO_2 is unstable even at low temperatures and can be quickly decomposed to nitrogen and water, which are the desirable products of the SCR process. As far as ammonium nitrate is concerned, it is established that at temperatures lower than 170 – 180 °C crystalline ammonium nitrate is formed on the catalytic surface whereas at higher temperatures NH_4NO_3 is decomposed yielding nitric acid and ammonia [90,99,108]. HNO_3 can further react with gaseous NO forming NO_2 and nitrous acid. Finally, the latter can react with ammonia to form N_2 and H_2O.

$$NH_3 + HONO \rightleftharpoons NH_4NO_2 \rightleftharpoons N_2 + 2H_2O \qquad \textbf{reac. 1.30}$$

$$NH_3 + HNO_3 \rightleftharpoons NH_4NO_3 \qquad \textbf{reac. 1.31}$$
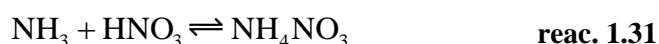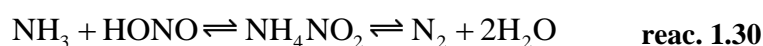
The abovementioned SCR reactions occur over acidic and metallic sites previously reported for formation of NH_3 and NO_x adspecies. As already discussed in section 1.4.3, monomeric and binuclear Fe species mainly contribute to the SCR of NO_x at temperatures up to 300 °C, whereas oligomeric iron species and even Fe_2O_3 particles at higher ones. The ideal, generic SCR scheme described in this section is summarized in Figure 1.10. However, effects which inhibit the SCR process, as well as non-selective reactions are also evident, deteriorating the SCR converter $deNO_x$ performance. Such aspects will be discussed in more details in the next section.
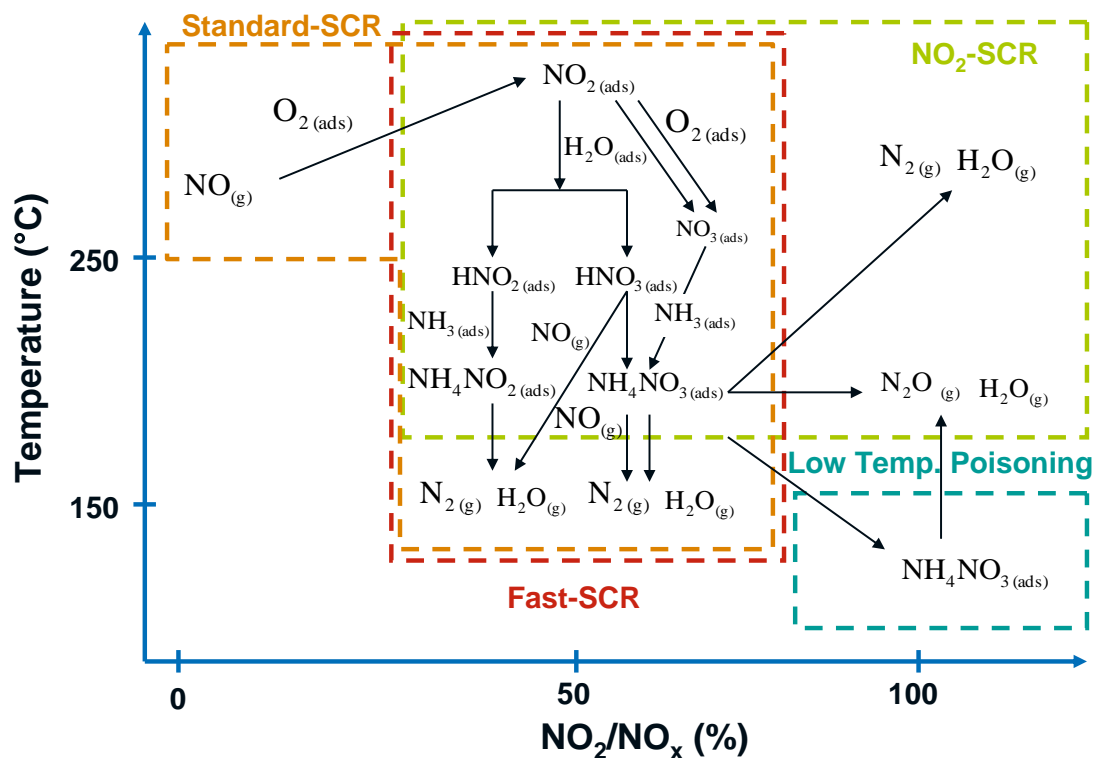
Figure 1.10 Generic SCR-reactions network over Fe-exchanged zeolites.

1.5.2 Inhibition of the NH₃-SCR

Besides the reactions presented in sections 1.5.1, undesired phenomena occur in parallel with the SCR process, limiting catalyst deNO$_x$ efficiency. Among them, the NH$_3$ oxidation provokes undesired overconsumption of the reducing agent, at temperatures higher than 420 °C [101,102]. Akah et. al. [103,104] have studied in details ammonia selective catalytic oxidation (SCO) over H- and Fe-exchanged ZSM5 concluding that SCO occurs through a two step mechanism including i) oxidation of NH$_3$ to NO and ii) selective catalytic reduction of NO by additional ammonia yielding N$_2$ and H$_2$O (reactions 1.32 and 1.33 respectively). The second step is supposed to be the rate determining step of the oxidation process. The same authors suggested that the abovementioned mechanism occurs mainly over Fe binuclear species. However ammonia decomposition towards nitrogen monoxide with a minor yield of nitrogen was also proposed over Fe$_2$O$_3$ particles. Finally, NH$_3$ oxidation to NO was observed over the bare H-ZSM5 zeolite. The latter was also confirmed by DFT calculations reported elsewhere [105]. Recently, Nedyalkova et al. [106] experimentally proved, parasitic ammonia oxidation in the presence of NO, at temperatures as low as 250 °C. This reaction leads to the formation of NO that can be subsequently reduced by NH$_3$ towards N$_2$.

$$4\,NH_3 + 5\,O_2 \quad \rightarrow \quad 4\,NO + 5\,H_2O \qquad \textbf{reac. 1.32}$$

$$4\,NO + 4\,NH_3 + 3O_2 \quad \rightarrow \quad 4\,N_2 + 6\,H_2O \qquad \textbf{reac. 1.33}$$
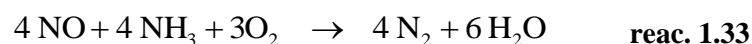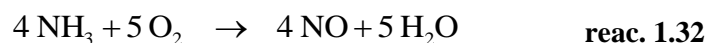
Low temperature temporary catalyst deactivation due to formation of NH_4NO_3 is another undesirable phenomenon. As explained earlier, when nitrates and ammonia adspecies interact at temperatures below 100 °C, ammonium nitrate is formed and deposits on the catalytic surface, blocking the active sites for the SCR reactions. At higher temperatures however, the SCR catalyst is regenerated, since NH_4NO_3 undergoes thermal decomposition yielding several gaseous products, including N_2, H_2O, N_2O and HNO_3 [97,107,108]. Pure NH_4NO_3 is a solid with a melting point of 170 °C, undergoing four different solid phase transitions when heated [109,110,111]:

- Phase V tetragonal: T < -16 °C

- Phase IV orthorhombic: -16 < T < 32 °C

- Phase III orthorhombic: 32 < T < 84 °C

- Phase II tetragonal: 84< T < 125 °C

- Phase I cubic: 125< T < 170 °C

According to a recent review of Chaturvedi and Dave [111], six global reaction pathways could somehow explain the complexity of the ammonium nitrate thermal decomposition (Table 1.3). The process is initiated by the already mentioned NH_4NO_3 decomposition towards HNO_3 and NH_3, followed by further decomposition of nitric acid to nitrites, nitrates and water. Interaction of NH_3 and nitrites/nitrates at temperatures around 260 °C leads to N_2, NO and H_2O, whereas at higher temperatures the decomposition becomes significantly exothermic and NH_4NO_3 is suggested to explode yielding N_2, NO_x and N_2O.

Table 1.3 Possible reaction pathways of NH_4NO_3 thermal decomposition.

Reactions	Temperature (°C)	ΔH (cal/g)
$NH_4NO_{3(s)} \rightarrow NH_{3(g)} + HNO_{3(g)}$	170	- 521
$NH_4NO_3 \rightarrow 1/2 N_2 + NO + 2H_2O$	260	+ 86
$NH_4NO_3 \rightarrow N_2O + 2H_2O$	320	+ 108
$8NH_4NO_3 \rightarrow 5N_2 + 4NO + 2NO_2 + 16H_2O$	560	+ 201
$NH_4NO_3 \rightarrow 3/4 N_2 + 1/2 NO_2 + 2H_2O$	860	+ 316
$NH_4NO_3 \rightarrow N_2 + 2H_2O + 1/2 O_2$	950	+ 354

Even though the thermal decomposition of NH_4NO_3 is reported in several studies little information is available with respect to catalytic decomposition over acidic and metallic sites of iron zeolites. Regarding acidity, Li et al. [112] and Savara et al. [113] have experimentally investigated the thermal decomposition of NH_4NO_3, physically mixed with Ba/Na-Y and H-Y zeolites respectively. Production of NO_x (NO, NO_2) N_2O and N_2 was observed in both cases. Moreover, Savara et al. have proposed a

decomposition mechanism over acidic sites including catalytic reduction of NH_4NO_3 through NO at temperatures as low as 70 °C, yielding HNO_3 and NH_3, decomposition of the former towards nitrites and nitrates and interaction between NO_x and NH_3 adspecies to form unstable ammonium nitrite, which finally yields N_2 and H_2O. As far as the effect of iron species included in Fe-exchanged zeolites is concerned, to the author's knowledge no results are available in literature. Studies of ammonium nitrate decomposition in the presence of pyrite (FeS_2) have been reported by Gunawan et al. [114], suggesting that the presence of iron accelerated NH_4NO_3 decomposition, which becomes evident at around 58 °C. However, the nature of iron in the zeolitic structure is completely different and thus, any direct conclusions can not be drawn.

Another SCR inhibiting mechanism, related to low temperature catalyst deactivation due to formation of NH_4NO_3 is the ammonia blocking effect. Dedicated transient studies, over a commercial Fe-BETA sample reported by Grossale et al. [108] showed that at temperatures as low as 50 °C and in the presence of NH_3 the reduction of nitrates via NO (backward reaction 1.17) is inhibited and the respective light-off temperature is shifted to 140 – 160 °C. According to the same authors the blocking of nitrates reduction is caused due to interactions of NH_3 and HNO_3, which favor the formation of solid ammonium nitrate (reaction 1.33). Devadas et al. suggested that the ammonia inhibiting effect is related to reduction of Fe^{3+} to Fe^{2+}, which is not SCR active [115]. At this stage it has to be pointed out that the deterioration of SCR activity is not associated with competitive adsorption between NH_3 and NO_x on active catalytic sites, but to the fact that ammonia selectively reacts with nitrate adspecies to form NH_4NO_3 at low temperature regime. The ammonia blocking effect attenuates with increasing temperature and it totally dissappears at 400 °C [116].

Finally, competitive adsorption between NH_3 and gaseous compounds included in diesel engines exhaust stream constitutes a very important concern, since they deteriorate surface ammonia availability. Water, unburned hydrocarbons, carbon monoxide (CO) and sulphur oxides (SO_x) have been reported to co-adsorb with ammonia on surface sites of iron zeolites. DFT computations of H_2O adsorption showed modification of surface acidity when H_2O dissociates on tricoordinated Al (Lewis acidic sites) forming new Brønsted acidic sites, characterized by significant acidity strength [117]. Hydrocarbons are supposed to inhibit SCR performance through i) formation of carbonaceous deposits that block zeolitic pores, ii) competitive adsorption with NH_3 and iii) hinderance of the NO oxidation (which is the rate determining step of the SCR process) [118,119]. CO can also be adsorbed on zeolites [120] but it is not reported to inhibit the selective catalytic reduction of NO_x. Interestingly, poisoning of the SCR catalyst can be also carried out through precious metals and namely Pt deposits, which may migrate from a DOC placed upstream the SCR converter at high temperature conditions [121].

1.5.3 Hydrothermal ageing issues

Durability of Fe exchanged zeolites at increased hydrothermal temperatures constitutes a great challenge for their application in automotive aftertreatment systems. Exposure of iron zeolite based catalysts to temperatures higher than 500 °C and water vapor causes irreversible modifications of

catalysts propoerties, leading to permanent deactivation. According to experimental studies on fresh and aged H- and Fe-BEA samples, reported by Shwan et al. [122], hydrothermal treatment resulted in significant decrease of catalysts ammonia storage capacity, whereas NO oxidation rate was enhanced up to a certain ageing degree. In another study, Toops et al. [123] have evaluated the SCR activity of a fresh and an aged Fe-zeolite, washcoated on a monolith. Respective results show that catalysts activity was significantly deteriorated both in the front and the rear part of the monolith (Figure 1.11).

Generally speaking, hydrothermal ageing may have two major effects on the catalyst: i) collapse of the zeolite structure due to dealumination and ii) aggregation of isolated iron species to inactive Fe_2O_3 particles [97]. Catalyst dealumination results in a significant loss of Brønsted type acidic sites and decrease of catalyst active surface area [97]. Therefore, NH_3 storage capacity is decreased, whereas reaction rates are hindered due to the limited active surface area. As far as the aggregation of iron species is concerned, the loss of metallic SCR active sites negatively affects the catalyst yield and simultaneously enhances undesirable side reactions (eg. NH_3 oxidation on Fe_2O_3 - see also section 1.5.3). Toops et al. [123] have verified the abovementioned phenomena through X-ray diffraction (XRD) and nuclear magnetic resonance (NMR) measurements on the fresh and aged Fe-zeolites shown in Figure 1.11. Formation of Fe_2O_3 particles was identified over the aged samples, whereas, migration of Al atoms to extra-framework positions of the zeolite were also evidenced, due to dealumination.
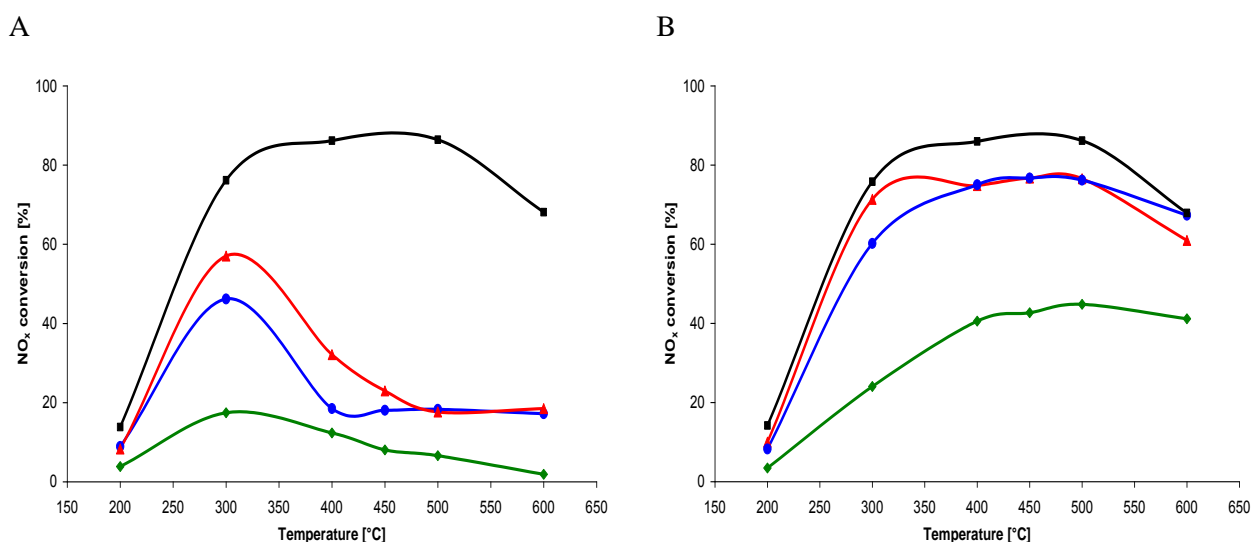
Figure 1.11 NO_x conversion over aged Fe–zeolite SCR catalysts at the A) front and B) rear sections of the monolith. (5% CO_2, 5% H_2O, 14% O_2, 350 ppm NO, 350 ppm NH_3, N_2 balance, GHSV = 30,000 h^{-1}): ▬■▬ fresh catalyast, aged catalyst at ▬●▬ 650 °C, ▬▲▬ 750 °C and ▬◆▬ 850 °C. Data extracted from reference [123].

1.6 Kinetic modeling of a Urea-SCR catalyst

The complete modeling of an Urea-SCR catalyst involves the modeling of (i) urea management, (ii) the catalytic reactor, with respect to flow, heat and mass transfer phenomena and (iii) chemical reactions. The herein review mainly focuses on the modeling of chemical reactions. Thus, other modeling aspects will be presented only briefly.

Modeling of the urea management is reported in several sources, including urea injection [79], evaporation [124] and decomposition [125]. The modeling of heat and flow phenomena within a monolith reactor is reported in [126,127]. The overall mass balance is expressed according to the continuity equation, assuming quasi steady flow (eq. 1.1). Typically, gas and solid phase heat balances are applied. For the gas phase balance (eq. 1.2) laminar flow is considered, whereas for the solid phase one (eq. 1.3) heat transfer through convection, conduction and radiation, as well as heat release due to chemical reactions are taken into account (eq. 1.4). A more detailed approach taking into account 3D flow phenomena inside the channel can be found elsewhere [128]. Finally, regarding the transfer of chemical species, diffusion phenomena in gas and solid phase should be included. Mixed diffusion models, well reported in literature, take into account both internal and external diffusion (diffusion in gas and solid phase respectively) combining the conventional molecular diffusivity either with intralayer diffusion equations [126,129] or a Thiele modulus expression [130].

$$\frac{\partial(\rho \cdot u)}{\partial z} + \frac{1}{r} \cdot \frac{\partial(r \cdot \rho \cdot v)}{\partial r} = 0 \qquad \text{eq. 1.1}$$

$$Cp_g \cdot \rho_g \cdot u_g \mid_z \cdot \frac{\partial T_g}{\partial z} = h_g \cdot \frac{4}{d} \cdot (T_s - T_g) \qquad \text{eq. 1.2}$$

$$\rho_s \cdot Cp_s \cdot \frac{\partial T_s}{\partial t} = \lambda_{s,z} \cdot \frac{\partial^2 T_s}{\partial z^2} + \lambda_{s,r} \cdot \frac{\partial}{r \partial r}\left(r \cdot \frac{\partial T_s}{\partial r}\right) + S \qquad \text{eq. 1.3}$$

$$S = H_{conv.} + H_{cond.} + H_{rad.} + H_{reac.} \qquad \text{eq. 1.4}$$

As far as the modeling of chemical reactions is concerned, an overview of available approaches, involving different levels of complexity, are reported elsewhere [131]. The kinetic modeling of the SCR reactions over Fe-exchanged zeolites is performed through different methodologies, ranging from molecular dynamics [132] to global kinetic models [133]. Tischer et al. have attempted a mixed approach combining detailed atomic scale with reactor scale modeling [134], whereas a neural network based approach is applied elsewhere [135].

Focusing on the kinetic modeling of the NH_3 adsorption and desorption over bare and Fe-exchanged zeolites numerous studies have already been published. Regarding kinetic models accounting for interactions of NH_3 with different surface sites, several approaches have been proposed in literature. Focusing on commercial Fe-zeolites, Sjövall et al. [136] and Colombo et al. [137] have developed similar dual-site kinetic models, including one site for NH_3 weak, low temperature physisorption (or weak adsorption) and a second one for strong chemisorption. Chatterjee et al. proposed another approach, assuming that NH_3 is chemisorbed on an acidic site and further spills over a redox one [138]. As far as Fe-BEA catalysts are concerned, Klukowski et al. have modeled NH_3 adsorption (over a 0.25 wt.% Fe-BEA, Si/Al = 12.5) involving one Brønsted acidic site and one additional site, on

which ammonia can be molecularly sorbed [139]. Moreover, Shwan et al. have recently proposed a more phenomenological model (for a 1 wt.% Fe-BEA, Si/Al = 38) accounting for NH_3 storage over one site for weak adsorption, one Brønsted acidic site and one monomeric Fe site, divided into two storage capacities [140]. These authors have also assumed spillover from the Brønsted site to one of the monomeric iron ones. Finally, a multi-site kinetic model developed by Sjövall et al. for NH_3 storage over Cu-ZSM5 catalysts is noteworthy [141]. Four surface sites were proposed including: A non acidic site, a Brønsted acidic site as well as two metallic sites that can adsorb up to four ammonia molecules. In all cases the NH_3 desorption activation energy is considered to be inhomogeneous throughout the catalytic surface and it varies as a function of local coverage. Therefore, a linear Elovich or Temkin expression is utilized [142]:

$$E_{des} = E_0 \cdot (1 - \alpha \cdot \theta_j)$$ **eq. 1.5**

where "α" corresponds to a surface coverage dependency factor. As it is going to be discussed in details in the following chapters, the "α" factor reflects the dispersion of acidic and redox surface sites of Fe exchanged zeolites.

Regarding the kinetic modeling of NO_x storage and nitrites/nitrate formation and decomposition over Fe-zeolites, mainly global, single site kinetic models exist in recent bibliography. Perdana et al. [143] modeled NO_x adsorption over a Na-ZSM5 film assuming an active site, which corresponds to cationic sodium species. These authors proposed a four step mechanism including NO_2 disproportionation to HNO_3 and NO in the presence of water vapor, coordination of nitrous acid and nitrites on the cationic site and HNO_3 decomposition towards NO_2, H_2O and O_2 at high temperature regime. Another single site kinetic model was recently presented by Metkar et al. [144], where the active site corresponded to iron sites. Moreover, a detailed reactions mechanism was adopted including nitrogen dioxide adsorption and disproportionation, accounting for NO_2 interactions with both oxygen and water. Modeling of O_2 and H_2O adsorption and desorption was also taken into consideration. Interestingly, Olsson et al. [145] have proposed a multi-site kinetic model for nitrates formation over Cu exchanged ZSM5 catalysts, suggesting NO_2 adsorption on non acidic, Brønsted type acidic and copper sites, and nitrogen dioxide disproportionation, exclusively occurring over the metallic sites. This implies that even though the model accounts for NO_3 formation over a single metallic site, an additional contribution of the bare zeolite to the formation of nitrates is also taken into consideration. NO_2 can be temporarily stored on Brønsted sites and further desorbed at elevated temperatures being thus available to readsorb on copper sites, where the disproportionation process can occur.

Similar global kinetic models have been reported for the oxidation of nitrogen monoxide. In the already mentioned work of Metkar et al. [144] direct gaseous NO oxidation is suggested over an oxidized iron site. Bacher et al. [146] suggested a more phenomenological approach, according to which NO oxidation is described through a Langmuir-Hinshelwood type reaction rate expression, where the inhibition of H_2O and NO_2 were taken into consideration. At this stage it has to be pointed out that in none of the abovementioned cases NO is assumed to be adsorbed on the catalytic surface of iron zeolites. Shwan et al. [140] described the adsorption of NO over a dual-site kinetic model, including on Brønsted type acidic site and one monomeric iron site. These authors have proposed NO oxidation over Brønsted acidic sites as well as Fe_2O_3 iron particles. However surprisingly, the actual

kinetic model supposed gas phase interactions between NO and O_2. The same approach has been applied elsewhere [136].

Finally, as far as NH_3-SCR kinetic models are concerned, single and dual site approaches are mainly reported. Metkar et al. [147] have recently published a global, single site kinetic model where gaseous NH_3 is stored on an acidic Brønsted site, before being available for SCR reactions. The standard, fast and NO_2-SCR reactions were depicted by a mechanism, which involved formation and decomposition of NH_4NO_3. Among the decomposition products, N_2O was included, which could further react with adsorbed NH_3 or self-decompose yielding N_2 and O_2. Chatterjee et al. [138] presented a dual site kinetic model accounting for an acidic and a redox site. An overall mechanism of ten reactions was considered, including ammonia adsorption, desorption over acidic sites, NH_3 and NO oxidation, a Standard and a Fast SCR reactions, as well as interactions between NO_2 and adsorbed NH_3 to form nitrous oxide, ammonium nitrate, nitrogen and water. Moreover, a NH_3 spill-over between acidic and redox sites was considered in order to account for the ammonia blocking effect (section 1.5). A "hybrid" dual-site approach was introduced by Sjövall et al. according to which an iron, SCR active site and a non acidic site for physisorption (inactive for SCR reactions) were taken into account. NH_3 adsorption, Standard, Fast and NO_2 SCR reactions were assumed over the active site. On the other hand, interactions of NO_2 with ammonia stored on the non acidic site were considered, in order to model formation and decomposition of NH_4NO_3 as in the case of the model of Metkar et al. [147].

As discussed in all presented modeling approaches, NH_4NO_3 formation and decomposition is taken into account by assuming a single global reaction step. However, according to experimental results discussed in section 1.5, build-up of crystalline ammonium nitrate at low temperature operating conditions may involve interactions between NO_x and NH_3 coordinated to different surface sites. A recent kinetic model of Colombo et al. [148] seems to be in chemical consistency with respect to the abovementioned observations. As in the case of Chaterjee et al. [138], these authors assumed an acidic and a redox site. Ammonia was modeled to adsorb on both sites, whereas a Standard SCR reaction was considered. The NH_3 blocking effect was also taken into account. Reaction of NO_2 with adsorbed NH_3 was suggested to yield solid NH_4NO_3, as well as gaseous N_2 and N_2O. Finally, the latter species was considered to be reduced by NO and NH_3.

1.7 Scope and methodology

The presented review of recent literature provides a quite broad overview of the state of the art over iron zeolite based Urea/NH_3-SCR catalysts. Focusing on the chemistry of the SCR of NO_x several mechanistic aspects were analyzed, including NH_3 and NO_x adsorption and desorption, NO oxidation, nitrite/nitrate adspecies formation through NO_2 disproportionation, as well as selective catalytic reduction of NO_x adspecies through the formation and decomposition of ammonium nitrite and ammonium nitrate. Hence, a generic SCR reaction scheme was developed (Figure 1.10). Moreover, the contribution of acidic and iron sites to the occurrence of the abovementioned reactions was discussed, based on IR spectroscopy measurements reported in literature. Finally, side reactions inhibiting SCR activity were briefly mentioned, namely the NH_3 oxidation, the build-up of crystalline

NH_4NO_3, the NH_3 blocking effect and the competitive adsorption between ammonia and compounds included in diesel engine exhaust stream. Evaluating reported SCR studies, it seems that the SCR chemistry over iron exchanged zeolites is quite well understood. Experimental works of Brandenberger et al. [75,97], Grossale et al. [82,90,91,108], Colombo et al. [52,137,148], Sjövall et al. [136,141] and Hadjiivanov et al. [87] are noteworthy. Nevertheless, analysis of mechanistic aspects related to ammonium nitrate formation and decomposition over Fe-zeolites, with respect to acidic and redox sites contribution was found to be somehow limited.

As far as kinetic modeling of SCR reactions is concerned, a great variety of global kinetic models, with respect to individual reaction pathways as well as the global SCR scheme, was presented and compared. Overall, existing approaches suggested adsorption and desorption of NH_3 and NO_x, as well as NO_2 disproportionation and SCR reactions mainly over metallic sites. The contribution of the zeolite support was marginally modeled and in most cases NH_3 and/or NO_x were considered to chemisorb on acidic sites without occurrence of NO_2 disproportionation, NO oxidation and nitrates/nitrites reduction. This simplification seems to be somehow in contradiction with experimental results discussed in section 1.5, according to which the SCR of NO_x could occur also over zeolitic acidic sites. Moreover, the nature of the proposed acidic and metallic model sites was explained in a quite generalized way and no consistent correlation was made between Brønsted and Lewis acidic sites and/or iron sites, characterized by different nuclearities.

Based on the abovementioned evaluation, the aim of the present doctoral thesis is to initially perform a detailed analysis of the SCR chemistry over iron-exchanged zeolites, in order to:

1. Elucidate the occurrence of the proposed generic SCR reactions scheme (Figure 1.8) over acidic and metallic sites

2. Qualitatively and quantitatively investigate the role of Fe-zeolite structural properties (eg. Al and Fe content) on the abovementioned reactions pathways

3. Understand the SCR catalyst behaviour, particularly under low temperature operating conditions, where formation of crystalline NH_4NO_3 may take place.

The final scope is to use the abovementioned analysis in order to develop a phenomenological, macro-kinetic model oriented to diesel engines aftertreatment system simulation. The thesis innovation constitutes not only the integration of mechanistic aspects related to individual reaction pathways of the NH_3-SCR process but the model development and calibration on the basis of structural properties of iron exchanged zeolites, namely catalyst Al and Fe contents, which are associated with acidic and metallic sites population and dispersion, as well as Fe-zeolites topologic characteristics, associated with synergistic effects.

For the purposes of the herein doctoral thesis only the main reaction steps of the SCR scheme are considered, without accounting for side reactions or inhibiting effects discussed in section 1.5.2. Regrouping the reactions network, illustrated in Figure 1.10, three main reaction pathways were analyzed, including:

1. The adsorption and desorption of NH_3

2. The storage of NO and NO_2, resulting in the formation of nitrite and nitrate adspecies

3. The formation and decomposition of NH_4NO_3

The abovementioned reactions were judged to be particularly critical since NH_3 dosing, as well as its inhibiting effect govern catalyst $deNO_x$ activity, especially in transient operating conditions [149]. As discussed in section 1.5, NH_3 storage over Fe-zeolites is quite well documented in literature. Nevertheless, the effect of the experimental protocol on NH_3 storage and release was not systematically investigated and results are reported mainly over Fe-ZSM5 catalysts.

Moreover, as far as modelling of NH_3 adsorption and desorption are concerned, even though many kinetic models exist, surface Brønsted and Lewis type acidity have never been interpreted through a modelling approach. Furthermore, even in the case of the multi-site model of Shwan et al. [140], the model was developed based on data reported in literature, whereas the respective simulation results were not evaluated through catalyst surface characterization. Finally, kinetics robustness has only been verified over a limited number of experimental conditions.

Similarly, NO_x storage is of great concern, since disproportionation of NO_2 leads to the formation of nitrites and nitrates, through which the fast-SCR reaction mechanism occurs. Forzatti et al. observed a $deNO_x$ efficiency comparable with that of the fast-SCR reaction when injecting, directly upstream a Fe-zeolite catalyst, an aqueous solution of nitrates instead of NH_3 [150]. Moreover, as already discussed, the NO oxidation, which occurrs when nitrogen monoxide is adsorbed in the presence of oxygen, is currently recognised as the rate determining step of the SCR process. Experimental works analyzed in section 1.5 elucidated mechanistic aspects related to nitrito and nitrato groups formation on acidic and metallic sites of Fe-zeolites. Nevertheless, to the author's knowledge, there are no kinetic models that exist in literature accounting for NO_2 adsorption/desorption and disproportionation over different surface sites of iron exchanged zeolites. Furthermore, the already reported kinetic approaches account only for generic types of nitrites and nitrates without specifying any coordination (bidentate, bridging), which is directly related to the adspecies thermal stability [87].

Finally, as far as NH_4NO_3 is concerned, it is supposed to be a key intermediate compound that controls catalyst activity at low temperature regime (T < 180 °C). Particularly focusing on ammonium nitrate decomposition, the evolution of this reaction over acidic and metallic sites must be investigated. Moreover, NH_4NO_3 catalytic decomposition, as well as phase transitions in presence of bare and Fe-exchanged zeolites should be clarified.

To achieve the abovementioned aims, an innovative methodology was applied, including experimental studies and macro-kinetic modelling accounting for Fe zeolites structural properties. Regarding the former, dedicated experimental studies were performed in order to unravel mechanistic aspects related to the abovementioned targeted reaction pathways. Thus, further evaluation of experimental studies reported in literature was enabled. Initially, a Fe-BETA zeolite was synthesized in the laboratory and subsequently characterized so as to perform a qualitative and quantitative screening of structural properties of the studied material. Then, the catalytic sample was tested for the abovementioned reactions, performing temperature programmed desorption (TPD) and temperature programmed reaction (TPR) experiments. Attempting to identify the nature of NH_3 and NO_x adspecies, IR spectroscopy measurements were applied, enabling a detailed characterization of surface species, bonded to different sites of the Fe-BETA catalyst.

As far as the kinetic modelling is concerned, 0D or multi-0D macro-kinetic modelling was considered. Experimental data, kinetics as well as results of theoretical studies (eg. DFT computations) reported in literature were compared to experimental results obtained over the lab-made Fe-BEA catalyst in order to develop a phenomenological macro-kinetic model. Special care was taken for kinetic parameters calibration in order to ensure model robustness as well as consistency with experimental data reporting in bibliography. Finally, structural properties of the Fe-BEA catalyst were considered in order to determine acidic and metallic sites nature and dispersion. Finally, the developed kinetic model was validated over experiments performed over the lab-made bare and iron exchanged BEA samples, as well as over other H- and Fe-zeolites reported in literature.

The desired outcome of the present doctoral thesis is to gain significant knowledge on the SCR of NO_x over iron zeolites, that could be then applied for the understanding as well as the modelling and simulation of commercial SCR catalytic converters, which are composed of mixtures of transition metal exchanged zeolites. Therefore, experiments performed over commercial Fe-exchanged zeolites were simulated.

1.8 PhD thesis organisation

The overall work performed in the framework of this PhD thesis is grouped in six chapters. In chapter 2, a complete model of a Urea-SCR catalytic converter is presented. The evaluation of the proposed model is subsequently described in chapter 3. Comparison between computed and experimental data allowed to point out advantages and limitations of the selected approach, whereas it enabled to schedule the type of experiments required in order to further capitalize the proposed kinetic model approach. Respective experimental details are presented in chapter 4. The following three chapters refer to the experimental investigation of the SCR reactions scheme and the development of the respective kinetic model. Chapter 5 focuses on NH_3 adsorption and desorption, whereas chapter 6 is dedicated to NO_x storage, nitrites/nitrates formation, as well as to NO oxidation. Finally, in chapter 7, interactions between nitrogen oxides and ammonia are discussed, with the formation and decomposition of NH_4NO_3 to be of particular concern. The most important conclusions of this work are summarized in chapter 7. Finally, an Appendices section is also included, where additional experimental details, kinetic parameters, as well as supporting experiments are presented.

Chapter 2

Urea-SCR Catalytic Converter Modeling

2 Urea-SCR Catalytic Converter Modeling

Abstract

A 0D model of a urea-SCR catalytic converter was developed and integrated into the IFP-Exhaust library of the simulation environment of LMS.Imagine.Lab AMESim. Models of monolith, fixed bed and single wafer reactors were developed, enabling increased simulation flexibility. For each reactor model, heat and mass transfer, as well as occurrence of chemical reactions were considered in order to precisely reproduce the behavior of the SCR catalyst. Energy and species balances were elaborated so as to account for heat flow and mass transport limitations in both gas and solid phases. Moreover, focusing on the kinetic modeling, a multi-site approach was employed, developed on the basis of the modeling of NH_3 storage and release over Fe-ZSM5 zeolites. The kinetic model, including five surface sites, was formulated through reaction rate expressions based on the mean-field approximation.

Résumé

Un modèle 0D d'un catalyseur SCR à l'urée a été développé et intégré dans la librairie IFP-Exhaust du logiciel de simulation LMS.Imagine.Lab AMESim. Des modèles de réacteurs de type monolithe, lit fixe et "single wafer" ont été développés, permettant une flexibilité de simulation accrue. Pour chaque modèle de réacteur, les transferts thermiques et de masse, ainsi que les réactions chimiques ayant lieu sont considérés de façon à reproduire précisément le comportement du catalyseur SCR. Les bilans d'énergie et d'espèces sont élaborés afin de prendre en compte le transfert de chaleur et le transport de masse à la fois dans la phase gazeuse et solide. De plus, en se focalisant sur la modélisation cinétique, une approche multi-site a été utilisée, développée sur la base de la modélisation du stockage et de la libération du NH_3 sur les zéolithes Fe-ZSM5. Le modèle cinétique, qui inclue cinq sites de surface, a été formulé à partir des expressions des taux de réaction basées sur l'approximation du champ moyen.

2.1 Modeling approach

The urea-SCR catalytic converter operation is characterized by significant complexity because of the simultaneous occurrence of several physicochemical phenomena. Generally, the latter could be categorized based on their type (thermal, flow and chemical phenomena) and their scale (converter, channel, washcoat), in order to precisely depict the converter behavior and elaborate the respective mathematical and computational models [126]. Moreover, interactions between phenomena may take place (eg. occurrence of chemical reactions is related to heat release, which affects both exhaust gas and converter wall temperatures), requiring the simultaneous resolution of the corresponding mathematical models, irrespectively the phenomena scale and/or type.

As explained in the previous chapter, modeling of SCR converters can be performed at different levels of complexity. The main objective however of this doctoral thesis is to develop a phenomenological macro-kinetic model for Fe-zeolite based Urea-SCR catalysts, oriented to diesel engines aftertreatment system simulation. Such models should be characterized by short computational times, and low physicochemical complexity, enabling fast and relatively precise simulations. Therefore, in the presented work 0D modeling was proposed, so as to achieve a reasonable compromise between simulation precision and CPU time.

The urea-SCR catalytic converter modeling was performed using the commercial simulation platform LMS.Imagine.Lab AMESim and particularly the IFP-Exhaust library [151]. The AMESim modeling environment is based on the bond graph theory, which accounts for energy flows exchange between ports of actual and conceptual components of a multi-physical engineering system [152]. The IFP-Exhaust library is equipped with three components/models in order to enable modeling of a complete SCR system (Figure 2.1), including:

a) an urea injector model, which computes mass and enthalpy flow rates, as well as mass fractions of exhaust gases, accounting for injection of the urea aqueous solution (AdBlue),

b) an exhaust pipe model, which computes urea and HNCO decomposition towards NH_3 in the exhaust line, upstream the SCR catalyst and

c) a SCR catalyst model, which aims to compute NO_x selective catalytic reduction by NH_3.
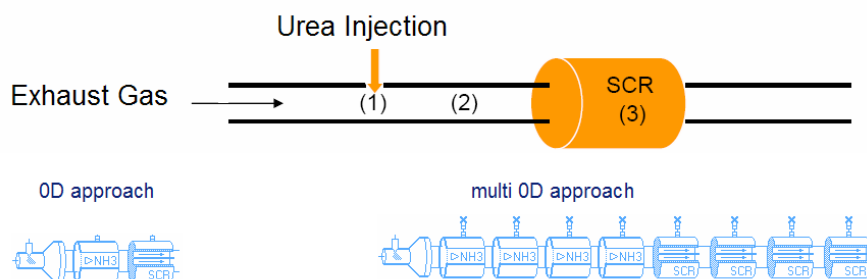
Figure 2.1 Modeling of an Urea-SCR catalytic converter, according to the IFP-Exhaust approach [153].
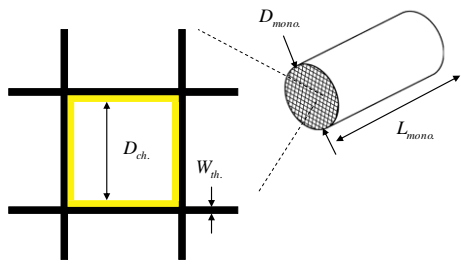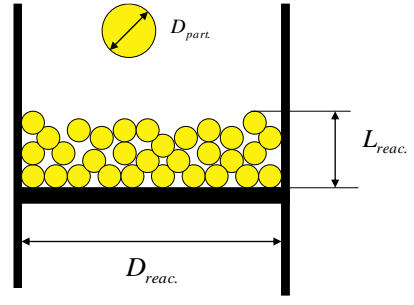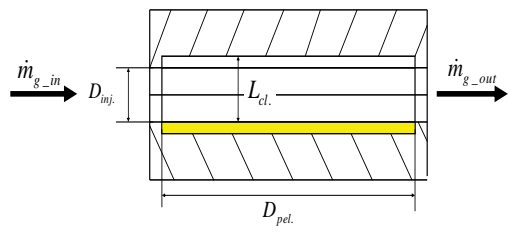
In the framework of the present doctoral thesis, a model of a SCR catalytic converter was developed and integrated into the SCR catalyst AMESim component. Since analysis of urea injection and thermolysis are out of the scope of this study, pure NH_3 is considered to be directly injected in the SCR catalytic reactor, whereas the urea injector and exhaust pipe AMESim components were not taken into account. Initially, reactor modeling was performed in order to precisely reproduce the SCR converter behavior. Mass and heat transfer, as well as flow phenomena were considered and details about the respective species, energy and momentum balances are discussed in the following paragraph. Moreover, as far as kinetic modeling is concerned, a skeleton of a macro-kinetic model for Fe-zeolites is presented, built on the basis of a multi-site approach, in order to depict SCR reactions on different surface sites.

2.2 Reactor models

Models of (i) monolith, (ii) fixed bed and (iii) single wafer reactors were developed and integrated into the SCR catalyst component of the IFP-Exhaust library. The motivation for this task was to increase simulation flexibility, so as to enable reproduction of experiments performed on different experimental configurations, applying various operating conditions. The modeling of the reactors geometries is briefly presented in Table 2.1. Regarding the monolith reactor model, the 0D single channel model approach was followed, as usually applied for flow through monoliths [154]. According to this approach, all monolith channels are considered to exhibit the same behaviour, which is true when heat losses are neglected and the flow upstream the converter is homogeneous [126]. The fixed bed model was developed according to the methodology proposed by Leistner et al. [155], taking into consideration bed's length and catalyst mean particles diameter. Finally, a single wafer reactor was modeled by adopting a simplified geometry, according to which the wafer is regarded as a closed cylinder through which the working medium flows as shown in Table 2.1.

Continuous reactors, which are the case for the monolith, fixed bed and single wafer ones, can be categorized on the basis of the type of the flow in: (i) plug flow reactors (PFR) and (ii) continuous stirred-tank reactors (CSTR). Concerning the former, the PFR model is valid when the fluid velocity profile is flat and axial mixing is negligible, whereas for the CSTR model, ideal perfect mixing is assumed [156]. Regarding 0D modeling of catalytic reactors reported in the literature, the CSTR approach is often followed. Sjövall et al. have modeled a Cu-ZSM5 catalyst washcoated on cordierite monoliths, using a series of 10 continuous stirred reactors [141]. Similarly to monoliths, fixed bed reactors can be also described as a single, or a series of CSTRs, since the bed length is usually very thin (often <1 mm) [155]. Finally, the discussed approach may be also appropriate for single wafer reactors modeling. Reported calculated gas velocity profiles over circular and square wafer reactors proved that flowing conditions are quite homogeneous up to a certain distance above the catalytic sample [157], which seems to somehow support the principle hypothesis of perfect mixing conditions. Therefore, in line with the abovementioned indicative examples, the three reactors discussed in the present work were considered as a single or a series of continuous stirred tanks, accounting for homogeneous temperature, pressure and species concentrations throughout the control volume.

Table 2.1 Geometrical model of a monolith, fixed bed and single wafer reactor, developed into the IFP-Exhaust library.

Type of Reactor	Geometrical Model	Geometrical Characteristics
Monolith	$V_{mono.} = \dfrac{\pi \cdot D_{mono.}^2}{4} \cdot L_{mono.}$ $D_{ch.} = \sqrt{\dfrac{6.451 \cdot 10^{-4}}{CPSI}} - W_{th.}$ $\varepsilon = \dfrac{D_{ch.}^2 \cdot CPSI}{6.451 \cdot 10^{-4}}$ $S_f = \dfrac{P_{ch.} \cdot CPSI}{6.451 \cdot 10^{-4}}$ $S_{geom.} = S_f \cdot V_{mono.}$ $A_{open.} = \varepsilon \cdot \dfrac{\pi \cdot D_{mono.}^2}{4}$	
Fixed Bed	$V_{reac.} = \dfrac{\pi \cdot D_{reac.}^2}{4} \cdot L_{reac.}$ $S_{geom.} = \dfrac{6 \cdot \varepsilon \cdot V_{reac.}}{D_{part.}}$ $A_{open.} = \dfrac{\varepsilon \cdot V_{reac.}}{L_{reac.}}$	
Single Wafer	$V_{reac.} = \dfrac{\pi \cdot D_{pel.}^2}{4} \cdot L_{cl.}$ $S_{geom.} = \dfrac{\pi \cdot D_{pel.}^2}{4}$ $A_{open.} = \dfrac{\pi \cdot D_{inj.}^2}{4}$	

Pressure drop through the reactor was computed from Darcy's law (eq. 2.1):

$$P_{in} - P_{out} = \frac{\dot{m}_g \cdot \mu \cdot L_{reac.}}{\rho_g \cdot A_{open}} \qquad \text{(N/m²)} \qquad \textbf{eq. 2.1}$$

where $L_{reac.}$ corresponds to the length of the reactor being flown by the exhaust gas ($L_{reac.}$ is equal to $D_{pel.}$ in the case of the single wafer reactor).

As far as the mass balance is concerned, disregarding gas phase reactions, the 1D plug-flow gas species equations can be written as presented in the review of automotive catalyst modeling by Depcik et al. [158].

$$\frac{\partial c_{g,i}}{\partial t} + u \cdot \frac{\partial c_{g,i}}{\partial z} = k_{m,i} \cdot s \cdot (c_{s,i} - c_{g,i}) + \frac{\partial}{\partial z}\left(D_{ax} \cdot \frac{\partial c_{g,i}}{\partial z}\right) \qquad \text{eq. 2.2}$$

Neglecting mass transport limitations could induce errors in the computation of adsorbed species [159]. Thus, the diffusion of species was taken into account in the gas phase and the washcoat. A film model was used to compute the mass transfer between the gas and the solid phase (external diffusion), whereas the diffusion within the washcoat (internal diffusion) was expressed using an effectiveness factor, based on a generalized Thiele modulus approach [160]. The mass balance equation of gas species in each tank can be simplified as shown in eq. 2.3:

$$\frac{dc_{g,i}}{dt} = (\dot{c}_{g,i\_in} - \dot{c}_{g,i\_out}) + \phi_{film} \qquad \text{eq. 2.3}$$

where ϕ_{film} is deduced from eq. 2.4 [161,162]:

$$k_{m,i} \cdot s \cdot (c_{g,i} - c_{s,i}) = \frac{\eta_i \cdot \dot{\omega}_i}{V_{wash}} \qquad \text{eq. 2.4}$$

$k_{m,i}$ is the mass transfer coefficient computed based on the Sherwood number and the ith-species diffusivity (eq. 2.5).

$$k_{m,i} = \frac{Sh \cdot D_i}{dh} \qquad \text{eq. 2.5}$$

The effectiveness factor for monolith reactors under isothermal conditions was computed using the Thiele Modulus and the Biot number (eq. 2.6) [163].

$$\eta_i = \frac{\tanh(\phi)}{\phi \cdot \left[1 + \dfrac{\phi \cdot \tanh(\phi)}{Bi_m}\right]} \qquad \text{eq. 2.6}$$

This effectiveness factor represents a ratio between the observed effective rate and the intrinsic reaction rate in the absence of mass transfer phenomena. [164] For a first order reaction, the Thiele modulus is determined as [162,163]:

$$\phi = e \cdot \sqrt{\frac{k(T_s)}{D_e}} \qquad \text{eq. 2.7}$$

where D_e stands for the effective diffusion coefficient computed through the Bosanquet equation, taking into account the effect of tortuosity and porosity on the species diffusion coefficient [165]. Finally, the Biot number (eq. 2.8) is another non-dimensional number expressing the ratio between the convective and the diffusive mass transfer (external versus internal mass transfer resistance) [159,162]:

$$Bi_m = \frac{k_m \cdot e}{D_i} \qquad\qquad \textbf{eq. 2.8}$$

Finally, a heat transfer submodel was developed on the basis of gaseous and solid energy balances. A single solid phase of homogeneous properties, corresponding to the zeolite catalyst, as well as axisymmetric gas flow were considered. Heat transfer phenomena occurring within the SCR reactor are summarized in the generic scheme illustrated in Figure 2.2.
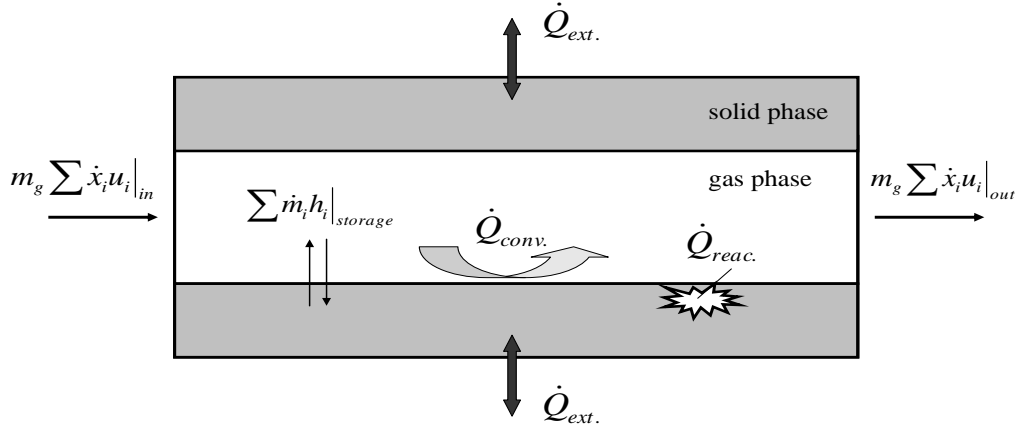
Figure 2.2 Heat transfer phenomena in a SCR catalytic converter.

Bulk temperature was deduced from a gaseous energy balance, based upon the 1st law of thermodynamics. The total rate of heat exchanged in gas phase ($\dot{Q}_{tot.}$) is equal to the convective heat transfer between the gas and the surface ($\dot{Q}_{conv.}$), as well as the heat flows, due to species storage ($\dot{Q}_{storage}$) and species inflow and outflow.

$$\dot{Q}_{tot.} = m_g \cdot C_v \cdot \frac{dT_g}{dt} + \frac{dm_g}{dt} \cdot \int C_v dT + P_g \cdot \frac{dV_{mixt.}}{dt} = \dot{Q}_{conv.} + \dot{Q}_{storage} + \dot{Q}_{inflow} - \dot{Q}_{outflow} \qquad \textbf{eq. 2.9}$$

Heat flow rates related to species storage and in/outflows through the reactor are computed according to eq. 2.10 and 2.11:

$$\dot{Q}_{storage} = \sum_i \dot{m}_i \cdot h_i \qquad\qquad \textbf{eq. 2.10}$$

$$\dot{Q}_{inflow} - \dot{Q}_{outflow} = -m_g \sum_i \frac{dx_i}{dt} \cdot u_i \qquad\qquad \textbf{eq. 2.11}$$

Replacing equations 2.10 and 2.11 in eq. 2.9, the energy balance illustrated in eq. 2.12 is deduced:

$$m_g \cdot C_v \cdot \frac{dT_g}{dt} = \frac{dQ_{conv.}}{dt} + \sum_i \dot{m}_i \cdot h_i - m_g \cdot \sum_i \frac{dx_i}{dt} \cdot u_i - P_g \cdot \frac{dV_{mixt.}}{dt} - \frac{dm_g}{dt} \cdot \int C_v dT \qquad \textbf{eq. 2.12}$$

Similarly to the gas phase, the solid phase temperature is computed by considering convective heat transfer between the gas and solid phases ($\dot{Q}_{conv.}$), heat exchange between the solid phase the ambient ($\Phi_{ext.}$) and heat release due to chemical reactions ($\dot{Q}_{reac.}$):

$$\rho_s \cdot Cp_s \cdot V_s \cdot \frac{dT_s}{dt} = \dot{Q}_{conv.} + \Phi_{ext.} + \dot{Q}_{reac.} \qquad \text{eq. 2.13}$$

Convective heat exchange is computed through a heat transfer coefficient and the reactor geometrical surface area available for the flow (eq. 2.14), whereas the heat flow related to chemical reactions is deduced form the specific heat of the ith reaction and the respective chemical source term $\dot{\omega}_i$ (eq. 2.15).

$$\dot{Q}_{conv.} = h_s \cdot S_{geom.} \cdot (T_g - T_s) \qquad \text{eq. 2.14}$$

$$\dot{Q}_{reac.} = \sum_i \left[-\Delta h_i \cdot M_i \cdot \dot{\omega}_i \right] \qquad \text{eq. 2.15}$$

Integration of equations 2.14 and 2.15 in eq. 2.13 results in eq. 2.16, which constitutes the final 0D solid phase energy balance.

$$\rho_s \cdot Cp_s \cdot V_s \cdot \frac{dT_s}{dt} = h_s \cdot S_{geom.} \cdot (T_g - T_s) + \Phi_{w\_ext} + \sum_i \left[-\Delta h_i \cdot M_i \cdot \dot{\omega}_i \right] \qquad \text{eq. 2.16}$$

The momentum, mass and energy balances, presented in this section are resolved through a variable time step slover, integrated into the AMESim software.

2.3 Kinetic model

Kinetic modeling of the selective catalytic reduction of NO_x through ammonia on iron exchanged zeolites is discussed in this section. The construction of a macro-kinetic model was initiated by studying NH_3 adsorption and desorption mechanisms over Fe-zeolites, since ammonia storage and release are probably one of the most important processes for the dynamic behavior of the SCR catalyst [116]. As already discussed in chapter 1, the $deNO_x$ performance of the SCR catalyst is strongly dependent on the NH_3 availability as well as its inhibiting effect.

Analyzing data reported in the literature, ammonia was found to adsorb on several surface sites of Fe-zeolites (see paragraph 1.5.1). The existing kinetic model for NH_3 adsorption and desorption, already integrated into the IFP-exhaust library was a global single-site model. A very similar model was also reported in a study of Olsson et al. (eq. 2.17 to 2.21) [166].

$$R_{NH_3\_ads} = k_{ads}(T_s) \cdot C_{NH_3} \cdot (1 - \theta) \qquad \text{eq. 2.17}$$

$$k_{ads}(T_s) = A_{ads} \cdot \exp\left(-\frac{E_{ads}}{R \cdot T_s} \right) \qquad \text{eq. 2.18}$$

$$R_{NH_3\_des} = k_{des}(T_s, \theta) \cdot \theta \qquad \text{eq. 2.19}$$

$$k_{des} = A_{des} \cdot \exp\left(-\frac{E(\theta)_{des}}{R \cdot T_s}\right)$$

<div align="right">**eq. 2.20**</div>

$$E(\theta)_{des} = E_0 \cdot (1 - \alpha \cdot \theta)$$

<div align="right">**eq. 2.21**</div>

This approach can not depict surface heterogeneity, associated with different surface sites. Therefore, an alternative modeling approach was required. A multi-site model was previously described by Sjövall et al. [141]. According to this approach, storage of NH_3 on a Cu-ZSM5 (Si/Al = 13.5, 2.03 wt.% Cu) was modeled through four surface sites: two metallic sites, an acidic site and a site for physisorption. The reaction rate expressions applied for each surface site were the same as those established for the single-site approach (eq. 2.17 to eq. 2.21).

Both modeling approaches were initially integrated into the SCR catalyst model of IFP-Exhaust library and further compared by simulating an NH_3 adsorption and TPD experiment on a Cu-ZSM5 (Si/Al = 13.5, 2.03 wt.% Cu) reported elsewhere [141]. For both models, all the assumptions and kinetic parameters (for model calibration) reported by the respective authors were taken into account [141,166]. Simulation results, presented in Figure 2.3 A) show that both approaches allow to correctly reproduce the experimental TPD curve. The single-site model produced a broad desorption peak centered at around 325°C, whereas the output from the multi-site model corresponded to a TPD signal composed of at least two distinct peaks, centered at 278 and 455 °C respectively. Each peak was assigned to NH_3 desorbed from different surface sites [141], hence the multi-site approach is somehow more phenomenological and precise towards the modeling of the NH_3 storage over Cu-zeolites.

The consistency of these models was subsequently evaluated over Fe-zeolite catalysts. An additional NH_3-TPD experiment performed over a Fe-ZSM5 (Si/Al = 13.5, 2 wt.% Fe), reported elsewhere [167] was simulated. The fitting of the experimental TPD signal, presented in Figure 2.3 C) confirms that both approaches are appropriate for the modeling of NH_3 storage over Fe-zeolites, with the multi-site model being more accurate, producing different desorption peaks corresponding to different temperatures. Overall, according to the abovementioned preliminary modeling and simulation studies, the multi-site kinetic model seems to be somehow a more phenomenological kinetic modeling approach, enabling to depict interactions of ammonia with different surface sites. Moreover, as clearly shown in Figure 2.3 B) and D) simulation results obtained through the multi-site kinetic model were relatively satisfactory, since the fitting of experimental curves was quite precise. As described in details in chapter 1.7 one of the principal objectives of this doctoral thesis is to understand and model mechanistic aspects related to the NH_3-SCR over Fe-zeolites, accounting for reactions occurring on different surface sites as well as the effect of catalyst structural properties. Therefore, the multi-site kinetic approach was judged to be appropriate for kinetic modeling of SCR reactions over Fe-zeolites. In the following paragraphs the development of this kinetic-modeling approach is presented, whereas the respective model validation and evaluation is discussed in chapter 3.
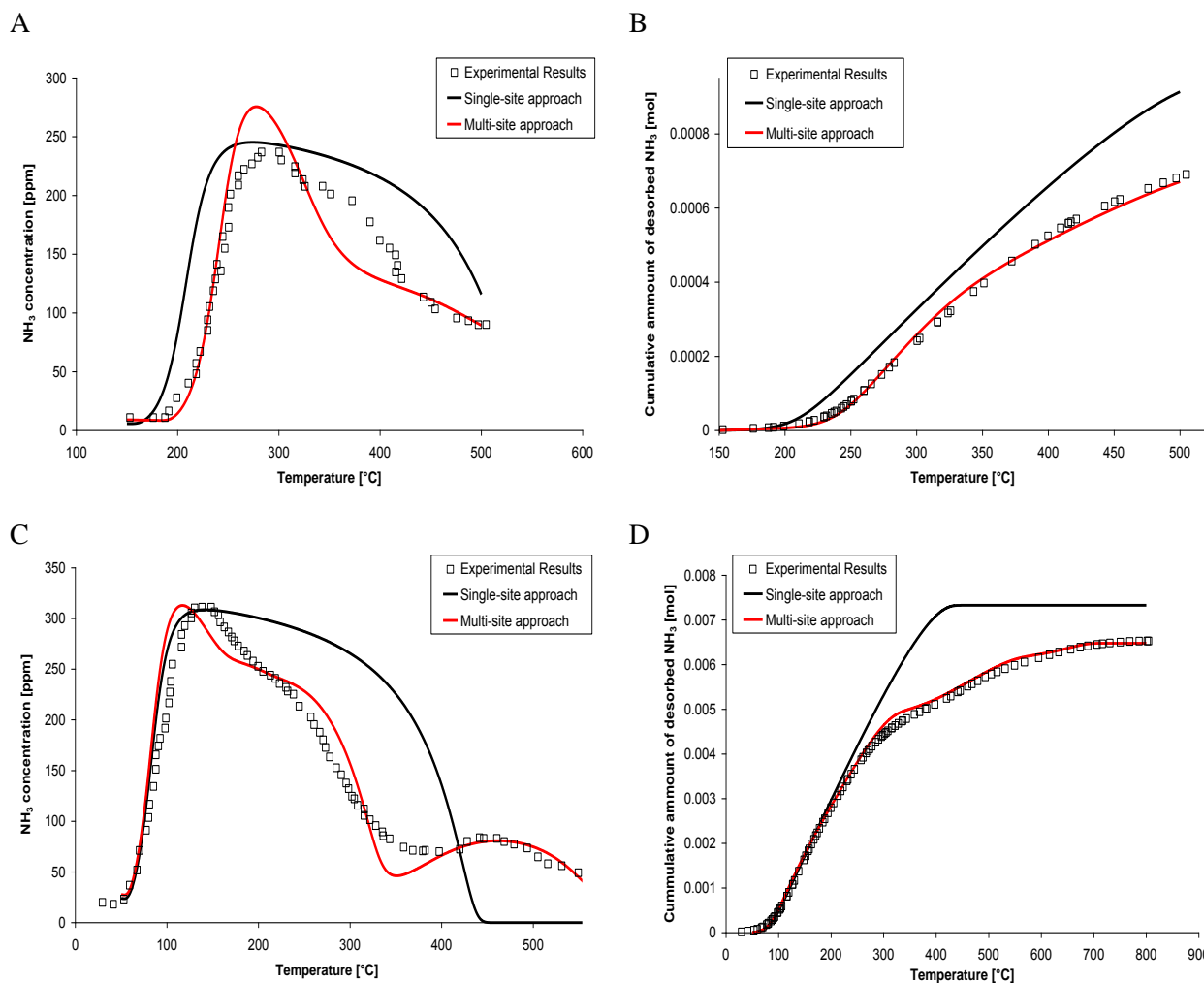
Figure 2.3. Comparison between the computed TPD signal obtained by the single-site and the multi-site model over A) and B) Cu-ZSM5 reported in reference [141] and C) and D) Fe-ZSM5 reported in reference [167].

2.3.1 Set-up of the multi-site kinetic model development

The multi-site kinetic model for the ammonia storage over Fe-zeolites was built by analyzing data of NH_3 adsorption and adsorption experiments over bare and Fe-exchanged ZSM5 samples, reported in the literature. Various NH_3-TPD tests as well as experiments involving optical techniques (eg. UV-vis and FTIR) were analyzed in order to determine the nature of surface sites, which contribute to the storage of NH_3 over Fe-ZSM5. Ammonia TPD provides information for surface sites identification but the TPD's concentration signals should be analyzed carefully because they do not directly reflect the desorption kinetics. The occurrence of parallel re-adsorption as well as mass transfer processes can cause a significant shift of the maximum temperature of TPD peaks [168]. Moreover, even though NH_3-TPD is one of the most widely used methods to characterize the Brønsted sites density [169], it is also a controversial technique due to several limitations [170]. The variation of particle sizes, in case of TPD tests using fixed-bed reactors, NH_3 readsorption as well as experimental conditions can

significantly affect the TPD concentration signal, leading to misleading results. Thus, in this study, results of TPD tests are used in order to identify a sufficient number of surface sites contributing to NH_3 storage, for modeling purposes.

2.3.1.1 NH_3 storage over bare H-ZSM5

NH$_3$ storage over H-ZSM5 zeolites is already very well documented and miscellaneous results and interpretations are reported in the recent literature. NH$_3$-TPD combined with IR-spectroscopic experiments, employing ZSM5 samples (Si/Al = 11.8 and 18) were carried out by Topsøe et al. [171] who identified three desorption peaks, observed within the ranges of 60−100 °C, 150−200 °C and 420−500 °C. The desorption peaks at ca 227 °C and 500 °C were attributed to NH$_3$ desorbed from weak and strong acidic sites respectively, which may be associated with Brønsted type acidic ones (IR bands at 3600 and 3725 cm^{-1}). The peak at low temperatures (ca 100 °C) corresponded to physisorbed and/or weakly adsorbed NH$_3$. According to Katada et al., these weak sites could be related to hydrogen-bonded ammonia and are irrelevant to the acidic properties of the zeolite [172]. Katada et al. reported the same observations over both MOR and ZSM5, highlighting also the role of diffusion phenomena, which cannot be excluded within this temperature regime [173]. Other NH$_3$-TPD experiments over bare ZSM5 zeolites characterized by different Si/Al ratios reported by Costa et al., revealed two desorption peaks centered at temperatures around 177 °C and 360 °C [169]. The desorption peak released at 360 °C was attributed to ammonia adsorbed over weak acidic sites. According to Rodriguez-Gonzalez et al., this peak, which appears within a temperature range of 370-440 °C is related to ammonia desorbed form Brønsted acid sites [174]. Similar observations were also reported elsewhere [103,175]. Moreover, Matsuura et al. showed that increasing the duration and consequently the maximum temperature of the TPD experiments, a third desorption peak was observed [176]. According to the same source, this peak appeared at around 500 °C and corresponded to NH$_3$ bonded to very strong acidic sites probably extra-framework Al-structure.

Based on the abovementioned results, three different sites have been taken into account in the proposed model to describe precisely the bare zeolite's surface sites involved in NH$_3$ storage. In order to capture the peak at low temperatures (L-T peak), a site for physisorption and/or weak adsorption, called S1, has been added. Furthermore, in order to describe the desorption peaks at intermediate temperatures (I-T peak) corresponding to weak acid sites and at high temperatures (H-T peak) attributed to a mixture of Brønsted and Lewis acid sites, two acidic sites were added, called S2 and S3 respectively.

2.3.1.2 NH_3 storage over Fe-ZSM5

As far as the Fe-exchanged zeolites are concerned, results of TPD measurements over Fe-ZSM5 catalysts with different iron loadings are reported by Brandenberger et al. [167]. These authors observed an increase in intensity of L-T and I-T peaks, whereas the H-T peak attenuated. This latter

change in intensity occurs due to the substitution of H protons by Fe cations taking place during the ion exchange process [177]. The increase in the amount of NH_3 desorbed at low and intermediate temperatures can be attributed to NH_3 storage over metallic sites. This increase in the amount of desorbed NH_3 is probably related to the creation of new Lewis type acid sites [178]. Anumiziata et al. have investigated the adsorption of pyridine over Fe-ZSM5 by means of FTIR spectroscopy [179]. The results show that pyridine interacts with Lewis metal sites such as pyridine-Fe^{2+} and pyridine-Fe^{3+}. Katada et al., performed several NH_3-TPD runs over ferrisilicates giving rise to desorption peaks at 277 °C and 427 °C [172]. Therefore, one metallic site, called S4 site was added, which was related to the enhancement of NH_3 desorption at intermediate temperatures.

Finally, analyzing the TPD curves reported in the same study of Brandenberger at al., another desorption peak was found at very high temperatures in the range of 650 °C. A small shoulder is also discernible over bare ZSM5 reported in the same article. Enhanced strong acid sites were reported by Mirodatos and Barthomeuf and attributed to an interaction between protonic $[(Si,Al)O_n(OH)_m]$ and Lewis sites [180]. Even though neither theoretical studies nor experimental results have allowed to interpret the nature of this peak satisfactorily, an additional site called S5, accounting for NH_3 desorption at very high temperature was included. The latter possibly corresponds to an interaction between ammonia and/or water desorbed during dehydroxylation [181,182].

2.3.1.3 The mathematical model

For each of the abovementioned surface sites, reaction rates of adsorption and desorption of NH_3 were applied as presented in eq. 2.22 to eq. 2.26. The adsorption rate constant is based on an Arrhenius expression, whereas that of desorption is described by a Temkin expression, the respective activation energy thus being surface coverage dependent (eq. 2.26). Finally, the chemical source term and each site surface coverage are computed through eq. 2.27 and 2.28 respectively.

$$R_{NH_3\_ads} = k_{ads}(T_s) \cdot C_{NH_3} \cdot (1 - \theta_j) \qquad \text{eq. 2.22}$$

$$k_{ads}(T_s) = A_{ads} \cdot \exp\left(-\frac{E_{ads}}{R \cdot T_s}\right) \qquad \text{eq. 2.23}$$

$$R_{NH_3\_des} = k_{des}(T_s, \theta_j) \cdot \theta_j \qquad \text{eq. 2.24}$$

$$k_{des} = A_{des} \cdot \exp\left(-\frac{E(\theta_j)_{des}}{R \cdot T_s}\right) \qquad \text{eq. 2.25}$$

$$E(\theta)_{des} = E_0 \cdot \left(1 - \alpha \cdot \theta_j\right) \qquad \text{eq. 2.26}$$

$$\dot{\omega}_{NH_3} = \left(\sum_{j=1}^{5} v_j R_j\right) \cdot m_{zeolite} \qquad \text{eq. 2.27}$$

$$N_j \cdot \frac{\partial \theta_j}{\partial t} = \sum_{j=1}^{5} v_j \cdot R_j \qquad \text{eq. 2.28}$$

2.4 Conclusions

A numerical model of a SCR catalytic converter was presented in this chapter. Aiming to develop a methodology suitable for diesel engines aftertreatment system simulation, a 0D approach was applied. Adopting simple geometries, models of monolith, fixed bed and single wafer type reactors were created and integrated into the IFP-Exhaust library of the LMS.Imagine.Lab AMESim simulation platform. Each component was considered as a single or a series of continuous stirred tank reactors, within which energy, mass and momentum balances are resolved. Heat exchange as well as mass species diffusion were taken into account in both gas and solid phases in order to precisely reproduce the operation of a SCR converter.

Since modeling of SCR reactions is the main objective of the present doctoral thesis, special care was taken for kinetic modeling. An extended kinetic model was developed upon analyzing data of NH_3 adsorption and desorption over H- and Fe-ZSM5 catalysts, reported in the recent literature. A multi-site approach was implemented, accounting for NH_3 storage over various surface sites. According to NH_3-TPD profiles over bare and Fe-exchanged ZSM5, reported in bibliography, four surface sites were taken into consideration: i) a site for weak adsorption and/or physisorption, two acidic sites, characterized by ii) weak and iii) increased acidity strength, as well as iv) a global iron site. Finally, a fifth site was included, related to dehydroxylation.

At this stage it has to be highlighted that the abovementioned kinetic model constitutes a reference "skeleton model", which could be further capitalized in order to account for the complete NH_3-SCR reactions scheme over Fe-zeolites. To investigate the feasibility of this concept, kinetic parameters were calibrated and the model was validated by simulating NH_3 adsorption and desorption experiments on H- and Fe-ZSM5 samples, reported in the literature. Respective results are discussed in the next chapter. Hence, advantages and drawbacks of the multi-site kinetic modeling approach could be evaluated, whereas methodologies related to model further capitalization could be identified.

Chapter 3

Multi-site Modeling of NH₃ Storage over Fe-ZSM5

3. Multi-site Modeling of NH$_3$ Storage over Fe-ZSM5

Abstract

The five site kinetic model, presented in chapter 2, is evaluated in this chapter. Kinetic parameters were calibrated and the model was subsequently validated by simulating a broad range of NH$_3$ adsorption and desorption experiments, performed on both H- and Fe-ZSM5 samples. For simulation purposes, the values of the NH$_3$ storage capacity used in the studied test cases were estimated based on structural properties of H- and Fe-exchanged ZSM5 zeolites (Si/Al and Fe/Al ratios). Comparison between the simulated and the experimental results shows the interest as well as the limits of the selected approach.

Résumé

Ce chapitre traite de l'évaluation du modèle cinétique, qui comprend cinq sites, présenté au chapitre 2. Les paramètres cinétiques ont été calibrés et le modèle a été ensuite validé en simulant une gamme des expériences d'adsorption et de la désorption du NH$_3$, sur les catalyseurs H- et Fe-ZSM5. A des fins de simulation, les valeurs du stockage de l'ammoniac, utilisées dans les tests étudiés ont été calculées à partir des propriétés structurelles des zéolithes ZSM5 non échangées et des zéolithes ZSM5 échangées au fer et notamment à partir des ratios Si/Al et Fe/Al. La comparaison entre les résultats des simulations et les résultats expérimentaux montre l'intérêt ainsi que les limitations de l'approche sélectionnée.

3.1 Storage of ammonia over H-ZSM5

The detailed multi-site kinetic model for the NH_3 storage, presented in section 2.3.1, was initially used for the simulation of NH_3 adsorption and TPD experiments over bare ZSM5 zeolites, reported in literature. All the experiments discussed in this chapter were performed using monolith reactors. Therefore, for simulation purposes the monolith reactor model was applied.

The calibration of kinetic parameters was performed in line with theoretical and experimental studies already published (Table 3.1). The activation energy of adsorption is set to zero. According to a recent work of Chen et al., the adsorption of NH_3 on bare and/or Fe-exchanged zeolites is a non-activated process, whereas NH_3 is activated on acidic sites for the reactive systems NH_3/NO and NH_3/O_2 [183]. In the present study, the pre-exponential factors of the adsorption were adjusted manually during calibration, so as to fit the experimental curves, taking into account respective values used for the model of Sjövall et al. [141].

The determination of the kinetic parameters of desorption was more complicated. First, the pre-exponential factor of desorption was set to 10^{13} mol/s·kg$_{cat.}$, according to the transition state theory for immobile adsorbed molecules [184]. Similar values are also reported elsewhere [141]. The activation energy of desorption was chosen based on several publications and it is discussed below. Recently, Metkar et al. recommended an average activation energy of desorption, around 115 kJ/mol [185]. Pinto et al. have reported a broad distribution of acid strengths by performing deconvolution of NH_3-TPD spectra over a H-ZSM5 zeolite [186]. This sample (Si/Al=15) was found to be composed of 47.7% weak adsorption sites (E_{des}= 50−65 kJ/mol), 43.1% strong acid sites (E_{des}= 75−140 kJ/mol) and 9.2% very strong acidic sites (E_{des}= 160−250 kJ/mol). According to another work of Sahoo et al., four types of acid sites related to activation energies of adsorption around respectively 100 kJ/mol, 110 kJ/mol, 130 kJ/mol and the 140 kJ/mol were identified [187].

Concerning the dependency of desorption energy on the surface coverage ("α" factors – equation 2.26), very few information was found in literature. Mishin et al. have performed calorimetric measurements of heats of adsorption of NH_3 over different ZSM5 samples, proving the variation of the respective activation energy as a function of surface concentration [188]. Wilken et al. obtained a value of α close to 0.38 during a NH_3-TPD test over a Cu-Beta catalyst [189]. This value was also used for the calibration of the multi-site kinetic model of Sjövall et al. [141].

Besides the existence of different surface sites there are other parameters affecting the formation of desorption peaks. As shown in eq. 2.19 the surface coverage, including θ and α, has a direct impact on the desorption activation energy. Sjövall et al. [141] has proposed a coverage dependent activation energy, for copper sites, so as to enable the simulation of broad desorption peaks at high temperature. Moreover, the effect of mass limitations on the temperature where each peak appears, cannot be excluded, as already discussed in chapter 2. Hence, kinetic parameters collected in Table 3.1 were used as a reference for the model calibration, enabling us to simulate experimental data obtained in wide operating conditions in order to verify the limits of the proposed approach.

Table 3.1 Kinetic parameters for the simulation of NH_3 adsorption and TPD tests, reported by Brandenberger et al. [167].

Type of site	A_{ads}	E_{ads}	A_{des}	E_{des}	α
	$(m^3/(s \cdot kg_{cat.}))$	(kJ/mol)	$(mol/s \cdot kg_{cat.})$	(kJ/mol)	[-]
S1 (sites for physisorption and/or weak adsorption)	1200^a	0^b	$10^{13\ c}$	95.0^g	0.390^f
S2 (weak acid sites)	700^a	0^b	$10^{13\ c}$	134.5^d	0.155^g
S3 (strong acidic sites)	950^a	0^b	$10^{13\ c}$	195.0^e	0.130^g
S4 (metallic sites)	500^a	0^b	$10^{13\ c}$	125.0^g	0.100^g
S5 (dehydroxylation effects)	800^g	0^b	$10^{14\ g}$	255.0^g	0.000^g

[a]: based on the parameters reported by Sjövall et al. [141], [b]: assuming that the NH_3 adsorption is a non-activated process [183], [c]: values corresponding to adsorbed immobile molecules [184], [d]: value reported by Pinto et al [186], [e]: value reported by Matsuura et al. [176], [f]: value reported by Wilken et al. [189], [g]: values manually calibrated during simulation, so as to fit experimental curves.

3.1.1 TPD of ammonia preadsorbed on H-ZSM5 at room temperature

The first experiment, which was used for the model's validation is a NH_3 TPD over H-ZSM5, earlier reported by Brandenberger et al [167]. A H-ZSM5 sample was exposed to 1%vol. NH_3 in nitrogen at room temperature, for 1 h. Then, a TPD was performed from 30 to 800 °C applying a T-ramp of 10 °C/min in flowing He. Simulated TPD curves are presented in Figure 3.1 and the respective kinetic parameters in Table 3.1. The existence of three desorption peaks, described in chapter 2, is confirmed. In this case the peaks are centered at three different temperatures: 140 °C, 230 °C and 490 °C. Initially, each desorption peak was separately simulated, before simulating the whole TPD signal. According to the analysis presented above, each of these peaks corresponds to NH_3 desorbed from different surface sites.

The first peak, appearing at low temperatures (140 °C), named as "L-T peak", is attributed to physisorbed and/or weakly adsorbed NH_3. The activation energy for this peak was manually calibrated in the order of magnitude of 100 kJ/mol so as to fit the experimental curves. The second peak, centered at 230 °C and named "Intermediate T peak" is related to NH_3 bonded to weak acidic sites. For this peak the activation energy of desorption is estimated to ca 135 kJ/mol, in agreement with Pinto et al. [186] who reported similar values for weak acidic sites. Moreover Rodriguez-Gonzalez et al. used values between 129 kJ/mol and 142 kJ/mol in order to simulate a NH_3 desorption peak over a H-ZSM5 zeolite (SiO_2/Al_2O_3=30) appearing at ca 350 °C [174,190]. Finally, the last peak found at high temperatures, named as "H-T peak", is attributed to strongly bonded NH_3 on acidic sites. For this peak the activation energy of desorption was set to 195 kJ/mol, in line with Matsuura et al., who assigned a similar value to a NH_3 desorption peak at around 500 °C [176].
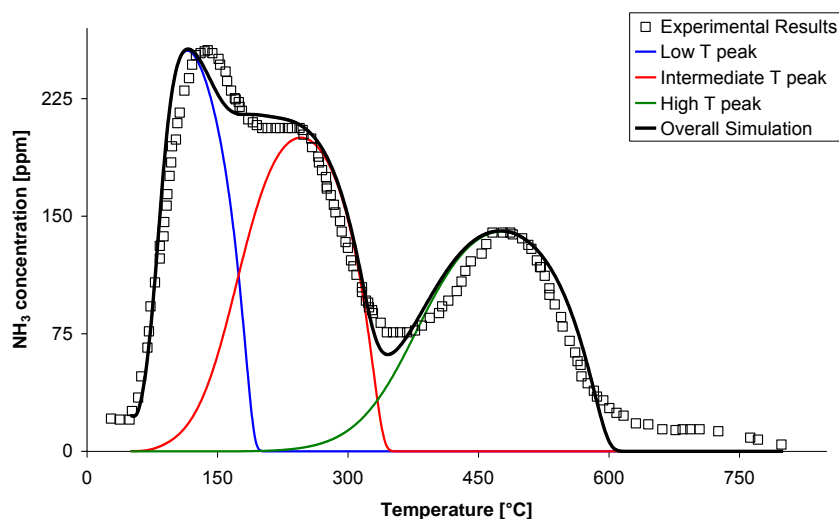
Figure 3.1 Measured and computed NH_3 outlet concentration during NH_3-TPD test reported in [167].

For each peak, the "α" factor was adjusted to specific values, in order to center the separate desorption peaks at low, intermediate and high temperature respectively, as described above. A value of 0.35, combined with an activation energy of desorption of around 95 kJ/mol was chosen for the simulation of the low temperature peak, which is in reasonable agreement with the study of Wilken et al. [189], where a combination of α= 0.38 and E_{des} = 120 kJ/mol was proposed. For the simulation of the remaining peaks lower values of α were applied in order to fit the experimental curves. The chosen values, which apparently are in the order of magnitude of 0.15, imply that the heterogeneity of the acidic sites S2 and S3 is quite limited. Sharma et al. has performed microcalorimetric measurements over two H-ZSM5 samples (Si/Al=34), using NH_3 and pyridine, observing an almost constant deferential enthalpy of adsorption (in the range of 150 kJ/mol) with increasing surface coverage [191]. Thus, these authors suggest a narrow distribution of acidic strength on the samples surface. More specific information is included in a review of A. Aroux, concerning the acidity characterization of different types of zeolites, including ZSM5, by means of microcalorimetry [192]. The analysis shows that zeolites containing very few Lewis acidic sites show a very homogeneous Brønsted acid strength distribution, which apparently corresponds to a differential heat of adsorption around 150 kJ/mol. Therefore, the parameters also suppose that the model's acidic sites S2 and S3 exhibit a quite homogeneous acidic strength distribution. However since the model is based explicitly on data reported in literature not enough information is provided about the ratio between Brønsted and Lewis sites that contributing to each desorption peak of the NH_3-TPD signal and thus, it is impossible to come to a safe conclusion. Further analysis on this topic is out of the scope of this study.

In order to compute the NH_3 surface coverage on each site, the NH_3 storage capacity over each surface site (N_j) needs to be evaluated (see eq. 2.28). Therefore, before starting the actual simulation these values were evaluated through a methodology presented below. Initially, the impact of the Si/Al ratio on the NH_3 total storage capacity over bare H-ZSM5 zeolites was investigated. For this purpose results from TPD performed by Hidalgo et al. were used [193]. Analyzing data with various Si/Al ratios, it was observed that for Si/Al of up to 28 the total NH_3 storage capacity is reduced

exponentially, when increasing the Si/Al ratio ($N_{tot} \sim e^{-0.11 \cdot Si/Al}$ [mol/kg$_{cat.}$]). For higher ratios an almost constant behavior is found ($N_{tot} \approx 0.5$ [mol/kg$_{cat.}$]), showing that if the Si content increases significantly, the total storage capacity is slightly affected by the sample's composition. For the next step, the effect of the Si/Al ratio on the storage capacity over Brønsted acidic sites (N_{acidic}) of H-ZSM5 samples was determined based on experimental studies performed by Gonzalez et al. [174], Sazama et al. [194] and Kapustin et al. [195]. Fitting the experimental data, a linear relation was confirmed between Brønsted acidity and the aluminium content ($N_{acidic} \sim 11 \cdot (Si/Al)$ [mol/kg$_{cat.}$]).

Rodriguez-Gonzalez et al. have obtained similar results, adding that when the zeolite' s crystallinity is perfect and no undesirable effects due to high aluminium concentration occur, each aluminium atom corresponds to a Brønsted site [174]. However, Costa et al. has proven experimentally that the aluminium content is not the only factor affecting the Brønsted acidity of ZSM5 zeolites [169]. Finally, applying a molar balance, the storage capacity of weak sites (N_{weak}) for physisorption and/or weak adsorption can be calculated by subtracting the storage capacity over acidic sites from the total storage capacity. The respective results, presented in Table 3.2, show that for the first test cases, where apparently a H-ZSM5 sample with Si/Al ratio of 13.5 is used, the calibrated values are quite in agreement with the evaluated ones.

Table 3.2 Comparison between the estimated and the actually used NH$_3$ storage capacity over each surface site of the H-ZSM5 samples discussed in 3.1.1.

(Si/Al =13.5)	N_{weak}	N_{acidic}	N_{tot}
	(mol/kg$_{cat.}$)	(mol/kg$_{cat.}$)	(mol/kg$_{cat.}$)
Evaluated storage capacity	1.15	1.15	2.30
Used values in TPD shown in Figure 3.1	1.15	1.08	2.23
Used values in TPD shown in Figure 3.2	1.20	1.14	2.34

3.1.2 TPD of ammonia preadsorbed on H-ZSM5 at 150°C

The second experiment is an NH$_3$ adsorption-desorption test over H-ZSM5 reported in the already mentioned publication of Sjövall et al.[141]. 500 ppm of NH$_3$ were injected for 60 min. at 150 °C followed by a period of Ar flush and a T-ramp of 10 °C/min. The results are presented in Figure 3.2. In this case, S1 sites are able to accurately describe NH$_3$ physisorption and/or weak adsorption taking place during the flush period. Therefore, the first L-T peak does not appear during the TPD test. The I-T peak appears at ca 260 °C, whereas the H-T peak appears at ca 400 °C.
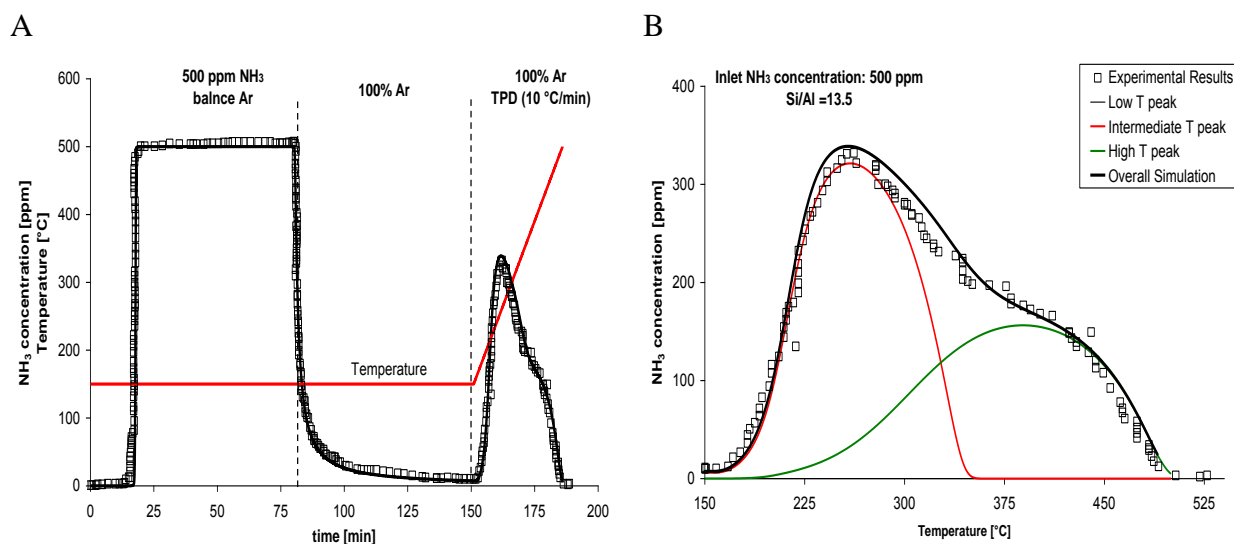
Figure 3.2. Validation of the detailed kinetic model for NH_3 storage through the NH_3 adsorption and TPD test, reported in [141]: A) Evolution of the NH_3 outlet concentration during an adsorption and TPD test: symbols correspond to experimental data and lines to simulation results B) Analysis of the TPD test.

Table 3.3. Modified kinetic parameters for the simulation of the NH_3 adsorption and TPD test reported by Sjövall et al. [141].

Type of site	A_{ads}	E_{ads}	A_{des}	E_{des}	α
	$(m^3/(s \cdot kg_{cat.}))$	(kJ/mol)	$(mol/s \cdot kg_{cat.})$	(kJ/mol)	[-]
S1 (sites for physisorption and/or weak adsorption)	1200[a]	0[b]	10^{13} [c]	92.7[d]	0.390[e]
S2 (weak acid sites)	700[a]	0[b]	10^{13} [c]	132.0[d]	0.155[d]
S3 (strong acidic sites)	950[a]	0[b]	10^{13} [c]	170.0[d]	0.130[d]

[a]: based on the parameters reported by Sjövall et al. [141], [b]: assuming that the NH_3 adsorption is a non-activated process [183], [c]: values corresponding to adsorbed immobile molecules [184], [d]: values manually calibrated during simulation so as to fit experimental curves, [e]:value reported by Wilken et al. [189].

The kinetic parameters used for the simulation of this experiment, shown in Table 3.3 are very similar to those reported in Table 3.1 (less than 10% deviation concerning the values of the activation energy). Notably, the activation energy of desorption for the S3 site is fixed to 170 kJ/mol instead of 195 kJ/mol, showing that in this sample less strong acidic sites exist, which can be attributed to the zeolite structure (see also 3.1.1). However an effect of the experimental conditions applied can not be excluded (eg. temperature of adsorption and mass flow rate). The values of the NH_3 storage capacity over each site are presented in Figure 3.2 and seem to be in quite accordance with the respective values, calculated through the algorithm (presented in 3.1.1).

3.2 Storage of ammonia over Fe-ZSM5

After evaluating the detailed model over bare ZSM5, its consistency over iron exchanged zeolites was evaluated. For this reason a series of NH_3 adsorption and TPD runs earlier reported in [167] were simulated. Each test includes the exposure of Fe-ZSM5 catalysts with different Fe loadings to 1 %vol. NH_3 in nitrogen at room temperature, for 1 h followed by a TPD from 30 up to 800 °C in a He flow applying 10 °C/min. The results of the simulation are reported in Figure 3.3 A) to F) and the kinetic parameters used for simulation purposes in Table 3.1.

Generally, the shape of the TPD curves does not change dramatically compared to the curves presented in section 3.1. The proton exchange results in the deterioration of the storage capacity over the (S3) strong acidic sites and consequently in a decrease of the "H-T desorption peak". On the other hand, the intensities of "L-T and I-T peaks" increase, which can be attributed to NH_3 bonded to metal sites, as mentioned in section 2.3.1.1. The S4 metallic site can sufficiently account for the increase in NH_3 storage capacity in the intermediate temperature range. Nevertheless, as shown in Figure 3 C) and E) the addition of Fe did not lead to enhnanced ammonia storage, which may be attributed to an effect of catalysts structural properties. Sugawara et al. observed that the amount of NH_3 desorbed at around 300 °C during NH_3-TPD over Fe-ZSM5 samples with different iron loading is lower than the amount of the catalysts' iron content [196]. These authors suggest that only specific metal species contribute to the NH_3 storage, which notably is not encountered at low iron loads. Brandenberger et al. have examined the surface composition of the studied samples through UV-vis spectroscopy in [197]. The results prove the abundance of isolated metal species at Fe/Al ratios up to 0.3 and metal clusters (dimeric and oligomeric species) as well as large metallic particles at higher ones. Thus, it can concluded that mainly the metal clusters contribute to the NH_3 adsorption rather than the isolated species, showing that the sample preparation has a crucial effect on the formation of surface sites responsible for the NH_3 storage. The adsorption of ammonia over iron clusters has also been proven by DFT studies [198]. Brandenberger et al. [197] have observed a large number of metallic particles at high Fe concentrations, that could explain the deterioration of the overall NH_3 storage capacity shown in Figure 3 E).
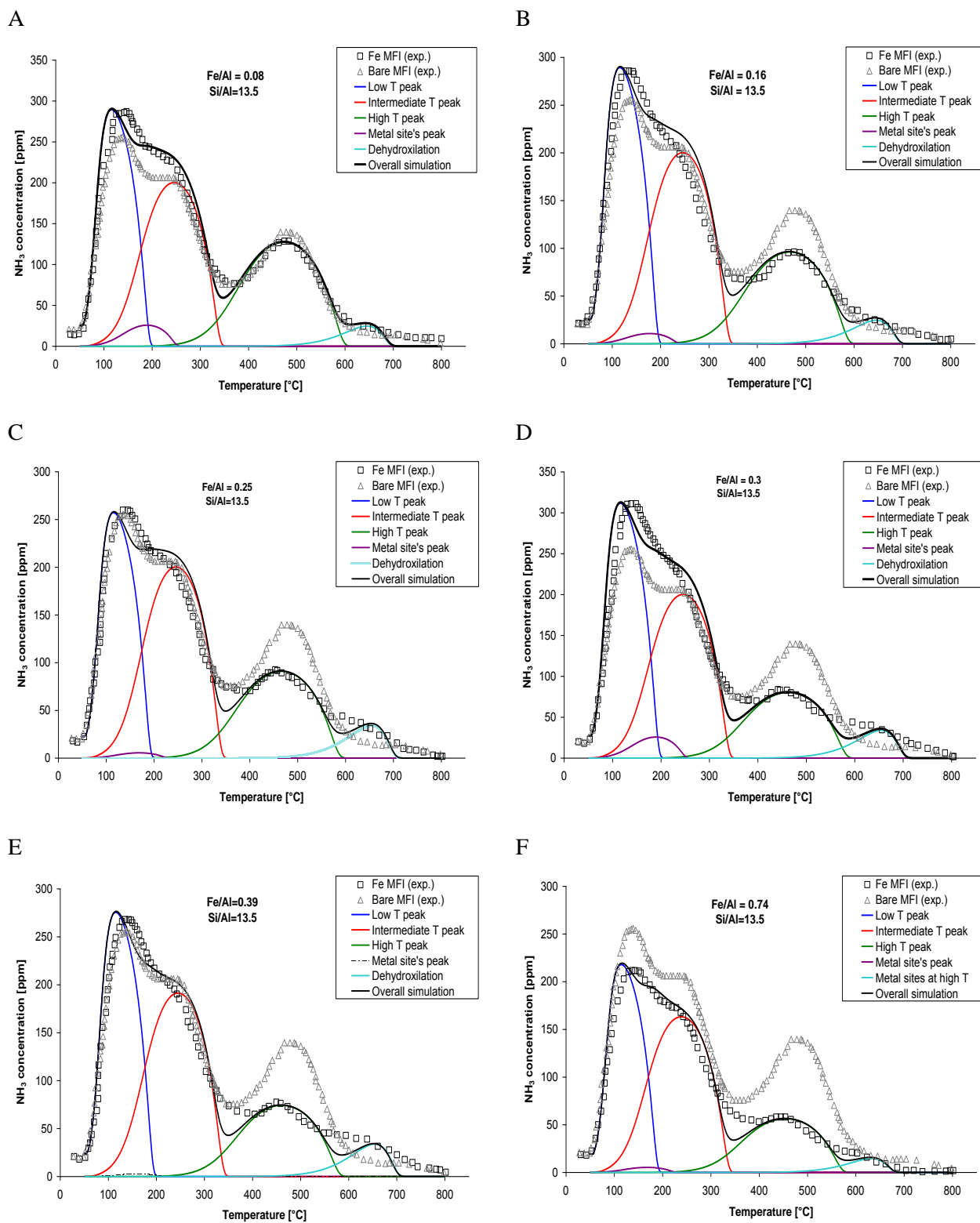
Figure 3.3 Validation of the detailed kinetic model through experimental results over Fe-ZSM5 zeolites with various Fe content, reported in reference [167].

Regarding the increase in the amount of NH_3 desorbed at around 110 °C, it was chosen on purpose not to be simulated through the metal site, since there is no evidence about interaction of ammonia and metal species at this temperature regime. Ates has observed that the iron loading can almost duplicate the zeolite's active surface area, due to the removal of impurities during the ion-exchange [199]. Therefore, the increase in the low temperature peak could be attributed to additional physisorbed or weakly adsorbed NH_3, and thus, it can be described by the (S1) site accounting for physisorption.

The activation energy related to the (S4) metal sites was fixed manually to 125 kJ/mol with an α set to 0.1 so as to fit the experimental curves. Extracting data from the work of Wahba and Kemball [200], an desorption activation energy of nearly 182 kJ/mol was found, with α = 0.47. However, in other studies, the activation energy of NH_3 desorption over iron crystals is set to 39.2 kJ/mol and 52.7 kJ/mol [201]. The "α" factor of S4 metal sites is set to 0.1 (in order to manually fit the experimental curves) assuming that the metal sites heterogeneity is narrow. Though, such aspects are quite unknown and should be definitely further investigated. Using the proposed set of kinetic parameters, the desorption peak assigned to metal sites (S4) is centered in the same area as the I-T peak and the respective computed concentration is maximized at around 200 °C. Interestingly, the contribution of the S2 sites is also evident within the same temperature range. As discussed in 2.3.1.2, the metallic sites are Lewis-type sites. However it has to be highlighted that they should not be associated to Lewis sites existing in the bare zeolite. Metallic Lewis type sites are connected with bridging hydroxyl groups between the metal cation and Si^{4+} [202], whereas the acidic Lewis sites of the non-exchanged zeolites are tri-coordinated aluminium atoms [203].

As was also described in chapter 2 a small peak appears at very high temperatures. The model captures this peak correctly through the (S5) site. The activation energy of this peak is manually calibrated to 255 kJ/mol in order to fit the experimental curves. Since this site is used to capture phenomena possibly associated with dehydroxylation effects, it is not considered as an actual surface site interacting with gaseous NH_3 during storage. Thus, a simple Langmuir expression is employed, leading to an α equal to zero.

To calibrate the storage capacity over each site of the Fe-ZSM5 samples, the impact of the iron loading was taken into account. Analyzing data from a NH_3 TPD test provided in the already mentioned experimental study of Brandenberger et al. [167], it was observed that the iron loading causes a linear deterioration of the storage capacity over acidic sites with an increase of the Fe/Al ratio ($N_{acidic\_exch} \sim 1.5 \cdot (Fe/Al)$ [mol/kg$_{cat.}$]). Regarding the created metallic sites, the respective storage capacity ($N_{metallic}$) was determined by the difference between the storage capacity of the acidic sites before and after the ionic exchange, taking into account the ion exchange degree. As it can be seen in Table 3.4, the abovementioned estimation introduces quite important deviations in comparison with the respective calibrated values (up to 58% and 97% for the storage capacity of acidic and metallic sites respectively), showing that more parameters should be taken into account, namely catalyst preparation, pretreatment method and/or ageing. For example, in the experimental work of Forni et al. [204], the application of different durations of isothermal desorption resulted in the disappearance of the desorption peak at intermediate temperatures (occurring at nearly 300 °C). Similar results are reported in [174] after flushing a H-ZSM5 sample with water-saturated He for 12 h.

Table 3.4. Comparison between the estimated and the actually used NH_3 storage capacity over each surface site of the Fe-ZSM5 samples discussed in 3.2.

Fe/Al	N_{weak} (mol/kg$_{cat.}$) Estimated	Used	N_{acidic_exch} (mol/kg$_{cat.}$) Estimated	Used	$N_{metallic}$ (mol/kg$_{cat.}$) Estimated	Used	Total capacity (mol/kg$_{cat.}$) Estimated	Used
0.57	1.15	1.15[a]	0.80	1.03[b]	0.14	0.20[c]	2.09	2.38
1.1	1.15	1.15[a]	0.68	0.91[b]	0.25	0.16[c]	2.08	2.22
1.7	1.15	1.15[a]	0.55	0.86[b]	0.34	0.01[c]	2.04	2.02
2	1.15	1.15[a]	0.48	0.85[b]	0.45	0.30[c]	2.08	2.30
2.6	1.15	1.15[a]	0.35	0.84[b]	0.46	0.15[c]	1.96	2.14
5	1.15	1.03	0.40	0.70[b]	0.21	0.01[c]	1.76	1.74

[a] Refers to the bare zeolite storage capacity over non acidic weak sites, [b] Sum of the storage capacities of Lewis and Brønsted acidic sites, [c] Sum of the storage capacities of Lewis-metallic sites and non acidic weak metallic sites.

Another NH_3 adsorption and TPD experiments reported in a recent publication of Sjövall et al. was finally simulated [136]. A commercial sample of Fe-ZSM5 was exposed to 510 ppm NH_3, 5 %vol H_2O and 5 %vol CO_2 for 40 min at 159 °C and 210 °C followed by a 60 min period of 5 %vol H_2O in Ar and a TPD, applying 10 °C/min in a 5 %vol H_2O and Ar flow. The results are shown in Figure 3.4 a) to d). The adsorption is performed at 159 °C and 210 °C respectively, thus, the "L-T peak" reasonably should not appear. Additionally, the very high temperature peak is not evidence since the TPD test is performed up to 450 °C.

Considering the Figure 3.4 D), a deviation is observed between experimental and simulated data, with respect to the trend of the two curves. The model, calibrated in the same way for both tests predict a maximum around 330 °C, (Figure 3.4 B) and D)) whereas the experimental TPD signal exhibits a maximum peak at around 370 °C. This deviation is attributed to experimental conditions applied (eg. a slight difference in the temperature ramp), since there is no justification why the maximum peak should shift to higher temperatures.
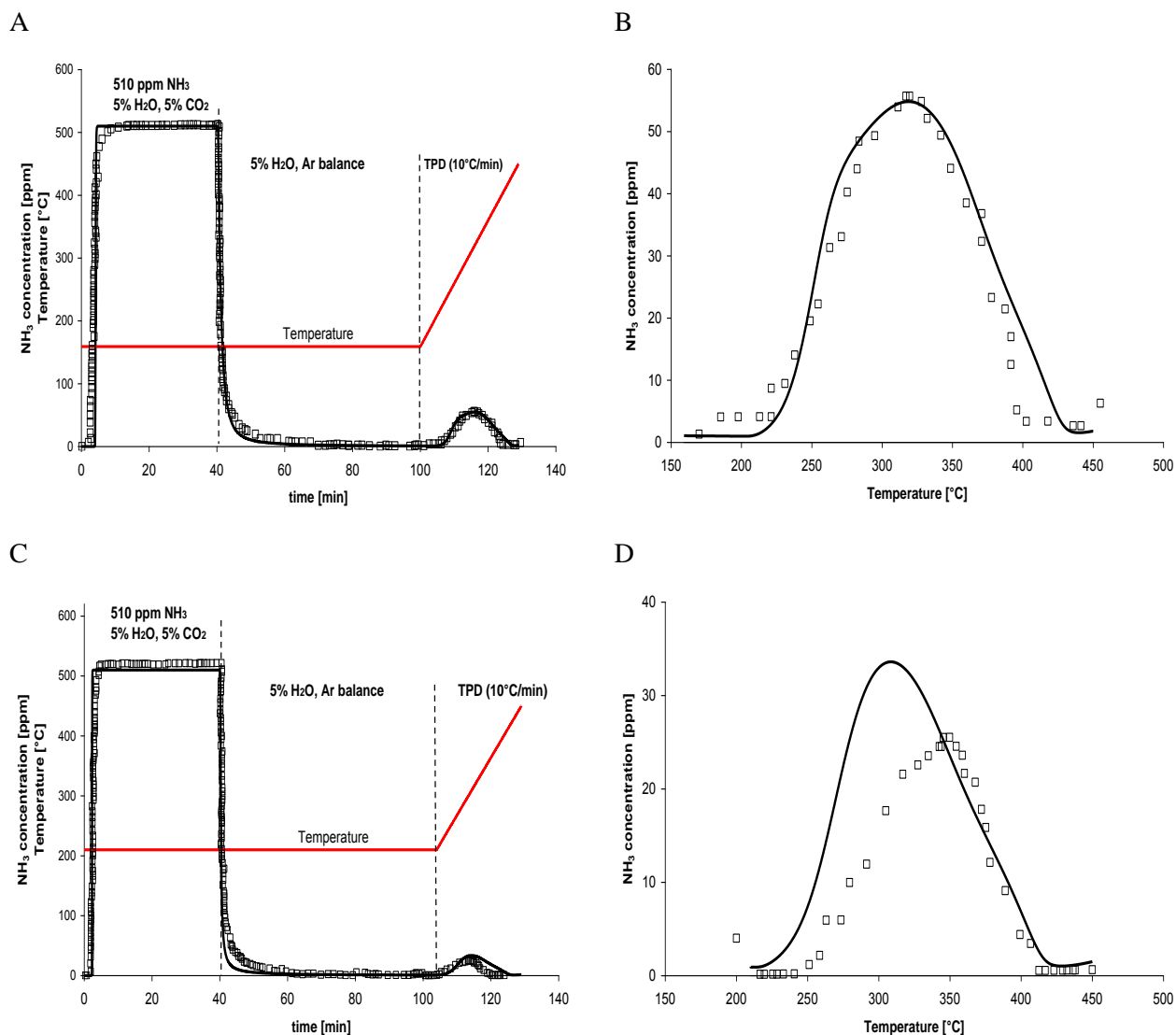
Figure 3.4 Validation of the detailed kinetic model through experimental results over a commercial Fe-ZSM5 zeolite, reported in reference [136]: symbols correspond to experimental data and lines to simulation results.

In this case, the kinetic parameters had to be manually recalibrated in order to correctly capture the desorption peaks. The respective values presented in Table 3.5, show deviations in both activation energies of desorption (maximum deviation in activation energies of desorption lower than 13% with respect to activation energy of desorption) and in the α factor for the S4 metallic sites. Regarding the recalibrated activation energies of desorption, which are 145 kJ/mol and 165 kJ/mol for S2 and S3 acidic sites respectively, they imply a much more narrow distribution of the sample's acidity strength compared to the Fe-ZSM5 samples already discussed in this study. This behavior could be assigned either to the catalyst's composition and namely to the Si/Al ratio as well as to the existence of water in the feed. Considering the latter, Sjovall et al. has shown experimentally that H_2O is competitively coadsorbed with NH_3 on all surface sites of a Cu-ZSM5, leading to a deterioration of NH_3 uptake at 150 °C [141]. Considering the α factor of S4 metallic sites, which is set to 0.4 implies a quite broad heterogeneity of these sites. Anyhow, since the sample is a commercial one, an impact of additives or

impurities can not be excluded. Finally, considering the storage capacities of NH_3 (N_j), they had to be manually adjusted so as to fit the experimental curves since no data about the structural properties of the sample were available so as to use the developed practical algorithm for the storage capacity estimation.

Table 3.5 Modified kinetic parameters for the simulation of NH_3 adsorption and TPD tests reported by Sjövall et al. [136].

Site	A_{ads}	E_{ads}	A_{des}	E_{des}	α	N_j
	$(m^3/(s \cdot kg_{cat.}))$	(kJ/mol)	$(mol/s \cdot kg_{cat.})$	(kJ/mol)	[-]	$(mol/kg_{cat.})$
S1	1200^a	0^b	$10^{13 \, c}$	92.7^d	0.390^e	1.00^d
S2	700^a	0^b	$10^{13 \, c}$	145.0^d	0.155^d	0.09^d
S3	950^a	0^b	$10^{13 \, c}$	165.0^d	0.130^d	0.05^d
S4	300^a	0^b	$10^{13 \, c}$	110.0^d	0.4100^d	0.20^d
S5	800^d	0^b	$10^{14 \, d}$	255.0^d	0.000^d	0.07^d

[a]: based on the parameters reported by Sjövall et al. [141], [b]: assuming that the NH_3 adsorption is a non-activated process [183], [c]: values corresponding to adsorbed immobile molecules [184], [d]: values manually calibrated during simulation so as to fit experimental curves, [e]: value reported in Wilken et al. [189].

3.3 Conclusions and outlook

The five-site kinetic model, presented in chapter 2 was evaluated by simulating NH_3 adsorption and TPD experiments over H- and Fe-ZSM5 samples, applying a broad range of operating conditions. Kinetic parameters calibration was performed based on results reported in the literature, concluding to a range of kinetics, which could fit in different experimental conditions. Even though the simulation results proved that the selection of these values was correct, it has to be highlighted that in all test cases catalysts characterized by a Si/Al ratio of 13.5 were used. Thus, it is likely that the obtained range of kinetic parameters would possibly not be applicable for the simulation of experiments involving samples with different Si/Al ratios. Moreover, values of NH_3 storage capacity over each surface site were initially estimated by analyzing structural properties of the studied catalyst and namely the Si/Al and Fe/Al ratios. Comparing the estimated values with the ones used for simulations, it was found that even though the former were reliable in some cases, significant deviations were also observed. Therefore, more parameters should be taken into account.

Simulation results proved that the five-site model, calibrated within the proposed range of kinetic parameters was quite sufficient for the description of NH_3 storage and release over H- and Fe-ZSM5. The selection of model sites, as well as the way the respective calibration was performed, enabled to account for surface acidity variation within different temperature windows and for interactions of NH_3 with metallic sites. Nevertheless, no straightforward correlation could be made between model acidic

sites and different types of H- and/or Fe-ZSM5 surface sites, such as Brønsted and Lewis acidic ones. Moreover, the nature of Fe sites contributing to ammonia adsorption could not be safely concluded.

Overall, the proposed multi-site kinetic model was a phenomonelogical approach allowing to depict interactions between ammonia and different catalytic positions of H- and Fe-ZSM5, whereas simulation results were satisfactorily in accordance with experimental curves. Nevertheless, significant limitations were also encountered. The determination of the number and the nature of model surface sites as well as the estimation of kinetic parameters necessitated an extensive analysis of a large experimental database. Moreover, structural properties of the studied samples and namely the Si/Al and Fe/Al ratios were essential in order to estimate the storage capacity on each of the selected sites. In order to adopt the multi-site kinetic modeling approach for the modeling and simulation purposes of the present work, two major issues should be taken into account. Considering the identification of model surface sites, a detailed surface species characterization is mandatory, in order to unravel interactions of NH_3 and NO_x with acidic and metallic sites of Fe exchanged zeolites. Furthermore, as far as model parameters are concerned, a detailed catalyst characterization is nessesary so as to obtain information about the quantity and the nature of zeolitic acidic sites, as well as the quantity and the dispersion of Fe redox sites.

Aiming to further capitalize the proposed multi-site kinetic model in order to account for additional reactions and considering the abovementioned conclusions, dedicated experimental studies were performed. Initially, a Fe-BEA catalyst was synthesized and extensively characterized, allowing to get a deep insigth into structural properties of the sample. Details about the catalyst systhesis and respective results of the characterization are presented in chapter 4. NH_3 adsorption/desorption (chapter 5), NO_2 adsorption and disproportionation (chapter 6), NO storage and oxidation (chapter 6) as well as NO_x – NH_3 SCR reactivity (chapter 7) were then experimentally investigated over the lab-synthesized catalytic sample. Employing IR spectroscopy, a detailed surface species characterization was accomplished, enabling to unravel mechanistic aspects related to the abovementioned reactions.

Chapter 4

Experimental Methods

4. Experimental Methods

Abstract

An overview of experimental methods used throughout the entire work is presented in this chapter. A Fe-BEA catalyst was synthesized by exchanging an H type BEA zeolite. Subsequently, the catalytic sample was characterized by applying a broad range of optical techniques, including IR, Raman and UV-vis spectroscopy as well as X-ray diffraction. Moreover, details about NH_3 and NO_x storage, as well as NH_3-NO_x reactivity experiments, applying in-situ IR spectroscopic measurements are discussed. Finally, experimental methods related to NH_4NO_3 thermal decomposition are presented.

Résumé

Ce chapitre porte sur un panorama des méthodes expérimentales, qui ont été utilisées dans le cadre de la thèse doctorale. Un catalyseur Fe-BEA a été synthétisé en échangent une zéolithe type BEA. Ensuite, l'échantillon a été caractérisé au moyen d'une gamme de techniques optiques, notamment: spectroscopie IR, spectroscopie Raman et spectroscopie UV-vis ainsi que diffraction des rayons X. De plus, des détails concernant des expériences du stockage du NH_3 et des NO_x ainsi que les essais de réactivité entre NH_3 et NO_x, en appliquant les mesures de spectroscopie IR, en conditions in-situ sont discutées. Finalement, les méthodes expérimentales liées à la décomposition thermique du NH_4NO_3 sont présentées.

4.1 Synthesis of a Fe-BEA catalyst

For the purposes of the experimental studies performed in the framework of this doctoral thesis the synthesis of Fe-exchanged zeolite sample was decided. Since a deep understanding of NH_3-SCR reaction mechanisms with respect to structural properties of the catalyst was intended, a lab-synthesized sample was judged to be more advantageous compared to a commercial one. Synthesizing a Fe-zeolite in the laboratory allows a complete control of the synthesis conditions as well as the pre- and post-treatment procedures, whereas unlimited characterization of sample properties can be performed.

A 1.75 wt.% Fe-BEA (Fe/Al=0.28) sample (Table 4.1) was prepared according to a conventional procedure described by Delahay et al. [74]. Briefly, 2 g of BEA zeolite (Si/Al=11.8) in the H form, supplied by IFPEN were mixed with a 0.0024 mol/L aqueous solution of $Fe(NO_3)_3$ (Sigma Aldrich, LOT number: STBB1594) that was used as an iron-precursor. The solution was stirred at 80 °C under air, for 48 h. During preparation, the pH was maintained within a range of 3.0 - 3.5 via the addition of 0.1 M of NH_3 aqueous solution. After filtration and overnight drying at 80 °C, the catalyst was finally calcined in air for 5 h, at 500 °C.

Table 4.1 Elemental analysis of the studied Fe-BEA catalyst.

Element	Composition (wt.%)	Molar amount [a] (mol/kg$_{Fe-BEA}$)
Fe	1.75	0.31
Al	2.98	1.11
Si	36.93	13.15

[a] values computed by multiplying species mass composition with the respective species molar weight.

The experimental set-up used for the Fe-BEA synthesis is illustrated in Figure 4.1 and the respective equipment used is listed below:

➢ **Experimental cell:** The equipment that was used during the exchange process was placed in a special designed cell, which provided ventilation for the abatement of vapors produced during the experiment as well as a drain system for safe removal of liquids.

➢ **Three-neck flask:** The H-BEA exchange was performed using a 1 L three-neck flask. Vessel ports were used to adjust the following tubes:

   o **Tube for NH$_4$OH solution storage:** This tube was used in order to store the NH$_4$OH solution, which was utilized for the control of the solution pH.

   o **Cooling tube:** A water cooled tube was used for condensing vapors released during the synthesis.

#	Equipment
1	Stirring machine
2	Electric Oven
3	Three-Neck Flask
4	Tube for NH_4OH storage
5	Cooling Tube

Figure 4.1 Experimental set-up for the Fe-BEA synthesis.

➢ **Electrical heater:** An electric apparatus (225 W) was used for heating of the Fe-precursor – zeolite solution. The device provided constant heating to the slurry, whereas a thermocouple was simultaneously measuring the temperature. Heat was thus manually controlled so as to achieve the required temperature conditions. At this point it has to be mentioned that using this technique, solution temperature could be adjusted within a range of values, with a precision of ca ± 10 °C.

➢ **Electronic stirring machine:** The stirring machine provided the chemical system with the kinetic energy, which was necessary for the accomplishment of homogeneous concentration within the slurry volume. The device bares a metal horizontal magnetic disc, which interacts with another small iron magnet placed inside the solution.

4.2 Catalyst characterization

The Fe-exchanged BEA sample was then characterized by means of Raman and IR spectroscopy, X-Ray Diffraction (XRD) and UV-vis spectroscopy. Raman spectra of bare H-BEA and 1.75 wt.% Fe-BEA were obtained within the visible range (495 – 570 nm) at room temperature (RT). IR spectra of both samples, were recorded at 500 °C, in vacuum using a Nicolet 460 Spectrometer. A XRD pattern of the 1.75 wt.% Fe-BEA sample was recorded by means of a D8 Advance BRUKER spectrometer, at RT, within $5°< 2\theta < 80°$ range, at a scanning rate of 0.015 °/min. Finally, diffuse reflectance UV-vis spectroscopic measurements of the 1.75 wt.% Fe-BEA were performed using a PerkinElmer Lambda 650S UV-vis spectrometer.

Raman spectra of the H- and Fe-BEA samples are illustrated in Figure 4.2. Regarding the H-BEA, Raman shifts at 438 and 474, 347 and 321 cm^{-1}, they were assigned to the vibrational modes of 4-, 5- and 6- membered rings, respectively [205,206]. Moreover a shift at 833 cm^{-1} was attributed to T-O asymmetric stretching mode (T=Si or Al) [205]. As far as the Raman spectrum of the Fe-BEA sample

is concerned, similar spectral features were observed, showing that the ion exchange process did not affect the bare BEA zeolite structure. Moreover, Gao et al. assigned a shift at 730 cm^{-1} to binuclear iron ions (O-Fe-O-Fe-O) [207], whereas maxima in the range of 1200 - 900 cm^{-1} were attributed to framework iron ions (1165, 1115 and 1005 cm-1) elsewhere [208]. However, as shown in Figure 4.2, it seems difficult to identify any distinguishable peak in this range because of fluorescence. Overall, similar spectral features were observed over both samples, which tends to indicate that the ion exchange process did not affect the bare BEA zeolite structure.
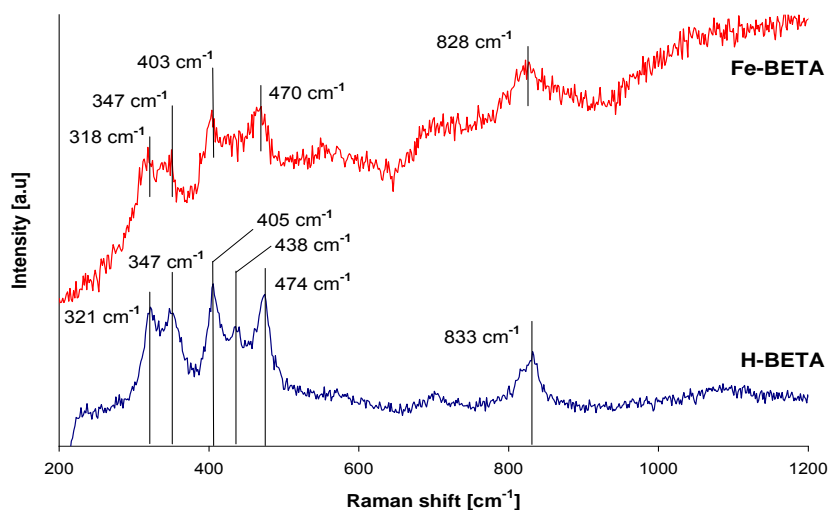
Figure 4.2 Raman spectra of the H- and Fe-BEA studied samples.

IR spectra of H- and Fe-BEA are illustrated in Figure 4.3. Bands with maxima at 3745 and 3606 cm^{-1} were attributed to non acidic terminal silanols (Si-OH) and Si-OH-Al, Brønsted type acidic sites respectively [96,209,210]. The intensity of the latter band attenuated over the Fe-BEA sample, likely due to the H$^+$ exchange by iron cations. Moreover, the 3782 cm^{-1} IR band was ascribed to Al-OH groups, exhibiting Lewis type acidity [210] and/or basic properties [96]. This tends to indicate that the network of the parent BEA zeolite is partially destroyed, suggesting a possible existence of defective sites [96]. Structural defects on H-BEA structure have also been reported elsewhere [211,212]. Finally, a maximum at 3665 cm^{-1} was observed, which was assigned to extra-framework Al [213].
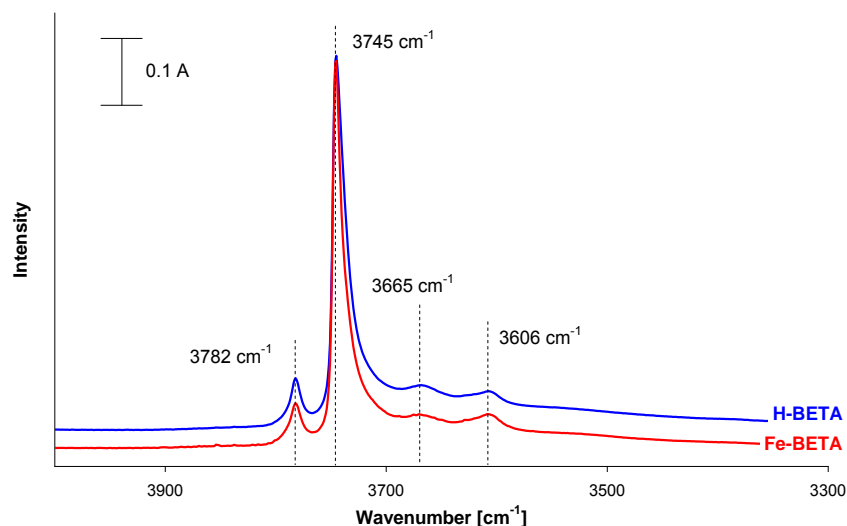
Figure 4.3 IR spectra of the H- and Fe-BEA samples recorded at 500 °C, in vacuum.

Insight into the nature of Fe species formed on the Fe-BEA catalyst was gained through UV-vis spectroscopic measurements, presented in Figure 4.4. UV-vis bands located between 200 – 300 nm were assigned to isolated Fe^{3+} species, namely Fe^{3+} in tetrahedral and higher coordination showing bands below 250 and at ca 290 nm respectively [214]. Moreover, bands observed in the 300 – 400 nm range and above 400 nm were attributed to oligomeric Fe clusters and Fe_2O_3 particles respectively [215,216].
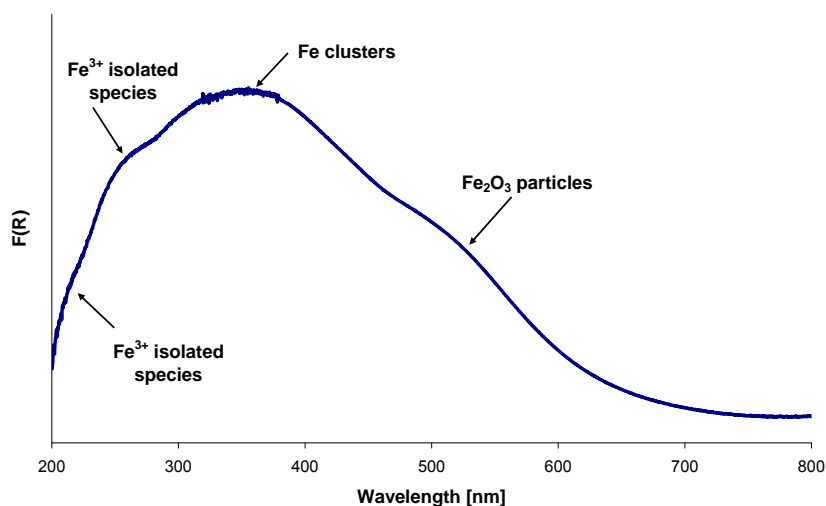
Figure 4.4 UV-vis spectrum of the Fe-BEA catalyst.

Finally, a X-Ray diffraction pattern of the Fe-BEA sample is presented in Figure 4.5. Typical diffraction peaks at 2θ=7.8° and 2θ=22.5° characterize crystalline H-BEA zeolite [217,218]. Furthermore, low intensity peaks at 2θ = 33.2° and 35.7 ° can be assigned to iron oxide particles (α-

Fe$_x$O$_y$) [219,220]. At this stage it has to be pointed out, that XRD results tend to confirm the existence of Fe$_2$O$_3$ particles over the Fe-BEA catalyst.
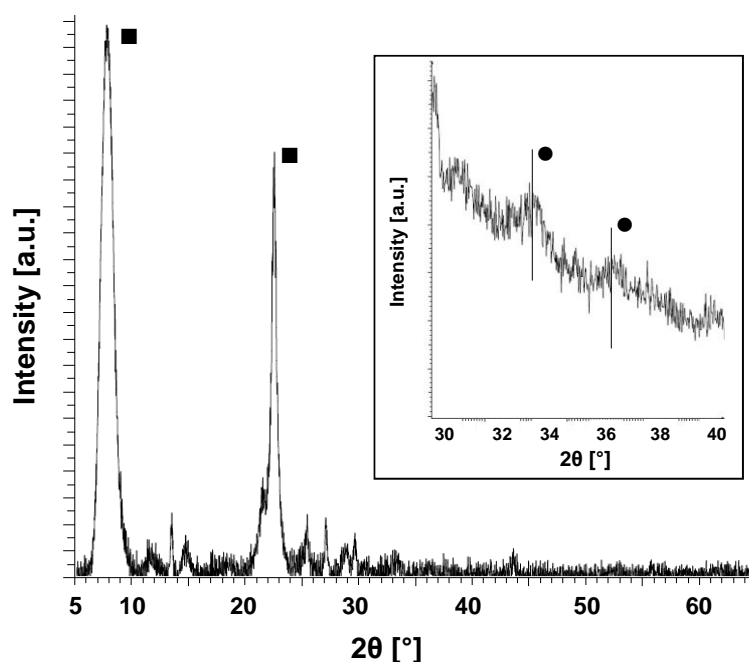
Figure 4.5 X-ray diffraction pattern of the studied Fe-BEA catalyst: ■ crystalline BEA zeolite, ● α-Fe$_x$O$_y$.

4.3 In-situ IR spectroscopy measurements

4.3.1 Interest of the method

The analysis of the NH$_3$-SCR reactions scheme over Fe-zeolites has already been extensively reported by several researchers (see conclusions in section 1.7). Nevertheless, correlations between reaction pathways and respective catalytic active sites were consistently established only in few studies. Moreover, as explained in section 3.3, the development and calibration of a multi-site kinetic model, which could account for such phenomena necessitates dedicated experimental studies in order to precisely determine the nature and the number of model surface sites, as well as to access structural information of the Fe-zeolite for kinetics calibration. In this context, infrared spectroscopy is probably one of the most suitable techniques, enabling to draw a link between chemical reaction steps and catalytic active sites.

The principles of the IR spectroscopy can be found in several academic sources. Here, only a short overview is given. When a molecule is exposed to infrared radiation, part of the radiation is absorbed and converted into energy of molecular vibration. To accomplish radiation adsorption, the radiant energy should match the energy of the specific molecular vibration. Hence, an IR spectrum represents the percentage of energy absorption or transition as a function of the absorbed/transmitted vibration frequency, which is equal to the frequency of the respective absorbed radiation. By identifying the

type of vibration frequency of a surface molecule, information related to the molecule-active site coordination can be extracted. From a quantitative point of view, the concentration of the absorbed species is linked with the absorbance, obtained form an IR spectrum through the Beer-Lambert law:

$$A = \varepsilon \cdot l \cdot C$$

<div align="right">**eq. 4.1**</div>

where A is the absorbance, ε is the molar absorption coefficient, l is the path length (which corresponds to the sample length traversed by IR radiation) and C is the adspecies concentration.

Regarding surface characterization studies employing IR spectroscopic measurements, a throughout review, published by Vimont et al. [221] is note worthy. Identification of catalytic active sites can be accomplished by performing adsorption of probe molecules, since recorded IR spectra provide information related to interactions between this molecule and a specific surface site. For example, CO and NO have been widely used as probe molecules for characterization of metallic and redox sites (see references included in [221]). Moreover, performing IR spectroscopy in in-situ and/or operando conditions, catalytic reactions and respective reaction mechanisms may be suggested, by interpreting formation/decomposition of intermediate adspecies during reactivity experiments. Nevertheless, IR spectra should be carefully interpreted, due to several limitations of the optical technique. The presence of surface impurities, such as water and carbonates, existing in the ambient air can be easily detected through IR spectroscopy, disturbing the correct spectral interpretation. Moreover, adsorption of certain molecules such as NO_x and CO_x leads to the formation of adspecies, which characterized by increased thermal stability (up to temperatures as high as 750 °C). Therefore, high temperature treatment of the catalytic sample is necessary before performing successive IR spectroscopic measurements. However, such treatment conditions may have severe effects on the studied sample, causing sintering and in the case of zeolites dealumination.

Taking the abovementioned advantages and disadvantages into consideration, NH_3 and NO_x adsorption and desorption as well as NO_x-NH_3 reactivity were studied employing in-situ IR spectroscopic measurements. Respective experimental details are presented in the following sections.

4.3.2 NH_3 and NO_x adsorption and TPD experiments

NH_3 and NO_x storage and release over H- and Fe-BEA were investigated by means of NH_3 adsorption and TPD experiments using IR spectroscopy. For NH_3 storage experiments, 9 mg of H-BEA and 10.3 mg of Fe-BEA were used, whereas ca 10 mg of H-BEA and 10 mg of Fe-BEA were weighted for NO_x adsorption and TPD tests. Powder catalysts were then pressed into self-supported wafers of 2 cm^2 and placed in a respective single wafer reactor. The latter was installed in an electric, lab-made oven so as to perform NH_3 and NO_x temperature programmed desorption experiments. A k-type thermocouple was connected to the reactor in order to measure catalyst temperature. Feed gas composition was controlled by individual mass flow controllers (Brooks Instrument) and the final mixture composition was handled via a four-way valve. Two parallel lines of He were employed, for NH_3 or NO_x dilution and catalyst flushing. The complete set-up was electronically managed through software developed by the UCCS laboratory.

Gaseous species concentration was measured via a Nicolet 380 FTIR spectrometer (resolution: 1 cm^{-1}, 64 scans per spectrum) operating at 70 °C. Moreover, a second spectrometer (Nicolet 6700 - resolution: 4 cm^{-1}, 64 scans recorded per spectrum) coupled with a high temperature cell was used for in-situ FTIR spectroscopy, in order to characterize surface adspecies. The complete experimental set-up is presented in Figure 4.6. In order to ensure experimental results reproducibility, a series of preliminary runs was performed and respective details are discussed in Appendix A.
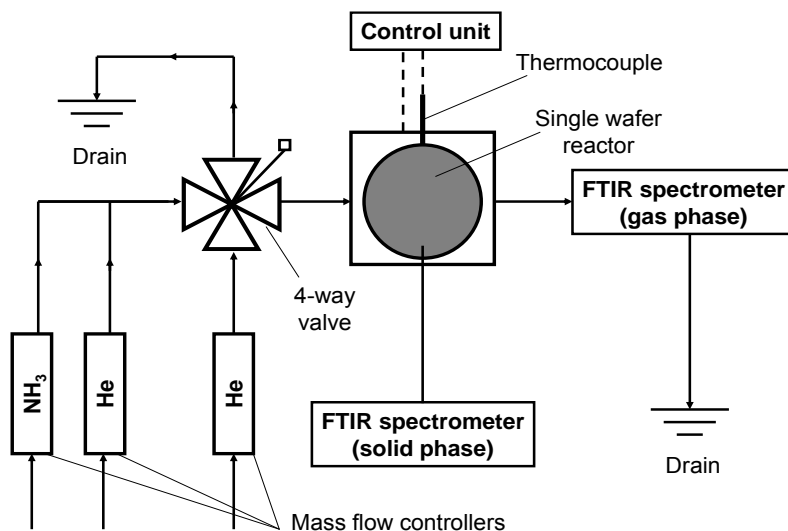
Figure 4.6 Experimental set-up used for NH$_3$ and NO$_x$ adsorption and TPD experiments.

For NH$_3$ adsorption and desorption experiments a common protocol was used, including samples exposure to ca 600 ppm of NH$_3$ in He for 80 min, at various temperatures (exceptionally a NH$_3$ adsorption experiment on H-BEA, performed at 30 °C, included 75 min of NH$_3$ injection), followed by He purging for a certain time, in order to remove weakly adsorbed and/or physisorbed ammonia, and a TPD up to 400 °C, under He, at a chosen heating rate. In the presented experimental set-up, the maximum reactor temperature could roughly exceed 400 – 405 °C, due to significant oven heat losses to ambient. Prior to each experiment, a TPD up to 400 °C was performed so as to desorb residual amounts of adspecies. The complete set of NH$_3$ adsorption/desorption experiments that are going to be discussed in following chapters is collected in Table 4.2.

A similar experimental protocol was adopted for NO$_x$ adsorption and TPD. In order to increase the maximum temperature of thermo-desorption the oven thermal insulation was enhanced, enabling to achieve TPD temperatures as high as 495 °C. NO storage was investigated by preadsorbing 0.3 % NO diluted in He on Fe-BEA for 100 min, at 30 °C. Then, the catalyst was flushed in He for 1 h at the same temperature and a TPD was performed up to 485 °C, under He, applying a temperature ramp of 10 °C/min. Nitrogen monoxide adsorption was also investigated under lean conditions. A mixture of 1100 ppm NO, 2% O$_2$ and He in balance were constantly injected on the Fe-BEA catalyst, while increasing stepwisely the reactor temperature from 100 to 485 °C. Initially, temperature was kept at 100 °C for 60 min, and then increased to constant steps of 150, 250, 300, 450, 485 °C. The duration of each step was 10 min, whereas the heating rate between T-steps was 10 °C/min. To ensure that no

residual amounts of NO_x adspecies remained on the surface of the Fe-BEA, the studied sample was heated at 485 °C for 1 h prior to each experiment. Finally, NO_2 adsorption and desorption experiments were performed on both the H- and Fe-BEA samples. A mixture of 0.45% NO_2, 8% O_2 and He in balance were introduced into the single wafer reactor at 30 °C for 100 min. Then, nitrogen dioxide and water were removed from the feed and the samples were purged with He for 1 h. Finally, temperature programmed desorption was performed up to 485 °C, at a rate of 10°C/min.

All the abovementioned experiments were performed at atmospheric pressure, with a total gas flow rate of 10 standard cm^3/min.

Table 4.2 Summary of NH_3 adsorption and TPD experiments.

Catalyst	NH_3 adsorption temperature (°C)	He flushing duration (min)	TPD heating rate (°C/min)
H-BEA	30	60	10
H-BEA	150	60	10
Fe-BEA	30	60	10
Fe-BEA	150	60	10
Fe-BEA	350	60	10
Fe-BEA	30	5	10
Fe-BEA	30	300	10
Fe-BEA	30	60	15
Fe-BEA	30	60	20

4.3.3 NO_x-NH_3 reactivity experiments

Interactions between nitrogen oxides and ammonia were investigated by means of NO_x-NH_3 transient reactivity and TPD experiments over the Fe-BEA lab-synthesized sample. Mixtures of 0.35% NO_2 / 2% O_2 and 0.35% NO / 0.1% NO_2 / 2% O_2 diluted in He were preadsorbed on the catalytic surface at 100 °C. Then, NO_x were removed from the feed and the sample was exposed to 0.45% NH_3 / 2% O_2 and He in balance, at the same temperature. Finally, a TPD was performed up to 485 °C, in He, at a rate of 10 °C/min. In this experimental case, a chromatographer (Varian 490-GC micro-GC) was also utitlized in order to detect N_2, produced during SCR of NO_x through ammonia. The apparatus pumped at around 7 cm^3/min gas, at intervals of 4 min so as to analyze gaseous composition. Hence, in order to avoid fluctuations of the NO_x and NH_3 gaseous concentration signals obtained from the FTIR spectrometer, the chromatographer was purposely placed downstream the latter device.

Finally, IR spectra of pure and mixed with H- and Fe-BEA powders crystalline ammonium nitrate (Aldrich, LOT Number: #MKBF2391V, 99.99% purity) were recorded through a Nicolet Protégé 460 IR spectrometer. 5 mg H- and Fe-BEA and 3 mg NH_4NO_3 were mixed with 50 mg KBR. Reference IR spectra of ammonium nitrate, H- and Fe-BEA, were also recorded for comparison purposes. The motivation of this analysis was to obtain information, which could support spectral features recorded during NO_x-NH_3 reactivity experiments.

4.4 Thermal decomposition of NH_4NO_3 – Methods

Thermal decomposition of crystalline powder ammonium nitrate was experimentally studied in order to get insight into respective reaction pathways and crystallographic phase transitions. NH_4NO_3 was obtained from Aldrich (LOT Number: #MKBF2391V, 99.99% purity). In order to investigate the effect of acidic and redox sites of H- and Fe-exchanged BEA on ammonium nitrate decomposition, H- and Fe-BEA powders were mechanically mixed (loose contact mixture) with powder NH_4NO_3. In order to obtain a homogeneous mixing, uniform distribution of particle sizes was required. Therefore, NH_4NO_3 was ground in a ceramic mortar. In order to minimize the risk of reactions during grinding and in line with caution notices reported by Savara et al. [113], very small quantities of ammonium nitrate, priory being mixed with zeolitic powders were ground each time.

4.4.1 TGA/DSC/MS measurements

NH_4NO_3 decomposition in the presence of bare and iron exchanged BEA was studied first, performing simultaneous thermogravimetric analysis (TGA) and differential scanning calorimetry (DSC), using a SDT 2960 thermogravimeter (TA instruments). 3 mg of crystalline ammonium nitrate were physically mixed with around 12 mg of the lab-synthesized H-BEA and Fe-BEA. An additional sample of 3 mg ammonium nitrate mixed with 12 mg SiO_2 (Sand Ottawa, LOT number: #1169555) was also prepared in order to study decomposition of pure NH_4NO_3. The three samples were deposited in an open alumina crucible and heated up from 25 to 350 °C, at a rate of 5 °C/min. All experiments were performed under a constant He flow of 100 mL/min. Finally, gaseous species released during NH_4NO_3 decomposition were monitored using a mass spectrometer (OmniStar Pfeiffer) connected downstream the thermo-gravimeter.

4.4.2 Thermo X-ray diffraction analysis

Ammonium nitrate crystallographic phase transformations during decomposition were studied by means of thermo X-ray diffraction. Initially, phase transitions of pure NH_4NO_3 were investigated, using a X8 APEX 2 BRUKER diffractometer, equipped with a molybdenum tube. Crystalline ammonium nitrate was ground and placed in a quartz capillary tube (0.1 mm), until filling completely the available volume. The tube was then installed on a rotating base, whereas the APEX 2 detector

was placed at a distance of 60 mm away from the tube. The sample was finally observed via an electronic camera. The complete experimental set-up is illustrated in Figure 4.7. An additional in-situ XRD experiment was performed aiming to study the reactivity between NH_4NO_3 and H-BEA. For safety reasons and in order to obtain results, comparable with the ones of TGA/DSC, 28 mg zeolite were mixed with 6 mg ammonium nitrate, keeping this way a H-BEA/NH_4NO_3 ratio equal to 20%. The mixture was placed in powder Rigagu, Smart Lab X-ray diffractormeter, equipped with a Cu filament. A similar experimental protocol was used in both cases. The samples were heated stepwisely from room temperature (ca 20 °C°) up to 200 °C, at intervals of 10 °C and a heating rate of 5 °C/min was applied between temperature steps.
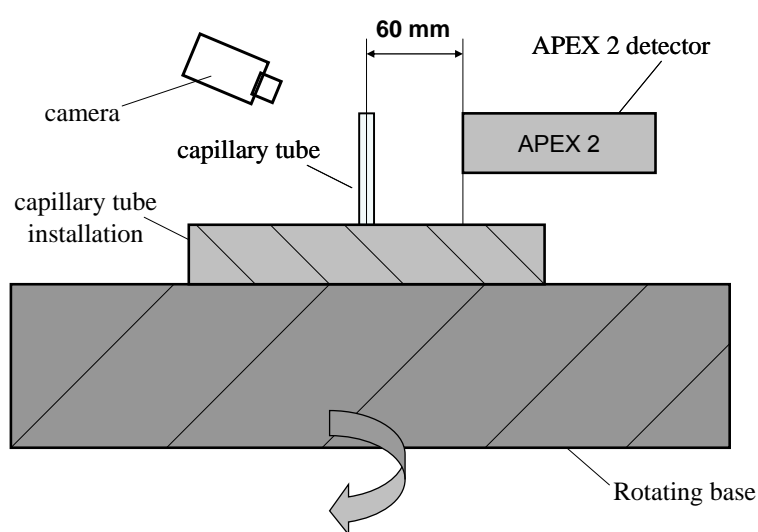
Figure 4.7 Experimental set-up for performing a thermo-XRD analysis during pure NH_4NO_3 decomposition.

Chapter 5

NH$_3$ Adsorption and Desorption on H- and Fe-BEA Catalysts

5. NH₃ *Adsorption and Desorption on H- and Fe-BEA Catalysts*

Abstract

Dedicated NH₃ adsorption and desorption experiments were performed over the lab-synthesized H- and Fe-exchanged BEA zeolites, in order to elucidate mechanistic aspects related to ammonia storage and release over these catalysts. Coupling FTIR spectroscopy, surface NH₃ species were characterized. NH₃ gaseous concentration profiles were subsequently simulated by means of a detailed multi-site kinetic model, being able to account for low temperature adsorption phenomena. Finally, correlations between surface acidity and model sites were enabled by comparing IR spectroscopy and model predicted results, leading to the development of a phenomenological semi-detailed, multi-site kinetic modeling approach.

Résumé

Des expériences d'adsorption et de désorption du NH₃ ont été réalisées sur des échantillons H- et Fe-BEA synthétisées en laboratoire, afin d'élucider des aspects mécanistiques liés au stockage de l'ammoniac sur ces catalyseurs. Les espèces NH₃ de surface ont été caractérisées en employant la spectroscopie FTIR. Les profils de concentration gazeuse de l'ammoniac ont été ensuite simulés au moyen d'un modèle cinétique détaillé de type "multi-site", qui a été capable de prendre en compte des phénomènes d'adsorption à basse température. Finalement, des corrélations entre l'acidité de surface et des sites du modèle ont été établis, par une comparaison des résultats de spectroscopie IR et de résultats obtenus par le modèle cinétique. Par conséquent, une approche de modélisation cinétique, phénoménologique et semi-détaillée a été élaborée.

5.1 Introduction

NH_3 adsorption and desorption over H- and Fe-zeolites is a very well documented topic (see section 1.5). Regarding H-BEA zeolites, numerous experimental studies have been reported, aiming to characterize surface acidity. Indicatively, NH_3 adsorption and TPD experiments, employing infrared (IR) spectroscopy have been presented by Hegde et al. [222]. The effects of Al content and steaming exposure on H-BEA acidity have been studied by Camiloti et al. [223], Barthel et al. [224] and Maier et al. [225]. Nevertheless, regarding Fe-exchanged BEA catalysts, very few published results were found. For example, in a very recent publication, Zhang et al. observed, by means of NH_3-TPD on Fe-BEA (Si/Al=12, Fe/Al=0.05) strong NH_3 adsorption on Brønsted acidic sites [226]. Moreover, the effect of the experimental protocol on NH_3 storage and release was not systematically investigated and only very little information is available, focusing exclusively on H-BEA samples. Among them, Lonyi et al. [227] and Penzien et al. [228] investigated the effect of temperature on NH_3 adsorption on bare BEA.

Regarding the kinetic modeling of ammonia adsorption and desorption over Fe-zeolites, accounting for interactions of NH_3 with different surface sites, several approaches have been proposed in literature (see details in section 1.6). Nevertheless, only those developed by Klukowski et al. [139] and Shwan et al. [140] were validated over Fe-BEA. Moreover, in all reported models, low temperature physisorption was only described by a global single site, without taking into account the specific nature of physically adsorbed molecules (eg. single layer adsorption, condensation etc). Furthermore, surface Brønsted and Lewis type acidity have never been interpreted through a modeling approach. Even in the case of the multi-site model of Shwan et al. [140], the model was developed based on data reported in literature, whereas the respective simulation results were not evaluated through catalyst surface characterization. Finally, kinetics robustness (irrespectively the type of catalyst modeled) has only been verified over a limited number of experimental conditions.

Overall, even though NH_3 storage and release on H-BEA was experimentally investigated by many researchers, respective results on Fe-BEA were very few, whereas the effect of experimental conditions was not examined in details. Thus, in this chapter, a dedicated experimental study of NH_3 adsorption and TPD on both H- and Fe-exchanged BEA catalysts is presented, according to which a broad range of operating conditions are investigated. These experiments were coupled with in-situ IR spectroscopy measurements so as to characterize NH_3 adspecies, involved in ammonia storage and release processes over these catalysts.

Moreover, since already published experimental results of NH_3 storage on Fe-BEA have neither been evaluated nor verified by kinetic modeling (except from the work of Klukowski et al. [139] and Shwan et al [140]), gas phase NH_3 concentration signals were simulated through the multi-site kinetic model presented in chapter 3. The existing model was further extended so as to adequately describe low temperature physisorption phenomena. Bridging the gap between model sites and actual surface Brønsted and Lewis acidic sites, simulation results were interpreted by means of IR spectra, unraveling mechanistic aspects of NH_3 interactions with different surface sites of H- and Fe-BEA.

5.2 Ammonia adsorption and TPD experiments on H- BEA

NH$_3$ adsorption and desorption were initially studied on the H-BEA zeolite, through an ammonia adsorption and TPD experiment. Briefly, ca 600 ppm of NH$_3$ in He balance were preadsorbed for 75 min, at 30 °C, followed by 1h of He flushing and a TPD, performed up to 400 °C, at a heating rate of 10 °C/min.

IR spectra recorded at different times of the adsorption phase are presented in Figure 5.1, whereas the detected ammonia adspecies and the respective occupied surface sites are summarized in Table 5.1. As it was expected, NH$_3$ adsorption led to the formation of broad IR bands [229], hence a subtraction between the IR spectra recorded at the beginning and the end of the adsorption was also collected in the same figure for comparison purposes. Focusing on the latter spectrum, negative maxima were observed in the OH region, at 3782, 3747 and 3610 cm^{-1} (a detailed analysis of these IR bands is presented in section 4.2) with a correlative increase in intensities of the IR signals within the ranges: 3500 – 2200 cm^{-1} and 1800 – 1350 cm^{-1}, indicating consumption of non acidic/acidic sites and formation of NH$_3$ adspecies respectively. Interestingly, a broad negative maximum centred at 3665 cm^{-1} (Figure 5.2 A) shows interactions of NH$_3$ with extra-framework Al species [213]. As illustrated in Figure 5.1, ammonia interacting with Lewis acidic sites gave rise to IR bands in the range of 3500 - 3100 cm^{-1} and 1630 cm^{-1}, related to v_{N-H} and $\delta_{N-H,asym.}$ stretching vibration modes respectively [86,229,230]. The nature of these sites could be either tricoordinated Al atoms [231] or Al species attached to defective sites, related to framework and extra-framework positions [232], which can not be ruled out as mentioned above. Moreover, formation of NH$_4^+$ on Brønsted type acidic sites was evidenced via the observation of broad bands at 3020, 3000 and 2770 cm^{-1} as well as in the range of 1500 - 1400 cm^{-1}, assigned to v_{N-H} stretching and $\delta_{N-H,asym.}$ bending modes respectively [86,229].
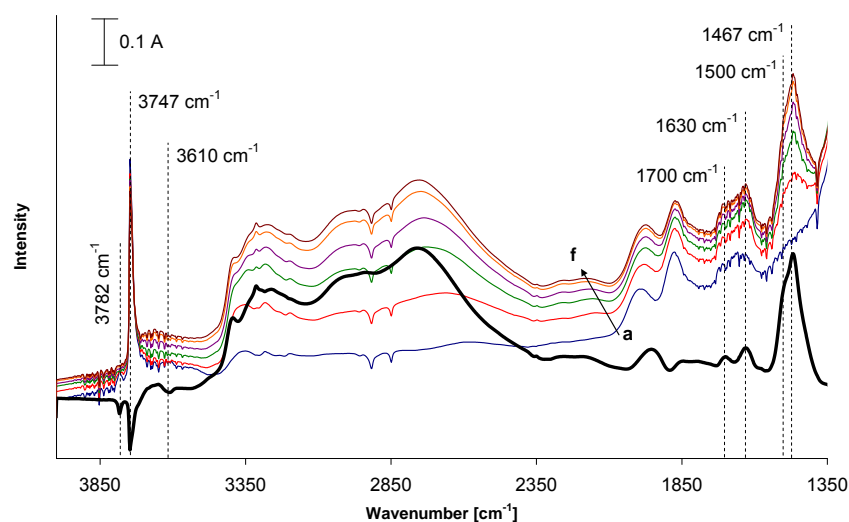
Figure 5.1 IR spectra recorded during NH$_3$ adsorption experiment on the H-BEA studied sample at 30 °C (injection of 600 ppm of NH$_3$ in He, for 75 min): thin lines correspond to IR spectra recorded at a) 0 min, b) 15 min, c) 30 min, d) 45 min, e) 60 min, f) 75 min. The thick line corresponds to a difference spectrum between the beginning and the end of the adsorption.

Table 5.1 Summary of ammonia adspecies and respective occupied surface sites of the H-BEA studied zeolite.

NH₃ adspecies		Consumed surface sites	
Adspecies	**IR bands**	**Surface site**	**IR bands**
physisorbed and/or weakly adsorbed NH₃	-	External silanols	3747 cm⁻¹
NH₃ on Lewis acidic sites	3500 – 3100 cm⁻¹ 1630 cm⁻¹	Extra-framework Al species	3665 cm⁻¹
NH₄⁺	3020, 3000, 2770 cm⁻¹ 1500 – 1400 cm⁻¹	OH⁺ Brønsted acidic sites	3610 cm⁻¹
N₂H₇⁺	1700 cm⁻¹	OH⁺ Brønsted acidic sites[1]	3610 cm⁻¹

[1]: $N_2H_7^+$ is formed over NH_4^+ ammonium cations, which are formed upon interactions between NH_3 and OH+ Brønsted acidic sites.
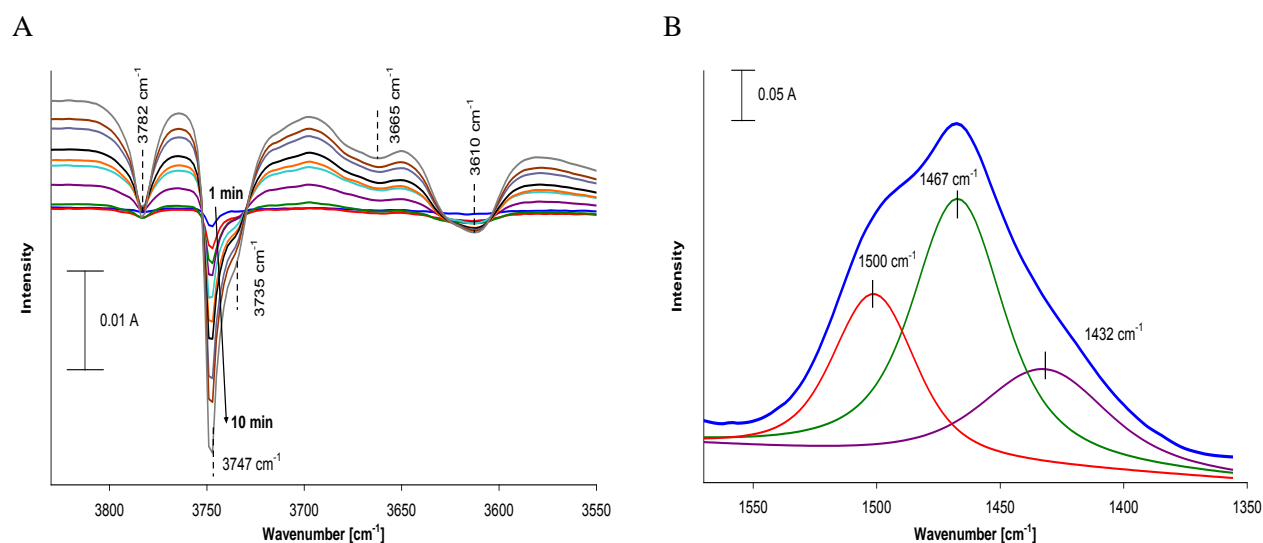
Figure 5.2 A) Difference spectra in the range of 3550 – 3900 cm⁻¹ recorded within the first 10 min of NH_3 adsorption on H-BEA B) Deconvolution of a difference IR spectrum in the range of 1500 – 1350 cm⁻¹ recorded at the end of NH_3 adsorption on H-BEA (t=75 min) – (Injection of 600 ppm of NH_3 at 30 °C in He). The reference spectrum subtracted, was recorded at the beginning of the adsorption experiment (t=0 min).

Deconvoluting the difference IR spectra in the latter range (employing a Gaussian Lorenzian equation) three components were observed centred at 1500, 1467 and 1432 cm⁻¹ (Figure 5.2 B), corresponding to different types of hydrogen bonded ammonium and namely monodentate, bidentate and tridentate complexes [233]. Simultaneously, a weak IR maximum at 1700 cm⁻¹ was observed,

being assigned to the bending mode of $N_2H_7^+$ hydrogen bonded to the zeolite framework [234]. This species is present when the catalyst is exposed to NH_3 excess $NH_3/H^+>1$) [233] and is created via bonding of an NH_3 molecule on an ammonium cation, since the latter may exhibit Brønsted acidity [235].

The latter tends to indicate that at low temperatures, NH_3 molecules can be weakly stored as multi-layers on other already chemisorbed molecules. It is recognized that during physisorption over microporous materials (such as BEA zeolites), upon pore filling three main structures can be formed, including a) molecular monolayers, b) multilayers or c) condensate, occupying residual pore space not covered by multi-layers (capillary condensation) [236]. The type of physical adsorption can be determined by means of adsorption isotherms. NH_3 adsorption isotherms of the studied H- and Fe-BEA samples were not measured so as to identify the actual isotherm type, since deeper analysis on this topic is out of the scope of the presented work. However, NH_3 volumetric adsorption isotherms over an H-BEA sample (Si/Al=12.5), reported by Dragoi et al. [237] showed a linear pressure dependency of the amount of adsorbed NH_3 (isotherm type I) for pressures higher than 0.01 Torr. This type of isotherm corresponds to physical monolayer or multilayer adsorption [238]. Capillary condensation is rather related to mesoporous materials and it is characterized by type IV adsorption isotherms including a hysteresis loop [236]. Thus, condensation can be possibly ruled out.After completing the discussion about IR spectra recorded during NH_3 adsorption, it has to be pointed out that a more precise interpretation of IR bands centred within the v_{N-H} stretching region $(3500 - 2200$ cm$^{-1})$ was purposely avoided. Interaction between strong and weak bands within the same energy range can create Evans transmission windows that can be misleading for spectra post-processing within the discuused range [239].

The thermal stability of the abovementioned NH_3 adspecies was evaluated through the TPD experiment, illustrated in Figure 5.3. Overall, 1.64 mol/kg$_{zeolite}$ NH_3 were stored and released during the adsorption and TPD phases. Analyzing the obtained TPD gas phase signal, at least three distinguishable desorption peaks could be observed. The low temperature desorption peak, lying at around 125 °C, was assigned to desorption of hydrogen-bonded NH_3, from non acidic surface sites [173]. The shoulder at ca 250 °C and the broad desorption peak at 350 °C were attributed to ammonia desorbed from weak and strong acidic sites respectively [240,241].

In order to get more insight into the nature of desorbed NH_3 species at different temperatures, IR spectra were recorded during the TPD experiment. Regarding the low temperature regime (Figure 5.4 A), after evacuation at 30 °C for 1h all IR bands attenuated, indicating a partial removal of weakly sorbed NH_3. A temperature increase up to 125 °C led to the disappearance of the IR maxima at 1700 and 1500 cm^{-1}, whereas the 1467 cm^{-1} band became almost symmetric, shifting to 1461 cm^{-1}. The abovementioned observations, tend to indicate that at such low temperatures, physically adsorbed ammonia from already chemisorbed Brønsted acidic sites ($N_2H_7^+$ at 1700 cm^{-1}) as well as loosely hydrogen bonded ammonium (possibly monodentate NH_4^+ at 1500 cm^{-1}) are removed revealing NH_4^+ coordinated to strong Brønsted acidic sites (IR peak at 1461 cm^{-1}). Therefore, it was confirmed that the NH_3-TPD peak at 125 °C is assigned to weakly adsorbed or physisorbed ammonia. Outgassing the H-BEA at 175 °C, the IR band at 1630 cm^{-1} (which had already significantly attenuated at 125 °C) vanished completely, whereas the IR maximum at 1461 cm^{-1} attenuated and shifted to 1448 cm^{-1}.

Thus, a shoulder of the NH$_3$-TPD centred at 175 °C is attributed to NH$_3$ desorbed from weak Lewis and Brønsted sites.
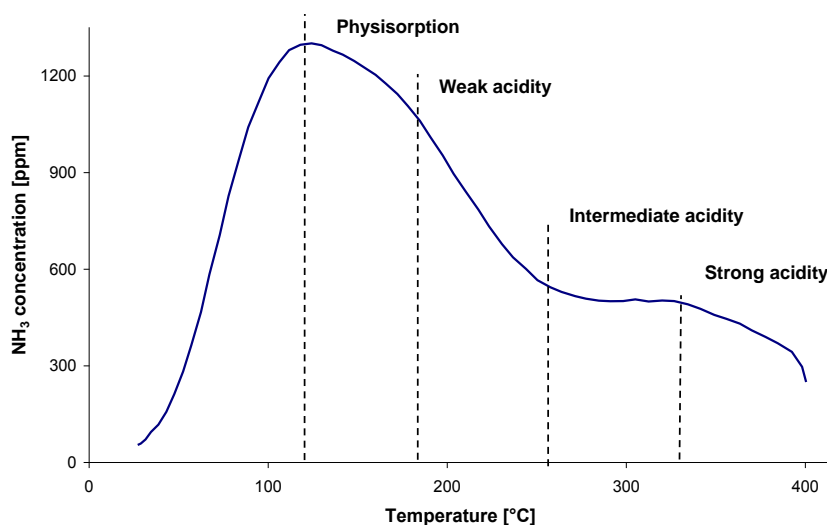
Figure 5.3 NH$_3$-TPD experiment on the H-BEA studied sample: Preadsorption of 600 ppm of NH$_3$ in He, for 80 min at 30 °C, followed by 60 min He flushing at the same temperature and TPD up to 400 °C at a heating rate of 10 °C/min.
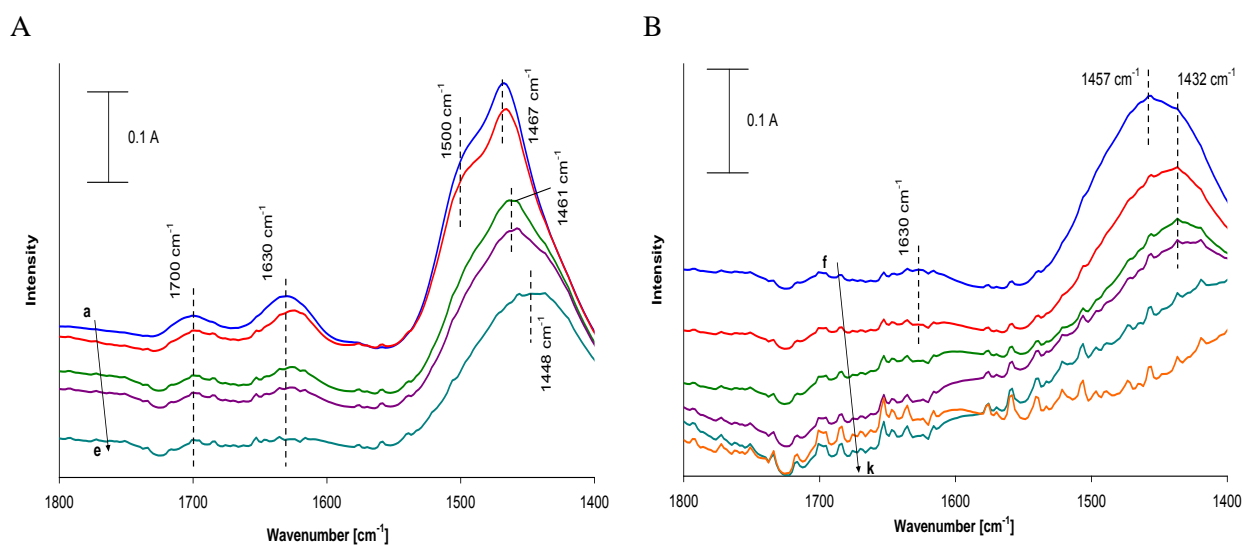
Figure 5.4 Evolution of the NH$_3$-TPD on H-BEA in the temperature ranges of A) 30 – 175 °C B) 150 – 400 °C. Difference spectra recorded at: (a) 30°C at the end of adsorption, (b) 30°C after 1h He purging, (c) 100°C, (d) 125°C, (e) 175°C, (f) 150°C, (g) 200 °C, (h) 250°C, (i) 300°C, (j) 350°C, (k) 400°C. The reference spectrum subtracted, was recorded at the beginning of the adsorption experiment (t=0 min).

Difference IR spectra recorded at higher temperatures are illustrated in Figure 5.4. At 150 °C the IR bands at 1457 and 1432 cm^{-1} could be observed. On the other hand, subsequent temperature increase

up to 250 °C led to a significant attenuation of the 1475 cm^{-1} IR band. Finally, upon evacuation at 350 °C the peak at 1432 cm^{-1} vanished completely and the surface was free of NH$_3$. Therefore, it could be concluded that the NH$_3$-TPD shoulder at around 250 °C and the broad peak at 330 °C correspond to NH$_3$ desorbed from Brønsted sites characterized of intermediate and strong acidity respectively. As already discussed, NH$_3$ chemisorption on strong Brønsted sites leads to the formation of bidentate and tridentade ammonium complexes, which are supposed to exhibit significant stability due to the negatively charged surroundings in zeolitic cavities [233].

5.3 NH$_3$ adsorption and TPD on Fe-BEA

The effect of Fe on NH$_3$ storage was investigated through NH$_3$ adsorption and TPD experiments performed on both the H- and the Fe-BEA studied samples. 600 ppm of NH$_3$ diluted in He were introduced in the single wafer reactor at 150 °C, for 80 min. Subsequently, the catalysts were flushed with He for 60 min, at the same temperature and a TPD from 150 to 400 °C was performed, applying a temperature ramp of 10°C/min. The adsorption temperature for these experiments was purposely chosen equal to 150 °C, rather than 30 °C (as in section 5.2) in order to avoid large NH$_3$ uptake through physisorption.

IR spectra recorded during adsorption over both catalysts are presented in Figure 5.5. Upon NH$_3$ admission (difference spectra - thick lines), IR bands observed at 1620 and 1460 cm^{-1}, whereas the same negative maxima were identified in the OH region: 3781, 3745 and 3610 cm^{-1}. The intensity of the peak centred at 1620 cm^{-1}, at the end of adsorption was higher in the case of the Fe-BEA catalyst, compared to the H-BEA one. As it has already been commented, this peak is connected with NH$_3$ coordinated to Lewis type acidic sites (section 5.2). Therefore, this increase in intensity was assigned to NH$_3$ bonded on Fe sites, that exhibit Lewis type acidity [178,179,242]. According to Connell et al., these sites are associated with bridging hydroxyl groups between iron and Si^{4+} cations [243]. Based on the analysis presented in chapter 3, it was concluded that NH$_3$ is most favourably adsorbed over dimeric and/or oligomeric iron clusters (possibly HO-Fe-O-Fe-OH). Nevertheless, adsorption of NH$_3$ on isolated iron cations can not be excluded. For example, Brandenberger et al have reported experimental results of NH$_3$ adsorption on Fe-ZSM5 catalysts of low iron content, wholly composed of Fe^{3+} cations [167,197].

On the other hand the IR maximal intensity at 1458 cm^{-1} attenuated over the Fe-BEA sample, showing a decrease in the amount of ammonia stored on strong Brønsted acidic sites. This reasonable phenomenon was straightforwardly related to a deterioration of the number of Brønsted acidic sites, upon the exchange of H$^+$ protons with Fe^{n+} cations [167]. Finally, it has to be pointed out that a very broad peak was found at 1690 cm^{-1}, whereas the IR shoulder at 1500 cm^{-1} was absent, indicating limited NH$_3$ physisorption and/or weak adsorption at 150 °C. Nevertheless, the absence of the latter band, due to the H$^+$ protons exchange by Fe cations can not be ruled out.
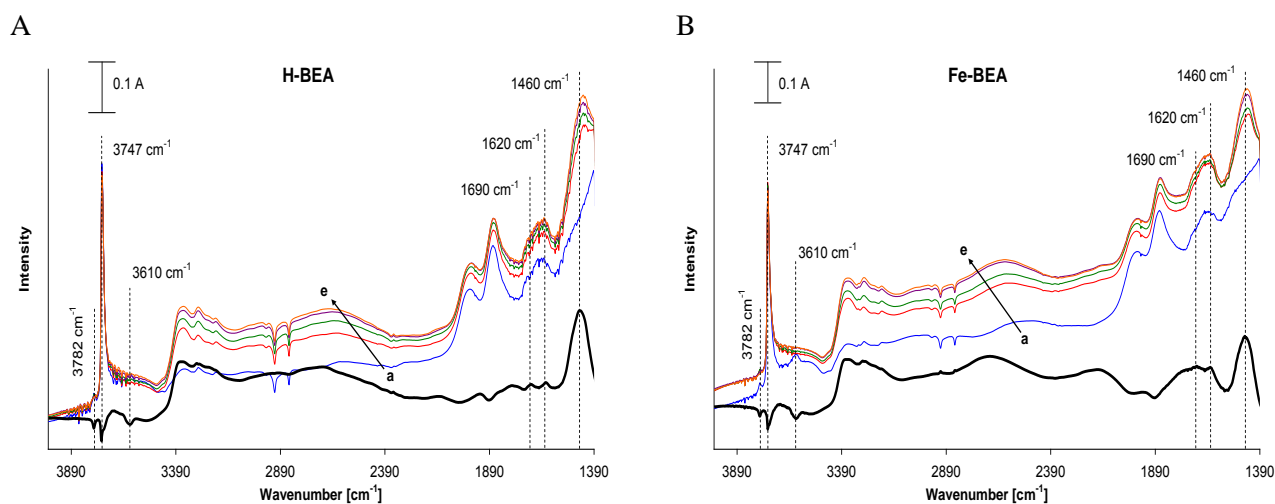
Figure 5.5 IR spectra recorded during NH$_3$ adsorption experiment on the A) H-BEA B) Fe-BEA studied sample at 150 °C (injection of 600 ppm of NH$_3$ in He, for 80 min): thin lines correspond to IR spectra recorded at a) 0 min, b) 10 min, c) 20 min, d) 40 min and e) 80 min. The thick line corresponds to difference spectrum between the beginning and the end of the adsorption.
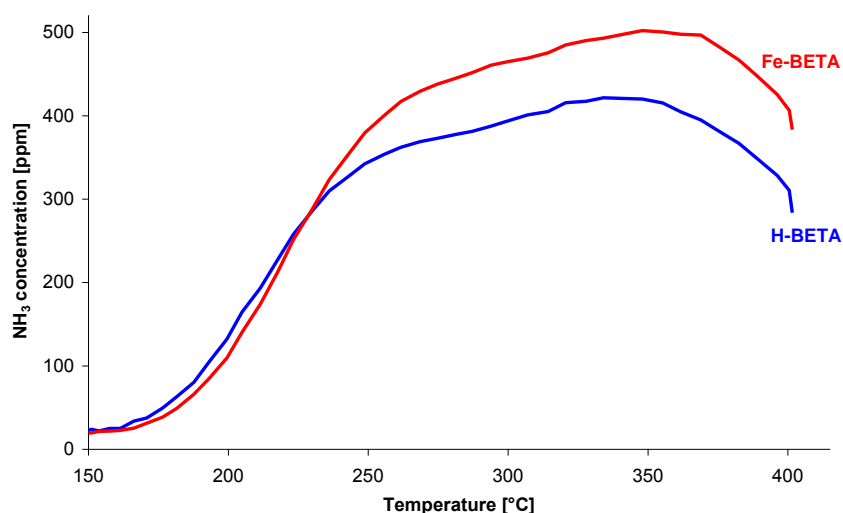
Figure 5.6 NH$_3$-TPD over the H- and Fe-BEA studied sample: Preadsorption of 600 ppm of NH$_3$ in He, for 80 min at 150 °C, followed by 60 min He flushing at the same temperature and TPD up to 400 °C at a heating rate of 10 °C/min.

The respective TPD signals over both samples are presented in Figure 5.6. In this case 0.56 and 0.66 mol/kg$_{catalyst}$ ammonia were adsorbed and desorbed over the bare and the iron exchanged BEA respectively. IR spectra recorded during the TPD experiments (Figure 5.7) show that upon flushing with He at 150 °C for 1 h (blue lines), the IR peak centred at 1458 cm^{-1} shifted to 1445 cm^{-1} indicating the removal of small amounts of physisorbed or weakly chemisorbed NH$_3$. As the evacuation temperature increased, the intensity of the band at 1620 cm^{-1} decreased and the peak finally vanished at 200 and 350 °C over the H-BEA and the Fe-BEA respectively. Thus, it was confirmed that the

increase in the NH$_3$-TPD profile over the Fe-BEA, within 240-390 °C was assigned to NH$_3$ coordinated on iron sites. Finally, ammonium ions (1445 cm^{-1}) were completely removed from strong Brønsted sites at 400 °C over both samples.
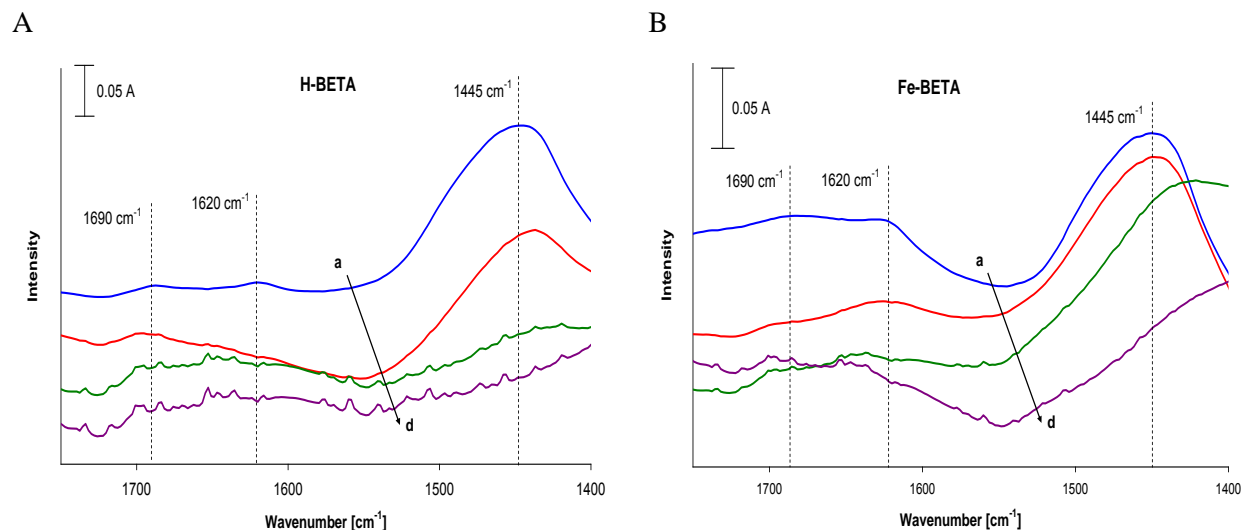
Figure 5.7 Difference IR spectra in the N-region, recorded during NH$_3$-TPD experiment on the A) H- and B) Fe-BEA studied samples: Preadsorption of 600 ppm of NH$_3$ in He, for 80 min at 150 °C, followed by 60 min He flushing and TPD up to 400 °C at a heating rate of 10 °C/min. Spectra recorded at a) 150 °C upon 1 h He purge, b) 250 °C, c) 350 °C and d) 400 °C. For each sample, the reference spectrum subtracted was recorded at the beginning of the adsorption experiment t=0 min).

5.4 Kinetic modeling of IR spectroscopy results

The abovementioned spectroscopic observations were subsequently depicted though multi-site kinetic modeling. In analogy with the sections 5.2 and 5.3, the kinetic modeling of NH$_3$ interactions with the H-BEA acidity was initially concerned. Subsequently, respective phenomena related to iron species of the Fe-BEA were rendered.

5.4.1 Multi-site kinetic model for NH$_3$ storage on H-BEA

Based on surface acidity characterization presented in section 5.2, a correlation between the multi-site kinetic model sites (presented in section 2.3.1) and the H-BEA acidic and non acidic sites was performed.

According to the discussion presented in section 5.2, weakly sorbed NH$_3$ was desorbed up to 125 °C whereas after evacuation at 175 °C ammonia weakly bonded to Lewis and Brønsted acidic sites was removed. Therefore, it was decided to divide the S1 model site into two different sites, named as S1a

and S1b in order to account for sites for weak adsorption and physisorption as well as weak Lewis and Brønsted acid sites respectively. Moreover, a multi-layer physisorption mechanism was considered, according to which up to two ammonia molecules can be physically sorbed on NH_3 already coordinated to S1a and S1b sites. This assumption seems consistent with the existence of the bending mode of $N_2H_7^+$, being identified through in-situ IR spectroscopy measurements. The proposed approach indicates that multi-site physisorption occurs on the S1b site, which partially corresponds to weakly acidic Brønsted sites, whereas no physisorption was taken into account on NH_3 bonded to strongly acidic Brønsted sites. This simplification was considered for two reasons: a) to simplify kinetics calibration, b) to take into account that the activation energy of NH_4^+ formation may change after coordinating one or more NH_3 molecules. Fripiat et al. [244] have proved via conductivity measurements that upon $NH_3 \cdot\cdot NH_4^+$ formation, a proton transfer along the $^+$N-N axis is possible, which indicates that the initially strongly chemisorbed ammonium cation can be weakly bonded to zeolite structure upon being hydrogen bonded to another NH_3 molecule. However, such aspects should be further investigated and they are out of the scope of the herein study.

Regarding S2 and S3 sites, they were attributed to Brønsted sites of different acidity strength. As discussed in section 5.2, two different NH_4^+ adsspecies (bidentate and tridentate), exhibiting thermal stability up to 250 and 350 °C were evidenced through IR bands within the 1500 – 1350 cm^{-1} region. Thus, S2 and S3 sites were assigned to intermediate and strong Brønsted sites respectively. The complete, modified multi-site kinetic model for the H-BEA zeolite is illustrated in Table 5.2.

Table 5.2 Multi-site kinetic model for NH_3 adsorption and desorption on H-BEA.

NH_3 storage on S1a sites for weak adsorption and physisorption	$NH_{3(g)} + S1a \rightleftharpoons NH_3 - S1a$
NH_3 storage on S1b weakly acidic sites	$NH_{3(g)} + S1b \rightleftharpoons NH_3 - S1b$
Multi-layer formation on S1a sites	$2\,NH_{3(g)} + NH_3 - S1a \rightleftharpoons NH_3 - NH_3 - NH_3 - S1a$
Multi-layer formation on S1b weakly acidic sites	$2\,NH_{3(g)} + NH_3 - S1b \rightleftharpoons NH_3 - NH_3 - NH_3 - S1b$
NH_3 storage on S2 intermediate Brønsted acidic sites	$NH_{3(g)} + S2 \rightleftharpoons NH_3 - S2$
NH_3 storage on S3 strong Brønsted acidic sites	$NH_{3(g)} + S3 \rightleftharpoons NH_3 - S3$

Kinetic model parameters for the H-BEA zeolite were calibrated based on different sources and they are presented in Table 5.3. Preexponential factors of NH_3 adsorption were computed based on NH_3 entropy change, according to equation 5.1 [184]. Translational, rotational and vibrational entropies of the NH_3 molecule in gas phase were determined by integrating partition functions q (eq. 5.2) in DMol

(Accelrys) using GGA-PW91 functional and TNP basis set. For the purposes of this study it is assumed that when ammonia is adsorbed on the H-BEA surface, it loses certain degrees of freedom resulting in entire loss of its translation entropy, as well as partial loss of its rotational one, at around 34.2%, 26.3% and 30.5% for S1a, S1b and S2, S3 sites respectively. Vibrational entropy was not taken into consideration since it was negligible compared to translation and rotation ones. These values are somehow in good agreement with results of Sharma et al. [191] according to which NH₃ adsorbed on H-ZSM5 loses all its translation entropy as well as ca 30% of its rotational and vibrational ones. Olsson et al. also implemented the same methodology for O_2, NO and NO_2 adsorption on H- and Cu-exchanged ZSM5 [145].

$$\Delta S = R \cdot \ln\left(\frac{A_{ads}}{A_{des}}\right)$$

eq. 5.1

$$S = R \cdot \ln(q) + R \cdot T \cdot \frac{d[\ln(q)]}{dT}$$

eq. 5.2

Table 5.3 Kinetic parameters for the multi-site kinetic model of NH₃ adsorption/desorption on H-BEA.

Type of site	$A_{j\_NH_3\_ads}$	$E_{j\_NH_3\_ads}$	$A_{j\_NH_3\_des}$	$E_{j\_NH_3\_des}$	α_j
	[m³/(s·kg zeolite)]	[kJ/mol]	[mol/s·kg zeolite]	[kJ/mol]	[-]
S1a (sites for weak adsorption and physisorption)	700[a]	0[b]	$1.8 \cdot 10^{12}$ [c]	80.80[d]	0.11[d]
S1b (weak acidic sites)	1200[a]	0[b]	$1.0 \cdot 10^{13}$ [c]	97.79[d]	0.11[d]
Multi-layer formation on S1a, S1b sites	$6.6 \cdot 10^{8}$ [e]	0[e]	$9.6 \cdot 10^{13}$ [e]	40.00[f]	0.00[e]
S2 (intermediate Brønsted acidic sites)	900[a]	0[b]	$1.0 \cdot 10^{13}$ [c]	119.50[d]	0.11[d]
S3 (strong Brønsted acidic sites)	900[a]	0[b]	$1.0 \cdot 10^{13}$ [c]	148.80[d]	0.11[d]

[a]: based on entropy loss calculations, [b]: assuming that the NH₃ adsorption is a non-activated process [183], [c]: values corresponding to adsorbed immobile molecules [184], [d]: values calibrated based on thermo-gravimetric measurements reported by Pinto et al. [186], [e]: manually calibrated through simulation of several NH₃ adsorption and TPD experiments on H-BEA studied sample (not shown in the herein work: NH₃ adsorption at 30 °C on H-BEA, followed by 1 h He flushing at the same temperature and a TPD at 15 and 20 °C/min, as well as ammonia adsorption on H-BEA at 30 °C, followed by 5 h He flushing at the same temperature and a TPD at 10 °C/min), [f]: value calibrated based on the work of Bolis et al. [245].

Activation energies of adsorption were set to zero in line with Chen et al. [183], assuming that adsorption is a non-activated process. Pre-exponential factors of desorption rate constants were tuned to the order of magnitude of 10^{13} s⁻¹, according to the transition state theory for immobile molecules

[184], considering that NH$_3$ storage capacity values are centred around 1 mol NH$_3$/kg$_{zeolite}$. The reader is referred to reference [184] for more details concerning the transition state theory and its application for molecular adsorption and desorption processes. The activation energies of desorption of S1a, S1b, S2, and S3 sites were chosen based on thermo-gravimetric measurements performed by Pinto et al. on a H-BEA sample (Si/Al=25) [186]. Furthermore, respective surface coverage dependency parameters named as α, affecting desorption activation energies were manually calibrated to low values, assuming a quite uniform Brønsted type acidity distribution over the catalytic surface (see also kinetics calibration in sections 3.1.1, and 3.2). Indeed, the studied H-BEA sample is mainly composed of Brønsted sites and only weak Lewis ones. Finally, kinetic parameters for the NH$_3$ double-layer formation mechanism were determined via simulation of several NH$_3$ adsorption and TPD experiments on the studied H-BEA zeolite, which are not presented in this work.

At this stage it has to be emphasized that even though the presented multi-site kinetic model includes different adsorption sites, it is important to keep surface coverage dependent activation energies of NH$_3$ desorption. Overall, the proposed multi-site kinetic approach accounts for sites dispersion at two different levels. The fist level includes an overall catalytic sites discretization, which enables to regroup surface sites of Fe-BEA into a) sites for physisorption and/or weak adsorption, b) weak Brønsted and Lewis acidic sites, as well as Brønsted sites, characterized by c) intermediate and d) strong acidity strength. The acidity strength of each of these groups of sites is expressed in terms of a mean activation energy of desorption (annotated as $E_{j\_NH_3\_des}$ - Table 5.3). At a second level, the multi-site model assumes a further adsorption energy variation within each group of sites.

Regarding acidic sites of the H-BEA zeolite, NH$_4^+$ in monodentate, bidentate and tridentate coordinations was identified through IR spectroscopy. Monodentate NH$_4^+$ can be formed on "isolated Brønsted acidic sites", which corresponds to a Si atom bridged with a single Al neighbouring atom via an OH$^+$ hydroxyl. On the other hand, bidentate and/or tridentate ammonium can be formed on a Si-OH$^+$-Al site located in close vicinity with two or three Al atoms.

Generally speaking, acidity strength of a Brønsted site varies depending on the topology of the Si, O, H$^+$, Al atoms, and the chemical composition of the zeolitic cavity [59]. The OH$^+$ acidity increases when the O-H$^+$ bond is elongated and the Si-O and/or Al-O bond lengths decrease. Moreover, an increased number of neighbouring Al tetrahedra leads to a degradation of the local electronegativity of the framework and thus to low acidity strength. Considering these two factors it becomes obvious that the exact length of the OH$^+$ group of isolated Brønsted sites will determine the formation of monodentate NH$_4^+$ ions characterized by different acidity strength, the mean value of which may be around 98 kJ/mol (activation energy of desorption over S1b sites – Table 5.3). Similarly, as far as intermediate and strong Brønsted sites are concerned, the location of Al atoms in close vicinity with a Si-OH$^+$-Al site will determine the stability of bidentate and tridentate NH$_4^+$. Therefore, the acidity strength of these sites will also vary, around a central value of 120 and 149 kJ/mol respectively (activation energies of S2 and S3 sites – Table 5.3). Hence, a variation of acidity strength within each group of acidic sites should be expected, which justifies why the Temkin formalism was applied to model the NH$_3$ activation energy of desorption over each surface site of the kinetic model.

The proposed activation energies of desorption over the S1a site and for the multi-layer physisorption mechanism are quite different. These values, are further discussed in section 5.6.

Moreover, values of activation energies of NH_3 desorption from H-BEA, proposed in this study are lower compared to those, used for simulating NH_3-TPD experiments on H-ZSM5 catalysts (chapter 3). However, this calibration seems to be in reasonable agreement with values of differential heat of NH_3 adsorption, reported by Auroux, which show that H-BEA zeolite exhibits weaker acidity compared to H-ZSM5 one [67].

Finally, NH_3 storage capacity over each surface site was estimated though the NH_3-TPD experiment shown in Figure 5.3 and the respective results are illustrated in Table 5.4. Totally, 1.64 mol/kg$_{zeolite}$ were stored on the catalytic surface at 30 °C. According to the results of the elemental analysis (Table 1), the H-BEA zeolite was composed of 1.11 mol/kg$_{zeolite}$ Al. This means that all acidic and non acidic sites were completely saturated and thus around 0.53 mol/kg$_{zeolite}$ ammonia were physisorbed and/or weakly adsorbed on silanols (SiOH) in the form of single or multi-layers. NH_3 desorbed up to 175 °C (corresponding to NH_3 desorbed from non acidic and weakly acidic Lewis and Brønsted sites) was estimated equal to 1.03 mol/kg$_{zeolite}$, thus around 0.5 mol/kg$_{zeolite}$ are related to weak Lewis and Brønsted acid sites. Finally, 0.61 mol/kg$_{zeolite}$ NH_3 were desorbed from intermediate and strong Brønsted acidic sites within a temperature range of 175 – 400 °C. At this stage, it has to be highlighted that the abovementioned computations provided just approximate values of storage capacity, since as it is well know the shape of the NH_3-TPD signal (and thus measured NH_3 concentration during desorption) is very sensitive to experimental conditions (see discussion in section 2.3.1).

Table 5.4 NH_3 storage capacity over the characterized sites of the studied H- BEA sample.

Type of site	H-BEA (Si/Al=11.8) N_j [mol/kg$_{zeolite}$]	Model calibration values N_j [mol/kg$_{zeolite}$]
Sites for weak adsorption and physisorption (S1a)	0.53[a]	0.47[d,f]
Weak Brønsted and Lewis acidic sites (S1b)	0.5[b]	0.5[d,f]
Intermediate Brønsted acidic sites (S2)	0.61[c]	0.23[e,f]
Strong Brønsted acidic sites (S3)		0.38[e,f]

[a]:value computed by subtracting the NH_3-TPD area (Figure 5.3) within 30 – 400 °C (including NH_3 desorbed during He flushing at 30 °C), from the total amount of Al determined through elemental analysis, [b]: value obtained by subtracting the storage capacity of non acidic sites from the NH_3-TPD peak area (Figure 5.3) within 30 - 175 °C, c: value computed by integrating the NH_3-TPD peak area (Figure 5.3) within 175 - 400 °C, [d]: values used in combination with the multi-layer physisorption mechanism, e: manually calibrated values in order to fit experimental curves, respecting a total amount of intermediate and strong acidic sites equal to 0.61 mol/kg$_{zeolite}$, [f]: manually calibrated values in order to fit the NH_3-TPD experiment shown in Figure 5.3, as well as three additional NH_3 adsorption and desorption experiments on H-BEA, applying various operating conditions (not shown in the herein work).

Based on the abovementioned discussion, the values of NH_3 storage capacity used for the multi-site kinetic model were manually calibrated (Table 5.4, third column). This calibration was performed in order to fit the NH_3-TPD experiment illustrated in Figure 5.3 as well as three additional NH_3 adsorption and TPD experiments performed on H-BEA, applying various operating conditions (not shown in the presented work: NH_3 adsorption at 30 °C on H-BEA, followed by 1 h He flushing at the same temperature and a TPD at 15 and 20 °C/min, as well as ammonia adsorption on H-BEA at 30 °C, followed by 5 h He flushing at the same temperature and a TPD at 10 °C/min).

5.4.2 Multi-site kinetic model for NH_3 storage on Fe-BEA

Based on the discussion presented in section 5.3, NH_3 can be stored on Fe cations and or Fe binuclear species, which exhibit Lewis type acidity. Moreover, the acidity strength of metallic sites proved to be higher than that of zeolitic Lewis acid ones (NH_3-TPD results - Figure 5.6 and Figure 5.7). Thus, in order to account for the abovementioned phenomena and in line with the multi-site model description presented in section 2.3.1 a global Fe site, named S4 was considered. In contradiction with section 5.4.1 it was not chosen to consider different types of metallic sites a) since NH_3 is not a probe molecule for iron sites characterization and b) in order to keep model complexity in reasonable extents. Overall, the multi-site kinetic model for Fe-BEA is illustrated in Table 5.5.

Table 5.5 Multi-site kinetic model for NH_3 adsorption and desorption on Fe-BEA.

NH_3 storage on S1a sites for weak adsorption and physisorption	$NH_{3(g)} + S1a \rightleftharpoons NH_3 - S1a$
NH_3 storage on S1b weakly acidic sites	$NH_{3(g)} + S1b \rightleftharpoons NH_3 - S1b$
Multi-layer formation on S1a sites	$2\,NH_{3(g)} + NH_3 - S1a \rightleftharpoons NH_3 - NH_3 - NH_3 - S1a$
Multi-layer formation on S1b weakly acidic sites	$2\,NH_{3(g)} + NH_3 - S1b \rightleftharpoons NH_3 - NH_3 - NH_3 - S1b$
NH_3 storage on S2 intermediate Brønsted acidic sites	$NH_{3(g)} + S2 \rightleftharpoons NH_3 - S2$
NH_3 storage on S3 strong Brønsted acidic sites	$NH_{3(g)} + S3 \rightleftharpoons NH_3 - S3$
NH_3 storage on S4 iron sites	$NH_{3(g)} + S4 \rightleftharpoons NH_3 - S4$

The respective kinetic parameters are listed in Table 5.6. The pre-exponential factor of adsorption over the S4 site was adjusted to 550 $m^3/(s \cdot kg_{zeolite})$ assuming that NH_3 looses all its translational energy and ca 39.1% of its rotational one upon adsorption on this site. Moreover, desorption activation energy, as well as the respective surface coverage dependency factor α, were manually calibrated so as

to fit the NH_3-TPD experiment shown in Figure 5.6. It has to be highlighted that the used value of heat of adsorption and thus the activation energy is much higher compared to that of zeolitic Lewis acidic sites (partially S1b), whereas the α factor is reasonably adjusted to higher values compared to those used for Brønsted acidic sites, somehow reflecting the heterogeneity of Fe species acidity (Fe^{n+}, Fe binuclear species) as discussed above and as also explained in section 3.2. Therefore, as explained in section 5.4.1, surface coverage dependent activation energy for NH_3 desorption over S4 sites was applied. Finally, the remaining kinetic parameters are the same with those presented in Table 5.2, assuming that the addition of Fe affects the storage capacity of H-BEA acidic sites rather than the zeolitic acidic strength. Indeed, as shown in Figure 5.5, IR bands which correspond to NH_3 chemisorbed on Lewis and Brønsted acidic sites are centred at the same wavenumbers, for both the H- and the Fe-BEA samples. On the other hand, the signal intenities over the H- and the Fe-BEA, are different since a certain amount of OH^+ protons has been exchanged by iron cations upon the ion exchange process. Therefore, the discussed hypothesis seems to be somehow confirmed by the presented IR spectroscopic analysis.

Table 5.6 Kinetic parameters for the multi-site kinetic model of NH_3 adsorption/desorption on Fe-BEA.

Type of site	$A_{j\_NH_3\_ads}$	$E_{j\_NH_3\_ads}$	$A_{j\_NH_3\_des}$	$E_{j\_NH_3\_des}$	α_j
	$[m^3/(s \cdot kg_{zeolite})]$	[kJ/mol]	$[mol/s \cdot kg_{zeolite}]$	[kJ/mol]	[-]
S1a (sites for weak adsorption and physisorption)	700[a]	0[b]	$1.8 \cdot 10^{12}$ [c]	80.80[d]	0.11[d]
S1b (weak acidic sites)	1200[a]	0[b]	$1.0 \cdot 10^{13}$ [c]	97.79[d]	0.11[d]
Multi-layer formation on S1a, S1b sites	$6.6 \cdot 10^8$ [e]	0[e]	$9.6 \cdot 10^{13}$ [e]	40.00[f]	0.00[e]
S2 (intermediate Brønsted acidic sites)	900[a]	0[b]	$1.0 \cdot 10^{13}$ [c]	119.50[d]	0.11[d]
S3 (strong Brønsted acidic sites)	900[a]	0[b]	$1.0 \cdot 10^{13}$ [c]	148.80[d]	0.11[d]
S4 iron sites	550[a]	0[b]	$1.0 \cdot 10^{13}$ [c]	145.00[g]	0.15[g]

[a]: based on entropy loss calculations, [b]: assuming that the NH_3 adsorption is a non-activated process [183], [c]: values corresponding to adsorbed immobile molecules [184], [d]: values calibrated based on thermo-gravimetric measurements reported by Pinto et al. [186], [e]: manually calibrated through simulation of several NH_3 adsorption and TPD experiments on H-BEA studied sample (not shown in the herein work: NH_3 adsorption at 30 °C on H-BEA, followed by 1 h He flushing at the same temperature and a TPD at 15 and 20 °C/min, as well as ammonia adsorption on H-BEA at 30 °C, followed by 5 h He flushing at the same temperature and a TPD at 10 °C/min), [f]: value calibrated based on the work of Bolis et al. [245] [g]: parameters manually calibrated in order to fit the NH_3-TPD experiment on the Fe-BEA shown in Figure 5.6.

The amount of NH_3 adsorbed on Fe sites was estimated employing the IR spectra showed in Figure 4.3. The amount of the Brønsted acidic sites remaining after the ion exchange was determined

according to the methodology described by Brandenberger et al [167], which consists in normalizing the intensity of the peak area centred at 3606 cm^{-1} over the Fe-BEA to the respective one over the H-BEA zeolite. Approximately, 74% of the H-BEA total amount of Brønsted sites remained over the Fe exchanged BEA, which corresponds to 0.45 mol/kg$_{Fe-BEA}$, according to results presented in 5.4.1. Integrating the NH$_3$-TPD areas for H- and Fe-BEA within 175 – 400 °C, shown in Figure 5.6 (without taking into account the amount of desorbed NH$_3$ during the 1 h He flushing) similar amounts of desorbed NH$_3$ were computed (ca 0.34 mol/kg$_{Fe-BEA}$). Therefore, the total amount of intermediate and strong Brønsted sites of the H-BEA is assumed to be roughly equal to the sum of the residual amount of Brønsted sites and the Fe sites occupied by NH$_3$ over the Fe-BEA catalyst. The computation results in approximately 0.16 mol/kg$_{Fe-BEA}$ iron available for NH$_3$ storage. Nevertheless, the total amount of Fe was equal to 0.31 mol/kg$_{Fe-BEA}$ (Table 4.1). According to UV-vis spectroscopic measurements performed over the Fe-BEA studied catalyst (see section 4.2), this amount corresponds to a sum of isolated Fe species, oligomeric iron clusters, as well as Fe$_2$O$_3$ particles. Therefore the computed NH$_3$ storage capacity of 0.16 mol/kg$_{Fe-BEA}$ seems to further validate the the fact that only certain iron species are preferable for NH$_3$ adsorption. NH$_3$ storage capacity over different surface sites of the Fe-BEA is illustrated in Table 5.7.

Table 5.7 NH$_3$ storage capacity over each characterized site of the studied Fe-BEA sample.

Type of site	Fe-BEA (Fe/Al=0.28) N_j (mol/kg $_{zeolite}$)	Model calibration values N_j (mol/kg$_{zeolite}$)
Sites for weak adsorption and physisorption (S1a)	-	0.47[c]
Weak acidic Brønsted and Lewis sites (S1b)	0.5[a]	0.5[a]
Intermediate Brønsted acid sites (S2)	0.45[b]	0.15[d]
Strong Brønsted acid sites (S3)		0.3[d]
Metallic sites (S4)	0.16[b]	0.16

[a]:value computed as shown in section 5.4.1, [b]: values obtained by estimating the degradation of Fe-BEA Brønsted acidity, upon the ion exchange, through normalizing the intensity of the peak area centred at 3606 cm^{-1} over the Fe-BEA to the respective one over the H-BEA zeolite (Figure 4.3), subtracting the storage capacity of non acidic sites from the NH$_3$-TPD peak area (Figure 5.3) within 30 - 175 °C, [c]: value used in combination with the multi-layer physisorption mechanism and validated over NH$_3$ adsorption and desorption experiments shown in section 5.5, [d]: manually calibrated values in order to fit experimental curves shown in sections 5.5, respecting a total amount of intermediate and strong acidic sites equal to 0.45 mol/kg$_{Fe-BEA}$.

5.5 Validation of the multi-site kinetic model

The proposed multi-site kinetic model was finally validated by simulating NH$_3$ adsorption and desorption experiments over the H- and Fe-BEA studied samples. In order to evaluate model robustness, a broad range of experimental conditions were taken into account, whereas kinetic

parameters listed in sections 5.4.1 and 5.4.2 were applied as they stand. Finally, since the experiments discussed in this chapter were performed in the single wafer reactor, the respective single wafer reactor model was applied for simulation purposes.

5.5.1 Simulation of NH₃ adsorption and desorption experiments over the H-BEA

The multi-site kinetic model for the H-BEA zeolite, shown in Table 5.2 was validated by simulation of NH₃ adsorption and TPD experiments performed at T_{ads} = 30 and 150 °C. The sample was exposed to around 600 ppm NH₃ in He balance, at T_{ads} for 75 and 80 min respectively, before being flushed with He for 1 h at the same temperature. Finally, a TPD was performed up to 400 °C, at a heating rate of 10 °C/min. The applied kinetic parameters are presented in Table 5.3 and Table 5.4.

Comparison between experimental and simulation results is illustrated in Figure 5.8. Initially, each desorption peak was separately simulated, before simulating the complete experiment. S1a, S1b, S2 and S3 sites appear to be responsible for NH₃ desorption peaks centred at around 119, 168, 245 and 350 °C respectively. In line with the interpretation of IR spectra shown in section 5.2, S1a model site corresponds to non acidic sites for weak adsorption and physisorption, S1b one to a mixture of weak Lewis and Brønsted sites, whereas S2 and S3 sites are related to Brønsted sites of intermediate and strong acidity respectively. The values of storage capacity over each site used for simulation purposes are illustrated in Table 5.4. In accordance with respective values determined through the NH₃-TPD experiment shown in Figure 5.3 and the elemental analysis, the storage capacity over S1b sites was set to 0.5 mol/kg$_{zeolite}$, whereas the sum of S2 and S3 sites capacities was calibrated to 0.61 mol/kg$_{zeolite}$. In order to fit experimental curves, individual storage capacities of S2 and S3 surface sites were manually calibrated to 0.23 and 0.38 mol/kg$_{zeolite}$ respectively. Finally, the storage capacity over S1a sites was calibrated to 0.49 mol/kg$_{zeolite}$ including the multi-layer physisorption mechanism.

Overall simulation results are in relative good agreement compared to experimental data. Nevertheless, concerning the NH₃ adsorption experiment at 30 °C (Figure 5.8 A) significant deviations appear below 100 °C, since the S1a site cannot precisely simulate the experimental curve. This observation was attributed either to experimental conditions, since the H-BEA was completely fresh during this experiment, or to a weakness of applied reaction rate expressions to describe physisorption phenomena. A multi-layer adsorption model was previously proposed by I. Kusunoki [246] according to which a sticking coefficient is computed based on atomic beam flux and residence times of adatoms. Recently Koltsakis et al. [129] have proposed an alternative NH₃ adsorption model for zeolite washcoats, based on a Dubinin-Radushkevich isotherm. According to this approach surface properties such as pore size distribution, adsorbate affinity and saturation pressure are taken into consideration. Since low temperature physisorption is related to surface characteristics of zeolites such as porosity, the abovementioned methodology seems to be somehow suitable for depicting low temperature physisorption phenomena. Finally, as far as the multi-layer mechanism is concerned, it could indicate that a larger number of NH₃ layers should have been taken into consideration. However, as already mentioned, further analysis of this topic is out of the scope of the herein work.
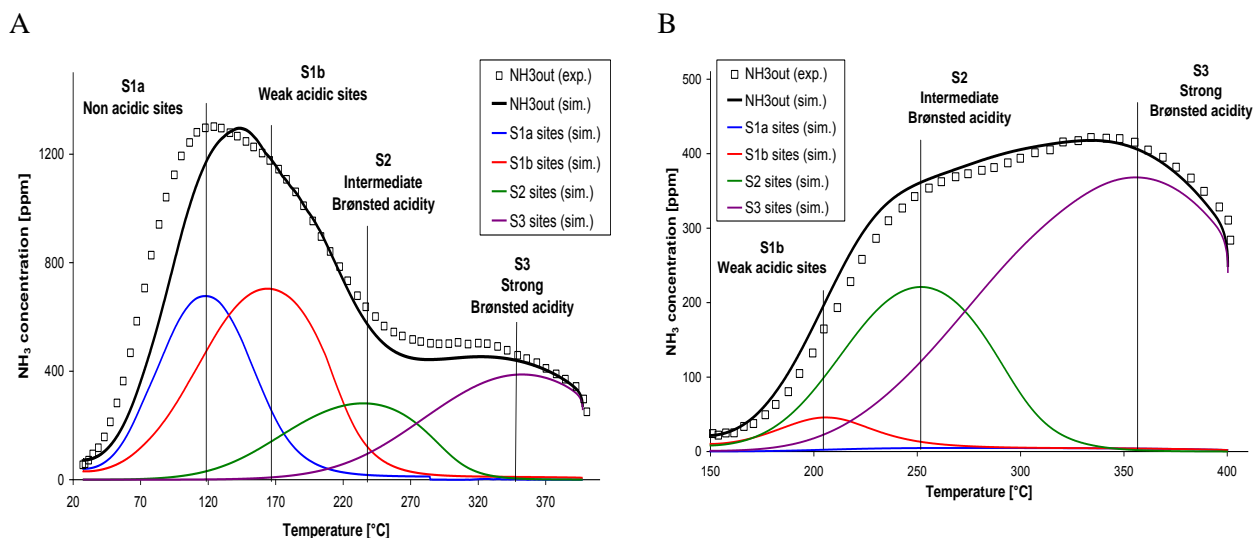
Figure 5.8 Simulation of ammonia adsorption and TPD experiments performed over the H-BEA sample. Preadsorption of 600 ppm of NH_3 in He, for 75 and 80 min at A) 30 °C and B) 150 °C respectively, followed by 60 min He flushing at the same temperature and TPD up to 400 °C at a heating rate of 10 °C/min.

5.5.2 Simulation of NH_3 adsorption and desorption experiments over the Fe-BEA

Putting results of sections 5.2 and 5.3 together, it appears that experimental conditions and in particular the adsorption temperature can affect the formation of NH_3 adspecies. Thus, in this section a broad range of NH_3 adsorption and desorption test cases over the Fe-BEA catalyst is presented and respective experimental results are evaluated through simulation. The multi-site kinetic model presented in Table 5.5 was employed, whereas for all simulations the set of kinetic parameters and the values of storage capacity presented in Table 5.6 and Table 5.7 were used, without further modification.

5.5.2.1 Effect of adsorption temperature

The effect of adsorption temperature on NH_3 storage over the Fe-BEA catalyst was investigated by performing NH_3 adsorption experiments at Tads = 30, 150 and 350 °C, for 80 min, followed by 60 min of He purging and TPD from the adsorption temperature up to 400 °C, at a heating rate of 10 °C/min.

Gas phase concentrations measured during NH_3 adsorption and TPD are shown in Figure 5.9. The significant NH_3 storage capacity at 30 °C (1.30 mol/kg$_{Fe-BEA}$) was mainly attributed to physisorption forming single or multi-layers as discussed in sections 5.2 and 5.3. Thus, it is not surprising that even after 80 min of adsorption the catalyst is not saturated (Figure 5.9 A). The total amount of desorbed NH_3 from the Fe-BEA catalyst is lower compared to that over the H-BEA zeolite, which may be

attributed to several reasons and namely: the decrease of the catalyst acidic sites upon the ion exchange process, and/or a partial blocking of zeolitic cavities due to formation of Fe oxide particles. Additionally, experimental conditions could have a contribution to this phenomenon because a) the duration of NH_3 injection was not the same for both experiments (thus low temperature desorption and readsorption was not the same) and b) the H-BEA was not calcined before testing as it had been performed for the Fe-BEA catalyst after its synthesis. On the other hand, at 150 °C the catalytic surface is saturated after around 20 min of adsorption, resulting in a NH_3 uptake of ca 0.66 mol/kg$_{Fe\text{-}BEA}$. According to the corresponding TPD signal, at this temperature the TPD peak at around 150 °C has disappeared and only desorption peaks at 250 and 350 °C can be distinguished. As shown in Figure 5.10 and explained in sections 5.2 and 5.3, these TPD peaks correspond to Brønsted sites of intermediate and strong acidity (1500 -1400 cm^{-1}), as well as to metallic sites (1630 cm^{-1}). Finally, at 350 °C, only 0.157 mol/kg$_{Fe\text{-}BEA}$ ammonia were stored on the catalyst, only on strong Brønsted sites (1440 cm^{-1}), which is also confirmed by the very low NH_3 concentration measured.

Concerning simulation of these three NH_3 adsorption experiments, the multi-site kinetic model and the proposed set of kinetic parameters enabled a quite satisfactory reproduction of the experimental data during the adsorption, the He flushing and the TPD phase. S1a and S1b sites, in combination with the multi-layer adsoption mechanism allow to represent the broad TPD peak at 140 °C, accounting for physisorption and chemisorption on weakly acidic Brønsted and Lewis sites. Moreover, S2, S3 acidic sites as well as S4 metallic sites were crucial for depicting the TPD signal at higher temperatures. A deviation between simulation and experimental data is observed at the end of the adsorption experiment at 30 °C, where the model predicted a beginning of the sample saturation after around 50 min, which could be attributed to low temperature multi-layer NH_3 adsorption. The presented model assumes adsorption of two molecules of ammonia over another NH_3 molecule, preadsorbed on S1a and S1b sites. Increasing the number of layers would lead to better results, at the expense of the model simplicity. Moreover, as already discussed in 5.5.1, reaction rate expressions used for physisorption may not be adequate, leading to imprecise simulation.
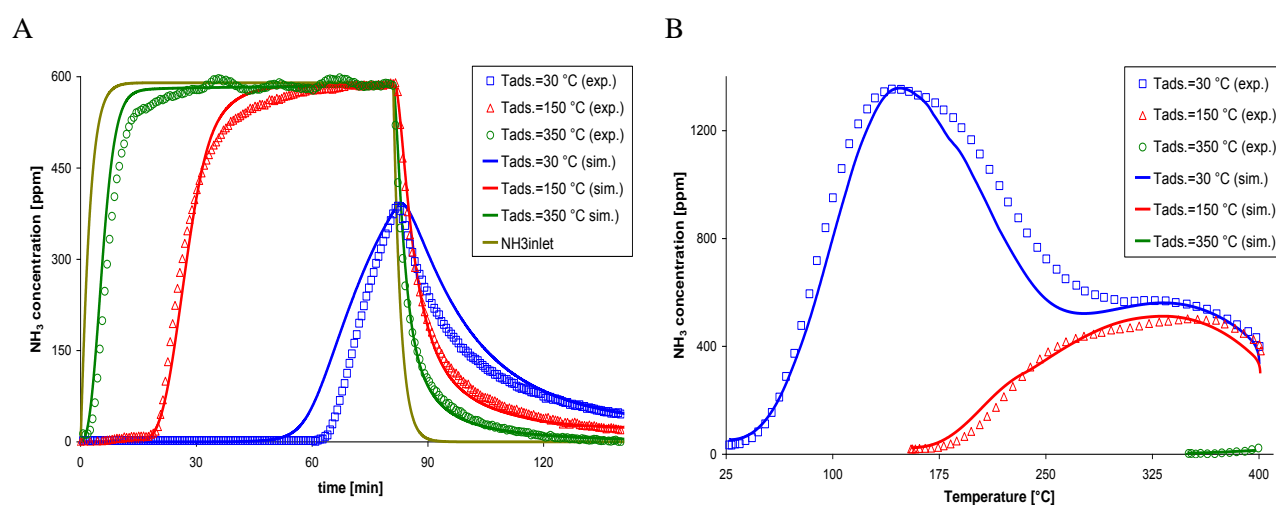
Figure 5.9 Effect of temperature on NH_3 A) adsorption and B) desorption on the Fe-BEA studied sample.
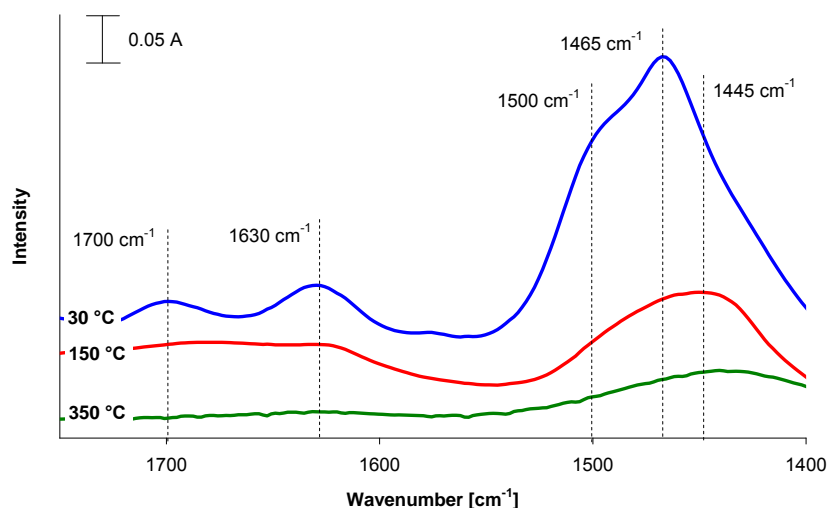
Figure 5.10 Difference IR spectra, recorded at the end of NH$_3$ adsorption experiments performed at 30, 150 and 350 °C: the reference spectra subtracted was recorded at the beginning of each adsorption experiment (t=0 min).

5.5.2.2 Effect of low temperature He flushing duration

Since physisorption is the major mechanism of NH$_3$ storage over Fe-BEA, at low temperatures, it was decided to further investigate the effect of He flushing duration on the shape of the NH$_3$-TPD signal. Therefore, additional ammonia adsorption experiments were performed on the Fe-BEA catalyst, injecting 600 ppm of NH$_3$ at 30 °C, for 80 min in He atmosphere. Then, physisorbed ammonia was removed by purging the sample with He at 30 °C for three different durations: 5 min, 1 h and 5 h. Finally, a TPD experiment was performed up to 400 °C, applying a heating rate of 10 °C/min. NH$_3$ gas phase concentrations, presented in Figure 5.11, show that the increase in the duration of He flushing resulted in the attenuation of the low temperature peak of ammonia, centered at ca 125 °C (as discussed in section 5.2). Interestingly, even after 5 h purge the low temperature desorption peak remained. Similar effects were reported for H-ZSM5 zeolites elsewhere [204]. Simulation of the gas phase TPD signals confirms the abovementioned observations. From a kinetic point of view, this seems to somehow explain the fact that activation energy of desorption from S1a sites had to be calibrated to 80.8 kJ/mol, which is quite higher compared to a value of 40 kJ/mol, usually proposed for physisorption [245]. Overall, the multi-site kinetic model led to a quite satisfactory fitting of the experimental curves, since prolonging the purge duration, NH$_3$ is increasingly desorbed from the S1a sites for weak adsorption and physisorption, removing simultaneously the NH$_3$ multi-layer from S1a and S1b sites. On the other hand, in all test cases, NH$_3$ strongly chemisorbed on acidic and metallic sites remained unaffected and was thus reasonably desorbed from S1b, S2, S3 acidic and S4 metallic sites at temperatures higher than 160 °C.
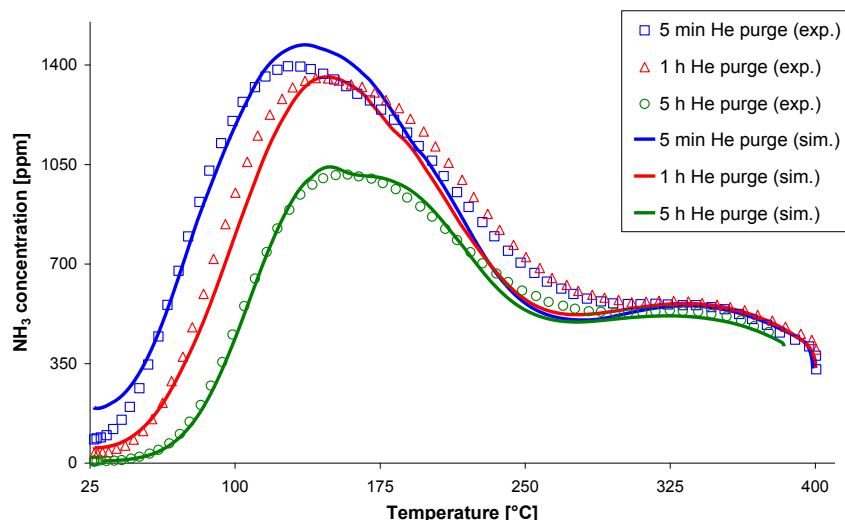
Figure 5.11 Effect of He flushing duration on NH$_3$ storage over the Fe-BEA studied sample.

5.5.2.3 Effect of heating rate

Finally, NH$_3$ adspecies thermal stability was further evaluated by performing thermo-desorption at different temperature ramps. Thus, respective NH$_3$-TPD experiments were performed at heating rates of 10, 15 and 20 °C/min in He. Prior to TPD, 600 ppm of NH$_3$ and He in balance, were preadsorbed for 80 min. at 30 °C, followed by 1 h He purge at the same temperature. Respective results are presented in Figure 5.12. Increasing the temperature ramp, time available for NH$_3$ desorption, at low temperature regime was shorter. Thus, reasonably TPD peaks shifted to higher temperatures, with a simultaneous increase in NH$_3$ gaseous concentration at the same temperature range. Integrating the TPD profiles, identical amounts of NH$_3$ were estimated to desorb (1.30 mol/kg$_{Fe-BEA}$), hence the heating rate had no impact on the actual amount of desorbed NH$_3$. Similar results have been reported over Fe-ZSM5 [104].

The multi-site kinetic model was able to reproduce the tendency observed on the experimental data, namely the increase of NH$_3$ concentration at low temperatures and the shift of TPD peaks towards higher ones. TPD experiments performed at 10 and 15 °C/min were quite accurately reproduced, whereas significant deviations were observed for the case of 20 °C/min. These discrepancies could be attributed either to experimental uncertainties (namely to the response of the electric oven) or to limitations, of the heat transfer model. Since the heating rate was quite high, it is possible that the temperature field on the Fe-BEA pellet was not uniform, resulting in high temperature areas close to the wafer wall and colder areas in the center. However, the proposed single wafer rector model, considers only a homogeneous temperature, since the precise modeling of heat transfer was out of the scope of this study.
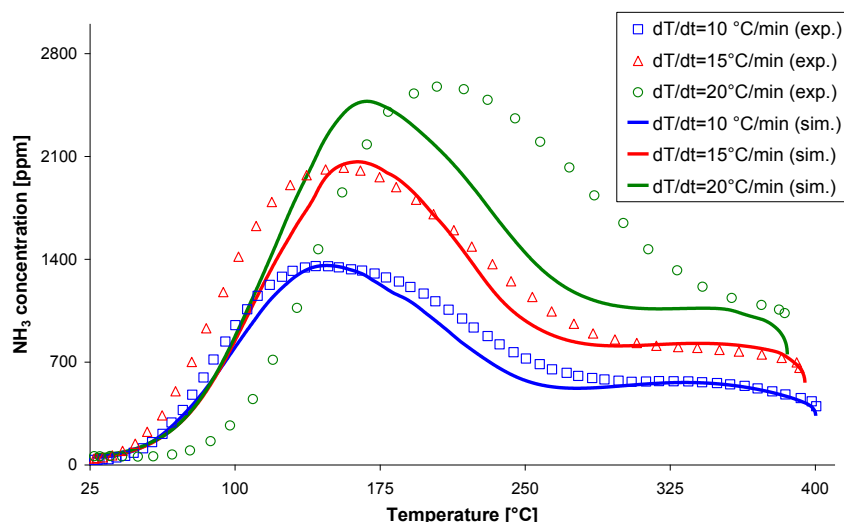
Figure 5.12 Effect of the TPD heating rate on NH$_3$ desorption over the Fe-BEA studied sample.

5.6 Conclusions

This chapter was focused on an extended experimental and modeling study on NH$_3$ adsorption and desorption over H- and Fe-BEA, in order to gain more insight into the mechanism of NH$_3$ storage and release processes. Interpretation of IR spectroscopy and TPD experiments suggests that physisorption (and/or weak adsorption) is the predominant NH$_3$ adsorption mechanism at low temperature conditions (T≤125°C) resulting in the formation of weakly-hydrogen bonded ammonia on the zeolite framework as well as NH$_3$ multi-layers, attached to the former ammonia adspecies. Ammonia physically sorbed species are stable at temperatures as low as 120 °C. Nevertheless, the importance of physisorbed ammonia lies in the fact that NH$_3$ released from non-acidic sites can be further available, by readsorption on neighboring acidic and metallic sites, or it can escape the catalytic converter, causing significant ammonia-slip.

Concerning acidity, Lewis and Brønsted sites were identified. The former could be assigned to either tricoordinated Al or defective sites, since IR spectra indicated partial deformation of the parent zeolite structure. Ammonia complexes formed on these sites were discriminated by low stability, being outgassed upon 175 °C. On the other hand, Brønsted acidic sites were related to strong acidic Si-OH-Al groups that gave rise to thermally stable monodentate, bidentate and tridentate NH$_4^+$ up to 175, 250 and 350 °C respectively. Formation of Lewis type acidic sites is the case of metallic sites, possibly isolated and binuclear ones.

The abovementioned conclusions were further used to perform kinetic modeling studies. Satisfactory simulation results of a broad range of test cases proved that the multi-site kinetic modeling approach, previously validated over NH$_3$ adsorption/desorption on H- and Fe-ZSM5 (chapter 3), could also be applied to Fe-BEA. For the purposes of the herein work the existing model had to be modified so as to account for low temperature adsorption and desorption phenomena. One non acidic site and one global Brønsted and Lewis weakly acidic site were considered, including a multi-layer physisorption mechanism. Model surface sites distinction with respect to their nature and

their quantity, as well as acidity strength variation was in quite good agreement with IR characterization and NH$_3$-TPD experimental results. S1a sites for weak adsorption and physisorption as well as the NH$_3$ multi-layer formation mechanism enabled to predict low temperature physisorption quite satisfactorily. S1b sites depicted NH$_3$ storage on weak Brønsted and Lewis sites, whereas S2 and S3 sites could account for Brønsted sites characterized by intermediate and strong acidity respectively. Finally, S4 sites represented Fe Lewis type sites of higher acidity compared to Lewis zeolitic ones. Furthermore, selected kinetic parameters showed to be robust over all examined test cases. However it has to be highlighted that all simulated experiments were performed over the same catalytic sample. Therefore, as previously discussed (chapter 3), examining catalysts of different Si/Al and/or Fe/Al ratios, surface acidity will definitely vary, leading to a different kinetic parameters calibration. Finally, as far as deviations between simulation and experimental results are concerned, they were mainly attributed either to the NH$_3$ multi-layer mechanism and/or the inadequacy of physisorption rate expressions applied as well as to the limitations of the continuously stirred reactor model. Concerning the former, a reasonable compromise was made between an acceptable level of modeling and parameters calibration complexity and simulation precision. Alternative approaches discussed in section 5.5.1 (models of Kusunoki [246] and Koltsakis et al. [129]), would require evaluation of more parameters and a detailed identification of structural properties, namely samples porosity, studies which go beyond the scope of the herein work. Regarding the reactor model, heat transfer within the solid phase, as well as macro-mixing aspects should be under further consideration so as to evaluate modeling assumptions presented in section 2.2. On the other hand, it has to be emphasized that, using a simplified 0D single reactor model for kinetic modeling studies, very short computational times were achieved. Simulation of a NH$_3$ adsorption and TPD experiment, of a 3 h duration required a computational time in the order of magnitude of only $15 - 18$ sec., since all reactor model variables were deduced through differential equations discretized only in the field of time.

Chapter 6

NO$_x$ Storage and NO Oxidation on H- and Fe-BEA Catalysts

6. NO$_x$ Storage and NO Oxidation on H- and Fe-BEA Catalysts

Abstract

A multi-site kinetic model for NO$_x$ adsorption and desorption as well as NO oxidation on Fe-BEA was developed based on IR spectroscopy measurements. Initially, NO and NO$_2$ adsorption and TPD, along with NO/O$_2$ stepwise TPD experiments were performed over H- and Fe-BEA lab-synthesized samples. Employing in-situ IR spectroscopy, a variety of NO$_x$ adspecies was characterized, including iron nitrosyls, nitrosium anions, nitrites as well as aluminium and iron based nitrates. Based on recorded spectral features a multi-site kinetic model for NO$_x$ storage and NO oxidation on Fe-BEA catalysts was developed, accounting for interactions of nitrogen oxides with different surface sites. The model was finally validated, through simulation of various experimental conditions, depicting satisfactorily mechanistic aspects related to NO$_x$ storage and NO oxidation on acidic and metallic sites.

Résumé

Un modèle multi-site pour l'adsorption et la désorption des NO$_x$ ainsi que pour l'oxydation du NO sur Fe-BEA a été développé à partir des mesures de spectroscopie IR. Initialement, des expériences d'adsorption et de TPD du NO et du NO$_2$ ainsi que des expériences de STPD des NO/O$_2$ ont été réalisées sur des échantillons de H- et de Fe-BEA, synthétisés au laboratoire. Diverses espèces de NO$_x$ ont été caractérisées par spectroscopie IR, y compris les nitrosyles, les ions nitrosium, les nitrites ainsi que les nitrates liés à l'aluminium et au fer. Sur la base des mesures spectrales, un modèle cinétique multi-site pour le stockage des NO$_x$ et de l'oxydation du NO sur les catalyseurs Fe-BEA a été développé, prenant en compte les interactions entre les oxydes d'azote et les différents sites surfaciques. Le modèle a été finalement validé par simulations des expériences réalisées, avec des conditions de fonctionnement différentes, décrivant de façon satisfaisante les aspects mécanistiques liés au stockage des NO$_x$ et à l'oxydation du NO sur les sites acides et métalliques.

6.1 Introduction

Besides ammonia storage and release presented in the previous chapter, nitrogen monoxide and nitrogen dioxide adsorption and desorption constitute reactions of particular interest in order to understand the SCR chemistry over Fe exchanged zeolites. As explained in chapter 1.5, nitrite and nitrate adspecies, formed upon nitrogen dioxide adsorption and disproportionation, involve reaction pathways through which the fast-SCR occurs. Furthermore, NO oxidation is supposed to be the rate determining step of the SCR process, affecting catalyst $deNO_x$ performance.

NO_x adsorption and desorption over iron exchanged BEA zeolites is experimentally investigated in several studies. Colombo et al. [94] have performed series of NO_2 adsorption and subsequent TPD experiments over commercial Fe-BEA catalysts (Si/Al = 24, Fe/Al = 1.5) of different redox states, in order to elucidate the role of Fe^{2+} and Fe^{3+} species in nitrogen dioxide storage and disproportionation. In another study, Iwasaki et al. [95] have correlated the abovementioned reactions with oligomeric iron sites, by performing FTIR measurements over Fe-zeolites, synthesized by different methods. Moreover, Shwan et al. [140] have presented NO adsorption and TPD experiments over fresh and aged Fe-BEA catalysts (1 wt.% Fe, Si/Al = 38), underlying the effect of hydrothermal ageing on iron sites oxidation state. In a detailed study of Ahrens et al. [96], NO and NO_2 adsorption experiments were performed over a 0.76 wt.% Fe-BEA catalyst (Si/Al = 40) and followed by IR spectroscopy measurements, allowing to unravel mechanistic aspects related to NO_2 disproportionation and nitrate adspecies formation over acidic and redox sites. Regarding nitrogen monoxide oxidation, studies of Ahrens et al. [96] and Kefirov et al. [247] are note worthy. Employing IR spectroscopy, both teams have experimentally investigated NO oxidation over Fe-BEA catalysts, which enabled to deduce redox cycles over isolated and/or binuclear iron species. Even though the discussed studies provide convincing arguments related to the role of iron active sites on NO_x storage and NO oxidation, the respective role of Fe-BEA acidity seems to remain unclear. Moreover, the thermal stability of NO_x adspecies has only been investigated through gaseous NO_x-TPD profiles [94,140]. However, the respective results have not been further validated through surface characterization.

Regarding kinetic modeling of NO_x adsorption/desorption and NO oxidation over metal exchanged zeolites, an overview of respective approaches reported in the recent literature is presented in section 1.6. Among them, only the kinetic models of Shwan et al. [140] and Olsson et al. [145] account for interactions of NO_x with acidic and metallic sites. The kinetic model proposed by Shwan [140] included NO adsorption/desorption and oxidation over Fe-BEA catalysts. However, the latter reaction was modeled in the gas phase and the redox cycle was not depicted. On the other hand, the kinetic model of Olsson et al. [145], which considered NO_2 storage and disproportionation as well as NO oxidation on different sites was oriented to Cu-ZSM5 catalysts. Nevertheless, a respective multi-site approach has never been attempted over Fe-BEA catalysts.

In the light of the abovementioned discussion, it seems obvious that NO_x storage and release as well as NO oxidation over Fe-BEA catalysts have been extensively experimentally investigated. However, the role of the zeolitic acidity has not been completely understood, whereas NO_x adspecies thermal stability has not been characterized in details. Thus, in this chapter, dedicated NO and NO_2 adsorption and TPD experiments on both H- and Fe-exchanged BEA catalysts are presented. In-situ IR

spectroscopy was employed in order to characterize in details NO_x adspecies, enabling a deep insight into the contribution of catalyst acidity as well as redox properties.

From a kinetic modeling point of view, the kinetic model of Olsson et al. [145] is the only complete multi-site kinetic model, which allows to depict NO_2 storage and NO oxidation over different sites of Cu-ZSM5 catalysts. Nevertheless, there are no such models for Fe-zeolites (except from the kinetic model of Shwan et al. [140], which accounts for NO storage and oxidation). Thus, a multi-site kinetic model was developed on the basis of the IR spectroscopic measurements, performed over the lab-synthesized H- and Fe-BEA samples. The proposed model was then validated by simulating NO_2 adsorption and TPD as well as NO oxidation experiments performed over the lab-synthesized catalysts and respective catalytic samples reported in the literature.

6.2 In-situ IR spectroscopy measurements

Dedicated in-situ IR spectroscopic measurements, performed parallel to NO, NO_2 and NO/O_2 adsorption on Fe-BEA are presented in this section. The scope of this experimental study was to characterize different nitrogen monoxide adspecies formed on different surface sites, namely acidic and metallic ones, in order to elucidate their contribution on NO_x adsorption, NO_2 disproportionation and NO oxidation.

6.2.1 NO adsorption and desorption on Fe-BEA

Nitrogen monoxide storage and release were studied through a NO adsorption and TPD experiment, performed over the Fe-BEA lab-synthesized catalyst. Around 3000 ppm nitrogen monoxide, diluted in He were introduced into the single wafer reactor at 30 °C for 100 min. Then, the NO feed was switched off and the sample was flushed with He at the same temperature for 60 min. Finally, a TPD experiment from 30 to 493 °C, under He was performed, at a heating rate of 10 °C/min. The outlet gas concentration profiles are illustrated in Figure 6.1. Interestingly, upon 5 min of NO admission, the catalytic surface became saturated, resulting in an overall NO uptake of only 0.22 mol/kg$_{Fe-BEA}$. Minor NO storage over Fe-exchanged zeolites has been previously reported by Grossale et al. [90] and Hadjiivanov et al. [248]. Moreover, during the TPD phase only gaseous NO was observed, whereas neither N_2 nor NO_2, nor N_2O were detected.
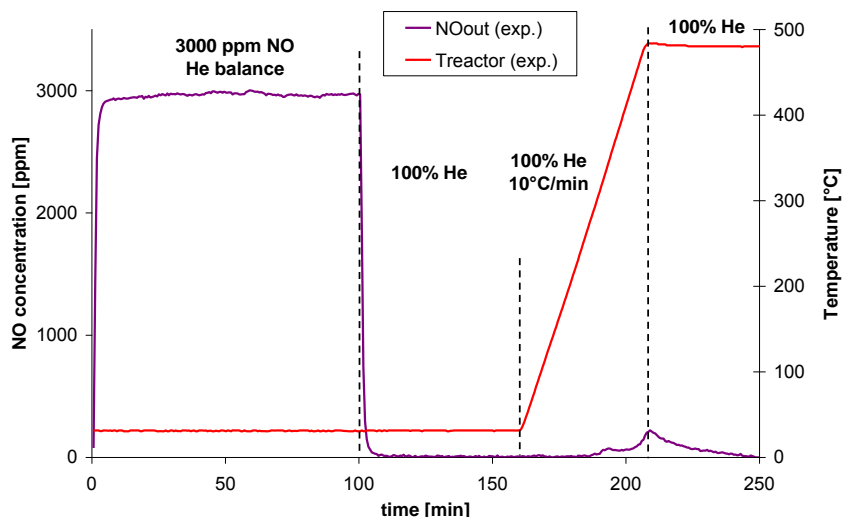
Figure 6.1 NO adsorption and desorption experiments over the Fe-BEA studied catalyst: Preadsorption of 3000 ppm in He, for 100 min at 30 °C, followed by 60 min He flushing at the same temperature and TPD up to 480 °C at a heating rate of 10 °C/min.

The nature of surface sites contributing to nitrogen monoxide storage was elucidated through difference IR spectra recorded during the adsorption phase (Figure 6.2 and Figure 6.3). In order to facilitate results review, the NO_x adspecies as well as the respective IR bands evidenced in section 6.2.1 are summarized in Table 6.1.

Table 6.1 Summary of NO_x adspecies observed during NO adsorption over the Fe-BEA lab-synthesized sample.

Adspecies	IR band [cm^{-1}]	References
NO^+	2133	[87,248]
N_2O_3	1913	[87]
$(Fe-NO)^{2+}$	1874	[87]
trans-$(NO)_2$	1767	[87]
bridging Al based NO_3	1653	[87]
adsorbed H_2O	1624	[249]
bidentate Al based NO_3	1594	[87]
chelating Al based NO_3	1580	[87,249]

Regarding the OH region, negative IR maxima were identified at 3782, 3745, 3685, 3665 and 3610 cm^{-1}. According to previous spectroscopic measurements for NH_3 adsorption and desorption (see chapter 5), the band at 3782 cm^{-1} was assigned to consumption of terminal Al-OH groups, which exhibit basic or Lewis acidic properties, whereas, the ones lying at 3741 and 3665 cm^{-1} were related to

interactions of NO with non acidic terminal silanols (Si-OH) and hydroxyl groups bonded to extra-framework aluminium respectively. A weak negative band, centred at 3610 cm^{-1} was attributed to consumption of Si-OH$^+$-Al hydroxyls, corresponding to Brønsted acidic sites. Finally, a decrease in intensity was observed at 3685 cm^{-1} and was assigned to Fe^{3+}-OH [247].

Simultaneously, several IR bands were observed in the ON region (2300 – 1400 cm^{-1}), being assigned to different NO$_x$ adspecies (Figure 6.3). Focusing on the first 10 min of the adsorption phase, during which the Fe-BEA became saturated, IR maxima centred at 2133 and 1874 cm^{-1} were identified (Figure 6.3 A) and were attributed to nitrosium ion (NO$^+$) and (Fe-NO)$^{2+}$ mono-nitrosyl respectively [87]. Hadjiivanov et al. suggested formation of NO$^+$ through interactions of NO with Brønsted acidic sites [248]. According to these authors, the interaction of nitrogen monoxide with cationic OH$^+$ leads to the formation of NO$^+$ coordinated to framework oxygen (of basic properties) and adsorbed H$_2$O. Moreover, Kefirov et al. [247] proposed interaction of NO with Fe^{3+}-OH forming Fe^{2+} and HNO$_2$. The latter, can further react with cationic OH$^+$ sites yielding NO$^+$ on lattice oxygen and H$_2$O. Indeed, in the presented experiment the 2133 cm^{-1} IR band arose along with a broad band at 1624 cm^{-1}, which could be assigned to adsorbed water [249]. Moreover, negative IR bands at 3610 and 3685 cm^{-1} were evidneced, which correspond to zeolitic OH$^+$ and Fe^{3+}-OH respectively. Therefore, both the abovementioned mechanisms seem to be valid in the present study.
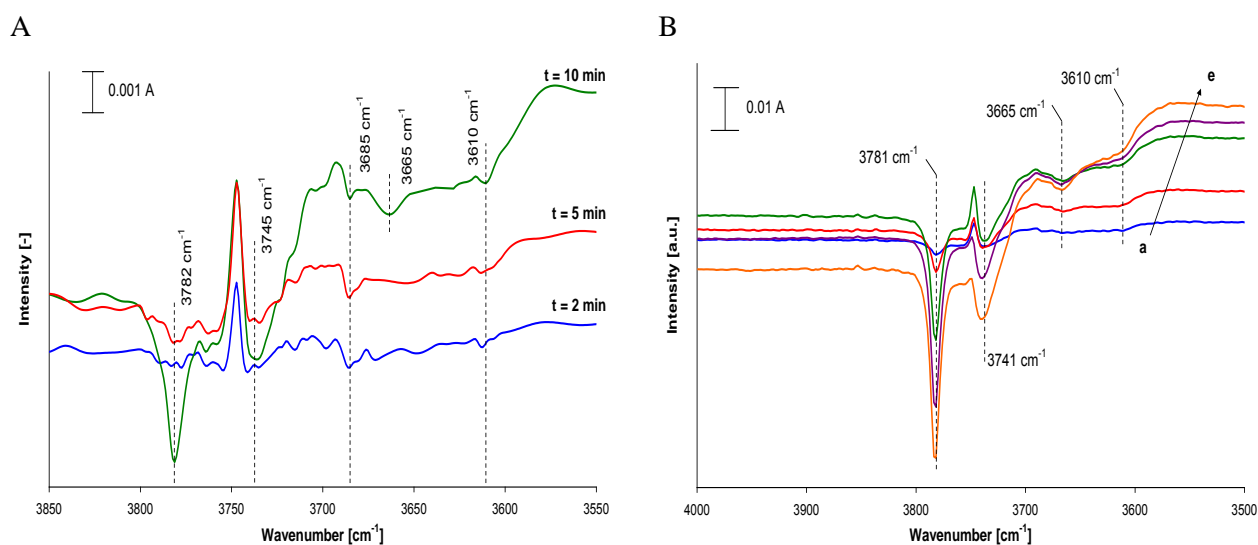
Figure 6.2 Difference IR spectra in the range of 3500 – 3900 cm^{-1} recorded during NO adsorption over the Fe-BEA studied sample at 30 °C (injection of 3000 ppm NO in He). Lines shown in figure B correspond to IR spectra recorded at: a) 10 min, b) 20 min, c) 40 min, d) 60 min and e) 100 min.
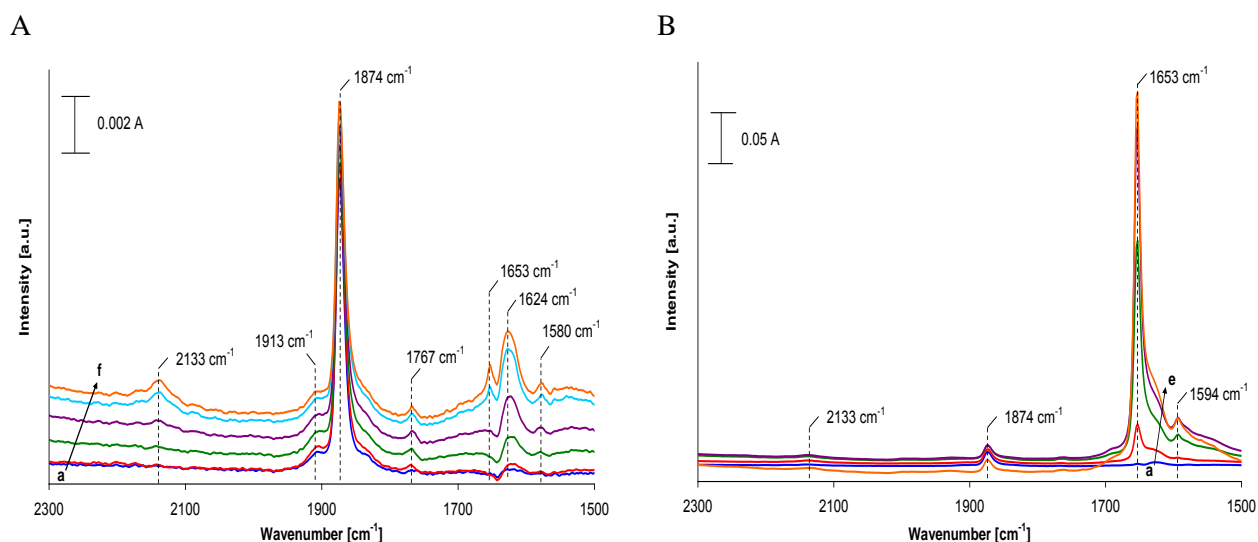
Figure 6.3 Difference IR spectra recorded during NO adsorption over the Fe-BEA studied sample at 30 °C (injection of 3000 ppm NO in He). A) Lines correspond to IR spectra recorded at: a) 1 min, b) 3 min, c) 5 min, d) 7 min, e) 9 min and f) 10 min. B) Lines correspond to IR spectra recorded at: a) 10 min, b) 20 min, c) 40 min, d) 60 min and e) 100 min.

Moreover, weak IR bands at 1913 and 1767 cm^{-1} were attributed to dinitrogen trioxide (N_2O_3) and trans-$(NO)_2$ dimer, which coexist in equilibrium with NO at low temperatures [87]. Finally, IR maxima at 1653 and 1580 cm^{-1} were assigned to bridging and chelating nitrate adspecies (NO_3^-) respectively [87,249]. Increasing exposure time (Figure 6.3 B), the intensity of the 1653 cm^{-1} IR band increased, the band lying at 1580 cm^{-1} vanished, whereas another band arose at 1594 cm^{-1}, being related to bidentate nitrates [87]. Based on several experimental studies, nitrates are formed on Fe-exchanged zeolites upon NO_2 adsorption and successive disproportionation [90,92]. However, the presented NO adsorption experiment was performed in the absence of oxyge. Consequently, NO oxidation to NO_2 should not occur significantly. Hence, the formation of nitrates under the applied experimental conditions may involve interaction of NO with zeolitic lattice oxygen. Sedlmair et al. observed formation of monodentate nitrates (1580 cm^{-1}) on extra-framework Al species, upon NO admission on NaY (Si/Al=2.59) [249]. The negative band centred at 3665 cm^{-1} (Figure 6.2), being assigned to extra-framework Al-OH may further support this interpretation. Therefore, one can not completely rule out this process over the Fe-BEA catalyst, in the absene of gaseous O_2.

Compiling information obtained through IR spectroscopic measurements, it could be concluded that NO was preferably adsorbed over Brønsted acidic and Fe^{2+} monomeric sites. Moreover, reduction of Fe^{3+}-OH was speculated, leading to the formation of HNO_2, which further reacting with OH^+ formed NO^+ and H_2O. Finally, formation of nitrate adspecies was also possible through interactions of nitrogen monoxide with lattice oxygen, possibly included in Al-OH positions. These observations are summarized through reactions 6.1 to 6.5.

$$NO_{(g)} + 2H^+ - OZ \rightleftharpoons NO^+ - Z + HO \cdot H^+ - Z \qquad \textbf{reac 6.1}$$

$$NO_{(g)} + HO-Fe^{3+}-Z \rightleftharpoons HNO_2 - Fe^{2+} - Z \qquad \textbf{reac 6.2}$$

$$HNO_2 + H^+ - OZ \rightleftharpoons NO^+ - Z + H_2O - Z \qquad \textbf{reac 6.3}$$

$$NO_{(g)} + Fe^{2+} - Z \rightleftharpoons [NO-Fe]^{2+} - Z \qquad \textbf{reac 6.4}$$

$$NO_{(g)} + 2O - Al - Z \rightleftharpoons Z - Al - O - (NO) - O - Al - Z \qquad \textbf{reac 6.5}$$
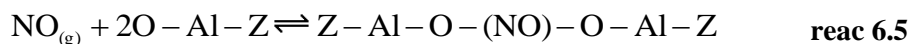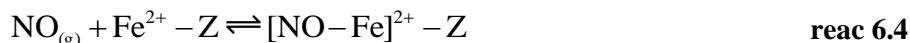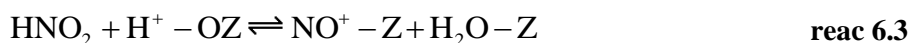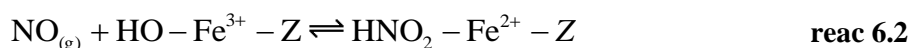
6.2.2 NO₂ adsorption and desorption

NO₂ adsorption and desorption were initially studied over the H-BEA zeolite, in order to evaluate the effect of zeolitic acidity on nitrogen dioxide storage and release. Then, in-situ IR spectroscopic measurements were performed over the Fe-BEA catalyst so as to examine the respective contribution of Fe species.

6.2.2.1 In-situ IR spectroscopy measurements on H-BEA

A mixture of 0.45% NO₂ and 8% O₂ diluted in He were preadsorbed for 100 min at 30 °C over the H-BEA zeolite. Then, feed gases were terminated and the sample was purged with He for 1 h, at the same temperature, so as to remove weakly adsorbed NO$_x$ species. Finally, a TPD was performed from 30 to 493°C, at a heating rate of 10°C/min. Gas phase results recorded during adsorption are shown in Figure 6.4.
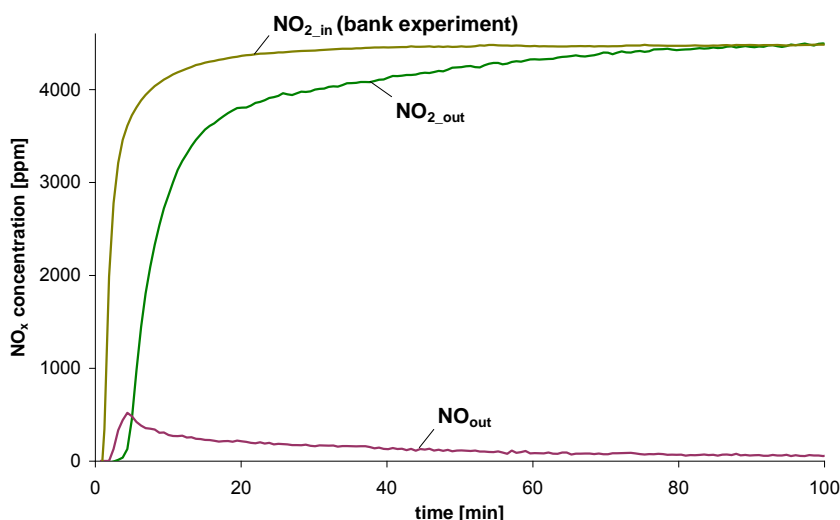
Figure 6.4 NO₂ storage and NO evolution on H-BEA, during NO₂/O₂ adsorption at 30 °C, during 100 min (feed gas composition: 0.45% NO₂, 8% O₂ and He in balance).

Overall 1.64 mol/kg$_{zeolite}$ NO₂ were stored on the bare BEA zeolite. Upon 2.5 min of NO₂/O₂ uptake, zeolite active sites for adsorption started to become saturated. Immediately after this point, a weak NO

concentration peak arose, which was associated to the well known NO_2 disproportionation [82,95]. NO concentration was maximized at 4.5 min (ca 519 ppm) and then attenuated without becoming zero, indicating that an equilibrium between NO_2 adsorption and disproportionation was reached [250]. The ratio between the amount of NO_2 consumed and that of NO produced, upon the saturation point, was estimated equal to 3 ($N_{NO2\_consumed} = 1.53$ mol/kg$_{zeolite}$, $N_{NO\_produced} = 0.55$ mol/kg$_{zeolite}$), which corresponds to the stoichiometry of the reaction 6.6. Nevertheless, it has to be highlighted that the abovementioned estimation is only approximate, since i) at 30 °C, NO_2 physisorption may also take place, leading to an increased nitrogen dioxide uptake and ii) as it going to be discussed later, interactions between NO and NO_2 may simultaneously occur, resulting in the formation of additional adspecies (besides NO_3).

$$3NO_2 + \frac{1}{2}O_2 = 2NO_3 + NO \qquad\qquad \textbf{reac. 6.6}$$

Adsorbed species formed during NO_2 adsorption and disproportionation were identified employing IR spectra, recorded during NO_2/O_2 introduction (Figure 6.5 and Figure 6.6). In analogy with section 6.2.1 and in order to facilitate IR spectroscopic analysis results review, the NO_x adspecies as well as the corresponded IR bands discussed in section 6.2.2.1 are summarized in Table 6.2.

Table 6.2 Summary of NO_x adspecies observed during NO_2 adsorption over the H-BEA lab-synthesized sample.

Adspecies	IR band [cm^{-1}]	References
N_2O, N_2, NO_2^+	2175	[87]
N_2O_4		[252]
NO^+	2133	[87,248]
N_2O_3	1865	[95,251]
trans-$(NO)_2$	1767	[87]
N_2O_4	1743	[251,253]
NO_2	1675	[255]
bridging Al based NO_3^-	1653	[87]
bridging Al based NO_3^-	1628	[87,96]
adsorbed H_2O	1624	[249]
bidentate Al based NO_3^-	1592	[87]
chelating nitrite	1517	[87]

Regarding the first 10 min of the adsorption, three negative IR maxima were distinguished in the OH-region (Figure 6.5 A), centred at 3782, 3745 (including a component at 3741 cm^{-1}) and 3665 cm^{-1}. Surface sites corresponding to these IR bands have already been discussed in section 6.2.1. Along with the latter bands, broad IR maxima appeared at ca 2900 and 2400 cm^{-1}, being ascribed to the bending

and stretching modes of OH respectively [251]. According to Szanyi et al. [251] the shape and the intensity of these bands reflect the strength of the coordination between the protonated OH groups and the NO_2 adsorbed molecule. Comparing results shown in Figure 6.5 A with those obtained upon NH_3 adsorption (at 30 °C), earlier discussed in chapter 5, it could be suggested that the interaction of Brønsted sites with NO_2 was significantly weaker. The weak IR band at 3610 cm^{-1} seems to be in reasonable agreement with this conclusion.

Simultaneously, several IR bands were observed in the 23100 – 1400 cm^{-1} region, which were assigned to different NO_x adspecies (F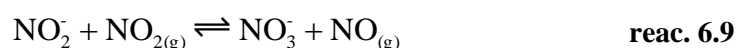igure 6.5 B and Figure 6.6). Focusing on the same time interval (t = 2 - 10 min - Figure 6.5 B), two minutes after the beginning of NO_2/O_2 admission, intense IR maxima arose at 1653 and 1592 cm^{-1} and were assigned to bridging and bidentate nitrates (NO_3^-) respectively, as discussed in section 6.2.1. Weak IR bands also appeared at 2133 and 2175 cm^{-1}. The former was attributed to nitrosium ion NO^+ (see section 6.2.1) whereas the nature of the latter is quite unclear. Hadjiivanov et al. [87] reported that the 2200-2100 cm^{-1} range is related to several adspecies including N_2O, N_2, NO_2^+, as well as NO^+. Elsewhere, it was assigned to N_2O_4 species [252], combined with an IR band at 1750 cm^{-1} [96]. Moreover, an IR band of increasing intensity was observed at 1743 cm^{-1} and was attributed to N_2O_4 species [251,253]. N_2O_4 formation is suggested either through NO_2 dimerization, or N_2O_3 oxidation [251]. The latter compound was evidenced via the IR band centred at 1865 cm^{-1}, and probably originated from an interaction between NO and NO_2 [95,251]. The N_2O_4 dimer has been previously suggested as an intermediate species of the NO_2 disproportionation process [90,254] (reaction 6.7).

$$2NO_2 \rightleftharpoons N_2O_4 \rightleftharpoons NO_3^- + NO^+ \qquad \text{reac. 6.7}$$

Nevertheless, Szanyi et al. [251] and Lobree et al. [253] have proved by means of in-situ IR spectroscopic measurements over Cu and Fe exchanged ZSM5 catalysts, that N_2O_4 species (corresponding to the 1743 cm^{-1} IR band) may only be weakly adsorbed on the catalyst surface. The nature of this dimer is going to be also discussed later.

Increasing exposure time (t > 2 min: Figure 6.5 B and Figure 6.6) the 2133 and 2175 cm^{-1} IR bands, corresponding to NO adspecies vanished, whereas that related to bridging NO_3^- (1653 cm^{-1}) remeained almost unchanged. Simultaneously, IR maxima centred at 1675 and 1517 cm^{-1} arose, and were assigned to weakly adsorbed nitro groups (asymmetric bending mode of NO_2) [255] and chelate nitrite [87] adspecies respectively. Finally, a broad IR band was identified at 1630 cm^{-1}, gradually sifting to 1624 cm^{-1}. The interpretation of this band is not evident. According to literature a 1628 cm^{-1} IR band may correspond to bridging Al based NO_3^- [87,96], whereas adsorbed water was related to a band centred at 1624 cm^{-1} (see section 6.2.1). Apostolescu et al have proposed a sequential mechanism of NO^+ conversion to gaseous NO and NO_3^-, employing surface oxygen and one additional molecule of gaseous NO_2 [256]. According to it, initially, nitrosium undergoes oxidation yielding nitrites (reaction 6.8), whereas the latter can be further oxidized by NO_2 (which apparently constitutes a strong oxidant) forming gaseous NO and nitrates (reaction 6.9).

$$NO^+ + O^{2-} \rightleftharpoons NO_2^- \qquad \text{reac. 6.8}$$

$$NO_2^- + NO_{2(g)} \rightleftharpoons NO_3^- + NO_{(g)} \qquad \text{reac. 6.9}$$

Adding reactions 6.7, 6.8 and 6.9, the reaction 6.6 was found, which is in agreement with the stoichiometry of consumed NO_2 and generated NO, discussed above.

A   B
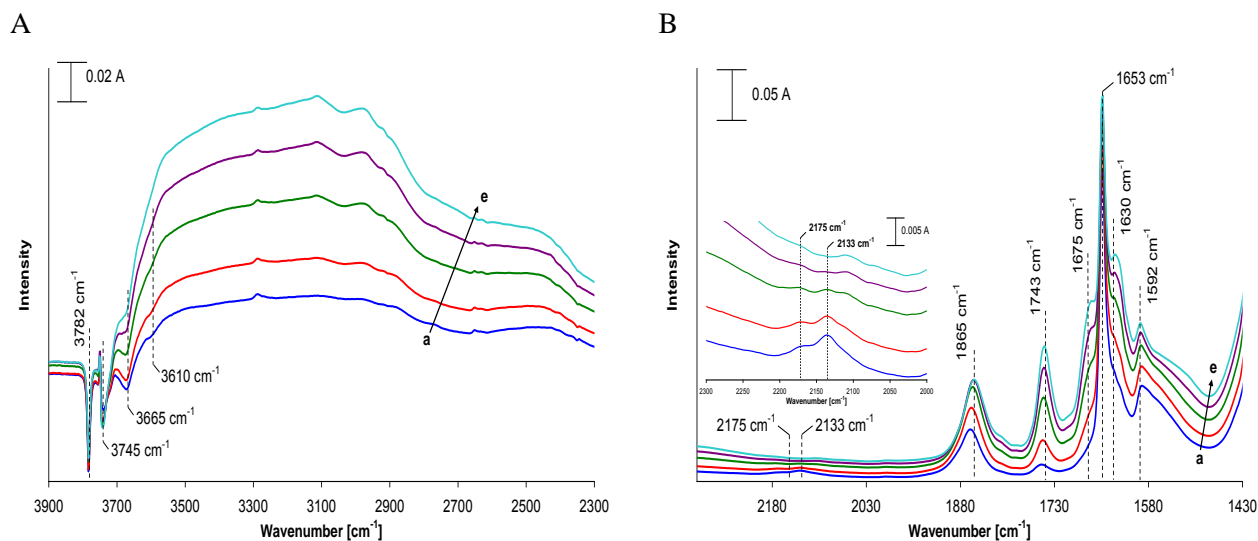
Figure 6.5 Difference IR spectra recorded during NO_2 adsorption over the H-BEA zeolite at: a) t = 2 min, b) t = 4 min, c) t = 6 min, d) t = 8 min, e) t = 10 min. (Injection of a mixture of 0.45% NO_2 and 8% O_2 diluted in He, at 30 °C, during 100 min).
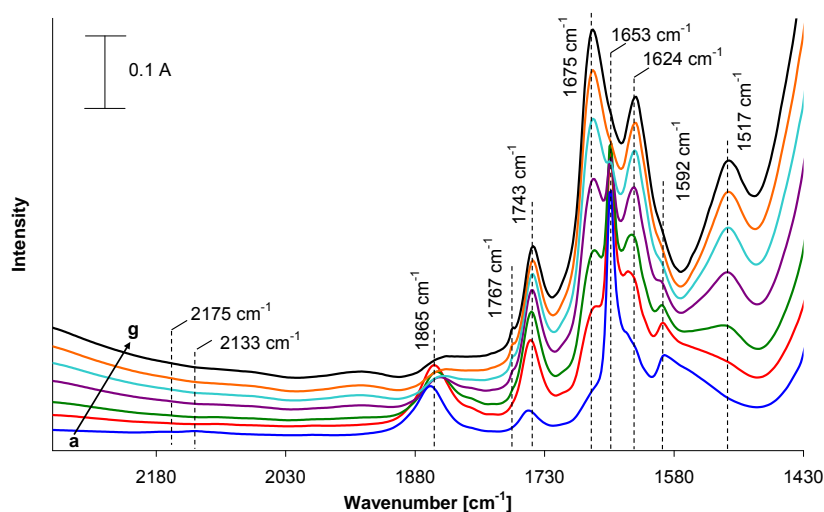
Figure 6.6 Difference IR spectra recorded during NO_2 adsorption over the H-BEA zeolite at: a) 4 min, b) 10 min, c) 20 min, d) 40 min, e) 60 min, f) 80 min, g) 100 min. (Injection of a mixture of 0.5% NO_2 and 8% O_2 diluted in He, at 30 °C, during 100 min).

In order to further elucidate the nature of surface sites contributing to NO_2 adsorption and disproportionation, normalized intensity profiles of IR maxima observed in the OH (3900 – 2300 cm^{-1}) and ON (2300 – 1400 cm^{-1}) region were compared (Figure 6.7). At around 2.5 min, a maximum point at 2133 and 1653 cm^{-1} was observed, which in excellent agreement with gas phase results (see Figure

6.4) indicates the occurence of NO_2 disproportionation, which yielded NO_3^- (1653 cm^{-1}) and NO^+ (2133 cm^{-1}). Profiles of the 1653 and 3782 cm^{-1} bands were somehow symmetric, suggesting that bridging NO_3^- was formed on terminal Al-OH, which exhibits Lewis type acidity or basicity. A similar behavior was identified for the 2133 and 3610 cm^{-1} profiles, which tends to indicate occupation of Si-OH$^+$-Al Brønsted sites by NO^+, according to the mechanism discussed in section 6.2.1. Finally, normalized intensities of IR peaks lying at 1592 and 3665 cm^{-1}, exhibited relative symmetry, thus it could be suggested that bidentate NO_3^- were formed on extra-framework aluminium.

Overall, the abovementioned results imply that NO_2 disproportionation occurred employing framework and/or extra-framework Al (and thus a Lewis acidic site for nitrates formation) and basic framework oxygen, generated upon interaction of Si-OH$^+$-Al Brønsted acidic sites with NO. IR studies of NO+O_2 adsorption on H-MOR [257] and Na-Y [249], as well as DFT computations of N_2O_4 disproportionation on alkali exchanged X [93] and Y [258] zeolites somehow validate this conclusion. However, if we accept the heterolytic chemisorption of NO_2, close vicinity between Lewis and Brønsted sites is required. Indeed, Wang et al. have confirmed this conclusion for H-MOR zeolites, highlighting the existence of attractive interaction between the aluminium coordinated NO_3^- and a neighboring H$^+$ cation [257]. Further analysis of such aspects would require additional experimental analysis (eg. Al-NMR studies for evaluation of the amount of framework and extra-framework aluminium, as well as DFT computations), which goes beyond the scope of the herein work.
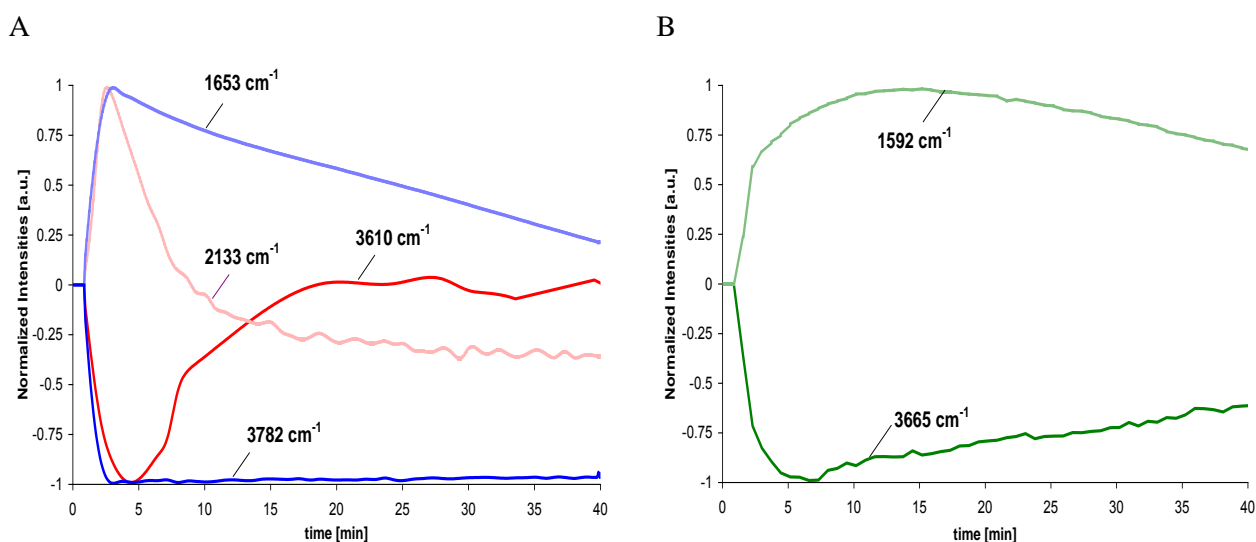
Figure 6.7 Normalized intensity of the peaks associated with NO_2 disproportionation. Normalization was performed at maximum or minimum peak intensity for each of the presented IR bands, according to the methodology reported elsewhere [95].

Finally, the thermal stability of the abovementioned nitrite and nitrates adspecies was evaluated by means of the TPD experiment illustrated in Figure 6.8 B). Respective IR spectra are presented in Figure 6.9. Overall, 1.64 mol/kg$_{zeolite}$ NO_2 were desorbed, in line with the respective amount of nitrogen dioxide stored during the adsorption phase. Focusing on low temperatures, an intense NO_2

gaseous concentration peak, along with a weak NO peak were observed at around 100 °C. As clearly shown in Figure 6.9 A, upon the 1 h He purging at 30 °C, the IR peak at 1743 cm^{-1} vanished completely. Therefore, it can be suggested that the 1743 cm^{-1} is related to weakly sorbed N$_2$O$_4$. Similar observations have been reported elsewhere [251,253]. Interestingly, a short desorption delay was evidenced in both gas and solid phase up to 50 °C, whereas reaching 75 °C, all IR maxima in the ON region attenuated. Among them, that at 1767 cm^{-1} (trans-(NO)$_2$) disappeared , indicating desorption of weakly bonded NO. Finally, evacuating the sample at 100 °C, bands located at 1675, and 1518 cm^{-1}, related to nitrites were ceased. Therefore, the NO$_2$-TPD peak at 100 °C was assigned to weakly adsorbed and/or physisorbed NO$_2$, as well as to NO$_2$ deriving from nitrite adspecies. Finally, small amounts of NO desorbed at the same temperature range were attributed to removal of weakly sorbed trans-(NO)$_2$.

As far as the high temperature regime is concerned (Figure 6.9 B), only nitrates were observed. Upon evacuation at 200 °C, the IR maxima at 1653 and 1592 cm^{-1} attenuated significantly, whereas a band centred at 1628 cm^{-1} almost disappeared. Therefore, it could be concluded that the NO$_2$ TPD peak at around 200 °C was related to NO$_2$ mainly deriving from decomposition of Al based NO$_3^-$, in bridging and bidentate coordinations (1653 and 1592 cm^{-1} respectively). Finally, further temperature increase led to the elimination of bidentate NO$_3^-$ at around 210 °C and bridging NO$_3^-$ at 300 °C. Thus, the NO$_2$-TPD shoulder at around 250 °C and the broad desorpion peak observed at T > 300 °C was assigned to gaseous NO$_2$ generated after decomposion of bidentate and bridging NO$_3^-$ respectively.
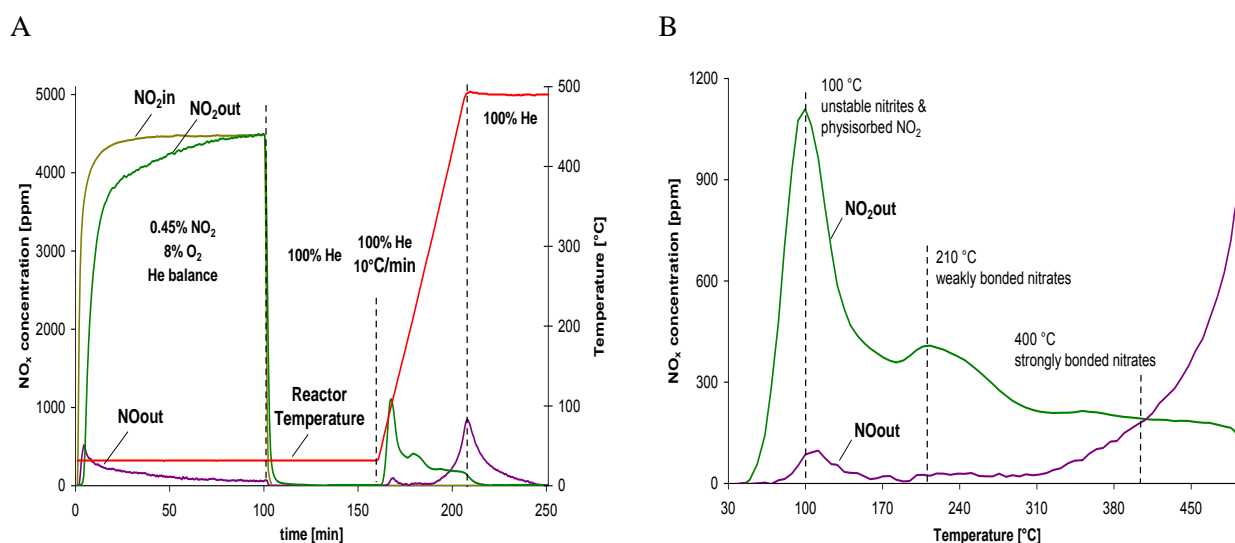
Figure 6.8 NO$_2$ adsorption and TPD on the studied H-BEA: Preadsorption of 0.45% NO$_2$ and 8% O$_2$ in He, for 100 min at 30 °C, followed by 60 min He flushing at the same temperature and TPD up to 490 °C at a heating rate of 10 °C/min.
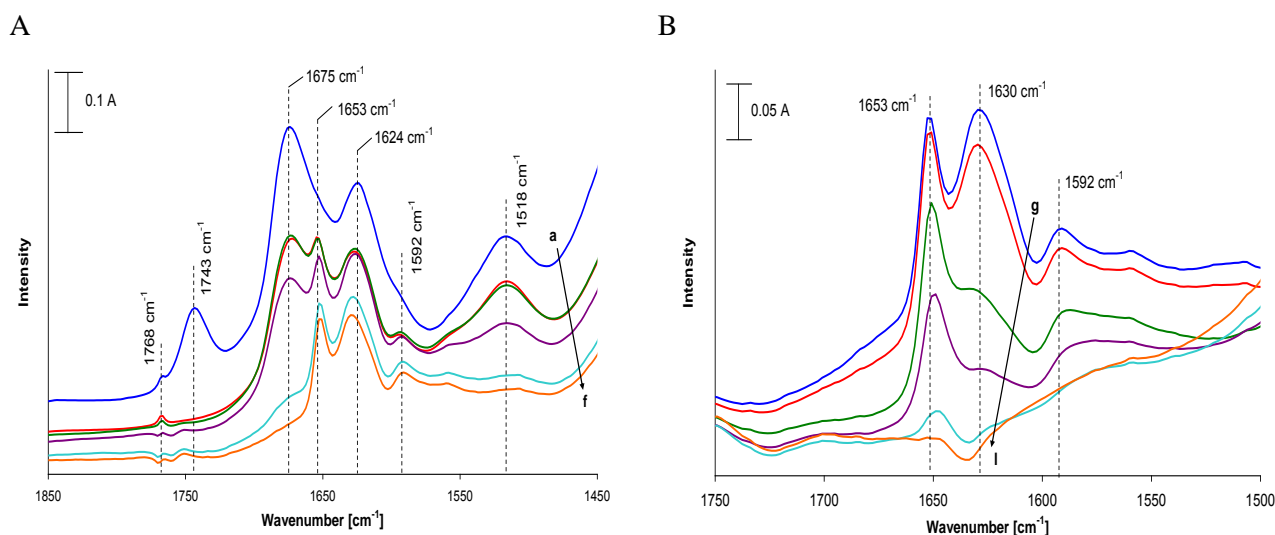
Figure 6.9 Difference IR spectra recorded during NO_2-TPD on H-BEA at a) 30 °C at the end of the NO_2/O_2 injection, b) 30 °C after 1 h He purging, c) 50 °C, d) 75 °C, e) 100 °C, f) 105 °C, g) 110 °C, h) 120 °C, i) 150 °C, j) 200 °C, k) 250 °C, l) 300 °C.

IR difference spectra recorded at temperature higher than 300 °C (not shown in this work) were not exploitable. Interestingly, upon this temperature NO_2 gaseous concentration remains almost stable, whereas a simultaneous NO breakthrough was observed. Olsson et al. have assigned this phenomenon to NO_2 dissociation on Brønsted sites [145]. Earlier it was shown that NO_3^- is formed on framework and extra-framework Al, Lewis type acidic sites, in vicinity with a Brønsted type one. Therefore, a decomposition of NO_3^- to NO_2 and a dissociation of the latter on a neighbouring H^+ proton could not be excluded. Moreover, gaseous NO_2 and NO are in thermodynamic equilibrium within at such high temperatures, which means that a possible gas phase reaction could be also possible. Nevertheless, further analysis of such high temperature phenomena is out of the consideration of this work.

6.2.2.2 In-situ IR spectroscopy measurements on Fe-BEA

The effect of iron species of the Fe-BEA on NO_2 adsorption and desorption was studied through an additional NO_2 adsorption and TPD experiment performed on the Fe-exchanged BEA at 30°C, using the same experimental protocol applied earlier for the H-BEA zeolite (section 6.2.2.1).

Gaseous concentration profiles obtained during NO_2/O_2 adsorption on Fe-BEA are shown in Figure 6.10. 1.44 mol/kg$_{Fe-BEA}$ NO_2 were stored over the Fe exchanged zeolite. Interestingly, surface saturation was observed upon ca 4.5 min of NO_2/O_2 introduction, whereas NO started to evolve already at around 1.8 min, indicating NO_2 storage and disproportionation. The amount of consumed NO_2 and evolved NO, were estimated equal to 1.44 and 0.64 mol/kg$_{Fe-BEA}$ respectively, suggesting a stoichiometry of NO_2 disproportionation according to reaction 6.6.
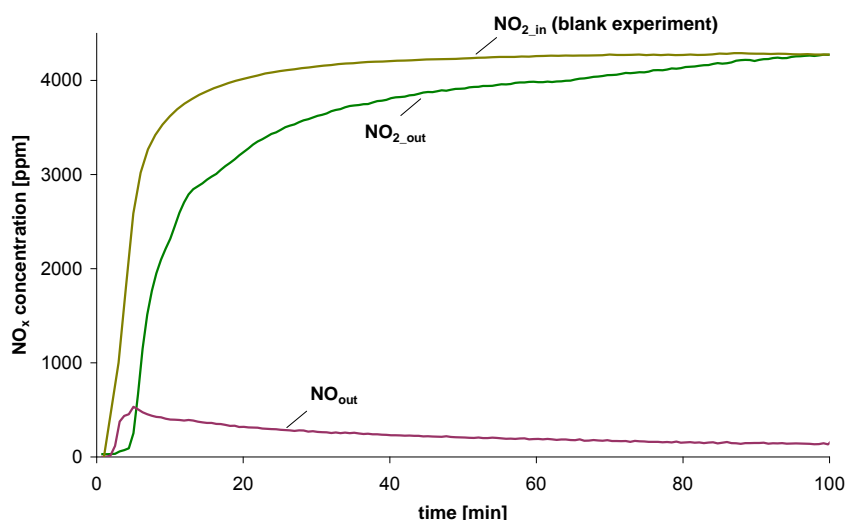
Figure 6.10 NO$_2$ storage and NO evolution on Fe-BEA, during NO$_2$/O$_2$ adsorption at 30 °C, during 100 min (feed gas composition: 0.43% NO$_2$, 8% O$_2$ and He in balance).

IR spectra recorded during the NO$_2$/O$_2$ introduction are presented in Figure 6.11, whereas the additional NO$_x$ adspecies and the respective IR bands observed over the Fe-BEA catalyst are summarized in Table 6.3.

Table 6.3 Summary of additional NO$_x$ adspecies observed during NO$_2$ adsorption over the Fe-BEA lab-synthesized sample.

Adspecies	IR band [cm^{-1}]	References
NO$^+$ included in N$_2$O$_4$	1945	[259]
bridging Fe based NO$_3^-$	1633	[96,260]

IR maxima corresponding to nitrosyl, nitro/nitrito and nitrato adspecies were detected. Upon 1.5 min of NO$_2$ uptake, distinguishable IR bands at 1652 and 2133 cm^{-1}, as well as a shoulder at 2175 cm^{-1} were identified, being attributed to NO$_3^-$, NO$^+$ and N$_2$O$_4$/NO$^+$ (or other species) respectively (as characterized in section 6.2.2.1). Further increasing exposure duration, besides IR bands characterized over the H-BEA (1865, 1743 and 1592 cm^{-1}) new IR maxima were identified on the Fe-BEA. A weak band at 1945 cm^{-1} was attributed to NO$^+$ included in N$_2$O$_4$ (NO$^+$NO$_3^-$) [259], whereas a peak centred at 1633 cm^{-1} was assigned to NO$_3^-$ formed on Fe species [96], possibly extra-framework Fe-Al-O ones [260]. Moreover, the 1517 cm^{-1} band related to NO$_2^-$ shifted to 1527 cm^{-1}.

Evidence of iron based nitrates corresponding to IR bands at 1633 cm^{-1}, tends to validate the fact that iron contributes to NO$_2$ disproportionation. Based on NH$_3$ adsorption experiments, applying in-situ IR spectroscopy, reported in chapter 5, it was proved that iron species of the studied Fe-BEA catalyst (mainly Fe^{3+} and Fe binuclear complexes) exhibit Lewis type acidity. Consequently, molecular NO$_2$ adsorption would be promoted by the presence of lowest unoccupied molecular

orbitals. Moreover, according to IR spectroscopic measurements over the Fe-BEA in vacuum, ca 74% of H-BEA Brønsted acidic sites remained on the Fe-BEA catalyst, upon the iron exchange process (see Figure 4.3 and analysis in section 5.4.2). Therefore, in analogy with the discussion in section 6.2.2.1, NO_2 disproportionation on the Fe-BEA could involve formation of NO_3^- on iron based, Lewis sites and NO^+ on Brønsted sites. NO_2 disproportionation through synergy between two metallic centres, located in vicinity, instead of one metallic site and a Brønsted one could not be proved in this study, since the presence of oxygen in the feed resulted in oxidation of the Fe^{2+} ions, where mononitrosyl $[Fe-NO]^{2+}$ can be formed. Nevertheless, as explained in section 6.2.1, NO may also weakly interact with Fe^{3+}. Thus, NO_2 disproportionation on neighboring metallic centers can not be excluded.
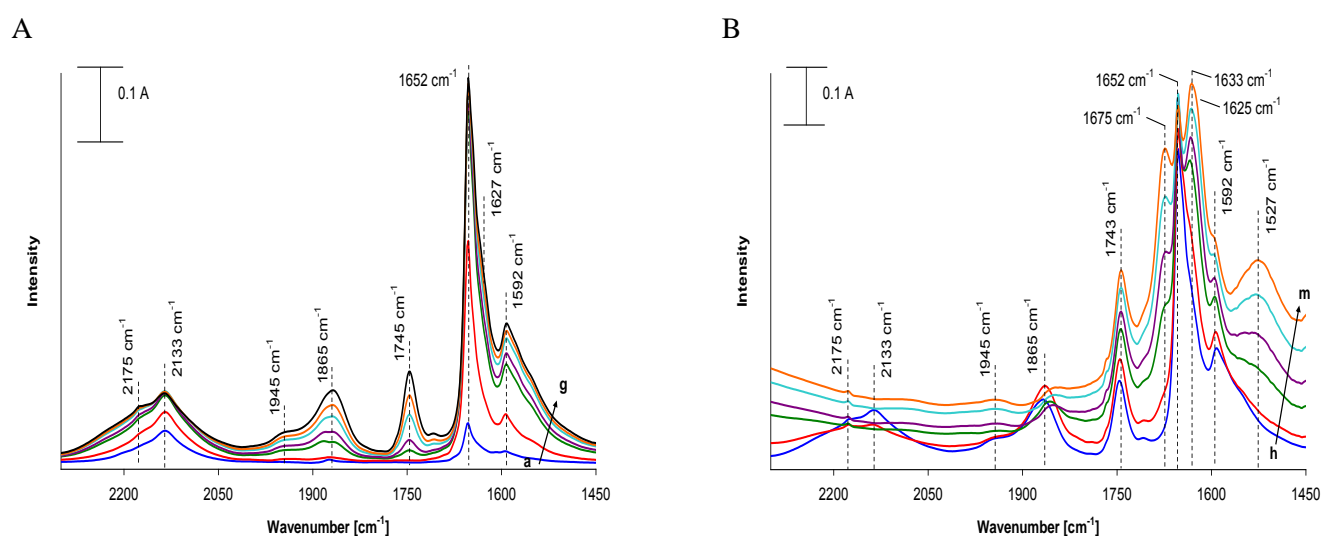
Figure 6.11 Difference IR spectra recorded during NO_2 adsorption over the Fe-BEA zeolite at: a) t = 1.5 min, b) t = 2 min, c) t = 3 min, d) t=4 min, e) t = 5 min, f) t = 7 min, g) t = 9 min, h) 10 min, i) 20 min, j) 40 min, k) 60 min, l) 80 min, m) 100 min. (Injection of a mixture of 0.43% NO_2 and 8% O_2 diluted in He, at 30 °C, during 100 min).

As far as the nature of iron species, being involved in NO_2 adsorption and disproportionation processes is concerned, monomeric $Fe^{n+}-O^-$ or $Fe^{n+}-OH$ [96,261], as well as Fe-O-Fe binuclear species [95] have been proposed in the recent literature. Concerning the latter sites, also termed as α-sites, the work of Dubkov et al. [262] is note worthy. These authors have proved by means of Mössbauer spectroscopy that an α-site constitutes a binuclear iron complex composed of two Fe centres, which could be either oxygen bridged by one single oxygen ion O^- (α-oxygen) or equally separately coordinated to one α-oxygen. According to UV-vis spectroscopic measurements over the studied Fe-BEA sample (chapter 4, Figure 4.4), Fe^{3+} isolated cations, iron binuclear complexes and Fe_2O_3 particles were found to coexist on the catalytic surface. Therefore, a contribution of both isolated and binuclear species can not be excluded.

The thermal stability of the iron based nitrates discussed above was evaluated through the TPD experiment shown in Figure 6.12. Three desorption peaks were identified, centred at 100, 184 and 400

°C, as well as gaseous NO evolution upon 220 °C. IR spectra recorded during thermodesorption enabled interpretation of gaseous concentration signals (Figure 6.13). In line with results shown in 6.2.2.1, the NO_2 gaseous peak at 100 °C derived from desorption of nitrogen dioxide previously stored as surface nitrites (1675 and 1527 cm^{-1}) and weakly sorbed N_2O_4 species (1743 cm^{-1}). Regarding the second maximum at 184 °C, it was assigned to weakly coordinated bidentate nitrates (IR band at 1592 cm^{-1}). Evacuating the sample at higher temperatures the IR maxima at 1653 and 1633 cm^{-1} attenuated but did not vanish, indicating that the high temperature NO_2-TPD peak at 400 °C was related to decomposition of strongly coordinated bridging Al- and Fe-based NO_3^-. In analogy with results presented in section 6.2.2.1, IR spectra were not exploitable upon heating the Fe-BEA at temperatures higher than 220 °C. In Figure 6.12 it is clearly illustrated that at this temperature NO started to evolve in the gas phase, which was attributed to NO_2 dissociation [263]. Interestingly, the NO evolution on the Fe-BEA began 80 °C lower compared to the H-BEA, which tends to indicate that NO_2 dissociation was catalyzed over the iron sites.
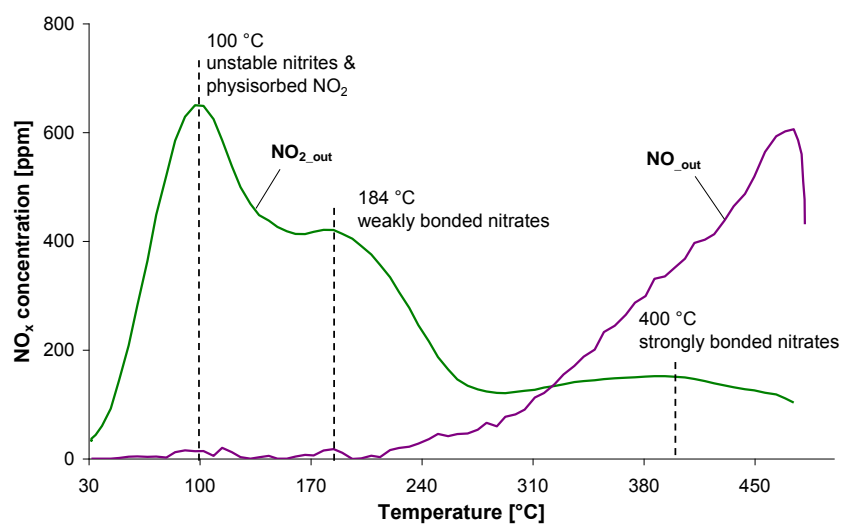
Figure 6.12 NO_2 TPD on the studied Fe-BEA, performed from 30 to 493 °C at a heating rate of 10 °C/min: Preadsorption of 0.43% NO_2, 8% O_2 and He in balance at 30 °C, for 100 min, followed by 1 He flushing at the same temperature.
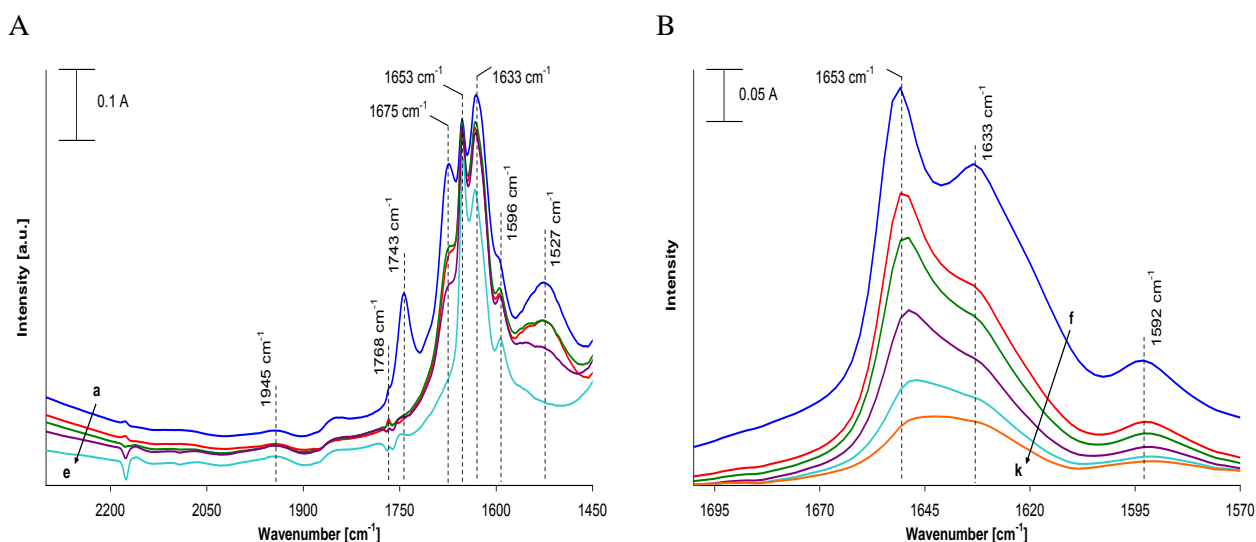
Figure 6.13 Difference IR spectra recorded during NO_2-TPD on Fe-BEA at a) 30 °C at the end of the NO_2/O_2 injection, b) 30 °C after 1 h He purging, c) 50 °C, d) 75 °C, e) 100 °C, f) 115 °C, g) 150 °C, h) 170 °C, i) 190 °C, j) 210 °C, k) 220 °C.

Compiling information obtained from IR spectroscopic measurements over the H- and Fe-BEA lab-synthesized samples it could be concluded that NO_2 can be weakly adsorbed and/or physisorbed, whereas it can be adsorbed on acidic sites forming nitrites. Furthermore, nitrogen dioxide can chemisorb and disproportionate over framework and extra-framework Al as well as monomeric and binuclear Fe sites, which are in close vicinity with cationinc OH^+ Brønsted acidic sites. Purging the catalytic samples with He, even at room temperature and/or increasing temperature above ambient, nitrates can decompose towards NO_2 and the latter can be released in the gas phase. Finally, at temperatures higher than 220°C nitrogen dioxide can dissociate to nitrogen monoxide over FAl and iron sites. These observations are summarized through reactions 6.10 to 6.16.

$$NO_{2(g)} + HO - Si - Z \rightleftharpoons NO_2 - HO - Si - Z \qquad \textbf{reac. 6.10}$$

$$NO_{2(g)} + T_1 - Z \rightleftharpoons (NO_2 - T_1)^- - Z \quad (T_1 = H^+ \text{ and/or Al}) \qquad \textbf{reac. 6.11}$$

$$2NO_{2(g)} + O - Al_F - Z + 2H^+ - OZ \rightleftharpoons NO_3 - Al_F - Z + NO^+ - Z + HO - H^+ - Z \qquad \textbf{reac. 6.12}$$

$$2NO_{2(g)} + O - Al_{EF} - Z + 2H^+ - OZ \rightleftharpoons NO_3 - Al_{EF} - Z + NO^+ - Z + HO - H^+ - Z \qquad \textbf{reac. 6.13}$$

$$2NO_{2(g)} + O - Fe^{3+} - Z + 2H^+ - OZ \rightleftharpoons NO_3 - Fe^{3+} - Z + NO^+ - Z + HO - H^+ - Z \qquad \textbf{reac. 6.14}$$

$$NO_3 - T_2 - Z \rightleftharpoons NO_{2(g)} + O - T_2 - Z \quad (T_2 = Al_F, Al_{EF}, Fe^{3+}) \qquad \textbf{reac. 6.15}$$

$$NO_2 - T_3 - Z \rightleftharpoons NO_{(g)} + O - T_3 - Z \quad (T_3 = Al_F, Fe^{3+}) \qquad \textbf{reac. 6.16}$$
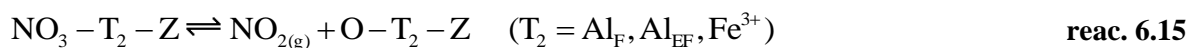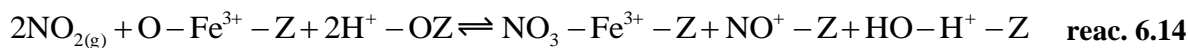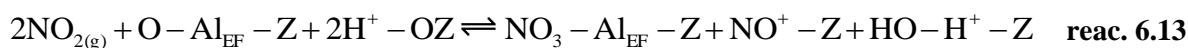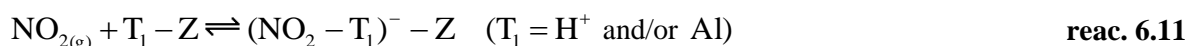
6.2.3 NO oxidation on Fe-BEA

Finally, NO oxidation over the Fe-BEA catalyst was studied through a stepwise TPD experiment (STPD). The catalyst was continuously exposed to a mixture of around 1100 ppm NO and 2% O_2, diluted in He. Reactor temperature was increased in steps, from 100 to 480 °C, maintaining the catalyst under steady state conditions at each temperature step (see experimental details in section 4.3.2). Gaseous phase results are illustrated in Figure 6.14. Nitrogen monoxide oxidation became evident already at 100 °C and a maximum conversion of around 37% was reached at 400 °C. At higher temperatures, the thermodynamic equilibrium shifted towards NO_2 and NO concentration was stabilized again at 1100 ppm.

IR spectra recorded during the NO oxidation experiment are presented in Figure 6.15. Concerning the initial isothermal period at 100 °C ($\Delta t = 0 - 60$ min), $[Fe-NO]^{2+}$ mononitrosyls (1872 cm^{-1}), bridging Fe based and monodentate NO_3 (1635 and 1580 cm^{-1} respectively) as well as N_2O_3 (1760 cm^{-1}) were identified (sections 6.2.1 and 6.2.2). Surprisingly, NO^+, which was previously evidenced at 2133 cm^{-1} during NO adsorption (section 6.2.1), was not observed. This could indicate either that the nitrosium ion is unstable at this temperature regime, or that significant interactions between O_2 and Brønsted acidic sites took place, inhibiting NO adsorption on cationic OH^+.

Upon 20 min of NO/O_2 admission, surface concentration of mononitrosyls started to attenuate and finally the species disappeared after 40 min. Simultaneously, NO_2 evolved in the gas phase somehow indicating that NO oxidation initially occurred over iron sites. Evacuating the sample at higher temperatures (Figure 6.15 B) intensities of IR maxima at 1635 and 1580 cm^{-1} decreased, whereas upon 200 °C, recorded IR spectra were no more exploitable. Therefore, it could be concluded that at this temperature range decomposition of NO_3 adspecies formed on Al contributed to the NO_2 gaseous evolution.
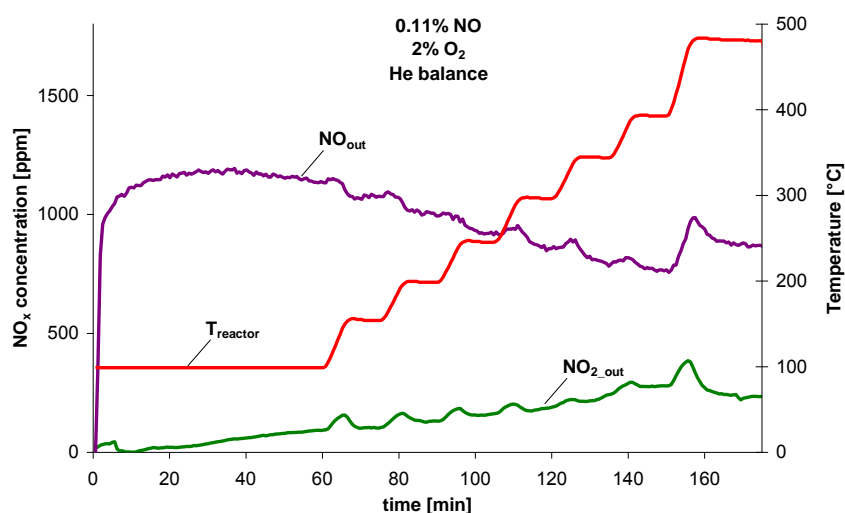
Figure 6.14 A) Gaseous NO_x concentrations recorded during NO oxidation experiment, B) NO oxidation yield (Injection of a mixture of 1100 ppm NO and 2% O_2 diluted in He and stepwise TPD from 100 to 480 °C).

A

B
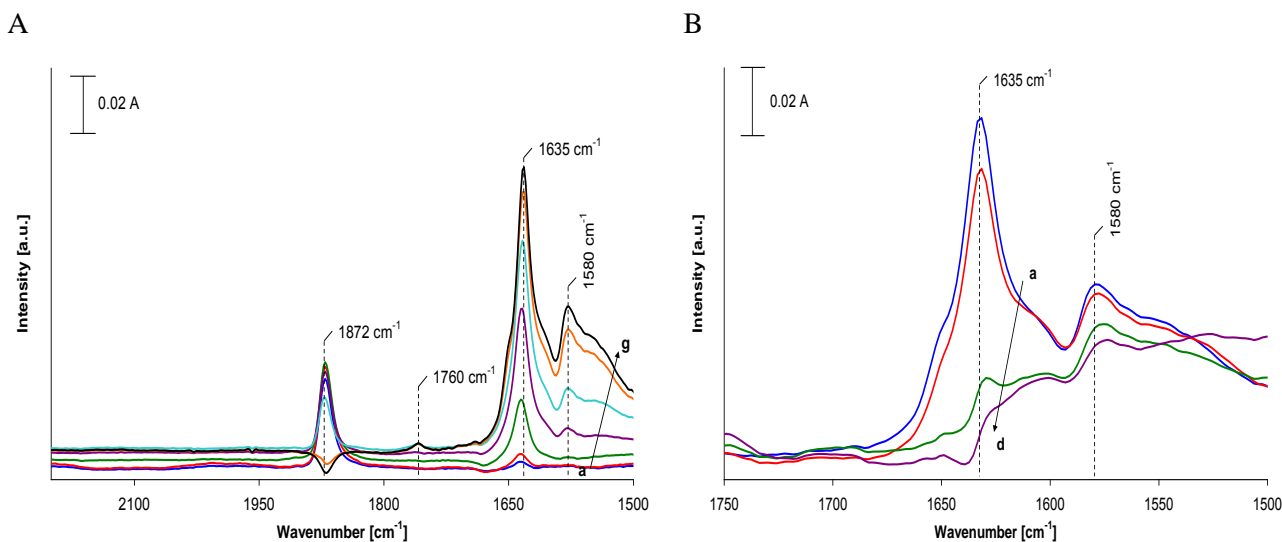
Figure 6.15 Difference IR spectra recorded during the NO oxidation experiment. A) Spectra recorded at a) 1 min, b) 2 min, c) 5 min, d) 10 min, e) 20 min, f) 40 min and g) 60 min, B) Spectra recorded at a) 100 °C, b) 145 °C, c) 155 °C and d) 200 °C.

Delahay et al. [74] and Panov et al. [264] proposed a sequential reaction mechanism including interaction of the Fe^{2+} ion with O_2 yielding $Fe^{3+}-O^-$ and reaction of the latter with NO towards $Fe^{3+}-ONO^-$. The abovementioned mechanism somehow explains the experimental results over the studied Fe-BEA catalyst, since the first 20 min of NO/O_2 adsorption were essential so as the catalyst could be oxidized or saturated with oxygen before the oxidation of NO becoming evidence. Therefore, the following redox cycle could be assumed:

$$O_2 + 2Fe^{2+} \rightleftharpoons 2Fe^{3+} - O \qquad \textbf{reac. 6.17}$$

$$NO_{(g)} + Fe^{3+} - O \rightleftharpoons (Fe-ONO)^{3+} \qquad \textbf{reac. 6.18}$$

$$(Fe-ONO)^{3+} \rightleftharpoons Fe^{2+} + NO_2 \qquad \textbf{reac. 6.19}$$

6.3 Kinetic model for NO_x storage and NO oxidation on Fe-BEA
6.3.1 Multi-site kinetic model development

Compiling information obtained through IR spectroscopic measurements, presented in section 6.2 a multi-site kinetic model for NO_x adsorption/desorption and NO oxidation was developed.

Regarding nitrogen monoxide adsorption and desorption, only minor quantities were stored over the studied Fe-BEA sample. Therefore, in order to keep the model as simple as possible, NO adsorption and desorption were not modeled. On the other hand, exposure of the H- and Fe-BEA samples to nitrogen dioxide led to a significant NO_2 uptake, followed by disproportionation yielding nitrites, nitrates and nitrosium ions. Therefore, NO_2 adsorption, desorption and disproportionation were

modeled in details. Based on the IR band centred at 1743 cm^{-1}, corresponding to weakly adsorbed N_2O_4, one site for weak NO_2 adsorption and/or physisorption named S1a, was included. Moreover, in order to depict formation of NO_2^- (IR maxima at 1653 and 1518 cm^{-1}), a second site, annotated S1b was considered, which was assigned to Brønsted sites. This assumption seemed to be in consistency with the fact that nitrites are generated through oxidation of NO^+, bonded on Brønsted sites (reaction 6.1 - section 6.2.1). The differentiation between NO_2^- species from NO_2 weakly adsorbed and/or physisorbed (even though they both exhibit low thermal stability) was judged to be essential, since the former have a crucial role to low temperature SCR. On the other hand weakly adsorbed and/or physisorbed NO_2 can only indirectly affect catalyst reduction activity through desorption and readsorption on redox sites.

Modeling of nitrate adspecies formation through NO_2 disproportionation was more complicated. According to spectroscopic measurements over the H-BEA zeolite (section 6.2.2.1), the disproportionation process requires a Lewis and a Brønsted acidic site in close vicinity. Moreover, nitrates can be coordinated in bidentate and bridging configurations involving framework and extra-framework aluminium, exhibiting different thermal stability. Therefore, two sites named S2 and S3 were taken into consideration and were attributed to extra-framework and framework aluminium atoms, located in proximity to cationic OH^+. Regarding NO_2 adsorption and disproportionation over Fe-BEA (section 6.2.2.2), monomeric iron cations as well as binuclear Fe species could contribute to NO_2 adsorption and disproportionation. Moreover, NO_2 disproportionation over a pair of two iron sites besides that occurring through synergy between an iron and a Brønsted site could not be ruled out. Nevertheless, since only one type of iron based nitrate was evidenced through IR spectroscopy (1633 cm^{-1}) and in order to keep the multi-site kinetic model as simple as possible, a single Fe site, named S4 was considered. This site was related either to a pair of metallic sites or to a pair of a metallic site and a Brønsted type one.

Regarding reactions mechanisms, an initial NO_2 adsorption and a subsequent NO_2 disproportionation were considered according to reactions 6.20 and 6.21:

$$NO_{2\_gas} \rightleftharpoons NO_{2\_ads} \qquad\qquad \textbf{reac. 6.20}$$

$$2NO_{2\_ads} \rightleftharpoons NO_{3\_ads} + NO_{(g)} \qquad\qquad \textbf{reac. 6.21}$$
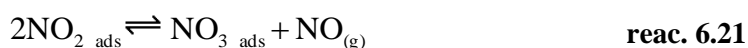
Both reactions were modeled on S2, S3 and S4 sites in order to depict formation of i) bidentate NO_3 on extra-framework Al (S2 sites), ii) bridging NO_3 on framework Al and iii) bridging NO_3 on Fe sites, monomeric and/or binuclear ones (S4 sites). Reaction 6.21 implies that nitrates can be decomposed to NO_2 when interacting with gaseous NO. Nevertheless, according to the TPD experiment presented in the previous section, NO_3^- was directly decomposed to NO_2 in the presence of He, without involvement of gaseous nitrogen monoxide. Therefore, in line with the approach of Olsson et al. [145], a reversible NO_3^- decomposition step was taken into account, yielding surface NO_2 and monatomic oygen (reaction 6.22). Adding reactions 6.21 and 6.22, reaction 6.6 is found.

$$NO_{2\_ads} + O_{ads} \rightleftharpoons NO_{3\_ads} \qquad\qquad \textbf{reac. 6.22}$$

Since surface oxygen is required in reaction 6.22, O_2 adsopriton and desorption were modeled on S2, S3, and S4 sites. Moreover, in order to account for the formation of monatomic oxygen species, O_2

dissociation over these sites was additionally considered. This modeling approach has been also reported elsewhere [141,145]. O_2 adsorption/desorption over S1a and S1b sites was purposely not considered, because oxygen does not react with NO_2 on them (even though it could competitively co-adsorb) and the detailed kinetic modeling of O_2 is out of the scope of the herein study. The multi-site kinetic model for O_2 adsorption/desorption and dissociation/recombination is illustrated in Table 6.4, whereas that for NO_2 adsorption/desorption and disproportionation/recombination in Table 6.5.

Table 6.4 Multi-site kinetic model for O_2 storage on Fe-BEA.

O_2 adsorption on S2 sites[1]	$O_2 + S2 \rightleftharpoons O_2 - S2$
O_2 adsorption on S3 sites[2]	$O_2 + S3 \rightleftharpoons O_2 - S3$
O_2 dissociation on S2 sites[1]	$O_2 - S2 + S2 \rightleftharpoons 2O - S2$
O_2 dissociation on S3 sites[2]	$O_2 - S3 + S3 \rightleftharpoons 2O - S3$
O_2 adsorption on S4 iron based sites[3]	$O_2 + S4 \rightleftharpoons O_2 - S4$
O_2 dissociation on S4 iron based sites[3]	$O_2 - S4 + S4 \rightleftharpoons 2O - S4$

[1]: S2 sites represent a pair of an Al based Lewis site and a Si-OH$^+$-Al Brønsted one, where bidentate NO_3^- can be formed, [2]: S3 sites represent a pair of an Al based Lewis site and a Si-OH$^+$-Al Brønsted one, where bridging NO_3^- can be formed, [3]: S4 sites represent a pair of an isolated or binuclear iron site in the Fe^{3+} state and a Si-OH$^+$-Al Brønsted and/or a second metallic one.

Table 6.5 Kinetic model for NO_2 storage and disproportionation on Fe-BEA.

NO_2 weak adsorption on S1a sites	$NO_2 + S1a \rightleftharpoons NO_2 - S1a$
NO_2^- formation on S1b Brønsted sites	$NO_2 + S1b \rightleftharpoons NO_2 - S1b$
NO_2 adsorption on S2 sites[1]	$NO_2 + S2 \rightleftharpoons NO_2 - S2$
NO_2 adsorption on S3 sites[2]	$NO_2 + S3 \rightleftharpoons NO_2 - S3$
NO_2 adsorption on S4 sites[3]	$NO_2 + S4 \rightleftharpoons NO_2 - S4$
NO_2 disproportionation on S2 sites[1]	$2NO_2 - S2 \rightleftharpoons NO_3 - S2 + NO_{(g)} + S2$
	$NO_2 - S2 + O - S2 \rightleftharpoons NO_3 - S2 + S2$
NO_2 disproportionation on S3 sites[2]	$2NO_2 - S3 \rightleftharpoons NO_3 - S3 + NO_{(g)} + S3$
	$NO_2 - S3 + O - S3 \rightleftharpoons NO_3 - S3 + S3$
NO_2 disproportionation on S4 sites[3]	$2NO_2 - S4 \rightleftharpoons NO_3 - S4 + NO_{(g)} + S4$
	$NO_2 - S4 + O - S4 \rightleftharpoons NO_3 - S4 + S4$

[1]: S2 sites represent a pair of an Al based Lewis site and a Si-OH$^+$-Al Brønsted one, where bidentate NO_3^- can be formed, [2]: S3 sites represent a pair of an Al based Lewis site and a Si-OH$^+$-Al Brønsted one, where bridging NO_3^- can be formed, [3]: S4 sites represent a pair of an isolated or binuclear iron site in the Fe^{3+} state and a Si-OH$^+$-Al Brønsted and/or a second metallic one.

Finally, regarding NO/O_2 adsorption on Fe-BEA, based on IR spectroscopic measurements, Al based acidic and Fe^{3+}-O sites were evidenced to be active for nitrogen monoxide oxidation. Regarding acidic sites, bridging nitrates (1635 cm^{-1}) were identified, which according to the proposed multi-site kinetic model, are formed on the S3 site. On the other hand, nitrogen monoxide reaction with oxygen occurred over oxidized isolated or binuclear iron species, which correspond to the S4 site. Therefore, NO oxidation was considered over the S3 and S4 sites (Table 6.6). At temperatures higher than 400 °C, the thermodynamic equilibrium shifted towards NO_2 and consumption of NO was hindered (Figure 6.14 A). Moreover, during the presented NO_2-TPD experiments over the H- and the Fe-BEA and at temperatures higher than 310 and 220 °C respectively NO evolution was evidenced, due to NO_2 decomposition. Thus, a reversible reaction step was taken into account, corresponding to NO_2 dissociation.

Table 6.6 Multi-site kinetic model for NO oxidation.

NO oxidation on S3 sites[1]	$NO_{(g)} + O - S3 \rightleftharpoons NO_2 - S3$
NO oxidation on S4 sites[2]	$NO_{(g)} + O - S4 \rightleftharpoons NO_2 - S4$

[1]: S3 sites represent a pair of an Al based Lewis site and a Si-OH$^+$-Al Brønsted one, [2]: S4 sites represent a pair of an isolated or binuclear iron site in the Fe^{3+} state and a Si-OH$^+$-Al Brønsted and/or a second metallic one.

Respective reaction rate expressions were formulated based on the power rate law and are summarized in Table 6.7. Regarding O_2 and NO_2 adsorption rate constants, typical Arrhenius equations were employed. The respective rate constant for NO_2 desorption was expressed on the basis of a Temkin type equation, in analogy with the desorption rate expressions applied for NH_3 (see chapters 2 and 5). Finally, the remaining reaction rates were formulated according to the respective expressions applied in the kinetic model of Olsson et al. [145].

Table 6.7 Reaction rate expressions used for reactions of the multi-site kinetic model.

Reaction	Reaction rate expression
$O_2 + Sj \rightleftharpoons O_2 - Sj$	$R_{j\_O_2\_ads} = A_{j\_O_2\_ads} \cdot \exp\left(-\dfrac{E_{j\_O_2\_ads}}{R \cdot T_s}\right) \cdot C_{O_2} \cdot (1 - \vartheta_{i,j})$
	$R_{j\_O_2\_des} = A_{j\_O_2\_des} \cdot \exp\left(-\dfrac{E_{j\_O_2\_des}}{R \cdot T_s}\right) \cdot \vartheta_{O_2,j}$
$O_2 - Sj + Sj \rightleftharpoons 2O - Sj$	$R_{j\_O_2\_diss} = A_{j\_O_2\_diss} \cdot \exp\left(-\dfrac{E_{j\_O_2\_diss}}{R \cdot T_s}\right) \cdot \vartheta_{O_2,j} \cdot (1 - \vartheta_{i,j})$
	$R_{j\_O_2\_rec} = A_{j\_O_2\_rec} \cdot \exp\left(-\dfrac{E_{j\_O_2\_rec} \cdot (1 - \alpha_{j,O_2\_rec} \cdot \vartheta_{O,j})}{R \cdot T_s}\right) \cdot \vartheta_{O,j}^2$
$NO_2 + Sj \rightleftharpoons NO_2 - Sj$	$R_{j\_NO_2\_ads} = A_{j\_NO_2\_ads} \cdot \exp\left(-\dfrac{E_{j\_NO_2\_ads}}{R \cdot T_s}\right) \cdot C_{NO_2} \cdot (1 - \vartheta_{i,j})$
	$R_{j\_NO_2\_des} = A_{j\_NO_2\_des} \cdot \exp\left(-\dfrac{E_{j\_NO_2\_des} \cdot (1 - \alpha_{j,NO_2\_des} \cdot \vartheta_{NO_2,j})}{R \cdot T_s}\right) \cdot \vartheta_{NO_2,j}$
$2NO_2 - Sj \rightleftharpoons$ $NO_3 - Sj + NO_{(g)} + Sj$	$R_{j\_NO_2\_disp} = A_{j\_NO_2\_disp} \cdot \exp\left(-\dfrac{E_{j\_NO_2\_disp}}{R \cdot T_s}\right) \cdot \vartheta_{NO_2,j}^2$
	$R_{j\_NO_2\_rec} = A_{j\_NO_2\_rec} \cdot \exp\left(-\dfrac{E_{j\_NO_2\_rec} \cdot (1 - \alpha_{j,NO_2\_rec} \cdot \vartheta_{NO_3,j})}{R \cdot T_s}\right) \cdot$ $\vartheta_{NO_3,j} \cdot C_{NO} \cdot (1 - \vartheta_{i,j})$
	$R_{j\_NO_3\_form} = A_{j\_NO_3\_form} \cdot \exp\left(-\dfrac{E_{j\_NO_3\_form}}{R \cdot T_s}\right) \cdot \vartheta_{NO_2,j} \cdot \vartheta_{O,j}$
$NO_2 - Sj + O - Sj \rightleftharpoons$ $NO_3 - Sj + Sj$	$R_{j\_NO_3\_dec} = A_{j\_NO_3\_dec} \cdot \exp\left(-\dfrac{E_{j\_NO_3\_dec} \cdot (1 - \alpha_{j\_NO_3\_dec} \cdot \vartheta_{NO_3,j})}{R \cdot T_s}\right) \cdot$ $\vartheta_{NO_3,j} \cdot (1 - \vartheta_{i,j})$
$NO_{(g)} + O - Sj \rightleftharpoons$ $NO_2 - Sj$	$R_{j\_NO\_ox} = A_{j\_NO\_ox} \cdot \exp\left(-\dfrac{E_{j\_NO\_ox}}{R \cdot T_s}\right) \cdot (C_{NO} \cdot \vartheta_{NO_2,j})$
	$R_{j\_NO_2\_diss} = A_{j\_NO_2\_diss} \cdot \exp\left(-\dfrac{E_{j\_NO_2\_diss}}{R \cdot T_s}\right) \cdot \vartheta_{NO_2,j}$

6.3.2 Simulation of NO₂ adsorption and desorption experiments

6.3.2.1 Simulation of experiments over the lab-synthesized H- and Fe-BEA samples

The proposed multi-site kinetic model was initially used for simulation of the NO_2 adsorption and TPD experiments over the studied H- and Fe-BEA samples, presented in sections 6.2.2.1 and 6.2.2.2 respectively. These experiments were performed using the single wafer laboratory reactor, hence the respective single wafer reactor model was applied for simulation purposes. Special care was taken for determining model kinetic parameters. A detailed description of kinetics calibration is presented in Appendix B (see Table B.1 to Table B.7).

Regarding NO_2/O_2 storage and release over H-BEA, simulation results are illustrated in Figure 6.16. Overall, the proposed multi-site kinetic model reproduced the tendency of the experimental curves during both the adsorption and TPD phases.
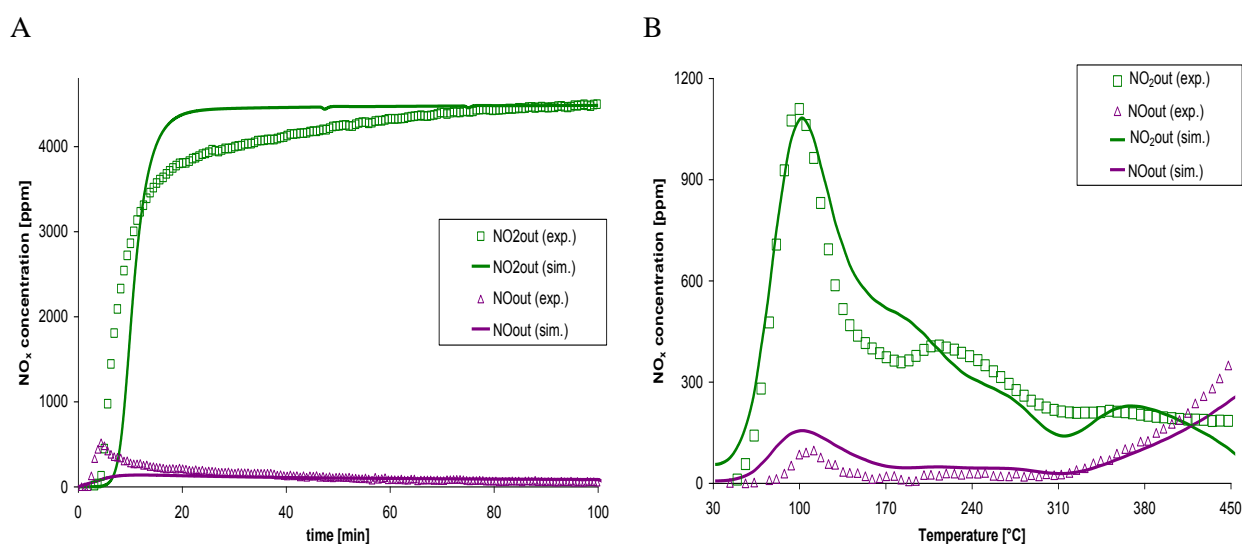
Figure 6.16 Simulation of NO_2/O_2 adsorption and TPD experiments over the H-BEA studied sample. Preadsorption of 0.45% NO_2, 8% O_2 and He in balance at 30 °C for 100 min, followed by 60 min He flushing and TPD up to 493 °C under He at heating rate of 10 °C/min.

Considering the first 100 min, NO_2 adsorption and disproportionation, as well as NO evolution, according to reactions 6.20 to 6.22 were simulated, resulting in a relatively acceptable fitting of the experimental curves (Figure 6.16 A). Nevertheless, computed nitrogen monoxide maximum concentration originating from NO_2 disproportionation was underestimated. Furthermore, the NO_2 simulated concentration signal was stabilized to the injected concentration of 0.45% nitrogen dioxide at around 17 min upon surface saturation, whereas the respective experimental one after 80 min. These discrepancies could be attributed to several reasons. First of all, the proposed kinetic model accounted only for a two step mechanism including NO_2 adsorption and a subsequent disproportionation, whereas interactions between NO and NO_2 (eg. formation of N_2O_3 and subsequent oxidation of the

latter towards N_2O_4) were not taken into consideration for simplicity purposes. Moreover, reviewing the sources according to which kinetic parameters were obtained (see Appendix B) it seems that the set of kinetic parameters proposed in this work were mainly validated for NO_2 adsorption experiments performed at higher temperatures. Finally, limitations of the single wafer reactor model can not be ruled out, since the latter was modeled as a 0D continuous stirred reactor (see also chapter 2 / section 2.2). As far as the TPD phase is concerned, three distinguishable desorption peaks, centred at around 100, 220 and 370 °C were correctly simulated, whereas at temperatures higher than 310 °C, NO evolution due to NO_2 dissociation (backward step of reaction 6.18) was satisfactorily depicted. Before simulating the TPD experiment, the contribution of each model site was simulated separately (Figure 6.17). In accordance with the IR spectroscopy measurements presented in section 6.2.2.1, weakly adsorbed NO_2 on S1a sites and nitrites on S1b Brønsted acidic sites were responsible for the low temperature NO_2-TPD peak centred at around 100 °C. As shown in Table B.3 (Appendix B), activation energies of NO_2 desorption from S1a and S1b sites were calibrated to 77 and 82 kJ/mol respectively, which in line with IR spectral features presented in section 6.2.2, indicates that weakly adsorbed NO_2 as well as nitrites exhibit low thermal stability. On the other hand NO_2 originating from NO_3 decomposition over S2 and S3 sites reproduced the respective thermodesorption peaks lying at 220 and 380 °C. As explained earlier, these peaks correspond to bidentate (1592 cm^{-1} IR band) and bridging (1653 cm^{-1} IR band) nitrates coordinated to extra-framework and framework Al respectively. Activation energies for NO_3 decomposition and subsequent NO_2 desorption on S2 sites were calibrated to quite lower values compared to those corresponding to the S3 site (see Table B.3 and Table B.5 in Appendix B). The proposed calibration seems to reflect the different thermal stability of the bidentate and bridging nitrates, in relatively good agreement with the spectroscopic analysis presented in section 6.2.2.
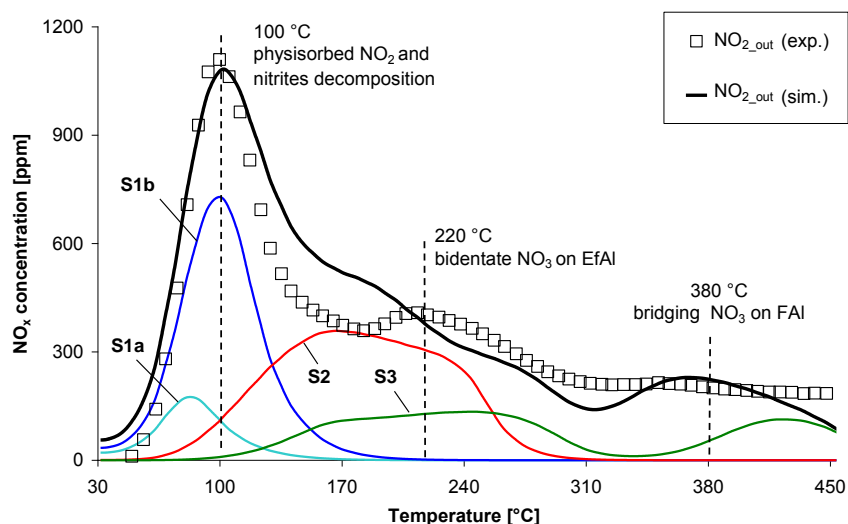

Figure 6.17 Contribution of each model site during the NO_2-TPD experiment over the lab-synthesized H-BEA zeolite: Preadsorption of 0.45% NO_2, 8% O_2 and He in balance at 30 °C for 100 min, followed by 1 h He purge at the same temeperature and a TPD up to 493 °C, under He at heating rate of 10 °C/min.

Comparison between simulation and experimental results of NO_2/O_2 storage and release over the Fe-BEA sample are presented in Figure 6.18. Similarly, the multi-site kinetic model and the proposed kinetics calibration gave rise to relatively satisfactory simulations, which depicted the tendency of the experimental curves. In the case of the iron exchanged catalyst, NO evolution upon surface saturation with NO_2/O_2 was somehow correctly simulated, due to the additional contribution of the metallic S4 site. Furthermore, focusing on the TPD experiment, the multi-site kinetic model succeeded in simulating gaseous NO_2 evolution originating from the decomposition of nitrites as well as Al and Fe based nitrates, in line with experimental results obtained from IR spectroscopic measurements, presented in section 6.2.2.2. Examining kinetic parameters presented in Table B.1 to Table B.6 (Appendix B) it seems that the reactions kinetics on the S4 metallic sites exhibit similarities compared to the ones corresponding to the S3 site, where bridging Al based NO_3 can be formed. This is somehow in accordance with the IR spectra presented in Figure 6.13, which show that both Al and Fe based bridging NO_3 adspecies are characterised by significant thermal stability.

Finally, NO_2 dissociation was predicted at temperatures higher than 200 °C. However, a significant deviation between computed and experimental NO gaseous profiles was observed within the range of 100 – 310 °C, where the multi-site kinetic model overestimated the nitrogen monoxide concentration signal. It is speculated that the fact that the NO adsorption/desorption over metallic sites (Fe^{2+}) was not modeled may be responsible for this discrepancy. Nevertheless, as mentioned in section 6.2.1, overall NO uptake over the studied Fe-BEA was limited and thus in order to keep model complexity at reasonable extends, the NO storage was not modeled.

A
B
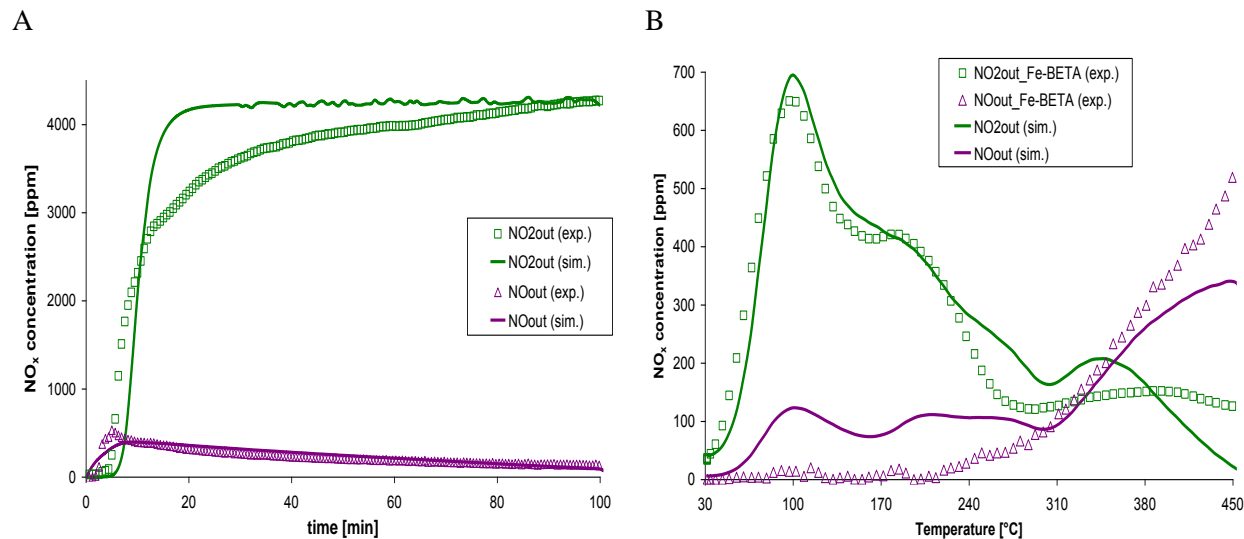
Figure 6.18 Simulation of NO_2/O_2 adsorption and TPD experiments over the Fe-BEA studied sample. Preadsorption of 0.43% NO_2, 8% O_2 and He in balance at 30 °C for 100 min, followed by 60 min He flushing and TPD up to 493 °C at heating rate of 10 °C/min.

So far, the proposed kinetic model for NO_2 storage and NO oxidation was evaluated with respect to NO_x gaseous profiles simulation. Taking a further step, model capability to reproduce the evolution of surface species was also tested. Therefore, an additional NO_2 adsorption and TPD experiment was

performed over the Fe-BEA lab-synthesiszed catalyst. Focusing on Al and Fe based NO_3 adspecies concentrations and in order to avoid low temperature weak adsorption and/or physisorption, 0.35% NO_2, 8% O_2 and He in balance were preadsorbed at 150 °C for 100 min. Then, oxygen and nitrogen dioxide were removed from the feed and the catalyst was flushed with He for 1 h at the same temperature. Finally, a TPD was performed up to 480 °C under He, at a heating rate of 10 °C/min. Comparison between experimental and simulation gas phase results is shown in Figure 6.19. Overall, the proposed kinetic model and the respective set of kinetic parameters allowed to obtain a relatively correct fitting of the NO and NO_2 gaseous experimental profiles. During NO_2/O_2 adsorption, a nitrogen dioxide uptake of 2.05 mol/kg$_{Fe-BEA}$ followed by a generation of 0.76 mol/kg$_{Fe-BEA}$ nitrogen monoxide were estimated, which verified the stoichiometry of reaction 6.6. In this case, the proposed kinetic model simulated correctly the NO evolution, which somehow tends to prove that the proposed kinetics are valid for experiments performed at temperatures higher than ambient. Regarding the TPD phase, since this thermodesorption was launched at 150 °C and according to the analysis presented in Figure 6.17, S1a and S1b sites did not contribute to the NO_2 released. Overall, the model succeeded in capturing the tendency of the experimental curves, whereas significant discrepancies were evidenced. The latter, could be attributed to either experiment reproducibilty issues and/or limitations of the 0D single wafer reactor model.
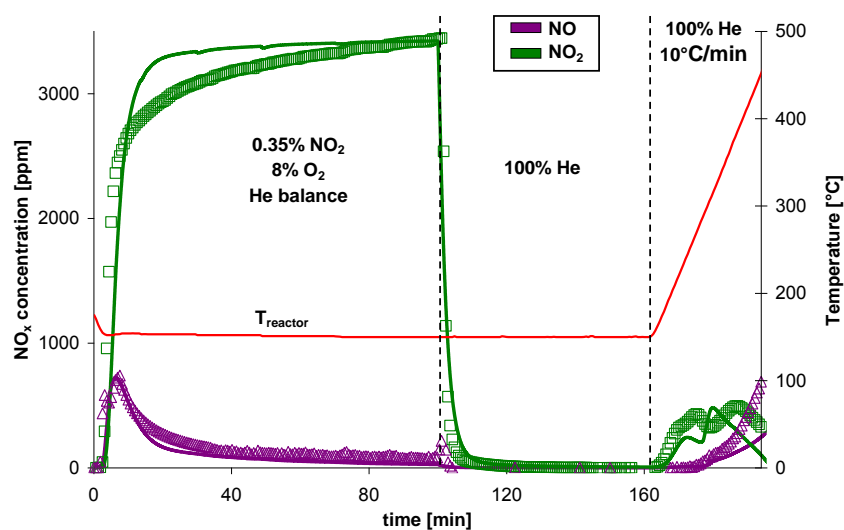
Figure 6.19 NO_2 adsorption and TPD on the lab-synthesized Fe-BEA: Preadsorption of 0.35% NO_2 and 8% O_2 in He, for 100 min at 30 °C, followed by 60 min He flushing at the same temperature and TPD up to 482 °C at a heating rate of 10 °C/min.

Respective simulated profiles of adspecies formed over the S2, S3 and S4 sites are illustrated in Figure 6.20 A to C (simulated curves are computed by eq. 2.28, upon calculating respective reaction rates). Focusing on the adsorption phase, all sites had become initially saturated with nitrogen dioxide, before nitrates formation took place, due to NO_2 disproportionation. The latter, is in excellent agreement with the spectroscopic analysis presented in section 6.2.2, showing the interest of the followed methodology. On the other hand, when NO_2 and O_2 were removed from the feed and the

catalyst was purged with He, nitrates removal was simulated over the S2 site, whereas NO_3 concentration was slightly increased over S3 and S4 sites. Finally, regarding the TPD experiment, NO_3 formed on S2 and S3 and S4 sites started to decompose at around 185 and 250 °C respectively and gaseous NO_2 was simulated (as shown in Figure 6.19), which is also in agreement with the analysis reported in section 2.2.2. Interestingly, at 230 °C atomic oxygen was produced over S3 and S4 sites, due to NO_2 dissociation (reactions presented in Table 6.6).

In situ IR spectroscopy was also employed during this NO_2 adsorption and TPD experiment (IR spectra are not shown). Therefore, for comparison purposes, IR bands, centred at 1653, 1633 and 1591 cm^{-1}, corresponded to NO_3 bonded to FAl, EfAl and Fe, were normalized (as explained in section 6.2.2.1). The respective profiles are illustrated in Figure 6.20 D. Concerning the NO_2 adsorption phase (t = 0 – 100 min), bridging NO_3 on FAl were almost immediately generated upon nitrogen dioxide introduction (t = 1.8 min), whereas nitrates on EfAl and iron were formed at a significantly slower rate. Subsequently, during the isothermal He flushing period, fraction of the preadsorbed NO_3 was removed from the discussed catalytic positions. Finally, decomposition of NO_3 adspecies during the TPD phase was initiated at around 170 and 190 °C over FAl and EfAl and Fe respectively. As explained in section 6.2.2.2, IR spectra recorded at temperatures higher than 220 °C were not exploitable and hence it was difficult to conclude at which temperature surface nitrates were completely removed.

Comparing simulated and experimental NO_3 adspecies concentration profiles, it seems that the proposed kinetic model accounted for nitrogen dioxide adsorption and disproportionation, as well as nitrates decomposition and NO_2 desorption and dissociation, which resulted in a relatively correct simulation of gaseous NO_x profiles. Nevertheless, even though surface phenomena were depicted, the dynamics of adspecies evolution could not be sufficiently reproduced, whereas the nitrates removal during the He flushing phase was only simulated over the S2 sites. Two main reasons were speculated regarding these discrepancies: i) the kinetic parameters calibration and ii) the fact that the proposed reactions mechanism was quite simple and thus a more detailed scheme was required, which could include more reactions and more intermediate species. Nevertheless, such aspects should be further investigated through micro-kinetics analysis and thus go beyond the scope of the present work.
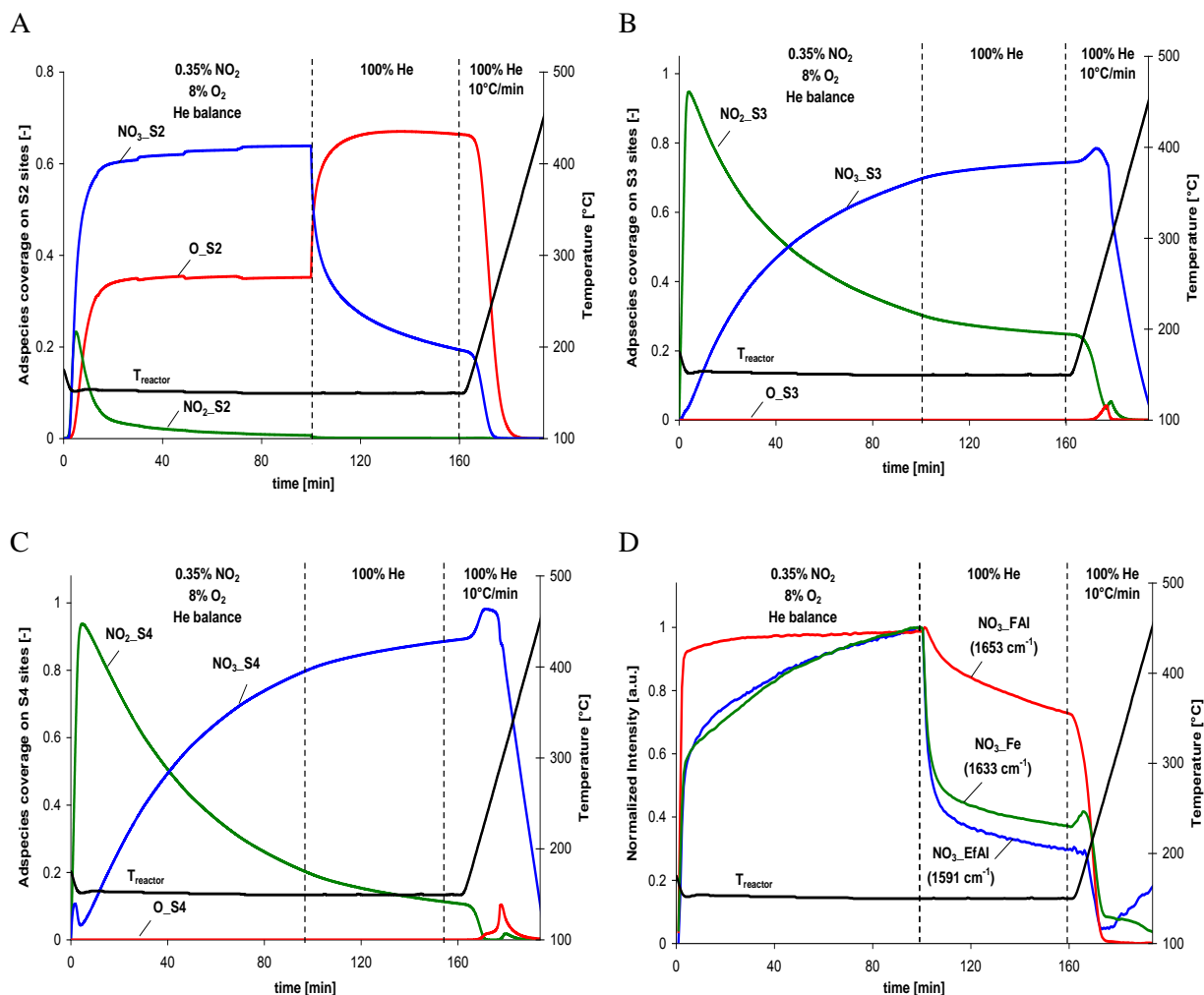
Figure 6.20 Simulated profiles of adspecies formed over the A) S2, B) S3 and C) S4 sites during a NO_2 adsorption and TPD experiment performed at 150 °C over the lab-synthesized Fe-BEA catalyst. D) Normalized intensities of IR peaks associated with Al and Fe based NO_3 adspecies (normalization was performed at maximum or minimum peak intensity for each of the presented IR bands).

6.3.2.2 Simulation of experiments over a commercial Fe-BEA catalyst

In order to further evaluate the multi-site kinetic modelling approach consistency, additional NO_2 storage/release experiments, reported by Colombo et al. [94] were simulated. Two NO_2 adsorption and TPD experiments were performed over a commercial, oxidized Fe-BEA catalyst (Si/Al = 24, Fe/Al = 1.5) in the absence and the presence of oxygen. A fixed bed reactor was used in both test cases and a detailed description of the respective reactor model is given in section 2.2.

During the first test case, 1000 ppm NO_2, diluted in He were preadsorbed at 200 °C, for 500 min, followed by a TPD up to 500 °C, at a heating rate of 10 °C/min. The same protocol was applied for the second experiment. However, in this case, the Fe-BEA catalyst was exposed to a mixture of 1000 ppm NO_2, 2% O_2, and He in balance. Experimental and simulation NO_x gas phase signals are illustrated in

Figure 6.21 A, B and C, D respectively. For simulation purposes, the multi-site kinetic model had to be recalibrated in order to correctly depict experimental curves. A single set of kinetic parameters, shown in Table B.8 to Table B.14 of Appendix B, was used for simulating both experiments. The need to recalibrate kinetics was somehow reasonable for two reasons. First of all, the Si/Al of the commercial sample was higher compared to the lab-synthesized Fe-BEA and thus a lower amount of Al was included. As discussed in section 6.2.2, the distribution of framework and extra-framework aluminium is crucial for NO_2 disproportionation, since Al constitutes the active sites where nitrates are formed. Moreover, the synthesis method (including catalyst post-treatment: eg. calcincation) is not mentioned and thus a conclusion related to the nature of iron species, as well as the state of the zeolite can not be safely drawn.

Concerning the adsorption phase (Figure 6.21 A and C) nitrogen dioxide adsorption and disproportionation were observed during both experiments, leading to NO evolution. According to experimental analysis reported by Colombo et al. [94], the ratio between consumed NO_2 and evolved NO was around 0.38 - 0.45, which seems to validate experimental results obtained over the lab-synthesized Fe-BEA catalyst (section 6.2.2.2). Computational results were in relatively good agreement with experimental ones, since the recalibrated multi-site kinetic model depicted satisfactorily NO_2 adsorption and surface saturation as well as NO production. Interestingly, the model succeeded in simulating nitrogen monoxide production quite precisely, which tends to further validate the fact that proposed kinetic parameters might be suitable mainly for NO_2 adsorption experiments performed at this temperature range (200 °C). Furthermore, it has to be pointed out that competitive adsorption between NO_2 and O_2 was correctly taken into account. Indeed, in the NO_2/He adsorption case, a maximum NO concentration of 409 ppm was simulated, whereas for the NO_2/O_2/He adsorption experiment a NO maximum of ca 315 ppm was computed.

As far as the TPD phase is concerned (Figure 6.21 B and D), a distinguishable NO_x desorption peak centred at 310 °C, as well as a shoulder lying within the temperature range of 350 – 450 °C were observed. Treating the catalyst in oxidizing and reducing atmosphere, Colombo et al. [94] observed changes in the former desorption peak, whereas the high temperature shoulder remained unchanged. This somehow suggests that the 310 and 400 °C NO_x-TPD peaks are related to decomposition of nitrates previously being formed on metallic and zeolitic acidic sites respectively. According to IR spectroscopic measurements obtained over the Fe-BEA lab-synthesized sample (section 6.2.2.2) it could be speculated that the latter could be assigned to decomposition of bridging NO_3 coordinated on framework aluminium. Considering this analysis, S4 and S3 model sites simulated NO_x-TPD peaks at 310 and 400 °C respectively, highlighting the contribution of Fe and the zeolitic support of the commercial Fe-BEA catalyst for NO_2 adsorption/desorption and disproportionation reactions.
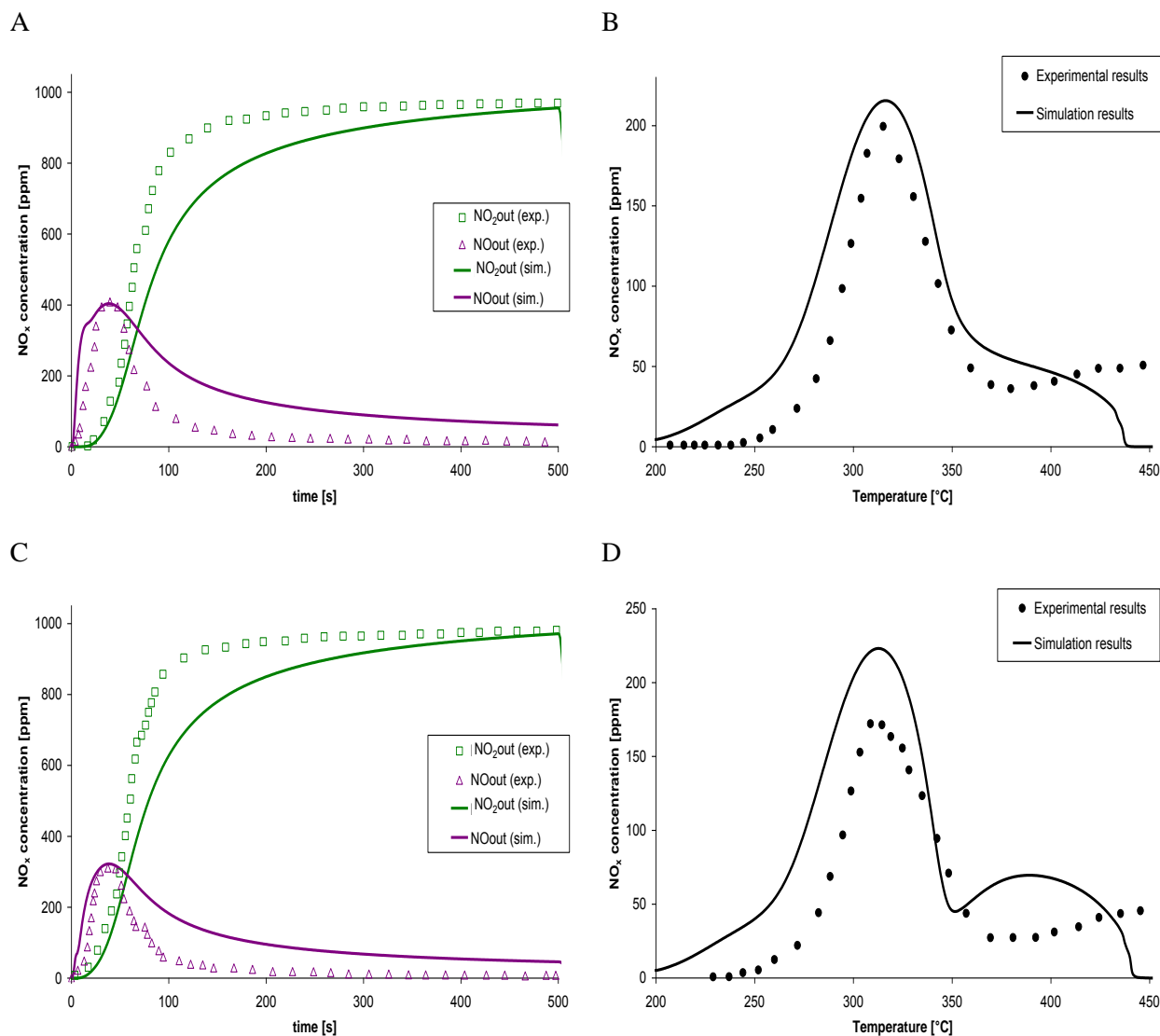
Figure 6.21 Simulation of NO_2 adsorption and TPD experiment over a commercial Fe-BEA catalyst, reported by Colombo et al. [94]. Preadsorption of 1000 ppm NO_2 diluted in He and 1000 ppm NO_2, 2% O_2 and He in balance at 200 °C for 500 s (Figures A and C), followed by a TPD performed from 200 to 500 °C, at 10 °C/min under He (Figures B and D).

Interestingly, for the experimental case where $NO_2/O_2/He$ were preadsorbed, the TPD peak at 310 °C attenuated from 200 to 173 ppm, which was not predicted by the kinetic model. Two reasons could be speculated for this discrepancy: a) experiment reproducibility issues, since the difference between the maximum NO_x concentration is less than 30 ppm and/or b) the simulation of compensating reactions. Regarding the latter, the model succeeded in simulating competitive adsorption between NO_2 and O_2, which could lead to a lower nitrogen dioxide uptake. The latter, may subsequently result in formation of a lower NO_3 quantity (reactions 6.20 and 6.21). Nevertheless, when oxygen coexist in the feed, reaction 6.22 is also activated, which could increase the amount of stored nitrate adspecies.
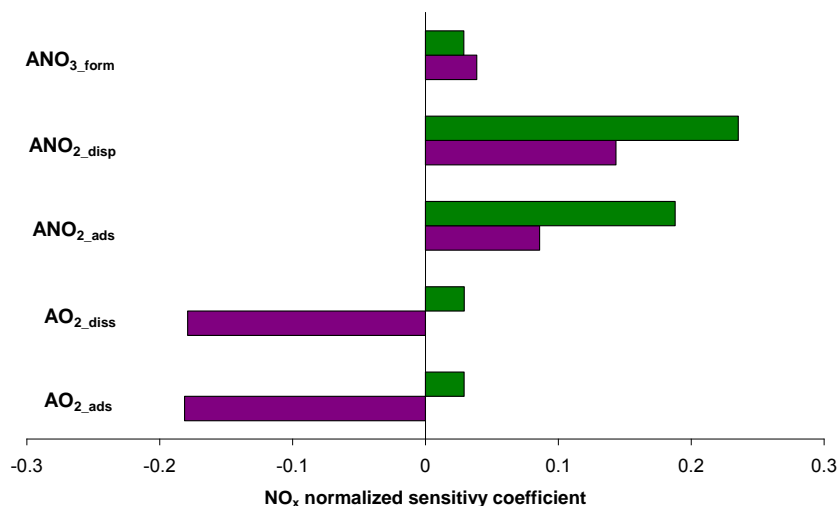
Figure 6.22 Sensitivity of NO_x outlet concentration with respect to pre-exponentials of reactions over the S4 metallic sites. Violet bars correspond to NO maximum outlet concentration during NO_2 disproportionation, whereas green ones to NO_2 oultet concentration at 310 °C.

In order to further understand the predominant reaction pathways for nitrates formation, a kinetic parameters sensitivity analysis with respect to the S4 site was performed for the abovementioned NO_2/O_2 adsorption and TPD experiment over the commercial Fe-BEA. As clearly shown in Figure 6.22 oxygen adsorption and dissociation as well as nitrogen dioxide disproportionation are the most important pathways, which control NO production upon surface saturation with NO_2/O_2. As previously explained, nitrogen monoxide evolution following NO_2 adsorption and disproportionation is hindered when O_2 is in the feed, due to NO_2/O_2 competitive adsorption. On the other hand, NO_x release at 310 °C, related to decomposition of Fe based NO_3 is reasonably governed by nitrogen dioxide adsorption and subsequent disproportionation (reactions 6.20 and 6.21). As it was suggested, when the Fe-BEA is exposed to a NO_2/O_2 mixture the reaction 6.22 is also activated, leading to the formation of additional amounts of nitrates. Therefore, the abovementioned assumption for compensating reaction pathways seems to be validated.

6.3.3 Simulation of NO oxidation experiments

The proposed multi-site kinetic model was subsequently used for simulating NO oxidation experiments. The NO/O_2 STPD experiment performed over the lab-synthesized Fe-BEA catalyst (section 6.2.3) was simulated first, applying the single wafer reactor model. Kinetic parameters used were the same with those applied for simulating the NO_2/O_2 TPD experiment over the same catalytic sample (Appendix B / Table B.1 to Table B.7), without any modification. Computed results, shown in Figure 6.23 seem to follow the tendency of the experimental curves, especially within the 250 – 400 °C range. Interestingly, the multi-site kinetic model did not succeed to depict NO oxidation at temperatures lower than 200 °C. Olsson et al. [145] similarly observed low temperature nitrogen monoxide oxidation over a Cu-ZSM5 ($SiO_2/Al_2O_3 = 27$, 2.03 wt.% Cu). These authors suggested NO

oxidation over non acidic sites and subsequently modeled the abovementioned phenomenon, which allowed to obtain satisfactory simulation results. Nevertheless, according to IR spectroscopic measurements over the lab-synthesized Fe-BEA catalyst, presented in section 6.2.3, only metallic and acidic sites were evidenced to contribute to NO oxidation. Moreover, the reaction was initially active over Fe sites at temperatures as low as 100 °C. Thus, it was supposed that there is more than one type of iron sites contributing to NO oxidation. Results of UV-vis spectroscopy, shown in chapter 4 tend to support this assumption, since isolated as well as binuclear iron species are included in the lab-synthesized Fe-BEA catalyst. However, in order to keep model complexity in reasonable extents it was decided to account for a single global Fe model site. Finally, it has to be highlighted that for temperatures higher than 400 °C, NO concentration increased, converging to 1100 ppm, in accordance with the NO_2/NO thermodynamic equilibrium discussed in section 6.2.3. An overestimation of nitrogen monoxide computed concentration signal could be assigned to the fact that NO adsorption/desorption modeling was neglected in the proposed multi-site kinetic model.
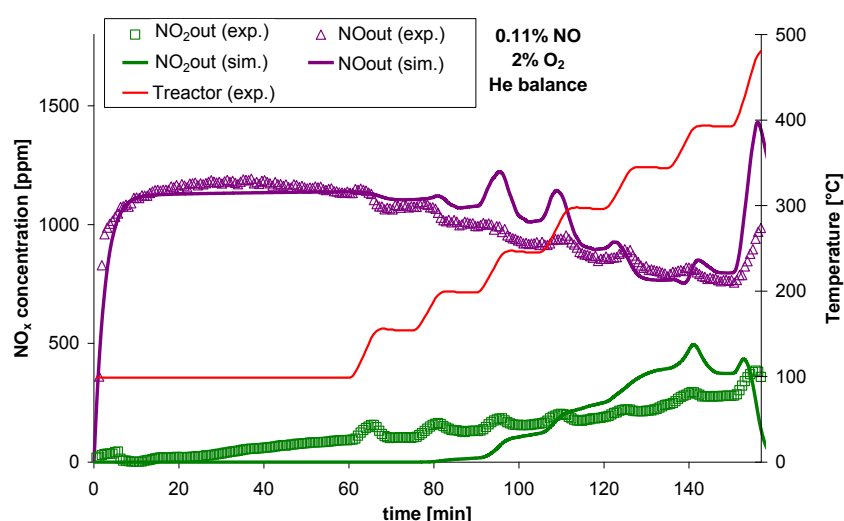
Figure 6.23 Simulation of a NO/O_2 STPD experiment over the Fe-BEA studied sample. Continuous injection of a 0.11% NO and 2% O_2 mixture diluted in He.

   Two additional NO/O_2 STPD experiments performed over a H- and a Fe-BEA samples, reported by Shwan et al. [140] were simulated in order to validate the consistency of the multi-site kinetic modeling approach for NO oxidation. A H-BEA zeolite (Si/Al = 38) and a 1wt.% Fe-BEA catalyst, loaded on a monolith reactor were exposed to a mixture of 400 ppm NO, 8% O_2 and 5% H_2O, with Ar in balance, whereas temperature was stepwisely increased from 150 to 500 °C. Comparison between simulation and experimental results is illustrated in Figure 6.24. For the simulation presented in Figure 6.24, the monolith reactor model was applied, whereas kinetic parameters previously applied for the lab-synthesized H- and Fe-BEA samples (Table B.1 to Table B.6) were used. Only the oxygen desorption activation energy over S4 metallic sites had to be calibrated to 40 instead of 48 kJ/mol in order to correctly fit experimental curves. The H-BEA reported by Shwan et al. [140] has similar Al content, compared to the respective lab-synthesized BEA zeolite studied in the herein study, whereas

wet ion exchange was the method used for synthesizing the Fe-BEA catalyst in both cases. These observations may explain why in this case similar kinetics could be applied.

Overall, simulation results are in relative agreement with experimental ones, indicating that the proposed set of kinetic parameters could constitute a quite reliable data base for the kinetic modeling of NO_x adsorption and NO oxidation over H- and Fe-BEA with similar structural properties. Results clearly prove the contribution of acidic and metallic sites to NO oxidation, in line with IR spectroscopic measurement presented in 6.2.3. Again, the NO gaseous concentration signal was overestimated for temperatures higher than 400 °C, for the reasons explained above.
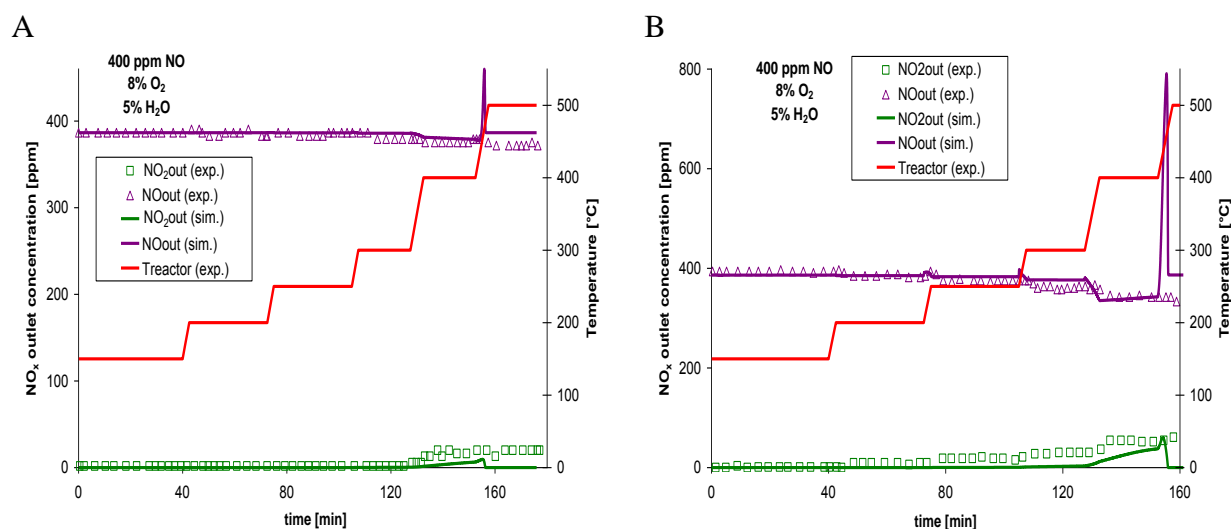
Figure 6.24 Simulation of a NO/O_2 STPD experiment over a A) H- and a B) Fe-BEA sample, reported by Shwan et al. [140]. Continuous injection of a mixture of a 400 ppm NO, 8% O_2 and 5% H_2O mixture diluted in Ar.

6.4 Conclusions

A throughout IR spectroscopy study over H- and Fe-BEA lab-synthesized samples was performed in order to develop a multi-site kinetic model for NO_x storage and NO oxidation over iron exchanged BEA catalysts. Analysis of NO adsorption/desorption experiments proved that only minor amounts of nitrogen monoxide were admitted on monomeric Fe^{2+}, cationic OH^+ and extra-framework Al-OH sites. On the other hand, nitrites, nitrates, as well as gaseous NO evolution were observed upon NO_2/O_2 adsorption, being related to nitrogen dioxide disproportionation. The latter reaction yielded nitrosium ions as well as nitrates on cationic OH^+ and Al and Fe respectively, which implied synergy of these sites located in neighbouring positions. Nitrites, as well as weakly adsorbed and/or physisorbed NO_2 were the predominant surface species at temperatures up to 100 °C, whereas NO_3 were found to be stable at higher ones. Three different types of nitrate adspecies were identified, including bidentate and bridging NO_3 coordinated on extra-framework and framework Al respectively, as well as bridging nitrates formed on oxidized monomeric and/or binuclear iron sites. Bidentate nitrates were thermally stable at temperatures as high as 250 °C, whereas at higher ones, bridging Al and Fe based NO_3 were

only evidenced. Finally, as far as NO oxidation is concerned, zeolitic aluminium and Fe^{3+}-O were found to be the respective active sites. Nitrogen monoxide conversion was initiated over oxidized iron positions already at 100 °C, whereas upon 150 °C contribution of acidic sites was also observed.

Compiling information obtained through IR spectroscopic measurements, a multi-site kinetic model for NO_x storage and NO oxidation was developed. Five surface sites were considered, including a site for weak adsorption and/or physisorption, as well as a Brønsted site for nitrites formation. Moreover, in order to precisely depict formation of Al and Fe based nitrate adpsecies, at bidentate and bridging cordinations three additional sites were considered, being assigned to pairs of $EFAl/OH^+$, FAl/OH^+ and isolated and/or binuclear Fe^{3+}/OH^+ respectively. NO_2 adsorption, desorption and disproportionation, O_2 storage and dissociation, as well as NO oxidation and NO_2 dissociation were modeled over the abovementioned sites, whereas NO adsorption/desorption were neglected. The model was then calibrated using kinetics deriving from a broad range of experimental and theoretical studies and finally validated through simulation of experimental results obtained over the lab-synthesized H- and Fe-BEA samples, as well as over bare and iron exchanged BEA catalysts, reported in the recent literature. Overall, computed results could reproduce the tendency of experimental curves, since formation of nitrite/nitrate adpsecies upon NO_2 storage and disproportionation, NO conversion due to oxidation and competitive NO_2/O_2 adsorption were predicted in a satisfactorily way. Discrepancies observed, were mainly attributed to the limited 0D reactor modeling and/or to the fact that NO storage and release were not taken into account. Moreover, even though gas phase results could be relatively correctly reproduced, dynamics of adspecies evolution could not be depicted by the presented model, which could imply that a more detailed kinetic model and an alternative calibration of kinetics should be adopted. Overall, the proposed multi-site kinetic modeling approach unraveled the contribution of acidic and metallic sites to the abovementioned reactions, over both lab-made and commercial Fe-BEA catalysts, highlighting the interest of the methodology used.

Chapter 7

NO$_x$–NH$_3$ SCR Reactivity on Fe-BEA: Insight into NH$_4$NO$_3$ Formation and Decomposition

7. NO_x–NH_3 SCR Reactivity on Fe-BEA: Insight into H_4NO_3 Formation and Decomposition

Abstract

Ammonium nitrate formation and decomposition over iron exchanged BEA zeolites, at low temperature SCR conditions are discussed in the present chapter. NO/NO_2-NH_3 transient reactivity experiments were performed over a Fe-BEA lab-synthesized sample. Employing in-situ IR spectroscopic measurements, interactions between NH_3 and NO_3, on acidic and metallic surface sites were evidenced. Subsequently, decomposition of ammonium nitrate formed during NO_x-NH_3 SCR, was investigated through TPD runs, so as to elucidate respective reaction pathways. In order to study NH_4NO_3 crystalline phase transitions during heating, thermal decomposition of crystalline, powder ammonium nitrate mixed with bare and iron exchanged BEA was examined by means of various experimental methods, including TGA, DSC and thermo-XRD. Overall comparison of experimental results enabled a deep insight into mechanistic aspects related to ammonium nitrate formation and decomposition with respect to Fe-BEA structural properties.

Résumé

Ce chapitre traite de la formation et de la décomposition du nitrate d'ammonium, sur les zéolithes BEA échangées au fer, sous conditions SCR à basse température. Des expériences de réactivité du système NO/NO_2-NH_3, en régime transitoire ont été réalisées sur un échantillon Fe-BEA, synthétisé au laboratoire. Les interactions entre NH_3 et NO_3 sur les sites acides et sur les sites métalliques ont été investiguées, en utilisant des mesures de spectroscopie IR. Ensuite, la décomposition du nitrate d'ammonium, formé au cours de la SCR, a été caractérisée au moyen de TPD, afin de mettre en évidence les voies réactionnelles correspondantes. En vue d'étudier la nucléation du NH_4NO_3 pendant le chauffage, la décomposition thermique du nitrate d'ammonium cristalline sous forme de poudre a été examinée en employant plusieurs méthodes expérimentales: analyse thermogravimétrique, calorimétrie différentielle à balayage et diffraction de rayons X in situ. La comparaison globale de résultats a permis une compréhension approfondie des aspects mécanistiques liés à la formation et la décomposition du nitrate d'ammonium, en relation avec des propriétés structurelles des catalyseurs Fe-BEA.

7.1 Introduction

Dedicated IR spectroscopy studies presented in the two previous chapters allowed to unravel mechanistic aspects related to interactions between NH_3 and NO_x and active sites of H- and Fe-BEA lab-synthesized samples. In chapter 5, ammonia adsorption/desorption was mainly evidenced over non acidic sites and/or sites for weak adsorption, at low temperatures, as well as on Brønsted acidic sites at higher ones. Additionally, in chapter 6, NO_2 adsorption and disproportionation, as well as NO storage and oxidation were identified on framework and extra-framework Al, as well as on Fe sites. In order to further capitalize knowledge gained from these studies, the present chapter focuses on NO/NO_2–NH_3 SCR reactivity on different catalytic sites of the lab-synthesized Fe-BEA catalyst. Low temperature SCR conditions are of particular concern. At this regime interactions between ammonia and nitrates may lead to the formation and accumulation of ammonium nitrate. There is a consensus in the literature that ammonium nitrate is a crucial intermediate of the SCR process over Fe-zeolites, since solid NH_4NO_3 built up can block active sites at temperatures as low as 170 °C, resulting in a temporary deactivation of the SCR catalyst (see also section 1.5.2). Hence, from a practical point of view, the ability of the SCR catalyst to efficiently convert NO_x at low temperature operating conditions (eg. during cold start) may be under question. On the other hand, at temperatures higher than 170 °C, ammonium nitrate decomposes, yielding undesired NO_x, as well as N_2O, which is considered as a greenhouse gas.

Grossale et al. have extensively investigated the reactivity between NH_3 and NO_x over commercial Fe-zeolite samples [90,91,92,108]. Based on their observations, respective reaction pathways were deduced, which involved formation of nitrate adspecies upon NO_2 adsorption and disproportionation and a subsequent built up of ammonium nitrate through interactions of NO_3 with surface NH_4^+. Reactivity between surface ammonia and nitrite adspecies was also suggested, leading to the relatively unstable ammonium nitrite, which can be easily decomposed to N_2 and H_2O. As far as Fe-exchanged BEA zeolites are concerned, the abovementioned observations have been experimentally validated over a commercial Fe-BEA catalyst by Grossale et al. [108]. Nevertheless, in all these studies the concluded reactions scheme was built on the basis of qualitative and quantitative analysis of experimental results in the gas phase, whereas surface characterization was not employed for cross-examination purposes. As a consequence of the latter, the nature of Fe-BEA zeolite surface sites, involved in the abovementioned phenomena remains under debate.

As far as ammonium nitrate decomposition is concerned, TPD experiments reported by Grossale et al. [92,108] are to be highlighted. Their results proved that at temperatures up to 170 °C NH_4NO_3 is decomposed, leading to a release of several gaseous species, namely N_2, N_2O and NO_2. According to an extended review of the corresponding literature (see section 1.5.2), thermal decomposition of pure crystalline ammonium nitrate is a quite complicated process, involving initial crystallographic phase transitions of the salt, before decomposition takes place. Nevertheless, despite the numerous reported studies covering this issue, very little information is available with respect to the effect of acidic and metallic sites on NH_4NO_3 crystallographic transformations and/or decomposition. Among them, Savara et al. [113] have investigated the catalytic reduction of ammonium nitrate by NO over different solid acids: Na-Y (Si/Al = 2.5), H-Y (Si/Al = 3.76 ± 0.45) and Ba-Na-Y (Si/Al = 2.62). In another

study, Li et al. [112] have performed thermal decomposition of a mixture of NH_4NO_3 and Ba-Na-Y (Si/Al = 2.62).

According to the abovementioned discussion, it seems that reaction pathways related to the reactivity between NH_3 and NO_x over Fe-zeolites are quite well documented. Particularly focusing on low temperatures, formation of NH_4NO_3 was suggested, which controls the SCR catalyst activity at this regime. Nevertheless, a correlation between these reactions and the respective acidic and metallic sites of the iron zeolite based catalyst is still not clearly reported. Moreover, concerning ammonium nitrate decomposition, even though the thermal behavior of pure crystalline NH_4NO_3 is extensively reported, very little information, associated with the respective effect of acidic and metallic sites exist in the recent literature. Therefore, in this chapter, a throughout study of NO_x–NH_3 SCR reactivity at low temperature regime is presented. Dedicated in-situ IR spectroscopic measurements, were initially performed over the Fe-BEA lab-synthesized sample, in order to depict interactions between NH_3 and NO_3, on acidic and metallic surface sites. Subsequently, thermal decomposition of NH_4NO_3 was investigated in the presence and the absence of the bare and Fe-exchanged BEA zeolites, employing a great variety of experimental methods.

7.2 Reactor experiments

Ammonium nitrate formation and decomposition were investigated by means of NO_x-NH_3 transient reactivity and TPD experiments over a Fe-BEA lab-synthesized sample. Details about the respective experimental set-up are presented in chapter 4. Mixtures of NO_2/O_2 and $NO/NO_2/O_2$ were preadsorbed on the catalytic surface at 100 °C, before exposing the sample to NH_3. In-situ IR spectroscopy was also utilized in order to examine interactions between nitrates and ammonia adspecies, formed on acidic and metallic sites.

7.2.1 NO₂-NH₃ transient reactivity and TPD experiments

Initially, a low temperature NO_2-NH_3 TRM experiment followed by temperature programmed desorption was performed. The Fe-BEA catalyst was exposed to a mixture of around 3500 ppm NO_2 and 2% O_2 diluted in He, at 100 °C, for 100 min. Then, the feed gas composition changed and 3500 ppm NH_3, 2% O_2 and He in balance were introduced into the IR cell, for 1 h at the same temperature. Finally, a TPD experiment was performed from 100 to 480 °C, under helium, at a heating rate of 10 °C/min. Gas phase results of the TRM run are illustrated in Figure 7.1. During NO_2/O_2 exposure (t = 0 – 100 min), around 1.78 mol/kg$_{Fe-BEA}$ nitrogen dioxide were adsorbed on the Fe-BEA sample. At 2.5 min, the catalyst became saturated and gaseous NO evolution was observed. The amount of generated nitrogen monoxide was estimated to 0.61 mol/kg$_{Fe-BEA}$, which corresponded to around one third of the respective amount of consumed NO_2. Therefore, in analogy with experimental results of NO_2/O_2 adsorption over H- and Fe-BEA, presented in chapter 6, it was concluded that NO_2 disproportionation took place during nitrogen dioxide admission, according to the stoichiometry of reaction 7.1. At this

stage, it has to be pointed out that in NO_2/O_2 experiments performed at 30 °C over the same Fe-BEA sample (chapter 6) around 1.44 mol/kg$_{Fe-BEA}$ NO_2 were consumed and 0.64 mol/kg$_{Fe-BEA}$ gaseous NO were released, which tends to indicate that NO_2 disproportionation becomes significantly active at temperatures higher than ambient.

$$3NO_2 + \frac{1}{2}O_2 = 2NO_3 + NO \qquad \qquad \textbf{reac. 7.1}$$
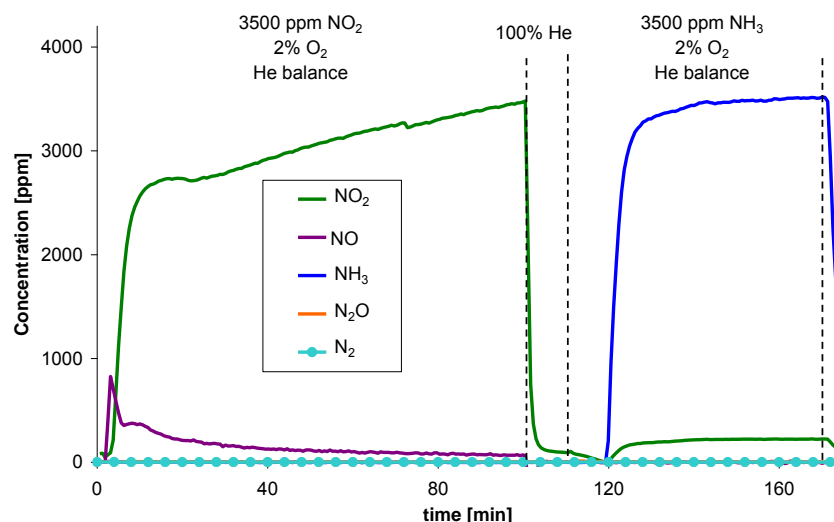
Figure 7.1 NO_2/O_2-NH_3 transient reactivity and temperature programmed desorption experiments: Preadsorption of a mixture of 3500 ppm NO_2 and 2% O_2 diluted in He for 100 min at 100 °C, followed by introduction of 3500 ppm NH_3, 2% O_2 and He in balance for 1 h at the same temperature.
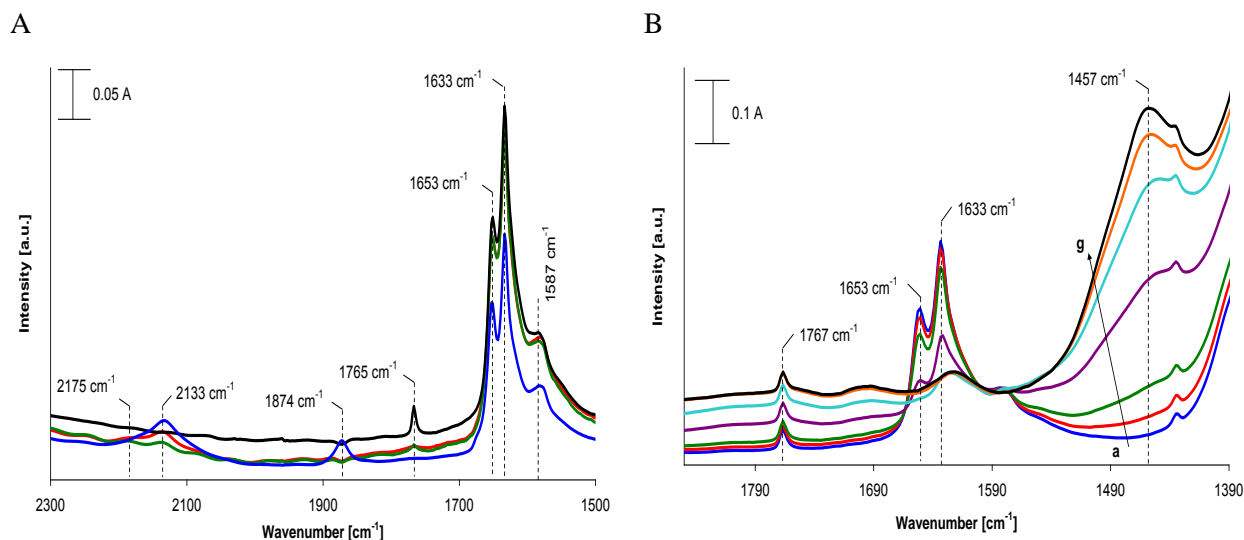
Figure 7.2 Difference IR spectra recorded during A) NO_2/O_2 (blue, red, green and black lines correspond to spectra recorded at 2.5, 10, 20 and 100 min respectively) and B) NH_3/O_2 adsorption at a) 110, b)112, c) 113, d) 114, e) 116, f) 119 and 170 min. The reference spectrum subtracted, was recorded at the beginning of the TRM experiment (t=0).

Formation of NO_x surface species was evidenced through difference IR spectra recorded during the same period (Figure 7.2 A). According to detailed IR spectroscopic analysis of NO_x adsorption on Fe-BEA, presented in chapter 6, IR maxima centred at 2175 and 2133 cm^{-1} were attributed to NO^+ bonded on lattice oxygen (upon interaction of NO with cationic OH^+), whereas IR bands lying at 1653, 1633 and 1587 cm^{-1} were assigned to nitrates coordinated to framework Al, Fe^{3+} monomeric and/or binuclear iron species and extra-framework aluminium respectively. Moreover, mono-nitrosyl (Fe-$NO)^{2+}$ and trans-$(NO)_2$ adspecies were evidenced through the 1874 and 1767 cm^{-1} bands respectively. As discussed in chapter 6, the latter coexist in equilibrium with NO at low temperatures. Interestingly, neither nitrites nor N_2O_4 were observed in the recorded IR spectra. As showed earlier (chapter 6) nitrites and weakly adsorbed NO_2 (corresponding to N_2O_4) are thermally stable at temperatures as low as 100 °C, which somehow explains why these species were not evidenced during the presented transient reactivity experiment.

Focusing on the subsequent NH_3 injection phase (t = 110 – 170 min), a 1.89 mol/kg_{Fe-BEA} overall ammonia uptake was estimated. In parallel, 0.71 mol/kg_{Fe-BEA} NO_2 were released in the gas phase, which may suggest the occurrence of competitive adsorption on the same sites and/or surface reaction between a fraction of NO_x adspecies and ammonia. According to the stoichiometry of reaction 7.1, around 1.12 mol/kg_{Fe-BEA} NO_3 were formed on the catalyst upon nitrogen dioxide admission. Therefore, the NO_2 removal during NH_3 introduction was assigned to partial decomposition of formed nitrates (reaction 7.2), whereas ca 0.41 mol/$kg_{zeolite}$ NO_3 remained stored on the catalytic surface.

$$NO_3^- \rightleftharpoons NO_2 + O^-$$ **reac. 7.2**

Interestingly, the amount of adsorbed NH_3 during this experiment was quite higher compared to respective NH_3 storage capacities estimated during ammonia adsorption at 30 and 150 °C over the same Fe-BEA sample (1.3 and 0.66 mol/kg_{Fe-BEA} NH_3 respectively - chapter 5). Same observations have been reported by Grossale et al. during a similar NO_2-NH_3 TRM run over a commercial Fe-BEA catalyst [108]. Therefore, it appears that in the presence of preadsorbed nitrates consumption of gaseous NH_3 occurred due to additional reaction mechanisms, besides ammonia adsorption.

The latter was validated through careful examination of difference IR spectra recorded during the NH_3/O_2 exposure period (Figure 7.2 B). Directly after ammonia introduction, intensities of the 1653 and 1633 cm^{-1} bands attenuated and after 4 min of exposure, both IR maxima vanished. Then, a broad band appeared at 1457 cm^{-1}, which according to analysis presented in chapter 5 was assigned to NH_4^+ bonded to Brønsted acidic sites in bidentate and tridentate coordinations. Therefore, it could be concluded that ammonia initially reacted with NO_3 adspecies, before being stored on cationic OH^+. Moreover, the amount of trans-$(NO)_2$ adspecies increased (1765 cm^{-1} band), prolonging the NH_3 introduction, which could indicate the existence of gaseous NO, possibly in equilibrium with desorbed NO_2. Finally, bidentate nitrates, coordinated to extra-framework aluminium (1581 cm^{-1} band) were completely removed during the feed gas composition switch, which took place within 100 – 110 min (spectra not shown).
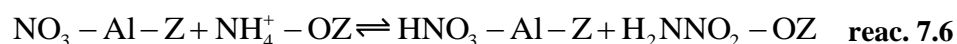
Regarding nitrates-ammonia reactivity, formation of ammonium nitrate is suggested. Ex-situ IR spectra of powder NH_4NO_3 mixed with bare and Fe-BEA, recorded in ambient conditions are shown in Appendix C / Figure C.1. IR bands centred at 3140 and 1400 cm^{-1} were related to crystalline

ammonium nitrate. Nevertheless, in the recorded IR spectra, illustrated in Figure 7.2 B, it was quite difficult to distinguish the 1400 cm^{-1} component, since the 1457 cm^{-1} band, related to NH$_4$$^+$, was quite broad, perturbing spectral features located in the same wavenumber range. Furthermore, considering the 3140 cm^{-1} band (Appendix C, Figure C.1 B), a broad band was identified within 2900 – 3100 cm^{-1}, which however could not be interpreted due to Evans windows, as discussed in chapter 5.

Grossale et al. [90] and Ciardelli et al. [265] have suggested NH$_4$NO$_3$ formation through interactions between HNO$_3$ and NH$_3$, according to reactions 7.3 and 7.4.

$$3NO_2 + H_2O = 2HNO_3 + NO \qquad \textbf{reac. 7.3}$$

$$HNO_3 + NH_3 = NH_4NO_3 \qquad \textbf{reac. 7.4}$$

Ammonium nitrate formation through reaction 7.4 is also suggested for the studied experimental case. Nevertheless, since the presented TRM run was performed in the absence of water, nitrous acid formation could not be deduced through recorded IR spectra. As explained in chapter 6, NO$_2$ disproportionation towards NO$_3$ and NO$^+$ occurs over Al and Fe sites, located in close vicinity with Brønsted acidic ones. Thus, it is speculated that NH$_4$$^+$ could be formed on the latter sites (reaction 7.5), followed by a subsequent proton transfer from the ammonium ions to nitrates, through the catalytic surface, yielding HNO$_3$ (reaction 7.6).

$$NH_3 + H^+ - OZ \rightleftharpoons NH_4^+ - OZ \qquad \textbf{reac. 7.5}$$

$$NO_3 - Al - Z + NH_4^+ - OZ \rightleftharpoons HNO_3 - Al - Z + H_2NNO_2 - OZ \quad \textbf{reac. 7.6}$$

HNO$_3$ formation through NH$_3$-NO$_2$ interactions has been earlier proved through density functional theory computations [266]. Briefly, the proposed mechanism includes initial ammonia adsorption on Brønsted sites, yielding NH$_4$$^+$, followed by N$_2O_4$ coadsorption. Then, a proton transfer occurs between the ammonium anion and the NO$_2$ dimmer, leading to the formation of nitramide (NH$_2$NO$_2$) and HNO$_3$.

Compiling gas and solid phase experimental results, a global generic reaction scheme could be proposed for ammonium nitrate formation over Fe-BEA, during low temperature NO$_2$-NH$_3$ SCR conditions (Figure 7.3). Admission of NO$_2$/O$_2$ was followed by nitrogen dioxide disproportionation, yielding Al and Fe^{3+} based nitrates. Subsequent introduction of NH$_3$ led to the formation of NH$_4$$^+$ on OH$^+$ Brønsted acidic sites. A proton transfer from a fraction of ammonium ions towards NO$_3$ could then lead to HNO$_3$ formation. The latter, finally reacted with ammonia forming solid ammonium nitrate, which deposited on the catalytic surface. The nature of surface sites being occupied by NH$_4$NO$_3$ is quite difficult to be determined based on the abovementioned experimental analysis. According to the experimental protocol followed in this work, NO$_3$ adspecies were pre-adsorbed on framework Al and Fe^{3+} positions, before being converted to nitrous acid and ammonium nitrate via interactions with NH$_3$. Thus, it is suggested that NH$_4$NO$_3$ deposited on aluminium and iron sites. This conclusion could also be substantiated due to the fact that surface NH$_3$ was merely evidenced on Brønsted acidic sites but not on Al and/or Fe Lewis type ones. Nevertheless, migration of NH$_4$NO$_3$ on cationic OH$^+$ positions can not be ruled out, particularly since proton transfer between NH$_4$$^+$ and NO$_3$ was speculated. Investigation of such aspects would require additional studies (eg. DFT computations and/or NH$_3$-NO$_x$ TRM runs), which however goes beyond the scope of the presented work.

Figure 7.3 Generic scheme of NH_4NO_3 formation on Fe-BEA under low temperature NO_2-NH_3 SCR.

Figure 7.4 TPD experiment following NO_2-NH_3 reactivity experiment over Fe-BEA.

Focusing on the TPD experiment (Figure 7.4) several gaseous species were released when heating up the catalyst. Nitrogen dioxide, nitrous oxide and nitrogen desorbed upon 170 °C, whereas the corresponding concentration signals were maximized at 237, 245 and 282 °C respectively. Furthermore, NH_3-TPD peaks centred at around 175 and 370 °C were identified and were assigned to ammonia stored on Brønsted sites, characterized by different acidity strength (see IR spectra analysis in chapter 5). Similar results have been reported elsewhere [108]. Crystalline ammonium nitrate melting point lies at 170 °C [111]. Thus, it was concluded that evolution of N_2, NO_2 and N_2O upon this temperature was related to NH_4NO_3 decomposition. Possible reaction pathways of ammonium nitrate decomposition are discussed below.

It is well documented that around 170 °C, NH_4NO_3 decomposition is initiated by a proton transfer, yielding ammonia and nitric acid (reaction 7.7) [111,267]. On the basis of IR spectroscopic analysis of NH_3 adsorption over the studied Fe-BEA catalyst presented in chapter 5, gaseous ammonia can be still readsorbed on cationic OH^+, as well as Fe sites within this temperature range (reactions 7.8 and 7.9).

$$NH_4NO_{3(s)} \rightleftharpoons NH_{3(g)} + HNO_{3(g)} \qquad\qquad \textbf{reac. 7.7}$$

$$NH_{3(g)} + H^+ - OZ \rightleftharpoons NH_4^+ - OZ \qquad\qquad \textbf{reac. 7.8}$$

$$NH_{3(g)} + Fe^{3+} - OZ \rightleftharpoons [NH_3 - Fe]^{3+} \qquad\qquad \textbf{reac. 7.9}$$

On the other hand, HNO_3 may further dissociate towards gaseous NO_2, H_2O and O_2 (reaction 7.10) [111]. Similarly to NH_3, nitrogen dioxide can be rebound to Al and Fe positions and may further disproportionate towards nitrates (reaction 7.11).

$$HNO_{3(g)} \rightleftharpoons NO_{2(g)} + \tfrac{1}{2}H_2O_{(g)} + \tfrac{1}{4}O_{2(g)} \qquad\qquad \textbf{reac. 7.10}$$

$$2NO_{2(g)} + 2S_{NO_2} \rightleftharpoons 2NO_2 - S_{NO_2} \rightleftharpoons NO_3 - S_{NO_2} + NO_{(g)} + S_{NO_2} \quad ^1 \qquad \textbf{reac. 7.11}$$

NH_3 and NO_x adspecies can finally interact, forming additional intermediate surface species. Savara et al. [113] have proposed formation of ammonium nitrite (NH_4NO_2) (reaction 7.12), which is a thermally unstable compound, able to decompose at around 100 °C, yielding N_2 and H_2O. Moreover, Grossale et al. have suggested decomposition of ammonium nitrate towards nitrimide, which can further decompose, releasing N_2O and water (reaction 7.13) [108]. Finally, according to the scheme illustrated in Figure 7.3, interactions between NO_3 and NH_4^+ may lead to the formation of HNO_3 species, which could further interact with ammonia bonded to iron and/or OH^+ sites, forming additional NH_xNO_y precursors.

$$NH_4^+ - OZ + NO_2 - S_{NO_2} \rightleftharpoons NH_4NO_{2(s)} \rightleftharpoons N_2 + 2H_2O \qquad\qquad \textbf{reac. 7.12}$$

$$NH_4^+ + NO_3 \rightleftharpoons NH_2NO_{2(s)} + H_2O \rightleftharpoons N_2O + H_2O \qquad\qquad \textbf{reac. 7.13}$$

The proposed reactions network for ammonium nitrate decomposition on different surface sites is summarized in Figure 7.5. Based on experimental results interpretation, it could be suggested that Fe-BEA Brønsted acidity plays a crucial role during ammonium nitrate decomposition, providing storage capacity for ammonia readsorption. Thus, the reducing agent remains further available for interactions with NO_2 and NO_3, bonded on Al and Fe Lewis type positions. Savara et al. have also highlighted the promoting effect of cationic OH^+ on NH_4NO_3 catalytic reduction by NO, over solid acids including Na-Y (Si/Al = 2.5), H-Y (Si/Al = 3.76 ± 0.45) and Ba-Na-Y (Si/Al = 2.62) [113]. At this stage, it has to be pointed out that the attempted analysis aims to a simplified interpretation of experimental results in order to elucidate the effect of Fe-BEA surface sites on NH_4NO_3 decomposition. The actual decomposition mechanism may include additional reaction steps and/or a greater number of intermediate species, investigation of which however goes beyond the scope of the presented work.

---

[1] S_{NO2} stands for an Al or a Fe^{3+} atom located in close vicinity with a cationic OH^+, according to the analysis presented in chapter 6.

Figure 7.5 Possible reaction pathways of NH$_4$NO$_3$ decomposition on Fe-BEA.

Quantifying the amounts of desorbed NO$_2$, N$_2$O and N$_2$ within the 170 -350 °C range, a total amount of ca 0.4 mol/kg$_{Fe-BEA}$ gaseous species was estimated (0.23 mol/kg$_{Fe-BEA}$ N$_2$, 0.07 mol/kg$_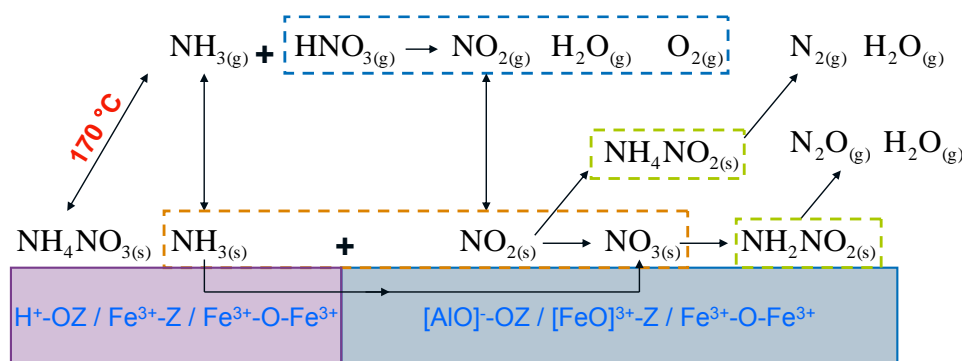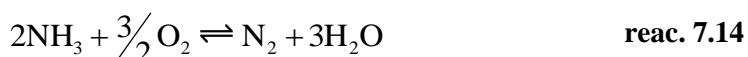{Fe-BEA}$ N$_2$O and 0.1 mol/kg$_{Fe-BEA}$ NO$_2$). Hence, assuming that these products come from a complete decomposition of NH$_4$NO$_3$, it could be suggested that the same quantity of ammonium nitrate was accumulated on the catalytic surface during the NO$_2$/NH$_3$ TRM experiment. This value seems to be in good agreement with the respective amount of 0.41 mol/kg$_{Fe-BEA}$ nitrates, which were consumed upon NH$_3$ admission. Nevertheless, it has to be pointed out that the presented calculations constitute just an approximate quantification of gas and solid phase species, in order to somehow validate the proposed reaction pathways of NH$_4$NO$_3$ formation and decomposition.

The total amount of desorbed ammonia was estimated equal to 0.95 mol/kg$_{Fe-BEA}$. Since a 0.4 mol/kg$_{Fe-BEA}$ NH$_4$NO$_3$ built up was supposed to take place during the TRM experiment, an equimolar amount of ammonia was required, according to the stoichiometry of reaction 7.4. This implies that around 0.55 mol/kg$_{Fe-BEA}$ NH$_3$ were consumed due to another mechanism related neither to adsorption nor to NH$_4$NO$_3$ formation.

Taking into account that the TRM experiment was performed in the presence of oxygen, NH$_3$ oxidation was speculated. To verify this hypothesis, a NH$_3$/O$_2$ STPD experiment was performed over the Fe-BEA sample. Experimental conditions and respective results are presented in Appendix D. As shown in Figure D.2 and Figure D.3, ammonia oxidation became evident at around 250 °C, yielding N$_2$, and NO, mainly within the temperature range of 350 – 500 °C. Negligible quantities of N$_2$O (13 ppm maximum concentration) were also evidenced at around 350 °C. Nitrogen monoxide and nitrogen were evolved during the TPD experiment presented in Figure 7.4. Integrating the respective N$_2$ gaseous concentrations signal, within 350 – 500 °C, an amount of 0.25 mol/kg$_{Fe-BEA}$ was estimated. According to Akah et al. [103], the selective catalytic oxidation of ammonia towards N$_2$ and H$_2$O follows the stoichiometry of reaction 7.14, supposing consumption of 2 moles NH$_3$ for generating 1 mol nitrogen.

$$2NH_3 + \frac{3}{2}O_2 \rightleftharpoons N_2 + 3H_2O \qquad\qquad \textbf{reac. 7.14}$$

Considering the abovementioned analysis, it appears that, 0.5 mol/kg$_{Fe-BEA}$ NH$_3$ were consumed during ammonia catalytic oxidation. Hence, the hypothesis of NH$_3$ consumption due to selective catalytic oxidation, at temperatures higher than 300 °C seems to be somehow supported.

7.2.2 NO₂/NO-NH₃ transient reactivity and TPD experiments

To study the effect of nitrogen oxides inlet composition on low temperature NO_x-NH_3 reactivity, additional TRM – TPD experiments were performed. A mixture of 3500 ppm NO, 1000 ppm NO_2, 2% O_2 and helium in balance were preadsorbed on the Fe-BEA sample at 100 °C, for 100 min. Then, NO_x were removed from the feed and the catalyst was exposed to 4500 ppm NH_3 and 2% O_2, diluted in He, at the same temperature. Finally, a TPD experiment was performed from 100 to 480 °C at a heating rate of 10 °C/min. Results of the TRM run are illustrated in Figure 7.6.

Gaseous NO and NO_2 were observed immediately after NO_x introduction. A small NO peak was identified at around 4.5 min (3644 ppm maximum concentration), whereas an initial rapid NO_2 release was observed at around 2.5 min, before the respective concentration signal starting increasing until stabilization. According to the analysis presented in the previous section, upon nitrogen dioxide adsorption and surface saturation disproportionation takes place leading to nitrate adspecies and gaseous NO. Nevertheless, in this test case NO_2 evolution was also evidenced during the same phase, which tends to indicate parallel occurrence of additional reactions.

Figure 7.6 NO/NO₂-NH₃ TRM and B) TPD experiments over the studied Fe-BEA catalyst: Preadsorption of a mixture of 3500 ppm NO, 1000 ppm NO_2 and 2% O_2 diluted in He for 100 min at 100 °C, followed by introduction of 4500 ppm NH_3, 2% O_2 and He in balance for 1 h at the same temperature.

To get deeper insight into the abovementioned observations, IR spectroscopy was employed during the $NO/NO_2/O_2$ storage experiment. NO adsorption on Brønsted acidic (NO^+ at 2133 cm^{-1}) and Fe^{2+} metallic sites (($Fe-NO)^{2+}$ at 1873 cm^{-1}) as well as NO_3 formation on FAl, EFAl and iron sites (1653, 1581 and 1633 cm^{-1} bands respectively) were evidenced during the first 10 min (Figure 7.7 A - for IR spectra interpretation see chapter 6). ($Fe-NO)^{2+}$ nitroslys vanished completely after 8 min of adsorption, whereas at the same time nitrates surface concentration was maximized. Interestingly, increasing exposure duration above 20 min, intensities of IR maxima corresponding to NO_3 attenuated and trans-$(NO)_2$ was evidenced through weak band at 1766 cm^{-1}. It has been experimentally proved

that NO_3 can be reduced by NO, yielding nitrites at temperatures as low as 50 °C [92,108]. The latter (reaction 7.15) was also speculated to occur during the first 10 min of the presented $NO/NO_2/O_2$ adsorption experiment. However, a further justification of this mechanism through IR spectroscopy was not feasible, since NO_2^- was not evidenced. As explained in section 7.1.1, the TRM experiment was performed at 100 °C, a temperature at which these species decompose rapidly to gaseous NO_2.

$$NO_3 + NO \rightleftharpoons 2NO_2 \qquad\qquad \textbf{reac. 7.15}$$

Based on this analysis, the direct evolution of NO_2 discussed above could be explained through the competition of reactions 7.1 and 7.15. Nevertheless, as showed in chapter 6, minor NO oxidation was evidenced over the studied Fe-BEA sample at 100 °C. Thus, a contribution of the latter reaction to NO_2 production could not be ruled out.

Figure 7.7 Difference IR spectra recorded during $NO_2/NO/O_2$ adsorption at a) 1, b) 2, c) 3, d) 4, e) 5, f) 8 g) 10, h) 20, i) 40, j) 60 and k) 100 min. The reference spectrum subtracted, was recorded at the beginning of the TRM experiment (t=0).

Figure 7.8 Difference IR spectra recorded during NH_3/O_2 adsorption at a) 110, b)114, c) 117 and d) 170 min. The reference spectrum subtracted, was recorded at the beginning of the TRM experiment (t=0).

Subsequently, when NO_x introduction was terminated and ammonia was injected, a 1.76 mol/kg$_{Fe-BEA}$ NH_3 uptake was estimated, whereas minor amounts of nitrog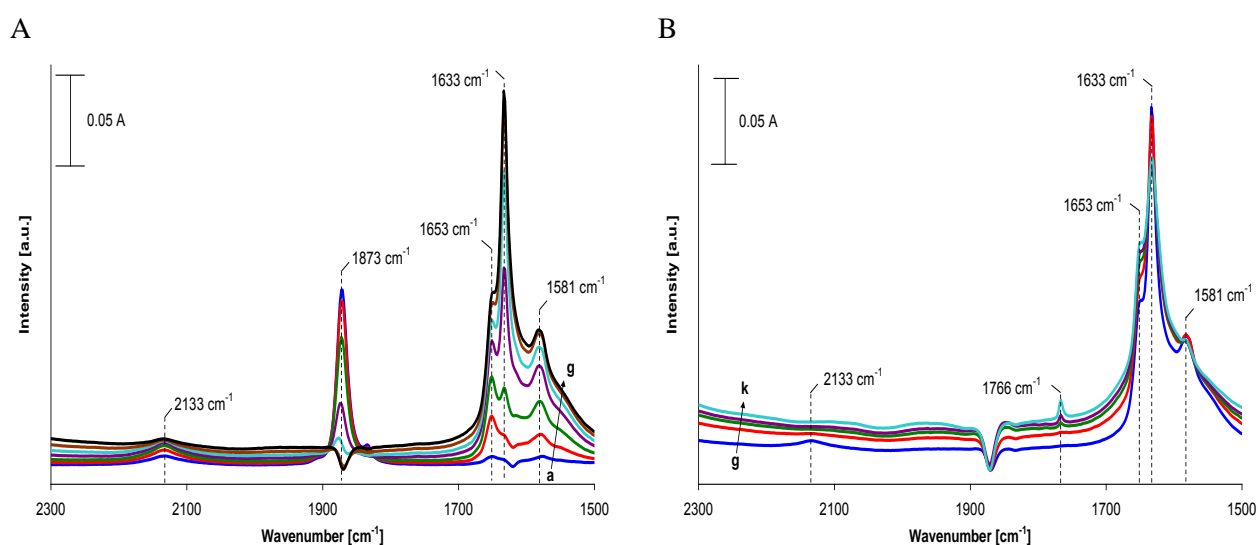en monoxide (0.06 mol/kg$_{Fe-BEA}$) were evolved. The amount of ammonia consumed during this experiment was around 0.13 mol/kg$_{Fe-BEA}$ lower compared to the respective one admitted during the experiment where only NO_2 was preadsorbed (Figure 7.1). According to IR spectra recorded during the NH_3 injection phase (Figure 7.8), 4 min after NH_3 introduction, nitrates were consumed, whereas increasing exposure duration a broad IR band centred at 1462 cm^{-1} arose, being assigned to NH_4^+ (chapter 5). Therefore, as discussed in section 7.2.1, during NH_3 injection a fraction of ammonia interacted with nitrates to yield NH_4NO_3, whereas the residual amount was stored on cationic OH^+. Taking into consideration that nitrates formed during NO_x admission were partially reduced by NO, a lower amount of NO_3 was available for ammonium nitrate build up, through interactions with ammonia. The latter, may somehow explain why a lower amount of ammonia was consumed during the presented TRM run.

This picture was further validated through quantification of TPD results, illustrated in Figure 7.9. NH_3, NO_2, N_2 and N_2O as well as N_2 and NO were observed within 100 – 310 °C and 350 – 480 °C respectively. Around 1.05 mol/kg$_{Fe-BEA}$ ammonia were desorbed, deriving from NH_3 previously adsorbed on Brønsted acidic sites. Moreover, 0.28 mol/kg$_{Fe-BEA}$ N_2 were released at temperatures higher than 350 °C, which as explained in section 7.2.1 were related to oxidation of 0.56 mol/kg$_{Fe-BEA}$ NH_3 (stoichiometry of reaction 7.14). Therefore, around 0.15 mol/kg$_{Fe-BEA}$ ammonia interacted with surface NO_3 towards ammonium nitrate. Indeed, ca 0.14 mol/kg$_{Fe-BEA}$ N_2, 0.01 mol/kg$_{Fe-BEA}$ N_2O and 0.03 mol/kg$_{Fe-BEA}$ NO_2, were desorbed up to 350 °C, somehow suggesting that equal amounts of NH_4NO_3 were formed and decomposed during the TRM-TPD experiment. At this stage, it has to be mentioned that quantification of nitrates formed during NO_2/NO adsorption was purposely avoided, since competitive NO_2 adsorption and NO_3 reduction as well as NO oxidation were simultaneously occurring during the first 100 min of the TRM experiment.

Interestingly, similar amounts of NH_3 was desorbed and oxidized during the TPD experiment illustrated in Figure 7.4, which seems to indicate that the presence of NO during the TRM run did not inhibit ammonia adsorption. The latter is in good agreement with experimental results shown in chapter 6, which proved that nitrogen monoxide adsorption on acidic and/or metallic sites of the Fe-BEA was negligible. On the other hand, the amount of formed NH_4NO_3 was ca 0.25 mol/kg$_{Fe-BEA}$ lower compared to the respective one estimated in section 7.2.1, which seems to support the abovementioned assumption, concerning catalytic reduction of nitrates by NO.

Figure 7.9 TPD experiment following NO_2/NO-NH_3 reactivity experiment: dT/dt = 10 °C/min, 100% He.

7.3 Study of NH_4NO_3 crystallographic phase changes during decomposition

NO_x-NH_3 and TPD experiments presented in section 7.2 enabled an investigation of mechanistic aspects related to NH_4NO_3 formation and decomposition. Infrared spectroscopic data provided useful information concerning the nature of surface adspecies, which may be involved in ammonium nitrate formation, whereas quantitative analysis of the TPD gaseous concentration signals enabled to unravel possible reaction pathways related to NH_4NO_3 decomposition. On the other hand, these observations do not provide structural information related to the ammonium nitrate crystallographic changes during decomposition. Therefore, thermo-gravimetric analysis, differential scanning calorimetry and in-situ X-ray diffraction measurements were performed in order to unravel the effect of H- and Fe-BEA surface sites on NH_4NO_3 crystalographic phase changes during decomposition.

7.3.1 TGA/DSC/MS experiments

Crystallographic transformations of NH_4NO_3 during decomposition in the presence of bare and iron exchanged BEA were studied first, employing thermogravimetric analysis and differential scanning

calorimetry. Two testing samples were prepared by mechanically mixing 3 mg of crystalline ammonium nitrate with around 12 mg of the lab-synthesized H-BEA and Fe-BEA (loose contact - see experimental details in section 4.4). At this stage it has to be noted that ammonium nitrate mechanically mixed with the H- and Fe-BEA samples may behave differently compared to the NH_4NO_3 formed under SCR conditions, which was discussed in section 7.2. A greater extent of interactions might be expected between the salt and catalyst, whereas the actual crystalographic structure of NH_4NO_3 may be different between the two configurations. Therefore, results discussed in this section should be compared with those presented in section 7.2 with particular attention. Decomposition of pure NH_4NO_3 was studied for comparison reasons, through an additional mixture of 3 mg ammonium nitrate and 12 mg SiO_2 (loose contact). The three samples were then heated up from 25 to 350 °C, at a rate of 5 °C/min, under helium. The SiO_2, H- and Fe-BEA samples were hydrated before analyzing, since they were exposed to ambient before being charged on the experimental apparatus (no pre-treatment was performed prior to TGA/DSC analysis). Water release during heating could affect the TGA-DSC signals. Thus, preliminary thermo-gravimetric analysis and differential scanning calorimetry of 15 mg SiO_2 and H-BEA were performed and these reference curves were subtracted from the ones obtained through measurements over the abovementioned ammonium nitrate mixtures.

Mass loss, and heat flow profiles obtained through TGA and DSC respectively are presented in Figure 7.10. Interestingly, similar endothermic peaks, related to NH_4NO_3 phase changes were observed over the three studied mixtures. The first two peaks centred at around 50 and 123 °C were attributed to the following phase transformations: orthorhombic phase IV → tetragonal phase II and tetragonal phase II → cubic phase I respectively [114,268,269]. Moreover, the endothermic peak lying at ca 166 °C corresponded to the melting point of ammonium nitrate, after which the decomposition starts [111]. According to mass loss curves, upon this temperature NH_4NO_3 decomposition was initiated and at around 206 – 213 °C the respective rate was maximized. The same results were observed over the three tested samples. According to similar experimental studies reported by Gunawan et al,. NH_4NO_3 maximum decomposition rate lied at ca 290 °C [114]. Experimental deviations could be assigned to the experimental protocols applied and namely to the selected NH_4NO_3 mass and heating rate [270,271].

Figure 7.10 Mass loss (TGA) and heat flow (DSC) curves of NH_4NO_3 decomposition: Mixtures of 3 mg NH_4NO_3 and around 12 mg A) SiO_2, B) H-BEA and C) Fe-BEA.

Gaseous species released during NH$_4$NO$_3$ decomposition were monitored by means of mass spectrometry (Figure 7.11). Interestingly, N$_2$, NO$_2$ and N$_2$O were observed within the 215 – 222 °C range, which is in quite good agreement with TPD signals presented in Figure 7.4 and Figure 7.9. Nevertheless, NO was also evolved (Figure 7.11 D), which was not evidenced in experiments presenteded in section 7.2. This could related to several reasons and namely to the fact that: i) the structure of NH$_4$NO$_3$ formed under in-situ conditions (experiments presented in section7.2) may be different compared to the ammonium nitrate mechanically mixed with H- and Fe-BEA powders and/or ii) the interactions between NH$_4$NO$_3$ and the catalyst (H- and Fe-BEA) at temperatures higher than 170 °C, might be stronger for the case ammonium nitrate built up under NO$_x$/NH$_3$ SCR reactions (eg. NO oxidation to NO$_2$ may be favorised).

Figure 7.11 Gaseous species released during thermal decomposition of NH$_4$NO$_3$: Black, blue and red lines correspond to mixtures of 3 mg NH$_4$NO$_3$ with around 12 mg SiO$_2$, H-BEA and Fe-BEA respectively. MS signals were normalized with respect to maximum peak intensities. Baseline correction was also included.

Experimental conditions may also play a role. Chaturvedi et al. [111] proposed nitrogen monoxide production during NH_4NO_3 heating from 200 to 230 °C, via the global reaction 7.16.

$$8NH_4NO_3 \rightarrow 5N_2 + 4NO + 2NO_2 + 16H_2O \qquad \textbf{reac. 7.16}$$
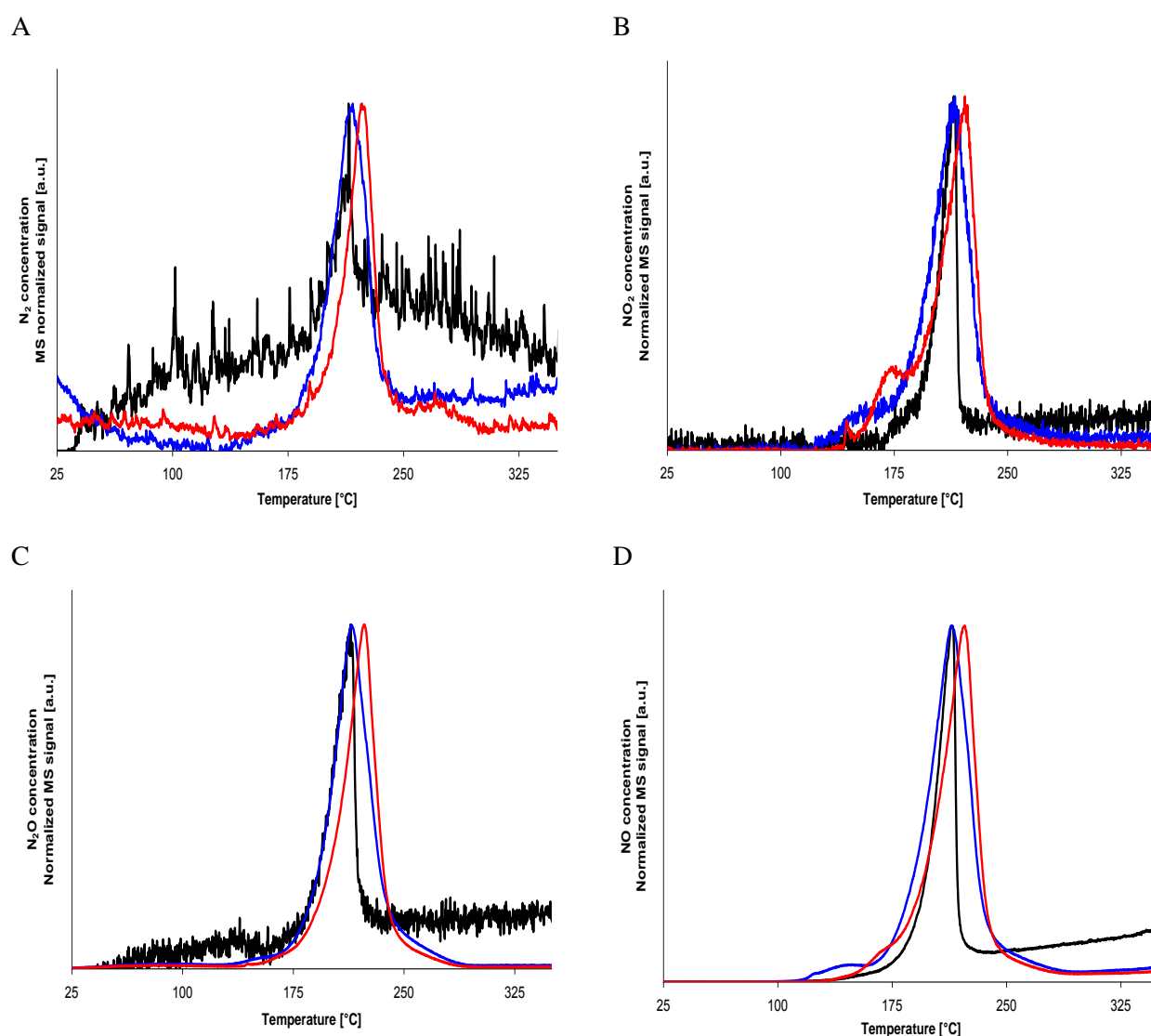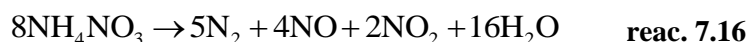
For the presented experimental cases the total mass flow rate was 100 ml/min, which is 10 times higher compared to that applied in the experiments shown in section 7.2. Thus, the heat transfer and namely convection may affect NH_4NO_3 decomposition. Moreover, it has to be mentioned that gaseous MS signals were not quantitatively calibrated and thus, the maximum NO concentrations may be negligible.

Overall, presented experimental results proved that NH_4NO_3 decomposition occurred through two successive phase transitions, before decomposition was initiated. Moreover, ammonium nitrate consumption was merely attributed to decomposition, whereas during crystallographic phase transformations no mass loss was observed. This behavior was evidenced over the three tested samples, which tends to suggest that acidic and/or metallic sites of H- and Fe-BEA have no effect on NH_4NO_3 crystalographic phase transitions and decomposition.

7.3.2 Thermo-XRD experiments

In order to further evaluate crystallographic transformation paths of NH_4NO_3 during decomposition thermo X-ray diffraction was utilized. In analogy to TGA-DSC-MS experiments, three testing samples were prepared including pure crystalline powder NH_4NO_3 as well as ammonium nitrate mechanically mixed with H-BEA and Fe-BEA (see experimental details in section 4.4.2). X-ray diffraction was then performed during heating up the samples from ambient temperature (ca 20 °C) to 200 °C. The temperature was increased stepwisely at intervals of 10 °C, applying a heating rate of 5 °C.

Diffraction patterns recorded during decomposition of pure NH_4NO_3 are shown in Figure 7.12. Heating the sample from 20 to 50 °C, the crystallographic transition IV → II was evidenced, whereas at 110 °C, orthorhombic ammonium nitrate was transformed to cubic one (phase I). Finally, reaching 150 °C no diffraction peaks were observed, indicating NH_4NO_3 decomposition. Similar XRD patterns are reported elsewhere [272]. The abovementioned results are in very good agreement with the ones obtained through differential scannic calorimetry, which enabled an initial validation of crystalographic transformations of pure NH_4NO_3 during decomposition.
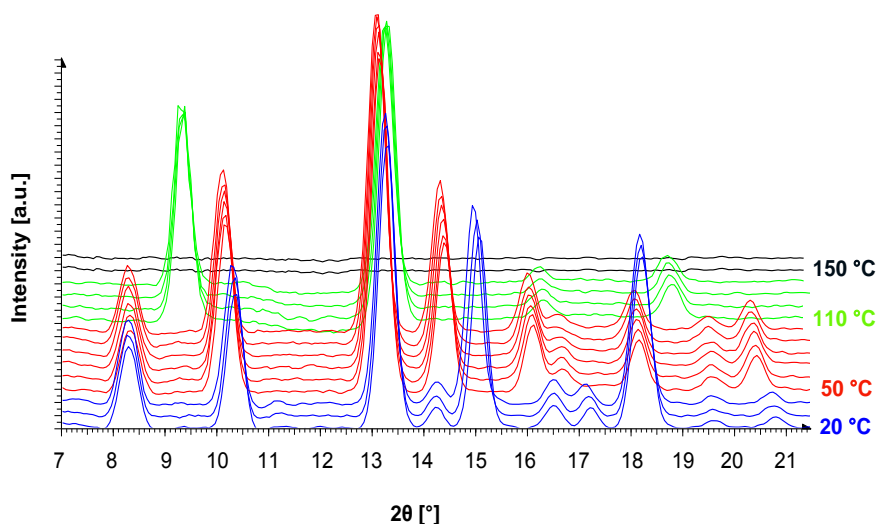
Figure 7.12 X-ray patterns recorded during decomposition of pure NH_4NO_3, within 20 - 200 °C, at intervals of 10 °C, applying a temperature ramp of 5 °C/min: Blue, red and green coloured curves correspond to NH_4NO_3 IV, II, I crystallographic phases respectively.

Respective XRD-patterns recorded during the heating of the NH_4NO_3-H-BEA mixture are illustrated in Figure 7.13. The same phase transitions of ammonium nitrate were observed at 50 and 110 °C, during thermal decomposition in the presence of H-BEA, whereas at 150 °C, only diffraction peaks, related to the zeolite were evidenced. The latter, in line with results obtained though TGA-DSC experiments over the NH_4NO_3-HBEA mixture, tends to indicate that the NH_4NO_3 phase transitions as well as its melting point were not affected by zeolite acidity.
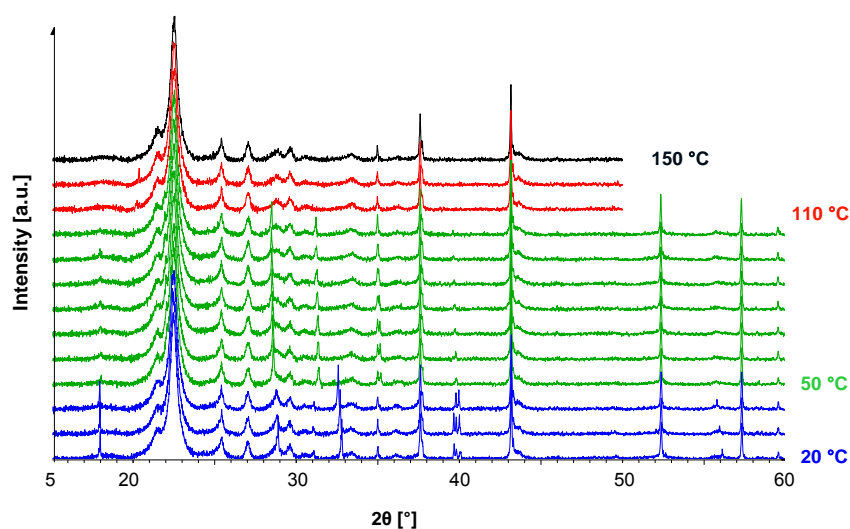

Figure 7.13 X-ray patterns recorded during decomposition of NH_4NO_3, physically mixed with H-BEA, within 20 - 200 °C, at intervals of 10 °C, applying a temperature ramp of 5 °C/min: Blue, green and red coloured curves correspond to NH_4NO_3 IV, II, I crystallographic phases respectively.

Finally, a XRD experiment was also attempted over the NH_4NO_3-Fe-BEA mixture. However surprisingly, exposing the mixture to ambient conditions, overnight (approximately 12-14 hours prior to XRD analysis) ammonium nitrate was no longer detected by XRD. The latter, was validated by preparing the same mixture and exposing it to ambient temperature overnight, for a second time, so as to ensure reproducibility. Therefore, the thermo-XRD experiment was abandoned. This observation could be attributed to several reasons. Ammonium nitrate is recognized to be deliquescent with a high solubility in aqueous phase (180 g per 100 g of water at 18°C). Consequently, prolonged exposure to ambient temperature and humidity may lead to a complete solubilization, which could explain the disappearance of X-ray patterns, characteristic of ammonium nitrates. Even if this is the case however, phase transitions from solid to liquid would not be expected to significantly impact the nature of chemical processes taking place at more elevated temperature during ammonium nitrate thermal decomposition. Moreover, it could be speculated that ammonium nitrate could be catalytically decomposed even at ambient temperature in the presence of iron, when contact between powders is prolonged. Li et al. [273] have similarly observed consumption of NH_4NO_2 mixed with Ba/Na-Y at ambient temperature, when exposing the sample to acidic HCl vapor for 13 hours. The latter, could imply a catalytic effect of this acid on ammonium nitrite decomposition. On the other hand, TGA-DSC measurements showed that ammonium nitrate decomposition was not affected by the presence of iron, since the same crystallographic transformations were evidenced during decomposition of pure NH_4NO_3 (section 7.3.1). To the author knowledge, such aspects have not been reported in the literature. Hence, it seems quite obvious that in order to evaluate such phenomena, additional experimental studies are required.

Compiling experimental results presented in section 7.3, it could be suggested that from a crystallographic point of view, ammonium nitrate undergoes thermal decomposition, through two phase transitions: a) IV → II and b) II → I, at 50 and 110 °C respectively. The presence of H-BEA acidity was proved to have no impact on NH_4NO_3 crystallographic phase transitions during decomposition, whereas the effect of iron contained in the Fe-BEA could not be safely evaluated. At 170 °C NH_4NO_3 starts melting yielding N_2, N_2O and NO_2, whereas release of NO could be also possible. Interestingly, respective gaseous concentration signals were maximized at around 210 – 220 °C, which is in relative agreement with respective results obtained during NO_x-NH_3 TRM and TPD experiments, presented in section 7.2.

7.4 Conclusions

An extensive experimental study of NH_4NO_3 formation and decomposition over an iron exchanged BEA catalyst was presented in this chapter. Dedicated NO_x-NH_3 TRM and TPD experiments employing in-situ IR spectroscopy were performed, over a lab-synthesized Fe-BEA sample in order to investigate ammonium nitrate formation and decomposition reaction pathways. Concerning the former, results indicated interactions of aluminium and iron based nitrate adspecies with NH_4^+ formed on Brønsted type acidic sites towards formation of solid ammonium nitrate. Comparing IR spectroscopic features and gas phase TRM signals obtained over the studied Fe-BEA, as well as data

reported in the recent literature, a respective detailed reactions mechanism was proposed, suggesting synergistic effects between different catalytic sites. Nevertheless, it was difficult to straightforwardly conclude on which of the abovementioned positions ammonium nitrate built up occurred. Interestingly the NO/NO_2 ratio turned out to have a significant effect on ammonium nitrate formation. When only NO_2 was preadsorbed on the catalyst, a higher ammonium nitrate build up was observed, whereas when NO/NO_2 coexisted in the feed NH_4NO_3 accumulation was limited. Catalytic reduction of nitrates by NO may play a key role, since it can significantly deteriorate the amount of surface NO_3, which constitute a NH_4NO_3 precursor.

As far as NH_4NO_3 decomposition is concerned, N_2, NO_2 and N_2O were released upon heating the catalyst at temperatures higher than 170 °C, which corresponds to the ammonium nitrate melting point. Possible reaction pathways included ammonium nitrate decomposition yielding gaseous NH_3 and HNO_3, decomposition of the latter towards NO_2 and readsorption of ammonia and nitrogen dioxide on acidic and redox surface sites. Finally, interactions of these species could lead to the formation of non stable intermediate compounds, which could be further decomposed to N_2, NO_2 and N_2O. Interestingly, a promoting effect of zeolitic Brønsted acidity was evidenced, since NH_3 could be rebound to cationic OH^+ positions, being further available to interact with NO_x adspecies.

Finally, NH_4NO_3 crystallographic phase transitions during thermal decomposition were studied employing TGA, DSC, MS and thermo-XRD measurements on powder ammonium nitrate mechanically mixed with bare and Fe exchanged BEA. Experimental results converged to the fact that NH_4NO_3 undergoes two crystallographic phase transformations before starting decomposing at 170 °C, irrespectively the presence of H- and/or Fe-BEA. Moreover, N_2, NO_2 and N_2O were released during decomposition and their respective concentrations maximized in the range of 210-220 °C, which is in good agreement with results obtained during TRM-TPD experiments. Interestingly, when NH_4NO_3 was kept in prolonged contact with Fe-BEA, at ambient temperature, the salt was completely decomposed. The latter may imply either NH_4NO_3 solublization due to ambient humidity and/or a significant catalytic effect of iron on ammonium nitrate decomposition at ambient temperature. Nevertheless, such aspects should be further investigated by additional experiments in order to draw safe conclusions.

Overall, the study presented in this section could not lead to a complete understanding of the physicochemical properties of NH_4NO_3 formed under SCR conditions. These properties can be a key point in determining the stability/reactivity of this intermediate during the SCR process. In this chapter, an attempt was made to investigate the NH_4NO_3 crystalographic phase transitions when ammonium nitrate is mechanically mixed with H-BEA and Fe-BEA. Clearly, the surface properties of these catalysts (acidity and redox proporties) mxde in loose contact with NH_4NO_3 had no significant impact and may not completely reflect the characteristic behavior of ammonium nitrate during strong interactions with the catalytic surface. As discussed previously, the effects of the contact duration, the humidity as well as the presence of iron should be further investigated.

Summary of Conclusions and Outlook

Summary of Conclusions and Outlook

Forthcoming stringent legislation related to nitrogen oxides emissions from mobile diesel sources calls for sophisticated exhaust gas aftertreatment technologies. The selective catalytic reduction of NO_x through urea or ammonia is a well established technique towards an efficient abatement of nitrogen oxides from mobile diesel engines exhaust stream. Fe-exchanged zeolites have been recently considered as promising SCR catalysts due to their high $deNO_x$ yield, as well as increased thermal stability. Deep understanding of the NH_3-SCR reactions network and catalyst structural properties is essential for developing highly efficient SCR systems. In this context, kinetic concept modeling can provide significant opportunities, allowing to optimize design parameters of the catalytic converter. Therefore, in the present work a throughout experimental study of NH_3-SCR reactions over Fe-zeolites was performed in order to develop a phenomenological macro-kinetic model, oriented to diesel engines aftertreatment simulation.

As far as kinetic modeling is concerned, a multi-site kinetic modeling approach was developed in order to depict reactions between NH_3 and NO_x and acidic and redox surface sites. Initially, a "reference skeleton" model was developed (chapter 2) on the basis of ammonia adsorption and TPD experiments over H- and Fe-ZSM5 catalysts, reported in the recent literature. Five sites were considered including: a site for physisorption and/or weak adsorption, two acidic sites characterized by different acidity strength, a metallic site and a site accounting for dehydroxylation phenomena at high temperature regime. Calibrating kinetic parameters and NH_3 storage capacities within certain ranges the model was successfully validated by simulating well documented ammonia adsorption and TPD experiments over laboratory and commercial H- and Fe-ZSM5 samples, showing the interest of the followed approach (chapter 3). On the other hand, significant limitations were also encountered, namely the fact that a detailed screening of structural properties was required in order determine model sites and estimate respective model parameters.

For this purpose, a Fe-BEA zeolite was synthesized in the laboratory and characterized by means of various optical techniques (chapter 4). Interestingly, different types of Fe sites were detected over the Fe-BEA catalyst, namely: i) isolated Fe species, ii) oligomeric Fe complexes, as well as iii) large Fe_2O_3 particles. Using this catalytic sample, reactions of the NH_3-SCR process were experimentally investigated and modelled. An extensive review of the recent literature (chapter 1) allowed a detailed consideration of possible reaction pathways related to the NH_3-SCR over iron exchanged zeolites. Aiming to get deeper insight into respective mechanistic aspects, the contribution of acidic and redox sites on the catalytic reactions was studied by means of in-situ IR spectroscopic measurements, over the lab-synthesized bare and Fe-exchanged BEA samples. To facilitate the intended analysis, the SCR reactions network was organised into three groups: i) NH_3 adsorption and desorption, ii) NO_x storage and NO oxidation and iii) reactivity between surface NH_3 and NO_x.

In chapter 5, ammonia adsorption and desorption were elucidated. At low temperature regime ammonia was predominantly physisorbed and/or weakly adsorbed. Interestingly, $N_2H_7^+$ species were evidenced, which tends to indicate built-up of ammonia multi-layers. Moreover, recorded spectra showed that NH_3 could be stably chemisorbed on Al based Lewis and OH^+ Brønsted acidic sites as

well as on metallic sites. The nature of the latter may be isolated and or binuclear species, which exhibit Lewis type acidity. Regarding interactions of ammonia with cationic hydroxyl groups, NH_4^+ in monodentate, bidentate and tridentate coordinations was detected, which suggested the existence of Brønsted acidic sites characterized by different acidity strength. Compiling results obtained from IR spectroscopic measurements, the "reference" multi-site kinetic model was further capitalized by drawing correlations between model sites and Fe-BEA catalytic sites. Kinetic parameters were calibrated employing literature data, whereas NH_3 storage capacities were carefully estimated on the basis of structural properties of the lab-synthesized catalysts and namely the Si/Al and Fe/Al ratios. Simulation of NH_3 adsorption and TPD experiments over the Fe-BEA, applying a broad range of operating conditions proved that the multi-site kinetic modeling approach, previously validated over NH_3 adsorption/desorption on H- and Fe-ZSM5 (chapter 3), could also be applied to the Fe-BEA catalyst. Nevertheless, it has to be pointed out that heat transfer and/or macro-mixing limitations should be further analyzed in order to improve the reactor model precision.

NO_x adsorption and desorption, as well as NO oxidation were investigated in chapter 6. NO was found to weakly chemisorb on monomeric Fe^{2+}, cationic OH^+ and extra-framework Al sites. On the other hand nitrate adspecies were produced upon NO_2 adsorption and disproportionation on framework and extra-framework aluminium as well as Fe sites, located in vicinity to cationic OH^+. Thus, synergy between neighbouring catalytic positions was suggested. Interestingly, nitrites were also evidenced, characterized by limited thermal stability. Finally, as far as NO oxidation is concerned, the reaction was initiated over oxidized iron sites at 100 °C and became active over zeolitic Al at 250 °C. Based on spectroscopic features a multi-site kinetic model for NO_x storage and NO oxidation was developed. In analogy with the NH_3 storage model, kinetics and storage capacities over each site were estimated considering literature data and structural properties of the studied samples. Simulation of NO_2 adsorption and TPD as well as NO oxidation experiments, performed over various lab-synthesized and commercial H- and Fe-BEA catalyst led to quite satisfactory reproduction of experimental results, highlighting the robustness of the proposed model.

Finally, reactivity of NH_3 and NO_x, at low temperature regime is discussed in chapter 7. At temperatures as low as 170 °C, ammonium nitrate formation was speculated upon reactions between Al and Fe based NO_3 and NH_4^+, bonded to cationic OH^+. The presence of NO in the feed was found to have a significant effect on the abovementioned reaction, since the latter can effectively reduce nitrates to nitrites at the studied temperature range. At higher temperatures decomposition of NH_4NO_3 took place leading to release of N_2, N_2O and NO_2. Additional thermal decomposition experiments on powder crystalline ammonium nitrate showed that NH_4NO_3 undergoes two phase transitions at around 50 and 110 °C, before decomposing at 170 °C. Interestingly, the presence of Lewis and Brønsted acidic sites did not seem to affect neither the sequence crystallographic phase transformations of the salt, nor the generated gas phase products. Unfortunately, no safe conclusion could be drawn for the respective impact of the iron content of the Fe-BEA catalyst and hence additional investigation is required. However, these observations were obtained on mechanical mixtures of NH_4NO_3 and H- and Fe-BEA catalysts in loose contact. Thus, the observed ammonium nitrate behavior may not completely reflect the thermal stability and/or the reactivity of the salt with the catalytic surface, under typical SCR conditions. Aspects such as the effect of the contact duration, the impact of humidity as the presence of iron should be further analyzed.

Overall, experimental results presented in this work provided a deep insight into mechanistic aspects related to the NH_3-SCR reactions network over Fe-zeolites. Correlations between catalyst structural properties and SCR reactions were drawn and formation and interactions between ammonia and nitrogen oxide adspecies were characterized in a qualitative and quantitative way. Utilizing experimental observations, a significant part of the NH_3-SCR reactions network was depicted by means of multi-site kinetic modeling. The proposed model was able to account for structural properties of the catalyst not only with respect to catalyst acidic and redox properties (eg. acidity strength variation) but concerning the actual elemental composition of the studied sample (eg. Al and Fe content) as well. Therefore, macro-kinetic modeling was linked with mechanistic aspects related to the NH_3-SCR on Fe-zeolites, via detailed surface chemistry analysis, which has not been attempted to this extent yet.

Commenting on applied experimental methods, detailed surface reactions characterization was performed by means of in-situ IR spectroscopic measurements. As shown in chapters 5, 6 and 7 this technique exhibits significant advantages towards the identification of NH_3 and NO_x surface species formed on acidic and metallic sites. Moreover, coupling between TRM and TPD with IR spectroscopic analysis allowed a quite satisfactory characterization of adspecies thermal stability and surface reactions. However, important limitations have to be pointed. The actual nature of iron species involved in NO_2 disproportionation and NH_3/NO_x SCR reactivity was not clearly deduced. The existence of bridging Fe based nitrates tends to support the fact that binuclear complexes might be the active sites for these reactions, but contribution of isolated Fe^{3+} cations could not be excluded. X-ray Atomic Spectroscopy has been earlier proposed by Roberio and co-workers [274,275] for Cu-zeolites, enabling to identify the nature of Cu complexes active for NO oxidation and NO_x standard SCR. Moreover, formation of NH_4NO_3 was concluded on the basis of quantitative analysis of NOx/NH3 TRM and TPD runs but was not directly detected through recorded IR spectra. In-situ Raman spectroscopy might be more sensitive in detecting deposited ammonium nitrate [276]. Finally, it has to be highlighted that all presented experiments were performed in the absent of water. As discussed in section 1.5.2 water may have significant effects on the SCR process, since it can interact with NH_3 and NO_x adpecies. In the frame of this work additional experiments were also performed and H_2O was included in the experimental protocol (not presented in the manuscript). Nevertheless, these runs were not considered in the SCR reaction mechanisms analysis because surface species characterization through IR spectroscopy was very difficult in the presence of water.

From a computer aided engineering point of view, the presented work may provide significant information in order to develop phenomenological kinetic models, oriented to diesel engines aftertreatment system simulation. Simplifying presented experimental results and particularly the ones obtained from NH_3/NO_x reactivity runs, it appears that nitrogen oxides preferably interact with framework and extra-framework aluminium, as well as binuclear iron sites, whereas ammonia is mainly chemisorbed on cationic OH^+ Brønsted acidic ones. Therefore, the proposed NH_3 and NO_x storage and NO oxidation multi-site models could be merged and globalized towards a simpler kinetic model, which could be able to account for reactions between ammonia and nitrogen oxide adspecies. A potential concept of a NH_3-SCR global multi-site kinetic model may include modeling of NO_2 storage and disproportionation, as well as NO oxidation on Al and Fe sites, and NH_3 adsorption on a global Brønsted acidic and a non acidic site. The latter, might be of high importance, since NH_3

released from non-acidic sites can be further available, by readsorption on neighboring acidic sites, or it can escape the catalytic converter, causing significant ammonia-slip. Finally, reactions between surface ammonia and nitrogen oxides could be taken into consideration, through the formation and decomposition of NH_4NO_3.

Résumé des Conclusions et Perspectives

Les normes futures, très restrictives, concernant les émissions d'oxydes d'azote des sources mobiles à moteur Diesel nécessitent l'utilisation de technologies sophistiquées de post-traitement des gaz d'échappement. La réduction catalytique sélective des NO_x par l'urée ou par l'ammoniac est une technique bien établie qui permet la réduction des oxydes d'azote des gaz d'échappement des moteurs Diesel de façon efficace. Les zéolithes échangées au fer ont été récemment considérées comme des catalyseurs SCR prometteurs, grâce à leur rendement de dénitrification élevé, ainsi que leur stabilité thermique significative. La compréhension détaillée des voies réactionelles NH_3-SCR et des propriétés structurelles du catalyseur est essentielle pour le développement de systèmes SCR efficaces. Dans ce contexte, le concept de modélisation cinétique peut offrir des possibilités importantes, permettant d'optimiser les paramètres du catalyseur. Par conséquent, ce travail constitue une étude exhaustive expérimentale des réactions de la SCR au NH_3, sur les zéolithes échangées au fer, afin de développer un modèle macro-cinétique phénoménologique, orienté vers la simulation de système de post-traitement des moteurs Diesel.

En ce qui concerne la modélisation cinétique, une approche de modélisation multi-site a été adoptée, afin de représenter les interactions entre le NH_3 et les NO_x et les sites acides et redox de surface. Un modèle - squelette de référence a été développé (chapitre 2) à partir des expériences d'adsorption et de TPD de l'ammoniac sur les catalyseurs H- et Fe-ZSM5, existant dans la littérature récente. Cinq sites ont été considérés: un site non acide de physisorption et / ou de l'adsorption faible, deux sites acides caractérisés par des forces d'acidité différentes, un site métallique et un site pour reproduire des phénomènes de déshydroxylation à haute température. Grâce à une calibration des paramètres cinétiques et des capacités de stockage du NH_3 sur certains intervalles, le modèle a été validé en simulant des expériences d'adsorption et de TPD de l'ammoniac, réalisées sur des échantillons H et Fe-ZSM5 du laboratoire et commerciaux, montrant l'intérêt de l'approche suivie (chapitre 3). D'autre part, des limitations significatives ont été rencontrés, notamment le fait qu'un examen détaillé des propriétés structurales a été nécessaire pour déterminer la nature et le nombre de sites du modèle et estimer les paramètres respectifs du modèle.

Par conséquent, une zéolithe de type BEA échangée au fer a été synthétisée en laboratoire et elle a été caractérisée au moyen de techniques optiques diverses (chapitre 4). Différents types de sites métalliques ont été détectés sur le catalyseur Fe-BEA, notamment i) les espèces Fe isolés, ii) les complexes Fe oligomères, ainsi que iii) les grandes particules Fe_2O_3. Employant cet échantillon catalytique, les réactions du processus NH_3-SCR ont été étudiées expérimentalement et ont été modélisées. Une recherche approfondie dans la littérature récente (chapitre 1) a permis un examen détaillé des voies réactionnelles possibles, associées à la SCR sur les zéolithes échangées au fer. Visant à obtenir un aperçu plus détaillé des aspects mécanistiques correspondants, la contribution des sites acides et redox sur les réactions catalytiques a été étudiée au moyen de mesures de spectroscopie IR, sur les échantillons H- et Fe-BEA synthétisés en laboratoire. Pour faciliter l'analyse, les voies réactionnelles SCR ont été séparées en trois groupes: i) adsorption et désorption du NH_3, ii) stockage des NO_x et oxydation du NO et iii) réactivité entre le NH_3 et les NO_x de surface.

Dans le chapitre 5, l'adsorption et la désorption de l'ammoniac ont été étudiées. A basse température, l'ammoniac a été, de façon prédominante, faiblement lié sur les sites non acides et/ou sur les sites d'adsorption faible. Les espèces $N_2H_7^+$ ont été mis en évidence, ce qui tend à indiquer que l'ammoniac a formé des multi-couches. En outre, les spectres enregistrés ont montré que le NH_3 pourrait être chimisorbée de façon stable sur des sites acides de type Lewis et de type Brønsted, qui correspondent aux positions Al et au OH^+ respectivement. En plus, l'ammoniac pourrait être aussi chimisorbée de façon stable sur les sites métalliques. La nature de ces derniers (qui peuvent être soit des espèces isolés, soit des espèces de type binucléaires) montrent une acidité de type Lewis. En ce qui concerne les interactions de l'ammoniac avec des groupes hydroxyles cationiques, le NH_4^+ dans les coordinations (ou configurations) monodentate, bidentate et tridentate a été détecté, ce qui suggère l'existence de sites acides de type Brønsted, caractérisés par des forces d'acidité différentes. En compilant des résultats obtenus à partir de mesures spectroscopiques IR, le modèle cinétique multi-sites "de référence" a été capitalisé en déduisant des corrélations entre les sites du modèle et les sites catalytiques du Fe-BEA. Les paramètres cinétiques ont été calibrés en utilisant les données de la littérature, alors que les capacités de stockage du NH_3 ont été soigneusement évaluées sur la base des propriétés structurales des catalyseurs synthétisés en laboratoire (notamment les rapports Si/Al et Fe/Al). La simulation des expériences de l'adsorption et de TPD du NH_3 sur le catalyseur Fe-BEA, en appliquant une large gamme de conditions de fonctionnement, a prouvé que l'approche de modélisation cinétique de type multi-site, qui a été déjà validée pour l'adsorption/désorption de l'ammoniac sur les catalyseurs H- et Fe-ZSM5 (chapitre 3), pourrait également être appliquée aux catalyseurs Fe-BEA. Néanmoins, il doit être souligné que le transfert de chaleur et/ou les limitations de macro-mélange doivent être analysées en détail, afin d'améliorer la précision du modèle de réacteur.

L'adsorption et la désorption de NO_x, ainsi que l'oxydation du NO ont été étudiées dans le chapitre 6. Il a été montré que le NO a été faiblement chimisorbé sur l'aluminium extra-réseau, sur les cations Fe^{2+} monomères, ainsi que sur les OH^+ cationiques. D'un autre côté, des nitrates ont été produits à partir de l'adsorption et de la disproportionation du NO_2 sur l'aluminium en position du réseau et en position extra-réseau de la zéolithe, ainsi que sur les sites métalliques, situés à proximité du OH^+ cationique. La synergie entre les positions catalytiques voisines a donc été suggérée. Des nitrites ont été également mis en évidence et ils ont été caractérisés par une stabilité thermique limitée. Enfin, concernant l'oxydation du NO, la réaction a été initiée à 100 °C, sur les sites de fer oxydés et elle est devenue active sur l'aluminium zéolithique à 250 °C. A partir des données de la spectroscopie IR, un modèle cinétique multi-site a été développé, portant sur le stockage des NO_x et sur l'oxydation du NO. En analogie avec le modèle de stockage du NH_3, les paramètres cinétiques et les capacités de stockage de chaque site ont été estimées compte tenu des données de la littérature et des propriétés structurales des échantillons étudiés. La simulation des expériences d'adsorption et de TPD du NO_2, ainsi que des expériences d'oxydation du NO, réalisées sur les échantillons H- et Fe-BEA synthétisés en laboratoire, ainsi que sur les catalyseurs commerciaux, a mené à une reproduction satisfaisante des curbes expérimentales. Donc, la robustesse du modèle proposé a pu être validé.

Finalement, la réactivité du NH_3 et des NO_x, à basse température est abordée dans le chapitre 7. A des températures aussi basses que 170 °C, la formation du nitrate d'ammonium a été spéculé à partir des réactions entre le NO_3 (formé sur l'Al et le Fe) et le NH_4^+ (lié au OH^+ cationique). La présence de NO dans l'alimentation a eu un effet significatif sur la réaction ci-dessus, car celle-ci peut

effectivement réduire les nitrates en nitrites dans la gamme de température étudiée. A des températures plus élevées, la décomposition du NH_4NO_3 a lieu entraînant la libération des N_2, N_2O et NO_2. Des expériences additionnelles, portant sur la décomposition thermique du nitrate d'ammonium cristalline, en poudre ont montré que le NH_4NO_3 subit deux transitions de phase à environ 50 et 110 °C, avant d'être décomposé à 170 °C. La présence des sites acides de type Lewis et de type Brønsted ne semble pas affecter ni la séquence des transformations de phases cristallographiques, ni les produits générés en phase gazeuse. Malheureusement, aucune conclusion sûre n'a pu être tirée concernant l'impact de la teneur en fer du catalyseur Fe-BEA et par conséquent des études supplémentaires sont nécessaires. Cependant, ces observations ont été obtenues sur des mélanges mécaniques de NH_4NO_3 et H- et de catalyseurs Fe-BEA en contact lâche. Le comportement observé sur nitrate d'ammonium peut donc ne pas refléter complètement la stabilité thermique et/ou la réactivité de cette espèce intermédiaire avec la surface catalytique, sous conditions typiques SCR. Les aspects tels que l'effet de la durée de contact, l'impact de l'humidité ainsi que la présence de fer devront être analysées ultérieurement.

Globalement, les résultats expérimentaux présentés dans ce travail ont fourni un aperçu détaillé des aspects mécanistiques liés aux voies réactionnelles de la SCR sur les zéolithes échangées au fer. Des corrélations entre les propriétés structurales du catalyseur et des réactions de la SCR ont été déduites. De plus, la formation des espèces ammoniac et oxydes d'azote surfaciques et leurs interactions entre elles ont été caractérisés de façon qualitative et quantitative. En utilisant des observations expérimentales, une partie importante des réactions SCR a été décrit par modélisation cinétique de type multi-site. Le modèle proposé a été capable de prendre en compte des propriétés structurelles du catalyseur, pas seulement par rapport aux propriétés acides et redox de catalyseur (par exemple la variation de la force d'acidité), mais également, par rapport à la composition élémentaire réelle des échantillons étudiés (par exemple le contenu en Al et en Fe). Par conséquent, la modélisation macro-cinétique a été corrélé aux aspects mécanistiques liés à la SCR sur les zéolithes au fer, au moyen d'une analyse chimique détaillée de surface, qui n'a pas encore été tenté à ce jour.

Par rapport aux méthodes expérimentales appliquées, la caractérisation des réactions de surface a été réalisée au moyen de mesures de spectroscopie IR. Comme il est indiqué dans les chapitres 5, 6 et 7, cette technique présentait des avantages importants pour l'identification des espèces du NH_3 et des NO_x de surface, formés sur des sites acides et métalliques. De plus, le couplage entre les expériences de TRM et de TPD et l'analyse spectroscopique ont permis une caractérisation très satisfaisante à la fois de la stabilité des espèces de surface et des réactions surfaciques. Cependant, des limitations importantes doivent être soulignées. La nature des espèces métalliques impliquées dans la disproportionation du NO_2 et dans la réactivité entre le NH_3 et le NO_x, n'a pas pu être déterminé. L'existence des nitrates de type 'bridging' sur Fe appuie le fait que les complexes métalliques binucléaires pourraient être les sites actifs de ces réactions, mais la contribution des cations Fe^{3+} isolés ne pouvaient pas être exclus. La spectroscopie atomique de rayons X a été précédemment proposé par Roberio et al. [269,270] pour les zéolithes échangées au cuivre, permettant d'identifier la nature des complexes Cu actifs pour l'oxydation du NO et pour la réaction de la "standard SCR". Par ailleurs, la formation du NH_4NO_3 a été conclu à partir d'une analyse quantitative des expériences de TRM des NO_x/NH_3 et des expériences de TPD, mais il n'a pas été détectée directement grâce aux spectres IR enregistrées. La spectroscopie Raman dans des conditions in-situ pourrait être plus sensible pour la détection de nitrate d'ammonium déposé [271]. Finalement, il doit être souligné que toutes les

expériences présentées ont été réalisées en l'absence d'eau. Tel que discuté dans la section 1.5.2, l'eau peut avoir des effets significatifs sur le processus SCR, car il peut interagir avec les espèces du NH_3 et les espèces des NO_x surfaciques. Dans le cadre de ce travail, d'autres expériences ont été également réalisées et le H_2O a été inclus dans le protocole expérimental (résultats pas présentés dans le manuscrit). Néanmoins, ces essais n'ont pas été considérés dans l'analyse des mécanismes de réaction SCR puisque la caractérisation des espèces de surface par spectroscopie IR a été très difficile en présence d'eau.

Du point de vue de la CAO (Conception Assistée par Ordinateur), le travail présenté peut fournir des informations importantes pour le développement des modèles cinétiques phénoménologiques, orientés vers la simulation de systèmes de post-traitement des moteurs Diesel. En simplifiant les résultats expérimentaux présentés et en particulier ceux obtenus à partir des expériences de la réactivité entre le NH_3 et les NO_x, il semble que les oxydes d'azote interagissent de préférence avec l'aluminium (qui est localisé aux positions du réseau et aux positions du extra-réseau zéolithique) et avec les sites metalliques. L'ammoniac est principalement chimisorbé sur les sites acides de type Brønsted. Par conséquent, le modèle "multi-site" qui porte sur le stockage des NO_x et sur l'oxydation du NO pourrait être fusionné avec le modèle du stockage du NH_3. Le modèle résultant pourrait être ensuite globalisé vers un modèle cinétique simple, qui serait capable de prendre en compte des réactions entre l'ammoniac et les espèces des NO_x surfaciques. Un concept potentiel d'un modèle cinétique multi-site, global de la SCR peut inclure i) la modélisation du stockage et de la disproportionation du NO_2, ainsi que celle de l'oxydation du NO sur des positions Fe et Al, et, ii) la modélisation de l'adsorption de l'ammoniac sur un site acide global de type Brønsted et sur un site non acide. Ce dernier pourrait être d'une grande importance, car le NH_3 libéré des sites non-acides peut encore être disponible, par réadsorption sur les sites acides voisins, ou il peut quitter le catalyseur, provoquant un "NH_3-slip" significatif. Finalement, les réactions entre l'ammoniac et les oxydes d'azote de surface pourraient être prises en compte, en considérant la formation et la décomposition du NH_4NO_3.

182

Appendices

Appendix A

Evaluation of the experimental-sup reliability

Reproducibility of experimental results obtained from the testing rig presented in (Figure 4.6) was evaluated by performing series of successive NH_3 adsorption and TPD experiments, on 9 mg of H-BEA zeolite. Around 550 ppm NH_3 were preadsorbed at 150 and 350 °C, for 80 min, followed by 1 h He flushing at the same temperature. Finally, a TPD was performed from the adsorption temperature up to 400 °C. Gas phase results are shown in Figure A1 and A2 respectively.
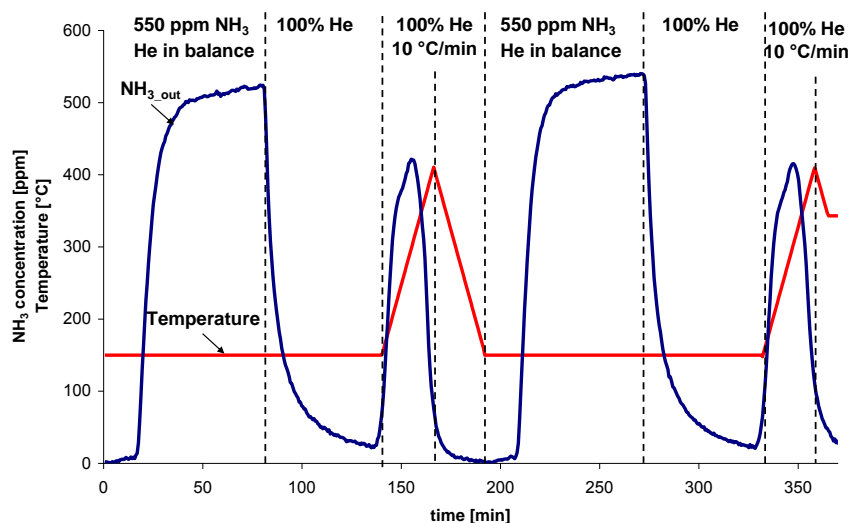
Figure A.1 Successive NH_3 adsorption and TPD experiments over H-BEA. Preadsorption of 550 ppm NH_3 for 80 min, at 150 °C, followed by 1 h He flushing and TPD at heating rate of 10 °C/min.
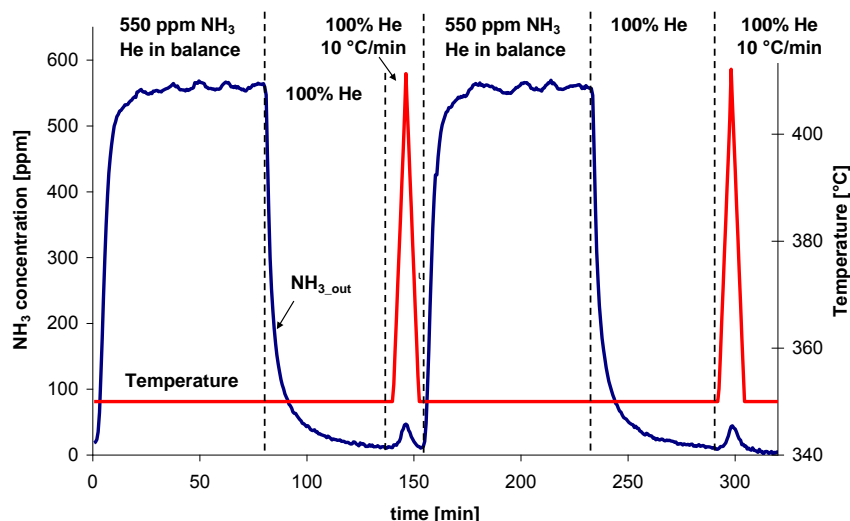
Figure A.2 Successive NH_3 adsorption and TPD experiments over H-BEA. Preadsorption of 550 ppm NH_3 for 80 min, at 350 °C, followed by 1 h He flushing and TPD at heating rate of 10 °C/min.

For both experimental cases, ammonia adsorption and TPD profiles seem to be qualitatively very similar. Mass flow controllers and control valves responses, during successive runs were unchanged and thus, reproducible NH_3 injection and removal were achieved. Moreover, the electrical oven was proved to be stable during steady and transient states, allowing reproducing identical temperature profiles. This picture was also validated by estimating the amounts of NH_3 stored on the H-BEA during the successive adsorption/TPD runs. Regarding the ammonia adsorption experiment at 150 °C, equimolar amounts of 0.62 and 0.64 mol/$kg_{zeolite}$ NH_3 were adsorbed and desorbed during the first and the second run respectively, resulting in a ca 3% deviation. On the other hand for the test case 0f 350 °C, 0.17 mol/$kg_{zeolite}$ NH_3 were calculated to be stored and released in both runs.
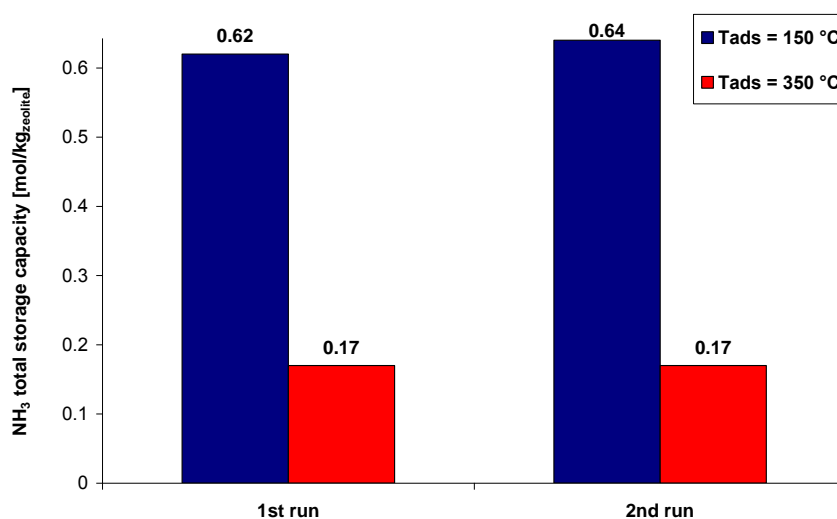
Figure A.3 Amounts of NH_3 stored on the H-BEA zeolite, during successive adsorption/TPD runs, at 150 and 350 °C.

186

Appendix B

Kinetic modeling of NO_x storage and NO oxidation: Parameters calibration

Kinetic parameters used for the simulation of experiments performed over the lab-synthesized H- and Fe-BEA catalysts (section 6.3) are discussed in this section.

Kinetics of O_2 storage and dissociation are illustrated in Table B.1 and Table B.2. Pre-exponential factors of O_2 adsorption were computed based on oxygen entropy change, applying the methodology presented in section 5.4.1. For the purposes of this study, it was assumed that O_2 adsorption on the Fe-BEA surface results in entire loss of its translation entropy, as well as in a loss of one third of its rotational one. Vibrational entropy was not taken into consideration since it was negligible compared to translation and rotation ones. Similar values have been reported elsewhere [145]. Respective activation energies of adsorption were set to zero in line with Chen et al. [183], assuming that adsorption is a non-activated process. Pre-exponential factors of desorption rate constants were tuned to the order of magnitude of 10^{13} s^{-1}, according to the transition state theory for immobile molecules [184], considering that O_2 storage capacity values are centred around 1 mol O_2/kg$_{catalyst}$. The activation energies of desorption over S2 and S3 sites were calibrated based on O_2 adsorption kinetic studies on a H-BEA zeolite, performed by Li et al. [277], whereas for the respective value over the iron S4 site, an activation energy of 48 kJ/mol, previously proposed by Metkar et al. [144] was adopted. For simplicity purposes, the desorption activation energy surface coverage dependency factors (α) were set to zero, assuming homogeneous acidity strength distribution. Concerning kinetics of oxygen dissociation and recombination, pre-exponential factors of dissociation were calibrated in line with respective values proposed by Olsson et al. [145], whereas the rest of the kinetics were chosen from kinetic modeling studies reported by Olsson et al. [145] and Metkar et al. [144].

Table B.1 Kinetic parameters for the multi-site kinetic model of O_2 adsorption and desorption over the Fe-BEA lab-synthesized catalyst.

Type of site	$A_{j\_O_2\_ads}$	$E_{j\_O_2\_ads}$	$A_{j\_O_2\_des}$	$E_{j\_O_2\_des}$	α_j
	[m^3/(s·kg $_{zeolite}$)]	[kJ/mol]	[mol/(s·kg $_{zeolite}$)]	[kJ/mol]	[-]
S2 sites[1]	394	0	$1.0 \cdot 10^{13}$	8.26	0.00
S3 sites[2]	394	0	$1.0 \cdot 10^{13}$	8.26	0.00
S4 sites[3]	394	0	$1.0 \cdot 10^{13}$	48.00	0.00

[1]: S2 sites represent a pair of an Al based Lewis site and a Si-OH$^+$-Al Brønsted one, where bidentate NO_3^- can be formed, [2]: S3 sites represent a pair of an Al based Lewis site and a Si-OH$^+$-Al Brønsted one, where bridging NO_3^- can be formed, [3]: S4 sites represent a pair of an isolated or binuclear iron site in the Fe^{3+} state and a Si-OH$^+$-Al Brønsted and/or a second metallic one.

Table B.2 Kinetic parameters for the multi-site kinetic model of O_2 dissociation and recombination over the Fe-BEA lab-synthesized catalyst.

Type of site	$A_{j\_O_2\_diss}$	$E_{j\_O_2\_diss}$	$A_{j\_O_2\_rec}$	$E_{j\_O_2\_rec}$	α_j
	[m^3/(s·kg $_{zeolite}$)]	[kJ/mol]	[mol/(s·kg $_{zeolite}$)]	[kJ/mol]	[-]
S2 sites[1]	$3.2 \cdot 10^{10}$	83.3	$1.0 \cdot 10^{13}$	161.00	0.10
S3 sites[2]	$3.2 \cdot 10^{10}$	83.3	$1.0 \cdot 10^{13}$	161.00	0.10
S4 sites[3]	$3.2 \cdot 10^{10}$	83.3	$1.0 \cdot 10^{13}$	161.00	0.10

[1]: S2 sites represent a pair of an Al based Lewis site and a Si-OH$^+$-Al Brønsted one, where bidentate NO_3^- can be formed, [2]: S3 sites represent a pair of an Al based Lewis site and a Si-OH$^+$-Al Brønsted one, where bridging NO_3^- can be formed, [3]: S4 sites represent a pair of an isolated or binuclear iron site in the Fe^{3+} state and a Si-OH$^+$-Al Brønsted and/or a second metallic one.

As far as kinetic parameters of NO_2 adsorption and desorption are concerned, the respective values are summarized in Table B.3. In analogy with NH_3 and O_2 storage, pre-exponential factors of adsorption were calibrated based on entropy change computations, whereas the respective activation energies were set to zero, supposing that the nitrogen dioxide adsorption occurs without energy barrier. Regarding entropy change, it was assumed that upon NO_2 adsorption translation entropy is completely lost for all sites whereas a rotational entropy change of around 33% and 44% occurs over S1a, S1b and S2, S3 and S4 sites respectively. Vibrational entropy was not taken into consideration since it was negligible compared to translation and rotation ones. Pre-exponential factors of desorption were set to the order of magnitude of 10^{13} s^{-1}, according to the transition state theory for immobile molecules [184], considering that NO_2 storage capacity values are centred around 1 mol NO_2/kgcatalyst, as already supposed for NH_3 and O_2 desorption. Respective values of desorption activation energies were calibrated based on various sources. An activation energy of 77 kJ/mol was used over the S1a sites, in order to fit the NO_2-TPD experiment presented in Figure 6.16. Earlier, Iwasaki et al. [278] have proposed a NO_2 differential adsorption energy of 67±1 kJ/mol over non acidic sites, which seems to somehow validate the slightly higher chosen value, since the S1a site corresponds to sites for physisorption and/or weak adsorption (see also discussion in section 5.4). Activation energies over S3 and S4 sites were calibrated in line with kinetic studies reported by Iwasaki et al. [278] and Metkar et al. [144]. Finally, respective values for S1b and S2 sites were manually tuned so as to simulate the NO_2-TPD experiment illustrated in Figure 6.16. Finally, desorption surface coverage dependency factors α, were calibrated to low values, accounting for relatively low heterogeneity within each group of model sites. The reader is referenced to section 5.4 for additional relative information.

Table B.3 Kinetic parameters for the multi-site kinetic model of NO_2 adsorption and desorption over the Fe-BEA lab-synthesized catalyst.

Type of site	$A_{j\_NO_2\_ads}$	$E_{j\_NO_2\_ads}$	$A_{j\_NO_2\_des}$	$E_{j\_NO_2\_des}$	α_j
	$[m^3/(s \cdot kg_{zeolite})]$	[kJ/mol]	$[mol/(s \cdot kg_{zeolite})]$	[kJ/mol]	[-]
S1a sites[1]	76	0	$1.0 \cdot 10^{13}$	77.00	0.10
S1b sites[2]	67	0	$1.0 \cdot 10^{13}$	82.00	0.10
S2 sites[3]	24	0	$1.0 \cdot 10^{13}$	106.00	0.12
S3 sites[4]	24	0	$1.0 \cdot 10^{13}$	141.00	0.14
S4 sites[5]	20	0	$1.0 \cdot 10^{13}$	144.5	0.18

[1]: S1a sites correspond to sites for physisorption and/or weak adsorption, [2]: S1b sites are assigned to Brønsted acidic sites on which nitrites can be formed, [3]: S2 sites represent a pair of an Al based Lewis site and a Si-OH$^+$-Al Brønsted one, where bidentate NO_3^- can be formed, [4]: S3 sites represent a pair of an Al based Lewis site and a Si-OH$^+$-Al Brønsted one, where bridging NO_3^- can be formed, [5]: S4 sites represent a pair of an isolated or binuclear iron site in the Fe^{3+} state and a Si-OH$^+$-Al Brønsted and/or a second metallic one.

Kinetic parameters of NO_2 disproportionation and recombination are presented in Table B.4. Pre-exponential factors of nitrogen dioxide disproportionation were manually adjusted in order to fit the NO_2-TPD experimental curves shown in Figure 6.16 and Figure 6.18. The rest of the kinetic parameters were calibrated in the order of magnitude of respective parameters reported by Olsson et al. [145].

Table B.4 Kinetic parameters for the multi-site kinetic model of NO_2 disproportionation and recombination over the Fe-BEA lab-synthesized catalyst.

Type of site	$A_{j\_NO_2\_disp}$	$E_{j\_NO_2\_disp}$	$A_{j\_NO_2\_rec}$	$E_{j\_NO_2\_rec}$	α_j
	$[m^3/(s \cdot kg_{zeolite})]$	[kJ/mol]	$[mol/(s \cdot kg_{zeolite})]$	[kJ/mol]	[-]
S2 sites[1]	$1.0 \cdot 10^{11}$	89	116	10.00	1.00
S3 sites[2]	$9.0 \cdot 10^{10}$	123	250	18.00	1.00
S4 sites[3]	$9.0 \cdot 10^{10}$	128	250	18.00	1.00

[1]: S2 sites represent a pair of an Al based Lewis site and a Si-OH$^+$-Al Brønsted one, where bidentate NO_3^- can be formed, [2]: S3 sites represent a pair of an Al based Lewis site and a Si-OH$^+$-Al Brønsted one, where bridging NO_3^- can be formed, [3]: S4 sites represent a pair of an isolated or binuclear iron site in the Fe^{3+} state and a Si-OH$^+$-Al Brønsted and/or a second metallic one.

Regarding nitrates decomposition and recombination, respective kinetics are summarized in Table B.5. pre-exponential factors of NO_3 formation were fixed to the order of magnitude of 10^{13} s^{-1}, in line with values reported by Olsson et al. [145], whereas respective activation energies were manually adjusted in order to fit experimental curves presented in Figure 6.16 and Figure 6.18. On the hand,

kinetics of nitrates decomposition were calibrated in accordance with values proposed by Olsson et al. [145] and Savara et al. [279]. Finally, decomposition surface coverage dependency factors were manually adjusted in order to simulate the NO_2-TPD experiments illustrated in Figure 6.16 and Figure 6.18.

Table B.5 Kinetic parameters for the multi-site kinetic model of NO_3 formation and decomposition over the Fe-BEA lab-synthesized catalyst.

Type of site	$A_{j\_NO_3\_form}$	$E_{j\_NO_3\_form}$	$A_{j\_NO_3\_dec}$	$E_{j\_NO_3\_dec}$	α_j
	[m^3/(s·kg $_{zeolite}$)]	[kJ/mol]	[mol/(s·kg $_{zeolite}$)]	[kJ/mol]	[-]
S2 sites[1]	$1.0 \cdot 10^{13}$	89	$5.0 \cdot 10^{13}$	115.00	0.30
S3 sites[2]	$1.0 \cdot 10^{13}$	86	$1.0 \cdot 10^{14}$	190.00	0.51
S4 sites[3]	$1.0 \cdot 10^{13}$	92	$1.0 \cdot 10^{14}$	195.00	0.45

[1]: S2 sites represent a pair of an Al based Lewis site and a Si-OH$^+$-Al Brønsted one, where bidentate NO_3^- can be formed, [2]: S3 sites represent a pair of an Al based Lewis site and a Si-OH$^+$-Al Brønsted one, where bridging NO_3^- can be formed, [3]: S4 sites represent a pair of an isolated or binuclear iron site in the Fe^{3+} state and a Si-OH$^+$-Al Brønsted and/or a second metallic one.

Finally, as far as NO oxidation and NO_2 dissociation are concerned, respective kinetic parameters are presented in Table B.6. Pre-exponential factors of nitrogen monoxide oxidation were calibrated according to kinetic modeling studies reported by Olsson et al. [145], whereas corresponding activation energies were adjusted in line with recently presented kinetic studies by Tronconi et al. [280]. Finally, kinetics for NO_2 dissociation were tuned to values, which are in relative agreement with values reported by Olsson et al. [145].

Table B.6 Kinetic parameters for the multi-site kinetic model of NO oxidation and NO_2 dissociation over the Fe-BEA lab-synthesized catalyst.

Type of site	$A_{j\_NO\_ox}$	$E_{j\_NO\_ox}$	$A_{j\_NO_2\_diss}$	$E_{j\_NO_2\_diss}$
	[m^3/(s·kg $_{zeolite}$)]	[kJ/mol]	[mol/(s·kg $_{zeolite}$)]	[kJ/mol]
S3 sites[1]	100	25	$7.0 \cdot 10^{11}$	133.00
S4 sites[2]	200	24	$7.0 \cdot 10^{11}$	127.00

[1]: S3 sites represent a pair of an Al based Lewis site and a Si-OH$^+$-Al Brønsted one, where bridging NO_3^- can be formed, [2]: S4 sites represent a pair of an isolated or binuclear iron site in the Fe^{3+} state and a Si-OH$^+$-Al Brønsted and/or a second metallic one.

For simulation purposes, NO_2 storage capacities over each surface site had to be estimated. In analogy with the analysis presented in sections 5.4.1 and 5.4.2 catalysts structural properties were taken into consideration. Regarding the H-BEA zeolite, an overall 1.64 mol/kg$_{zeolite}$ NO_2 uptake was

estimated at 30 °C. According to the results of the elemental analysis (Table 4.1), the H-BEA zeolite was composed of 1.11 mol/kg$_{zeolite}$ Al, which means that all acidic and non acidic sites were completely saturated and thus around 0.53 mol/kg$_{zeolite}$ NO$_2$ were physisorbed and/or weakly adsorbed on silanols (SiOH). The total amount of zeolitic aluminium may correspond to either Al based Lewis sites and/or OH$^+$ Brønsted sites. As explained in section 6.2.2.1, nitrogen dioxide desorbed between 200 – 500 °C corresponded to decomposition of bidentate and bridging nitrates. Integrating the respective TPD signal shown in Figure 6.8. within this temperature range an amount of 0.54 mol/kg$_{zeolite}$ NO$_2$ was estimated. From a modeling point of view, this amount of nitrates corresponds to the sum of storage capacities of S2 and S3 sites. Therefore, respecting this value, the storage capacities of S2 and S3 sites were manually adjusted to 0.24 and 0.3 mol/kg$_{zeolite}$ NO$_2$, in order to fit the NO$_2$-TPD presented in Figure 6.16. Finally, subtracting storage capacities of S1a, S2 and S3 from the total NO$_2$ uptake of 1.64 mol/kg$_{zeolite}$, a residual amount of 0.57 mol/kg$_{zeolite}$ was found, which was assigned to the storage capacity of S1b sites.

As far as the lab-synthesized Fe-BEA is concerned, a total amount of 1.44 mol/kg$_{Fe-BEA}$ nitrogen dioxide was estimated to adsorb and desorb during the NO$_2$ adsorption and TPD experiments presented in Figure 6.10 and Figure 6.12 respectively. The storage capacity over S1a sites for physisorption and/or weak adsorption was set to 0.54 mol/kg$_{Fe-BEA}$ NO$_2$, in line with the analysis presented for the H-BEA zeolite above. In the case of the Fe-BEA, the respective NO$_2$-TPD area (Figure 6.12) within the range of 200 – 500 °C was calculated equal to ca 0.57 mol/kg$_{Fe-BEA}$. As explained in section 6.2.2.2, this amount of nitrogen dioxide was generated through decomposition of EfAl, FAl and Fe based NO$_3$. Regarding the storage capacity of metallic sites, an amount of 0.16 mol/kg$_{Fe-BEA}$ was deduced, according to the analysis presented in section 5.4.2. Subtracting the latter value from the total amount of surface nitrates, a total capacity equal to 0.41 mol/kg$_{Fe-BEA}$ was found over S2 and S3. Fitting the NO$_2$-TPD experiment illustrated in Figure 6.18, individual capacities over S2 and S3 sites were adjusted to 0.21 and 0.2 mol/kg$_{Fe-BEA}$ respectively, hence respecting a total amount of 0.41 mol/kg$_{Fe-BEA}$. Finally, subtracting the sum of NO$_2$ storage capacities over the S1a, S2, S3 and S4 sites (1.11 mol/kg$_{Fe-BEA}$) from the overall NO$_2$ uptake over the Fe-BEA catalyst (1.44 mol/kg$_{Fe-BEA}$) a residual storage capacity of 0.33 mol/kg$_{Fe-BEA}$ was estimated, which corresponds to S1b sites. NO$_2$ storage capacities over the H- and Fe-BEA sites are summarized in Table B.7. At this stage, it has to be highlighted that the abovementioned computations provided just approximate values of storage capacity, since as already explained in chapters 3 and 5, the shape of the TPD signal (and thus measured concentration during desorption) is very sensitive to experimental conditions.

Table B.7 NO$_2$ storage capacity over the characterized sites of the H- and Fe-BEA lab-synthesized samples.

Type of site	H-BEA	Fe-BEA
	N$_j$ (mol/kg$_{zeolite}$)	N$_j$ (mol/kg$_{catalyst}$)
S1a sites[1]	0.54	0.54
S1b sites[2]	0.57	0.33
S2 sites[3]	0.24	0.21
S3 sites[4]	0.3	0.2
S4 sites[5]	-	0.16

[1]: S1a sites correspond to sites for physisorption and/or weak adsorption, [2]: S1b sites are assigned to Brønsted acidic sites on which nitrites can be formed, [3]: S2 sites represent a pair of an Al based Lewis site and a Si-OH$^+$-Al Brønsted one, where bidentate NO$_3^-$ can be formed, [4]: S3 sites represent a pair of an Al based Lewis site and a Si-OH$^+$-Al Brønsted one, where bridging NO$_3^-$ can be formed, [5]: S4 sites represent a pair of an isolated or binuclear iron site in the Fe^{3+} state and a Si-OH$^+$-Al Brønsted and/or a second metallic one.

Finally, kinetic parameters used for simulating the NO$_2$ adsorption and TPD experiments illustrated in Figure 6.21 are presented in Table B.8 to Table B.13. NO$_2$ storage capacities over different sites are shown in Table B.14. Since the presented NO$_2$ adsorption experiments were performed at 200 °C, S2, S3 and S4 sites were only active for NO$_x$ species formation. Respective storage capacities were manually calibrated in order to fit the NO$_2$-TPD experimental curves of Figure 6.21, respecting the fact the total amount of stored nitrates was reported to be equal to 0.025 mol/kg$_{catalyst}$. On the other hand, storage capacities over S1a and S1b sites, which are associated with sites for physisorption and/or weak adsorption and sites for nitrites formation respectively were not able to be estimated. Therefore, since these sites are not interfering in the simulation, a minimum value of 0.001 mol/kg$_{catalyst}$ was used.

Table B.8 Kinetic parameters for the multi-site kinetic model of O$_2$ adsorption and desorption over the Fe-BEA commercial catalyst, reported in [94].

Type of site	A$_{j\_O_2\_ads}$	E$_{j\_O_2\_ads}$	A$_{j\_O_2\_des}$	E$_{j\_O_2\_des}$	α$_j$
	[m^3/(s·kg$_{zeolite}$)]	[kJ/mol]	[mol/(s·kg$_{zeolite}$)]	[kJ/mol]	[-]
S2 sites[1]	394	0	1.0·10^{13}	8.26	0.00
S3 sites[2]	394	0	1.0·10^{13}	8.26	0.00
S4 sites[3]	394	0	1.0·10^{13}	40.00	0.00

[1]: S2 sites represent a pair of an Al based Lewis site and a Si-OH$^+$-Al Brønsted one, where bidentate NO$_3^-$ can be formed, [2]: S3 sites represent a pair of an Al based Lewis site and a Si-OH$^+$-Al Brønsted one, where bridging NO$_3^-$ can be formed, [3]: S4 sites represent a pair of an isolated or binuclear iron site in the Fe^{3+} state and a Si-OH$^+$-Al Brønsted and/or a second metallic one.

Table B.9 Kinetic parameters for the multi-site kinetic model of O_2 dissociation and recombination over the Fe-BEA commercial catalyst, reported in [94].

Type of site	$A_{j\_O_2\_diss}$	$E_{j\_O_2\_diss}$	$A_{j\_O_2\_rec}$	$E_{j\_O_2\_rec}$	α_j
	[m³/(s·kg $_{zeolite}$)]	[kJ/mol]	[mol/(s·kg $_{zeolite}$)]	[kJ/mol]	[-]
S2 sites[1]	$3.2 \cdot 10^{10}$	83.3	$1.0 \cdot 10^{13}$	161.00	0.10
S3 sites[2]	$3.2 \cdot 10^{10}$	83.3	$1.0 \cdot 10^{13}$	161.00	0.10
S4 sites[3]	$3.2 \cdot 10^{10}$	83.3	$1.0 \cdot 10^{13}$	161.00	0.10

[1]: S2 sites represent a pair of an Al based Lewis site and a Si-OH$^+$-Al Brønsted one, where bidentate NO_3^- can be formed, [2]: S3 sites represent a pair of an Al based Lewis site and a Si-OH$^+$-Al Brønsted one, where bridging NO_3^- can be formed, [3]: S4 sites represent a pair of an isolated or binuclear iron site in the Fe^{3+} state and a Si-OH$^+$-Al Brønsted and/or a second metallic one.

Table B.10 Kinetic parameters for the multi-site kinetic model of NO_2 adsorption and desorption over the Fe-BEA commercial catalyst, reported in [94].

Type of site	$A_{j\_NO_2\_ads}$	$E_{j\_NO_2\_ads}$	$A_{j\_NO_2\_des}$	$E_{j\_NO_2\_des}$	α_j
	[m³/(s·kg $_{zeolite}$)]	[kJ/mol]	[mol/(s·kg $_{zeolite}$)]	[kJ/mol]	[-]
S1a sites[1]	76	0	$1.0 \cdot 10^{13}$	77.00	0.10
S1b sites[2]	67	0	$1.0 \cdot 10^{13}$	82.00	0.10
S2 sites[3]	24	0	$1.0 \cdot 10^{13}$	106.00	0.12
S3 sites[4]	24	0	$1.0 \cdot 10^{13}$	141.00	0.14
S4 sites[5]	24	0	$1.0 \cdot 10^{13}$	120.00	0.18

[1]: S1a sites correspond to sites for physisorption and/or weak adsorption, [2]: S1b sites are assigned to Brønsted acidic sites on which nitrites can be formed, [3]: S2 sites represent a pair of an Al based Lewis site and a Si-OH$^+$-Al Brønsted one, where bidentate NO_3^- can be formed, [4]: S3 sites represent a pair of an Al based Lewis site and a Si-OH$^+$-Al Brønsted one, where bridging NO_3^- can be formed, [5]: S4 sites represent a pair of an isolated or binuclear iron site in the Fe^{3+} state and a Si-OH$^+$-Al Brønsted and/or a second metallic one.

Table B.11 Kinetic parameters for the multi-site kinetic model of NO_2 disproportionation and recombination over the Fe-BEA commercial catalyst, reported in [94].

Type of site	$A_{j\_NO_2\_disp}$	$E_{j\_NO_2\_disp}$	$A_{j\_NO_2\_rec}$	$E_{j\_NO_2\_rec}$	α_j
	[m³/(s·kg zeolite)]	[kJ/mol]	[mol/(s·kg zeolite)]	[kJ/mol]	[-]
S2 sites[1]	$1.0\cdot10^{11}$	89	116	10.00	1.00
S3 sites[2]	$9.0\cdot10^{10}$	123	250	18.00	1.00
S4 sites[3]	$9.0\cdot10^{10}$	100	250	17.00	1.00

[1]: S2 sites represent a pair of an Al based Lewis site and a Si-OH$^+$-Al Brønsted one, where bidentate NO_3^- can be formed, [2]: S3 sites represent a pair of an Al based Lewis site and a Si-OH$^+$-Al Brønsted one, where bridging NO_3^- can be formed, [3]: S4 sites represent a pair of an isolated or binuclear iron site in the Fe^{3+} state and a Si-OH$^+$-Al Brønsted and/or a second metallic one.

Table B.12 Kinetic parameters for the multi-site kinetic model of NO_3 formation and decomposition over the Fe-BEA commercial catalyst, reported in [94].

Type of site	$A_{j\_NO_3\_form}$	$E_{j\_NO_3\_form}$	$A_{j\_NO_3\_dec}$	$E_{j\_NO_3\_dec}$	α_j
	[m³/(s·kg zeolite)]	[kJ/mol]	[mol/(s·kg zeolite)]	[kJ/mol]	[-]
S2 sites[1]	$1.0\cdot10^{13}$	89	$5.0\cdot10^{13}$	115.00	0.30
S3 sites[2]	$1.0\cdot10^{13}$	86	$1.0\cdot10^{14}$	190.00	0.19
S4 sites[3]	$1.0\cdot10^{13}$	82	$1.0\cdot10^{13}$	134.00	0.20

[1]: S2 sites represent a pair of an Al based Lewis site and a Si-OH$^+$-Al Brønsted one, where bidentate NO_3^- can be formed, [2]: S3 sites represent a pair of an Al based Lewis site and a Si-OH$^+$-Al Brønsted one, where bridging NO_3^- can be formed, [3]: S4 sites represent a pair of an isolated or binuclear iron site in the Fe^{3+} state and a Si-OH$^+$-Al Brønsted and/or a second metallic one.

Table B.13 Kinetic parameters for the multi-site kinetic model of NO oxidation and NO_2 dissociation over the Fe-BEA commercial catalyst, reported in [94].

Type of site	$A_{j\_NO\_ox}$	$E_{j\_NO\_ox}$	$A_{j\_NO_2\_diss}$	$E_{j\_NO_2\_diss}$
	[m³/(s·kg zeolite)]	[kJ/mol]	[mol/(s·kg zeolite)]	[kJ/mol]
S3 sites[1]	100	25	$7.0\cdot10^{11}$	152.00
S4 sites[2]	200	24	$7.0\cdot10^{11}$	160.00

[1]: S3 sites represent a pair of an Al based Lewis site and a Si-OH$^+$-Al Brønsted one, where bridging NO_3^- can be formed, [2]: S4 sites represent a pair of an isolated or binuclear iron site in the Fe^{3+} state and a Si-OH$^+$-Al Brønsted and/or a second metallic one.

Table B.14 NO_2 storage capacity over the characterized sites of the Fe-BEA commercial catalyst, reported in [94].

Type of site	N_j (mol/kg$_{zeolite}$)
S1a sites[1]	0.01
S1b sites[2]	0.01
S2 sites[3]	0.01
S3 sites[4]	0.002
S4 sites[5]	0.011

[1]: S1a sites correspond to sites for physisorption and/or weak adsorption, [2]: S1b sites are assigned to Brønsted acidic sites on which nitrites can be formed, [3]: S2 sites represent a pair of an Al based Lewis site and a Si-OH$^+$-Al Brønsted one, where bidentate NO_3^- can be formed, [4]: S3 sites represent a pair of an Al based Lewis site and a Si-OH$^+$-Al Brønsted one, where bridging NO_3^- can be formed, [5]: S4 sites represent a pair of an isolated or binuclear iron site in the Fe^{3+} state and a Si-OH$^+$-Al Brønsted and/or a second metallic one.

Appendix C

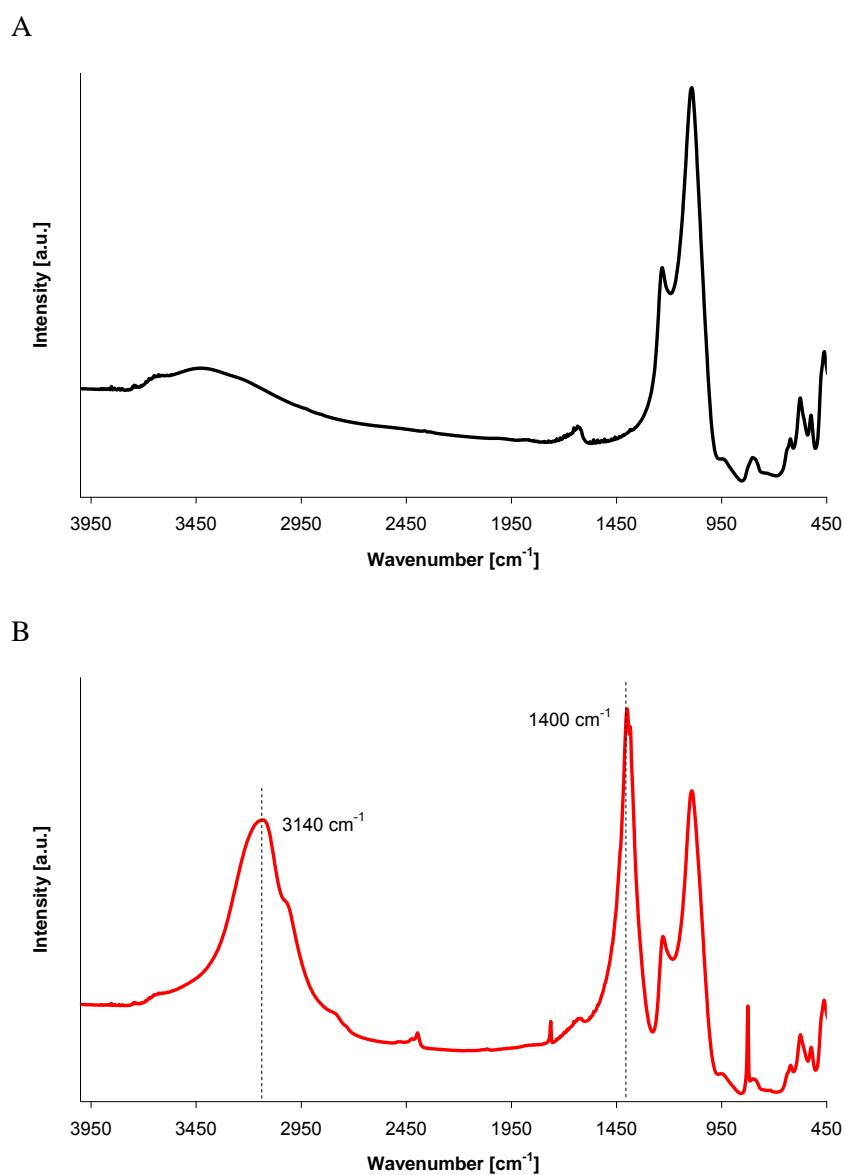## Ex-situ IR spectroscopic measurements

A

B

Figure C.1 Ex-situ IR spectra of A) the Fe-BEA lab-synthesized catalyst and B) a mixture of powder NH_4NO_3 and the Fe-BEA lab-synthesized catalyst.
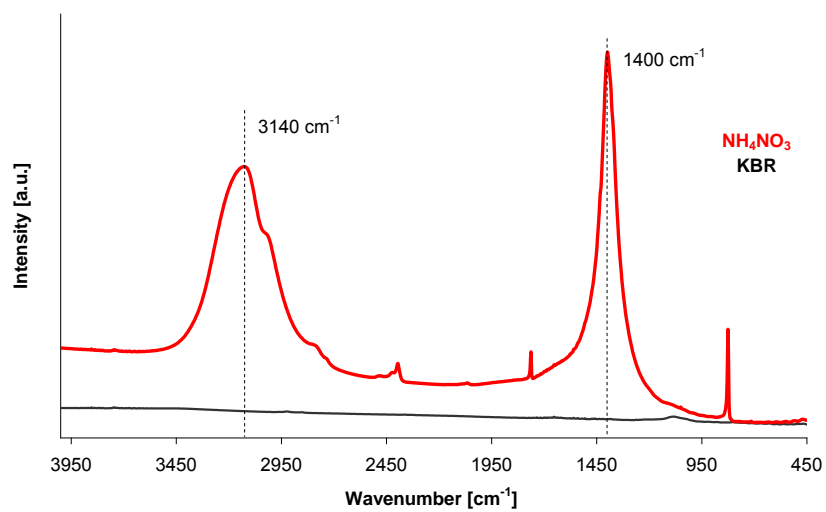
Figure C.2 Ex-situ IR spectra of powder crystalline NH_4NO_3 mixed with KBR.

Appendix D

NH₃ oxidation on Fe-BEA

A NH₃/O₂ stepwise TPD experiment was performed over the Fe-BEA lab-synthesized catalyst in order to investigate ammonia oxidation. Briefly, 10 mg Fe-BEA were continuously exposed to a mixture of around 500 ppm NH₃ and 2% O₂, diluted in He. The reactor temperature was ketpt at 100 °C for 60 min, and then increased to constant steps of 150, 250, 300, 450, 485 °C. The duration of each step was 10 min, whereas the heating rate between T-steps was 10 °C/min. Gaseous phase results are illustrated in Figure D.1, whereas the respective oxidation yield and gaseous products are presented in Figure D.2 and Figure D.3 respectively.
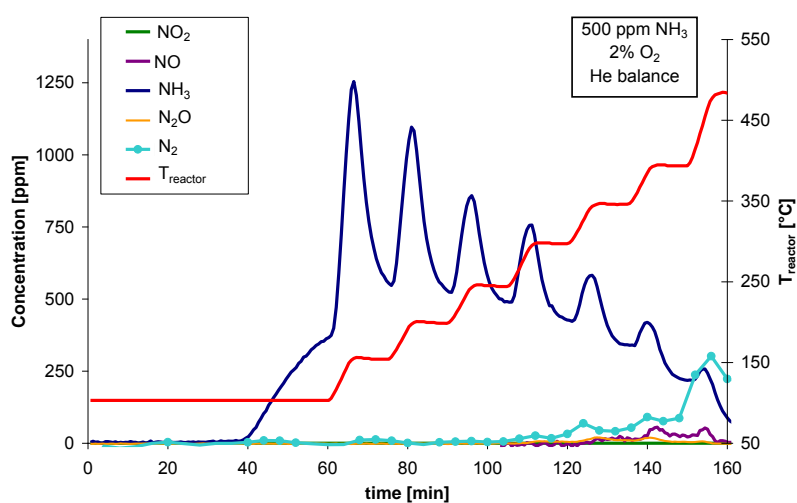
Figure D.1 NH₃/O₂ STPD experiment on the Fe-BEA lab-synthesized sample: 10 mg Fe-BEA, Injection of 500 ppm NH₃ and 2% O₂ diluted in He.
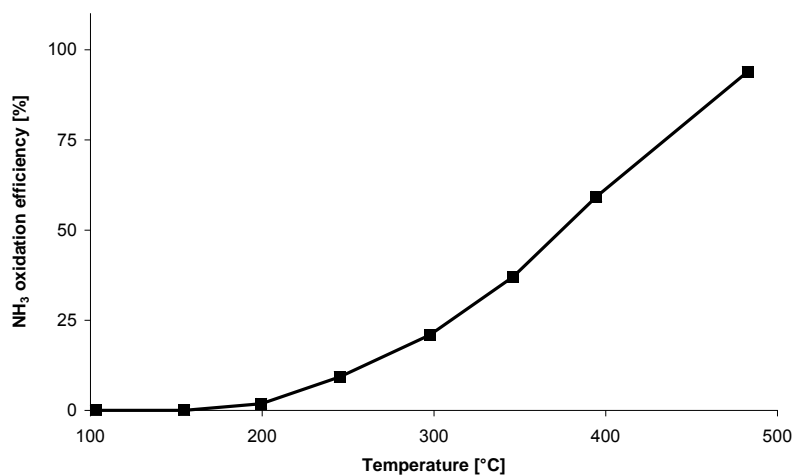
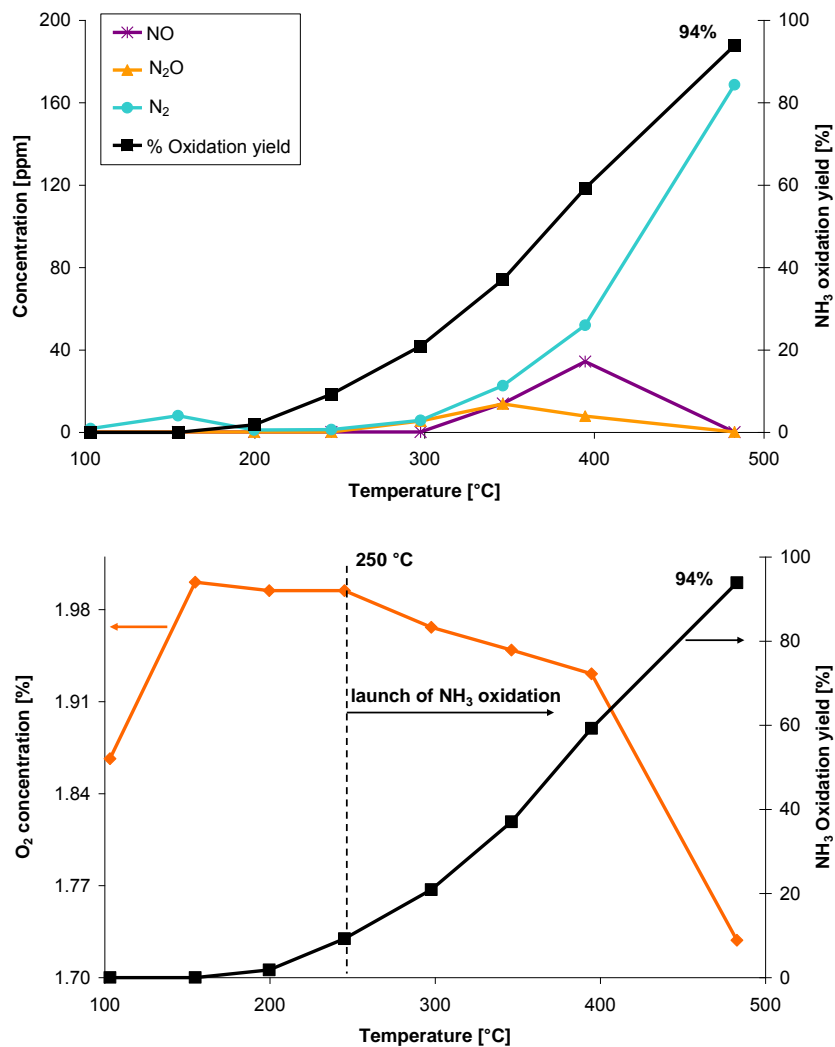**Figure D.2** Yield of NH₃ oxidation over the Fe-BEA lab-synthesized sample.

Figure D.3 Gaseous species released and O$_2$ consumption during NH$_3$ oxidation over the Fe-BEA lab-synthesized sample.

Appendix E

List of publications

A. Publications in journals

1. Stavros A. Skarlis, David Berthout, André Nicolle, Christophe Dujardin, Pascal Granger. (2012) "Multi-Site Modeling of NH_3 Adsorption and Desorption Over Fe-ZSM5", The Journal of Chemical Physical Chemistry C, 116 (15), pp 8437–8448.

2. Stavros A. Skarlis, David Berthout, André Nicolle, Christophe Dujardin, Pascal Granger. (2012) "Modeling NH_3 storage over Fe- and Cu-zeolite based, Urea-SCR catalysts for mobile diesel engines", Procedia-Social and Behavioral Studies. Transport Research Arena – Europe 2012, 48, pp 1672 - 1682.

3. Stavros A. Skarlis, David Berthout, André Nicolle, Christophe Dujardin, Pascal Granger. (2013) "IR Spectroscopy Analysis and Kinetic Modeling Study for NH_3 Adsorption and Desorption on H- and Fe-BEA Catalysts", The Journal of Chemical Physical Chemistry C, 117 (14), pp 7154–7169.

4. Stavros A. Skarlis, David Berthout, André Nicolle, Christophe Dujardin, Pascal Granger. (2014) "Combined IR spectroscopy and kinetic modeling of NO_x storage and NO oxidation on Fe-BEA catalysts". Applied Catalysis B Environmental, 148-149, 446-465.

5. Stavros A. Skarlis, David Berthout, André Nicolle, Christophe Dujardin, Pascal Granger. (2014) "Experimental and kinetic modeling study of ammonium nitrate thermal decomposition" (in preparation).

B. Publications in international congresses

1. Stavros A. Skarlis: "Storage of NH_3 and H_2O over Fe-zeolite based urea-SCR catalysts" 14th CLEERS Workshop, April 2011, Detroit, USA.

2. Stavros A. Skarlis: "Modeling NH_3 storage over Fe- and Cu-zeolite based, Urea-SCR catalysts for mobile diesel engines" Transport Research Arena – Europe 2012, April 2012, Athens, Greece.

3. Stavros A. Skarlis: "Multi-site modeling of Urea/NH_3-SCR over Fe-zeolites" 15th CLEERS Workshop, April 2012, Detroit, USA.

4. Stavros A. Skarlis: "IR based multi-site kinetic modeling for NH_3-SCR on Fe-BEA " 16th CLEERS Workshop, April 2013, Detroit, USA.

List of References

1 Ferguson, C. R. and Kirkpatrik, A. T. (2008). Internal Combustion Engines. Greek Translation: Koltsakis, G. C., Thessaloniki, Greece, Grapholine, pp. 367-374.

2 Dietsche, K. H. and Klingebiel, M. (2007). Automotive handbook – 7th Edition. 576. West Sussex, England, Robert Bosch GmbH, Willey, pp. 566 – 567.

3 Grassian, V. H. (2005). Environmental catalysis. New York, USA, Taylor & Francis Group, pp. 197-211.

4 Kley, D., Kleinmann, M., Sanderman, H. and Krupa, S. (1999). Photochemical oxidants: state of the science. Environmental Pollution, 100, 19-42.

5 US Environmental Protection Agency: http://www.epa.gov/captrade/documents/power.pdf. accessed 27-2-2013.

6 Pantazopoulou, A., Katsouyanni, K., Koureakremastinou, J. and Trichopoulos, D. (1995). Short-Term Effects of Air Pollution on Hospital Emergency Outpatient Visits and Admissions in the Greater Athens, Greece Area. Environmental Research, 69, 31-36.

7 Sarner, J. B., Brandom, B. W., Woelfel, S. K., Dong, M. L., Horn, M. C., Cook, D. R., McNulty, B. F. and Foster, V. J. (1989). Clinical pharmacology of mivacurium chloride (BW B1090U) in children during nitrous oxide-halothane and nitrous oxide-narcotic anesthesia. Anesthesia and analgesia, 68, 116-121.

8 Lashof, D. A., Ahuja, D. R. (1990). Relative contributions of greenhouse gas emissions to global warming. Nature, 344, 529-531.

9 European Environment Agency: http://www.eea.europa.eu/data-and-maps/indicators/eea-32-nitrogen-oxides-nox-emissions-1. accessed 13-1-2013.

10 European Union: http://europa.eu/legislation_summaries/environment/air_pollution/l28186. accessed 12-9-2011.

11 US Environmental Protection Agency: http://www.epa.gov/otaq/hd-hwy.htm#regs. accessed 12-9-2011.

12 Behrentz, E., Ling, R., Rieger, P. and Winer, M. A. (2004). Measurements of nitrous oxide emissions from light duty motor vehicles: a pilot study. Atmospheric Environment, 38, 4291-4303.

13 US Environmental Protection Agency: http://epa.gov/climatechange/ghgemissions/gases/n2o.html accessed 6-5-2013

14 DieselNet: http://www.dieselnet.com/standards/eu/ld.php. accessed: 24/06/2013.

15 Oikonomou, M. (2011). Emission control systems for piston engines, Diploma thesis, National Technical University of Athens, Greece.

16 Johnson, T. (2013). Vehicular Emissions in Review. SAE Technical Paper: 2013-01-0538.

17 Schubiger, R., Bertola, A. and Boulouchos, K. (2001). Influence of EGR on Combustion and Exhaust Emissions of Heavy Duty DI-Diesel Engines Equipped with Common-Rail Injection Systems. SAE Technical Paper: 2001-01-3947.

18 Tolga, M., Alper, H., Karadeniz, C. and Kazi, N. (2008). Modeling and Testing of the Throttle Body Usage in a Diesel Engine to Improve NO_x Emissions. SAE Technical Paper: 2008-01-2646.

19 Samiur, R., Maiboom, A., Tauzia, X. and Jean, F. (2009). Experimental Study of Inlet Manifold Water Injection on a Common Rail HSDI Automobile Diesel Engine, Compared to EGR with Respect to PM and NO_x Emissions and Specific Consumption. SAE Technical Paper: 2009-01-1439.

20 Kim, K. and Cho, S. (2010). The Emission Development for Lean NO_x Trap System to Meet Tier2Bin5. SAE Technical Paper: 2010-01-0566.

21 Shin'ichi, M. (1996). DeNO$_x$ catalyst for automotive lean-burn engine. Catalysis Today, 29, 43-45.

22 Granger, P. and Parvulescu, V. I. (2011). Catalytic NO_x Abatement Systems for Mobile Sources: From Three-Way to Lean Burn after-Treatment Technologies. Chemical Reviews, 111, 3155-3207.

23 Narula, C., Yang, X., Bonnesen, P.and Hagaman, E. (2011). High Performance NH_3 SCR Zeolite Catalysts for Treatment of NO_x in Emissions from Off-Road Diesel Engine. SAE Technical Paper: 2011-01-1330.

24 Takahashi, N., Shinjoh, H., Iijima, T., Suzuki, T., Yamazaki, K., Yokota, K., Suzuki, H., Miyoshi, N., Matsumoto, S. i., Tanizawa, T., Tanaka, T., Tateishi, S. S. and Kasahara, K. (1996). The new concept 3-way catalyst for automotive lean-burn engine: NO_x storage and reduction catalyst. Catalysis Today, 27, 63-69.

25 Matsumoto, S. (1996). DeNO$_x$ catalyst for automotive lean-burn engine. Catalysis Today, 29, 43-45.

26 Olsson, L., Blint, R. J. and Fridell, E. (2005). Global Kinetic Model for Lean NO_x Traps. Industrial & Engineering Chemistry Research, 44, 3021-3032.

27 Lambert, C., Hammerle, R., McGill , R., Khair, M., and Sharp, C. (2004). Technical Advantages of Urea SCR for Light-Duty and Heavy-Duty Diesel Vehicle Applications. SAE Technical Paper: 2004-01-1292.

28 Timothy, V. (2008). Diesel Emission Control in Review. SAE Int.J.Fuels Lubr., 1, 68-81.

29 Toops, T. J., Bunting, B. G., Nguyen, K. and Gopinath, A. (2007). Effect of engine-based thermal aging on surface morphology and performance of Lean NO_x Traps. Catalysis Today, 123, 285-292.

30 Li, J., Theis , J., Chun, W., Goralski, C., Kudla , R., Ura, J., Watkins, W., Chattha, M. and Hurley, R. (2001). Sulfur Poisoning and Desulfation of the Lean NO_x Trap. SAE Technical Paper: 2001-01-2503.

31 Morita, I., Hirano, M. and Bielawski G. T. (1998). Development and Commercial Operating Experience of SCR DeNO$_x$ Catalysts for Wet-Bottom Coal-Fired Boilers. Conf.: Power-Gen International '98, 12/1998, Orlando, Florida, U.S.A..

32 Gibson, J. and Groene, O. (1991). Selective catalytic reduction on marine diesel engines. Automotive Engineering, 99, 18-22.

33 Schommers J, Enderle C, Breitbach H, Lindemann B, Stotz M and Paule M. (2006) 15. Aachener Kolloquium. Aachen, Germany.

34 Nova, I., Ciardelli, C., Tronconi, E., Chatterjee, D. and Weibel, M. (2007). NH_3-NO/NO$_2$ SCR for diesel exhausts after treatment: mechanism and modeling of a catalytic converter. Topics in Catalysis, 42-43, 43-46.

35 DieselNet: http://www.dieselnet.com/tech/cat_scr_mobile.php. accessed: 19/11/2011.

36 Thompson, J., Op, D. B., Joubert, E. and Wilhelm, T. (2008). Case Studies of Urea SCR Integration on Passenger Cars Monitoring of Urea Inside the Tank During Hot and Cold Environment Test Missions. SAE Technical Paper: 2008-01-1181.

37 Zheng, G., Fila, A., Kotrba, A. and Floyd, R. (2010). Investigation of Urea Deposits in Urea SCR Systems for Medium and Heavy Duty Trucks. SAE Technical Paper: 2010-01-1941.

38 Gullett, B. K., Bruce, K. R., Hansen, W. F. and Hofmann, J. E. (1992). Sorbent/Urea slurry injection for simultaneous SO_2/NO_x removal. Environmental Progress, 11, 155-162.

39 Nishioka , A., Sukegawa , Y., Katogi , K., Mamada , H., Kowatari , T., Mukai , T. and Yokota , H. (2006). A Study of a New Aftertreatment System (2): Control of Urea Solution Spray for Urea-SCR. SAE Technical Paper: 2006-01-0644.

40 Van Helden, R., Verbeek , R., Willems , F. and Van der Welle. (2004). Optimization of Urea SCR deNO$_x$ Systems for HD Diesel Engines. SAE Technical Paper: 2004-01-0154.

41 Tsinoglou, D. N., Haralampous, O. A., Koltsakis, G. C. and Samaras, Z. S. (2007). Model-based optimization methods of combined DPF+SCR Systems. SAE Technical Paper: 2007-24-0098.

42 Jong, H., Michael, J. and David, B. (2008). Evaluation of Cu-Based SCR/DPF Technology for Diesel Exhaust Emission Control. SAE Int. J. Fuels Lubr., 1, 96-101.

43 Colombo, M., Koltsakis, G. and Koutoufaris, I. (2011). A Modeling Study of Soot and De-NOx Reaction Phenomena in SCRF Systems. SAE Technical Paper: 2011-37-0031.

44 Theis, J. R., Dearth, M., McCabe, R. (2011). LNT + SCR Catalyst Systems Optimized for NO_x Conversion on Diesel Applications. SAE Technical Paper: 2011-01-0305.

45 Kouakou, A., Dhainaut, F., Granger, P., Fresnet, F. and Louis-Rose, I. Study of Ammonia Formation During the Purge of a Lean NO$_x$ Trap. Topics in Catalysi, 52, 1734-1739

46 Exothermia SA. http://www.exothermia.com: Model-based comparison of DeNOx systems. accessed 18/2/2013.

47 Baik, J., Yim, S., Nam, I. S., Mok, Y., Lee, J. H., Cho, B. and Oh, S. (2004). Control of NO$_x$; emissions from diesel engine by selective catalytic reduction (SCR) with urea. Topics in Catalysis, 30-31, 37-41.

48 Vesna, T. (2007). Application of the monoliths in DeNO$_x$ catalysis. Catalysis Today, 119, 106-113.

49 Kröcher, O. (2007) Challenges for urea-SCR systems: From vanadia-based to zeolite based SCR catalysts. 1st MinNO$_x$ conference, Berlin, Germany.

50 Steven, J. and Jong, H. (2005). Evaluation of Supplier Catalyst Formulations for the Selective Catalytic Reduction of NO$_x$ With Ammonia. SAE Technical Paper: 2005-01-3881.

51 Skarlis, S. A. (2010). Soot Mass Limit Investigation in Diesel Particulate Filters. Diploma Thesis, Aristotle University of Thessaloniki, Greece.

52 Colombo, M., Nova, I. and Tronconi, E. (2010). A comparative study of the NH_3-SCR reactions over a Cu-zeolite and a Fe-zeolite catalyst. Catalysis Today, 151, 223-230.

53 Greenhalgh, B., Fee, M., Dobri, A., Moir, J., Burich, R., Charland, J. P. and Stanciulescu, M. (2010). DeNO$_x$ activity - correlations of NH$_3$-SCR catalysts. Journal of Molecular Catalysis A: Chemical, 333, 121-127.

54 In Sik Nam. (2011). Urea/SCR Technology for removing NOx from Diesel Engine. CLEERS Workshop 2011, Detroit, USA.

55. Rahkamaa-Tolonen, K., Maunula, T., Lomma, M., Huuhtanen, M. and Keiski, R. L. (2005). The effect of NO$_2$ on the activity of fresh and aged zeolite catalysts in the NH$_3$-SCR reaction. Catalysis Today, 100, 217-222.

56 Kamasamudram, K., Currier, N., Szailer, T. and Yezerets, A. (2010). Why Cu- and Fe-Zeolite SCR Catalysts Behave Differently At Low Temperatures. SAE Int.J.Fuels Lubr., 3, 664-672.

57 Pieterse, J. A. Z., Pirngruber, G. D., van Bokhoven, J. A. and Booneveld, S. (2007). Hydrothermal stability of Fe-ZSM-5 and Fe-BEA prepared by wet ion-exchange for N$_2$O decomposition. Applied Catalysis B: Environmental, 71, 16-22.

58 Heck, R. M., Farrauto, R. J. and Suresh, G. T. (2009) Catalytic air pollution control: Commercial Technology. 3rd Edition. New Jersey, USA, Willey & Sons, pp. 28-30.

59 Marcilly, C. (2006) Acido-basic catalysis – Application to refining and petrochemistry. IFP Publications, Editions TECHNIP, France, pp. 68 – 85.

60 Rakovan, J. (2004). A Word to the Wise: Placer. Rocks & Minerals, 79, 133-134.

61 Weitkamp, J. (2000). Zeolites and catalysis. Solid State Ionics, 131, 175-188.

62 Weitkamp, J., Puppe L. (1999) Catalysis and Zeolites – Fundamentals and Applications. Springer – Verlag Berlin Heidelberg, Germany, pp. 1-5.

63 Simon-Masseron, A., Marques, J. P., Lopes, J. M., Ribeiro, F. R. a., Gener, I. and Guisnet, M. (2007). Influence of the Si/Al ratio and crystal size on the acidity and activity of HBEA zeolites. Applied Catalysis A: General, 316, 75-82.

64 Baerlocher, Ch., McCuter, L. B., and Olson, D. H. (2007) Atlas of zeolite framework types. 6th Edition. Amsterdam, The Netherlands, Elsevier.

65 Marcilly, C. (2006) Acido-basic catalysis – Application to refining and petrochemistry. IFP Publications, Editions TECHNIP, France, pp. 12 – 23.

66 Costa, C., Dzikh, I. P., Lopes, J. M., Lemos, F., & Ribeiro, F. R. a. (2000). Activity-acidity relationship in zeolite ZSM-5. Application of Brønsted-type equations. Journal of Molecular Catalysis A: Chemical, 154, 193-201.

67 Aroux, A. (2002). Microcalorimetry Methods to Study the Acidity and Reactivity of Zeolites, Pillared Clays and Mesoporous Materials. Topics in Catalysis, 19, 205-213.

68 Chen, N.Y. and Garwood, W.E. (1978) Some catalytic properties of ZSM-5, a new shape selective zeolite. Journal of Catalysis, 52, 453-458.

69 Drews, T. O. and Tsapatsis, M. (2005). Progress in manipulating zeolite morphology and related applications. Current Opinion in Colloid & Interface Science, 10, 233-238.

70 Ribeiro F. R. (1993). Adaptation of the porosity of zeolites for shape selective reactions. Catalysis Letters, 22, 107-121.

71 Pieterse, J. A. Z., Booneveld, S., and Van den Brink, R. W. (2004). Evaluation of Fe-zeolite catalysts prepared by different methods for the decomposition of N_2O. Applied Catalysis B: Environmental, 51, 215-228.

72 Delahay, G., Guzmán-Vargas, A. and Coq, B. (2007) Deactivation of a Fe-ZSM-5 catalyst during the selective catalytic reduction of NO by n-decane: An operando DRIFT study. Applied Catalysis B: Environmental, 70, 45-52.

73 Long, R. Q. and Yang R. T. (2001) Fe-ZSM-5 for Selective Catalytic Reduction of NO with NH_3: A Comparative Study of Different Preparation Techniques. Catalysis Letters, 74, 201-205.

74. Delahay, G., Valade, D., Guzmán-Vargas, A., Coq, B. (2005) Selective catalytic reduction of nitric oxide with ammonia on Fe-ZSM-5 catalysts prepared by different methods. Applied Catalysis B: Environmental, 55, 149-155.

75 Brandenberger, S., Kröcher, O., Tissler, A. and Althoff, R. (2010). The determination of the activities of different iron species in Fe-ZSM-5 for SCR of NO by NH_3. Applied Catalysis B: Environmental, 95, 348-357.

76 Čapek, L., Kreibich, V., Dědeček, J., Grygar, T., Wichterlová, B., Sobalík, Z., Martens, J. A., Brosius, R. and Tokarová, V. (2005). Analysis of Fe species in zeolites by UV-VIS-NIR, IR spectra and voltammetry. Effect of preparation, Fe loading and zeolite type. Microporous and Mesoporous Materials, 80, 279-289.

77 Andersen, P. J., Baile, J. E., Casci, J. L., Chen, H. Y., Fedeyko, J. M., Foo, R. K. S. and Rajaram, R. R. Transition Metal/Zeolite SCR Catalyst. U.S. Patent 0,290,963, November 18, 2010.

78 Girard, J., Cavataio, G., Snow, R. and Lambert, C. (2008). Combined Fe-Cu SCR Systems with Optimized Ammonia to NO_x Ratio for Diesel NO_x Control. SAE Int. J. Fuels Lubr., 1, 603-610.

79 Wurzenberger, J. C. and Wanker, R. (2005). Multi-Scale SCR Modeling, 1D Kinetic Analysis and 3D System Simulation. SAE Technical Paper: 2005-01-0948.

80 Koebel, M., Elsener , M. and Madia , G. (2001). Recent Advances in the Development of Urea-SCR for Automotive Applications. SAE Technical Paper: 2001-01-3625.

81 Eichelbaum, M., Siemer, A. B., Farrauto, R. J. and Castaldi, M. J. (2010). The impact of urea on the performance of metal-exchanged zeolites for the selective catalytic reduction of NO_x, Part II. Catalytic, FTIR, and NMR studies. Applied Catalysis B: Environmental, 97, 98-107.

82 Grossale, A., Nova, I. and Tronconi, E. (2008). Study of a Fe-zeolite-based system as NH_3-SCR catalyst for diesel exhaust aftertreatment. Catalysis Today, 136, 18-27.

83 Chmielarz, L., Kustrowski, P., Dziembaj, R., Cool, P. and Vansant, E. F. (2006). Catalytic performance of various mesoporous silicas modified with copper or iron oxides introduced by different ways in the selective reduction of NO by ammonia. Applied Catalysis B: Environmental, 62, 369-380.

84 Long, R. Q. and Yang, R. T. (2000). Characterization of Fe-ZSM-5 Catalyst for Selective Catalytic Reduction of Nitric Oxide by Ammonia. Journal of Catalysis, 194, 80-90.

85 Devadas, M. (2006) Selective Catalytic Reduction (SCR) of Nitrogen Oxides with Ammonia over Fe-ZSM5. PhD Thesis ETH Zurich, Schwitzerland.

86 Castoldi, L., Bonzi, R., Lietti, L., Forzatti, P., Morandi, S., Ghiotti, G. and Dzwigaj, S. (2011) Catalytic behaviour of hybrid LNT/SCR systems: Reactivity and in situ FTIR study. Journal of Catalysis, 282, 128-144.

87 Hadjiivanov, K. I. (2000). Identification of Neutral and Charged N_xO_y Surface Species by IR Spectroscopy. Catalysis Reviews, 42, 71-144.

88 Chen, H. Y., El-Malki, E. M., Wang, X., van Santen, R. A. and Sachtler, W. M. H. (2000). Identification of active sites and adsorption complexes in Fe/MFI catalysts for NO_x reduction. Journal of Molecular Catalysis A: Chemical, 162, 159-174.

89 Gao, Z. X., Kim, H. S., Sun, Q., Stair, P. C. and Sachtler, W. M. H. (2001). UV-Raman Characterization of Iron Peroxo Adsorbates on Fe/MFI Catalyst with High Activity for NO_x Reduction. The Journal of Physical Chemistry B, 105, 6186-6190.

90 Grossale, A., Nova, I., Tronconi, E., Chatterjee, D. and Weibel, M. (2008). The chemistry of the NO/NO$_2$–NH$_3$ "fast" SCR reaction over Fe-ZSM5 investigated by transient reaction analysis. Journal of Catalysis, 256, 312-322.

91 Grossale, A., Nova, I., Tronconi, E., Chatterjee D. and Weibel (2009). NH$_3$–NO/NO$_2$ SCR for Diesel Exhausts Aftertreatment: Reactivity, Mechanism and Kinetic Modelling of Commercial Fe- and Cu-Promoted Zeolite Catalysts. Topics in Catalysis, 52, 1837-1841.

92 Grossale, A., Nova, I. and Tronconi, E. (2009). Role of Nitrate Species in the "NO$_2$-SCR" Mechanism over a Commercial Fe-zeolite Catalyst for SCR Mobile Applications. Catalysis Letters, 130, 525-531.

93 Pidko, E. A., Mignon, P., Geerlings, P., Schoonheydt, R. A. and van Santen, R. A. (2008). A Periodic DFT Study of N_2O_4 Disproportionation on Alkali-Exchanged Zeolites X. The Journal of Physical Chemistry C, 112, 5510-5519.

94 Colombo, M., Nova, I. and Tronconi, E. (2012). NO_2 adsorption on Fe- and Cu-zeolite catalysts: The effect of the catalyst red–ox state. Applied Catalysis B: Environmental, 111, 433-444.

95 Iwasaki, M. and Shinjoh, H. (2010). NO evolution reaction with NO_2 adsorption over Fe/ZSM-5: In situ FT-IR observation and relationships with Fe sites. Journal of Catalysis, 273, 29-38.

96 Ahrens, M., Marie, O., Bazin, P. and Daturi, M. (2010) Fe-H-BEA and Fe-H-ZSM-5 for NO_2 removal from ambient air – A detailed in situ and operando FTIR study revealing an unexpected positive water-effect. Journal of Catalysis, 271, 1-11.

97 Brandenberger, S., Kröcher, O., Tissler, A. and Althoff, R. (2008). The State of the Art in Selective Catalytic Reduction of NO_x by Ammonia Using Metal-Exchanged Zeolite Catalysts. Catalysis Reviews, 50, 492-531.

98 Ruggeri, M. P., Nova, I. and Tronconi, E. (2012) Is NO oxidation to NO_2 the rate determining step of the Standard SCR reaction? CAPOC Conference, Brussels, Belgium.

99 Devadas, M., Kröcher, O., Elsener, M., Wokaun, A., Söger, N., Pfeifer, M., Demel, Y. and Mussmann, L. (2006). Influence of NO_2 on the selective catalytic reduction of NO with ammonia over Fe-ZSM5. Applied Catalysis B: Environmental, 67, 187-196.

100 Schwidder, M., Heikens, S., De Toni, A., Geisler, S., Berndt, M., Brückner, A. and Grünert, W. (2008). The role of NO_2 in the selective catalytic reduction of nitrogen oxides over Fe-ZSM-5 catalysts: Active sites for the conversion of NO and of NO/NO_2 mixtures. Journal of Catalysis, 259, 96-103.

101 Qi, G., Gatt, J. E. and Yang, R. T. (2004). Selective catalytic oxidation (SCO) of ammonia to nitrogen over Fe-exchanged zeolites prepared by sublimation of FeCl3. Journal of Catalysis, 226, 120-128.

102 Long, R. Q. and Yang, R. T. (2001). Selective Catalytic Oxidation (SCO) of Ammonia to Nitrogen over Fe-Exchanged Zeolites. Journal of Catalysis, 201, 145-152.

103 Akah, A., Cundy, C. and Garforth, A. (2005). The selective catalytic oxidation of NH_3 over Fe-ZSM-5. Applied Catalysis B: Environmental, 59, 221-226.

104 Akah, A. C., Nkeng, G. and Garforth, A. A. (2007). The role of Al and strong acidity in the selective catalytic oxidation of NH_3 over Fe-ZSM-5. Applied Catalysis B: Environmental, 74, 34-39.

105 Brüggemann, T. C. and Keil, F. J. (2009). Theoretical Investigation of the Mechanism of the Selective Catalytic Oxidation of Ammonia on H-Form Zeolites. The Journal of Physical Chemistry C, 113, 13860-13876.

106 Nedyalkova, R., Kamasamudram, K., Currier, N. W., Li, J., Yezerets, A. and Olsson, L. (2013) Experimental evidence of the mechanism behind NH_3 overconsumption during SCR over Fe-zeolites. Journal of Catalysis, 299, 101-108.

107 Ciardelli, C., Nova, I., Tronconi, E., Chatterjee, D., Bandl-Konrad, B., Weibel, M. and Krutzsch, B. (2007). Reactivity of NO/NO_2-NH_3 SCR system for diesel exhaust aftertreatment: Identification of the reaction network as a function of temperature and NO_2 feed content. Applied Catalysis B: Environmental, 70, 80-90.

108 Grossale, A., Nova, I. and Tronconi, E. (2009). Ammonia blocking of the "Fast SCR" reactivity over a commercial Fe-zeolite catalyst for Diesel exhaust aftertreatment. Journal of Catalysis, 265, 141-147.

109 Chien, W. M., Chandra, D., Lau, K. H., Hildenbrand, D. L. and Helmy, A. M. (2010). The vaporization of NH_4NO_3. The Journal of Chemical Thermodynamics, 42, 846-851.

110 Ding, X. and Wu, G. (1995). The critical Raman intensity behavior of the nitrate v1 mode and its thermodynamic interpretation for the phase transitions of crystalline NH_4NO_3. Spectrochimica Acta Part A: Molecular and Biomolecular Spectroscopy, 51, 709-715.

111 Chaturvedi, S., Dave, P. N. (2012). Review on Thermal Decomposition of Ammonium Nitrate. Journal of Energetic Materials, 31, 1-26.

112 Li, M., Henao, J. Yeom, Y., Weitz, E. and Sachtler W. M. H. (2004) Low Activation Energy Pathway for the Catalyzed Reduction of Nitrogen Oxides to N_2 by Ammonia. Catalysis Letters 98, 5-9.

113 Savara, A., Li, M. J., Sachtler, W. M. H. and Weitz, E. (2008). Catalytic reduction of NH_4NO_3 by NO: Effects of solid acids and implications for low temperature $DeNO_x$ processes. Applied Catalysis B: Environmental, 81, 251-257.

114 Gunawan, R., Freij, S., Zhang, D. K., Beach, F. and Littlefair, M. (2006). A mechanistic study into the reactions of ammonium nitrate with pyrite. Chemical Engineering Science, 61, 5781-5790.

115 Devadas, M., Kröcher, O., Elsener, M., Wokaun, A., Mitrikas, G., Söger, N., Pfeifer, M., Demel, Y. and Mussmann, L. (2007). Characterization and catalytic investigation of Fe-ZSM5 for urea-SCR. Catalysis Today, 119, 137-144.

116 Malmberg, S., Votsmeier, M., Gieshoff, J., Söger, N., Mußmann, L., Schuler, A. and Drochner, A. (2007). Dynamic phenomena of SCR-catalysts containing Fe-exchanged zeolites - experiments and computer simulations. Topics in Catalysis, 42-43, 33-36.

117 Bolis, V., Busco, C. and Ugliengo, P. (2006). Thermodynamic Study of Water Adsorption in High-Silica Zeolites. The Journal of Physical Chemistry B, 110, 14849-14859.

118 Devarakonda, M., Tonkyn, R. and Herling, D. (2010). Hydrocarbon Effect on a Fe-zeolite Urea-SCR Catalyst: An Experimental and Modeling Study. SAE Technical Paper: 2010-01-1171.

119 Malpartida, I., Marie, O., Bazin, P., Daturi, M. and Jeandel X. (2011). An operando IR study of the unburnt HC effect on the activity of a commercial automotive catalyst for NH_3-SCR. Applied Catalysis B: Environmental, 102, 190-200.

120 Malpartida, I., Ivanova, E., Mihaylov, M., Hadjiivanov, K., Blasin-Aubé, V., Marie, O. and Daturi, M. (2010). CO and NO adsorption for the IR characterization of Fe^{2+} cations in ferrierite: An efficient catalyst for NO_x SCR with NH_3 as studied by operando IR spectroscopy. Catalysis Today, 149, 295-303.

121 Cavataio, G., Jen, H. W., Girard, J. W., Dobson, D., Warner J. R. and Lambert C. K. (2009). Impact and Prevention of Ultra-Low Contamination of Platinum Group Metals on SCR Catalysts Due to DOC Design. SAE Technical Paper: 2009-01-0627.

122 Shwan, S., Nedyalkova, R., Jansson, J., Korsgren, J., Olsson, L. and Skoglundh, M. (2013). Influence of Hydrothermal Ageing on NH_3-SCR Over Fe-BEA – Inhibition of NH_3-SCR by Ammonia. Topics in Catalysis, 56, 80-88.

123 Toops, T. J., Nguyen, K., Foster, A. L., Bunting, B. G., Ottinger, N. A., Pihl, J. A. Hagaman, E. W. and Jiao, J. (2010). Deactivation of accelerated engine-aged and field-aged Fe–zeolite SCR catalysts. Catalysis Today, 151, 257-265.

124 Birkhold, F., Meingast, U., Wassermann, P. and Deutschmann, O. (2006). Analysis of the Injection of Urea-Water-Solution for Automotive SCR DeNOx-Systems: Modeling of Two-Phase Flow and Spray/Wall-Interaction. SAE Technical Paper: 2006-01-0643.

125 Ebrahimian, V., Nicolle, A. and Habchi, C. (2011). Detailed modeling of the evaporation and thermal decomposition of urea-water solution in SCR systems. AIChE Journal, 58, 1998-2009.

126 Haralampous, O. A. (2004) A new advanced DPF model and an investigation of the thermal strain mechanisms during the regeneration phase. PhD Thesis, Aristotle University of Thessaloniki, Greece, pp. 40-52.

127 Tsinoglou, D. and Koltsakis, G. C. (2007). Modelling of the selective catalytic NO_x reduction in diesel exhaust including ammonia storage. Proceedings of the Institution of Mechanical Engineers, Part D: Journal of Automobile Engineering 221, 117-133.

128 Roduit, B., Baiker, A., Bettoni, F., Baldyga, J. and Wokaun, A. (1998). 3-D modeling of SCR of NOx by NH_3 on vanadia honeycomb catalysts. AIChE Journal, 44, 2731-2744.

129 Koltsakis, G. C., Haralampous, O. A. and Koutoufaris , I. Z. (2010). Applications of Multi-layer Catalyst Modeling in deNOx and DPF Systems. SAE Technical Papers: 2010-01-0893.

130 Leistner, K., Nicolle, A., Berthout, D. and Costa, P. d. (2012). Kinetic modelling of the oxidation of a wide range of carbon materials. Combustion and Flame, 159, 64-76.

131 Ertl, G., Knözinger, H., Schüth, F. and Weitkamp J. (2008) Handbook of Heterogeneous Catalysis. 2nd Edition. Willey & Sons, pp. 1479-1482.

132 Li, J. and Li, S. (2008). A DFT Study toward Understanding the High Activity of Fe-Exchanged Zeolites for the "Fast" Selective Catalytic Reduction of Nitrogen Oxides with Ammonia. The Journal of Physical Chemistry C, 112, 16938-16944.

133 Nova , I., Colombo , M., Tronconi , E., Schmeisser , V. and Weibel , M. (2011). The NH_3 Inhibition Effect in the Standard SCR Reaction over a Commercial Fe-zeolite Catalyst for Diesel Exhaust Aftertreatment: An Experimental and Modeling Study. SAE Int. J. Engines, 4, 1822-1838.

134 Tischer, S. and Deutschmann, O. (2005). Recent advances in numerical modeling of catalytic monolith reactors. Catalysis Today, 105, 407-413.

135 De Oliveira, M. L. M., Silva, C. M., Moreno-Tost, R., Farias, T. L., Jiménez-López, A. and Rodríguez-Castellón, E. (2009). Simulation of SCR equipped vehicles using iron-zeolite catalysts. Applied Catalysis A: General, 366, 13-21.Chap. 4 – ref. 21

136 Sjövall, H., Blint, R. J., Gopinath, A. and Olsson, L. (2009). A Kinetic Model for the Selective Catalytic Reduction of NOx with NH_3 over an Fe-zeolite Catalyst. Industrial & Engineering Chemistry Research, 49, 39-52.

137 Colombo, M., Koltsakis, G., Nova, I. and Tronconi, E. (2012). Modelling the ammonia adsorption-desorption process over an Fe-zeolite catalyst for SCR automotive applications. Catalysis Today, 188, 42-52.

138 Chatterjee, D., Kočí, P., Schmeißer, V., Marek, M., Weibel, M. and Krutzsch, B. (2010). Modelling of a combined storage and -SCR catalytic system for Diesel exhaust gas aftertreatment. Catalysis Today, 151, 395-409.

139 Klukowski, D., Balle, P., Geiger, B., Wagloehner, S., Kureti, S., Kimmerle, B., Baiker, A. and Grunwaldt, J. D. (2009). On the mechanism of the SCR reaction on Fe/HBEA zeolite. Applied Catalysis B: Environmental, 93, 185-193.

140 Shwan, S., Jansson, J., Korsgren, J., Olsson, L. and Skoglundh, M. (2012). Kinetic modeling of H-BEA and Fe-BEA as NH_3-SCR catalysts - Effect of hydrothermal treatment. Catalysis Today, 197, 24-37.

141 Sjövall, H., Blint, R. J. and Olsson, L. (2009). Detailed Kinetic Modeling of NH_3 and H_2O Adsorption, and NH_3 Oxidation over Cu-ZSM-5. The Journal of Physical Chemistry C, 113, 1393-1405.

142 Gilot, B. and Guiraud, R. (2004) Génie chimique – Cinétique et catalyse hétérogènes, 26-32. Ellipses.

143 Perdana, I., Creaser, D., Made Bendiyasa, I., Rochmadi and Wikan Tyoso, B. (2007). Modelling adsorption in a thin NaZSM-5 film supported on a cordierite monolith. Chemical Engineering Science, 62, 3882-3893.

144 Metkar, P. S., Balakotaiah, V. and Harold, M. P. (2012). Experimental and kinetic modeling study of NO oxidation: Comparison of Fe and Cu-zeolite catalysts. Catalysis Today, 184, 115-128.

145 Olsson, L., Sjövall, H., & Blint, R. J. (2009). Detailed kinetic modeling of NO_x adsorption and NO oxidation over Cu-ZSM-5. Applied Catalysis B: Environmental, 87, 200-210.

146 Bacher, V., Perbandt, C., Schwefer, M., Siefert, R. and Turek, T. (2013). Kinetics of the NO/NO_2 equilibrium reaction over an iron zeolite catalyst. Applied Catalysis B: Environmental, 134-135, 55-59.

147 Metkar, P. S., Harold, M. P. and Balakotaiah, V. (2013). Experimental and kinetic modeling study of NH_3-SCR of NO_x on Fe-ZSM-5, Cu-chabazite and combined Fe- and Cu-zeolite monolithic catalysts. Chemical Engineering Science, 87, 51-66.

148 Colombo, M., Nova, I., Tronconi, E., Schmeißer, V., Bandl-Konrad, B. and Zimmermann, L. (2012). $NO/NO_2/N_2O-NH_3$ SCR reactions over a commercial Fe-zeolite catalyst for diesel exhaust aftertreatment: Intrinsic kinetics and monolith converter modelling. Applied Catalysis B: Environmental, 111-112, 106-118.

149 Sharifian, L., Yuri, M., Boulouchos, K., Elsener, M. and Kröcher, O. (2011). Transient Simulation of NO_x Reduction over a Fe-Zeolite Catalyst in an NH_3-SCR System and Study of the Performance under Different Operating Conditions. SAE Int. J. Fuels Lubr., 5, 370-379.

150 Forzatti, P., Nova, I. and Tronconi, E. (2010). New "Enhanced NH3-SCR" Reaction for NOx Emission Control. Industrial & Engineering Chemistry Research, 49, 10386-10391.

151 Mauviot, G., Le Berr, F., Raux, S., Perretti, F., Malbec, L. and Millet, C. (2009). 0D Modeling: a Promising Means for After-treatment Issues in Modern Automotive Applications. Oil & Gas Science and Technology - Rev. IFP, 64, 285-307.

152 W. Borutzky, W. (2009). Bond graph modelling and simulation of multidisciplinary systems – An introduction. Simulation Modelling Practice and Theory, 17, 3-21.

153 LMS.ImagineLab IFP-Exhaust Library user manual: Rev 8A – June 2008, pp.68.

154 Dardiotis, C. K., Haralampous, O. A. and Koltsakis G. C. (2006). Catalytic Oxidation Performance of Wall-Flow versus Flow-Through Monoliths for Diesel Emissions Control. Industrial & Engineering Chemistry Research, 45, 3520-3530.

155 Leistner, K., Nicolle, A. Berthout, D. and Da Costa, P. (2012). Kinetic modelling of the oxidation of a wide range of carbon materials. Combustion and Flame, 159, 64-76.

156 Mavros, P., Matis, K., Triantafillidis, K., (2009) Chemical Processes, Thessaloniki, Greece, Tziola, pp. 2-73.

157 Carías-Henriquez, A., Pietrzyk, S., Dujardin, C. (2012). Modelling and optimization of IR cell devoted to in situ and operando characterization of catalysts. Catalysis Today, 205, 134-140.

158 Depcik, C. and Assanis, D. (2005). One-dimensional automotive catalyst modeling. Progress in Energy and Combustion Science, 31, 308-369.

159 Santos, H. and Costa, M. (2008). The relative importance of external and internal transport phenomena in three way catalysts. International Journal of Heat and Mass Transfer, 51, 1409-1422.

160 Hayes, R. E., Liu, B., Moxom, R. and Votsmeier, M. (2004). The effect of washcoat geometry on mass transfer in monolith reactors. Chemical Engineering Science, 59, 3169-3181.

161 Froment, G. F. (1986). The kinetics of catalytic processes: Importance in reactor simulation and design. Applied Catalysis, 22, 3-20.

162 Villermaux, J. (1993). Génie de la réaction chimique. Conception et fonctionnement de réacteurs; Lavoiser S.A.S., Tec & Doc.

163 Carberry, J. J.,Kulkarni, A. A. (1973). The non-isothermal catalytic effectiveness factor for monolith supported catalysts. Journal of Catalysis, 31, 41-50.

164 Mladenov, N., Koop, J., Tischer, S. and Deutschmann, O. (2010). Modeling of transport and chemistry in channel flows of automotive catalytic converters. Chemical Engineering Science, 65, 812-826.

165 Zalc, J. M., Reyes, S. C. and Iglesia, E. (2004). The effects of diffusion mechanism and void structure on transport rates and tortuosity factors in complex porous structures. Chemical Engineering Science, 59, 2947-2960.

166 Olsson, L., Sjövall, H., Blint, R. J. (2008). A kinetic model for ammonia selective catalytic reduction over Cu-ZSM-5. Applied Catalysis B: Environmental, 81, 203-217.

167 Brandenberger, S., Kröcher, O., Wokaun, A., Tissler, A., and Althoff, R. (2009). The role of Brønsted acidity in the selective catalytic reduction of NO with ammonia over Fe-ZSM-5. Journal of Catalysis, 268, 297-306.

168 Gorte, R.J. (1996). Temperature-programmed desorption for the characterization of oxide catalysts. Catalysis Today, 28, 405-414.

169 Costa, C., Dzikh, I. P., Lopes, J. M., Lemos, F. and Ribeiro, F. R. (2000). Activity-acidity relationship in zeolite ZSM-5. Application of Brønsted-type equations. Journal of Molecular Catalysis A: Chemical, 154, 193-201.

170 Gorte, R. J. (1999). What do we know about the acidity of solid acids? Catalysis Letters, 62, 1-13.

171 Topsøe, N. Y., Pedersen, K. and Derouane, E. G. (1981). Infrared and temperature-programmed desorption study of the acidic properties of ZSM-5-type zeolites. Journal of Catalysis, 70, 41-52.

172 Katada, N., Miyamoto, T., Begum, H. A., Naito, N., Niwa, M., Matsumoto, A. and Tsutsumi, K. (2000). Strong Acidity of MFI-Type Ferrisilicate Determined by Temperature-Programmed Desorption of Ammonia. The Journal of Physical Chemistry B, 104, 5511-5518.

173 Katada, N., Igi, H. and Kim, J. H. (1997). Determination of the Acidic Properties of Zeolite by Theoretical Analysis of Temperature-Programmed Desorption of Ammonia Based on Adsorption Equilibrium. The Journal of Physical Chemistry B, 101, 5969-5977.

174 Rodríguez-González, L., Hermes, F., Bertmer, M., Rodríguez-Castellón, E., Jiménez-López, A. and Simon, U. (2007). The acid properties of H-ZSM-5 as studied by NH$_3$-TPD and 27Al-MAS-NMR spectroscopy. Applied Catalysis A: General, 328, 174-182.

175 Bagnasco, G. (1996). Improving the Selectivity of NH$_3$ TPD Measurements. Journal of Catalysis, 159, 249-252.

176 Matsuura, H., Katada, N. and Niwa, M. (2003). Additional acid site on HZSM-5 treated with basic and acidic solutions as detected by temperature-programmed desorption of ammonia. Microporous and Mesoporous Materials, 66, 283-296.

177 Long, R. Q. and Yang, R. T. (2001). Temperature-Programmed Desorption/Surface Reaction (TPD/TPSR) Study of Fe-Exchanged ZSM-5 for Selective Catalytic Reduction of Nitric Oxide by Ammonia. Journal of Catalysis, 198, 20-28.

178 Mhamdi, M., Khaddar-Zine, S. and Ghorbel, A. (2008). Influence of the Co/Al ratio and the temperature of thermal treatment on cobalt speciation and catalytic properties of Co-ZSM-5 prepared by solid-state ion exchange. Applied Catalysis A: General, 337, 39-47.

179 Anunziata, O. A., Beltramone, A. R., Juric, Z., Pierella, L. B. and Requejo, F. G. (2004). Fe-containing ZSM-11 zeolites as active catalyst for SCR of NO$_x$: Part I. Synthesis, characterization by XRD, BET and FTIR and catalytic properties. Applied Catalysis A: General, 264, 93-101.

180 Mirodatos, C. and Barthomeuf, D. (1981). Superacid sites in zeolites. Journal of the Chemical Society, Chemical Communications, 39-40.

181 Borade, R., Sayari, A., Adnot, A. and Kaliaguine, S. (1990). Characterization of acidity in ZSM-5 zeolites: an x-ray photoelectron and IR spectroscopy study. The Journal of Physical Chemistry, 94, 5989-5994.

182 Chen, T., Men, A., Sun, P., Zhou, J., Yuan, Z., Guo, Z., Wang, J., Ding, D. and Li, H. (1996). Lewis acid sites on dehydroxylated zeolite HZSM-5 studied by NMR and EPR. Catalysis Today, 30, 189-192.

183 Chen, X., Li, W. and Schwank, J. W. (2011)Reactivity of NH$_3$ over (Fe)/H-ZSM-5 zeolite: Studies of temperature-programmed and steady-state reactions. Catalysis Today, 175, 2-11.

184 Chorkendorff, I. and Niemantsverdriet J.W. (2003) Concepts of Modern Catalysis and Kinetics. Weinheim, WILEY-VCH Verlag GmbH & Co. KGaA, pp. 113-128.

185 Metkar, P. S., Salazar, N., Muncrief, R., Balakotaiah, V. and Harold, M. P. (2011). Selective catalytic reduction of NO with NH$_3$ on iron zeolite monolithic catalysts: Steady-state and transient kinetics. Applied Catalysis B: Environmental, 104, 110-126.

186 Pinto, R. R., Borges, P., Lemos, M. A. N. D., Lemos, F., Vqdrine, J. C., Derouane, E. G. and Ribeiro, F. R. (2005). Correlating NH$_3$-TPD and 1H MAS NMR measurements of zeolite acidity: proposal of an acidity scale. Applied Catalysis A: General, 284, 39-46.

187 Sahoo, S. K., Viswanadham, N., Ray, N., Gupta, J. K. and Singh, I. D. (2001). Studies on acidity, activity and coke deactivation of ZSM-5 during n-heptane aromatization. Applied Catalysis A: General, 205, 1-10.

188 Mishin, I., Brueva, T. and Kapustin, G. (2005). Heats of Adsorption of Ammonia and Correlation of Activity and Acidity in Heterogeneous Catalysis. Adsorption, 11, 415-424.

189 Wilken, N., Kamasamudram, K., Currier, N. W., Li, J., Yezerets, A. and Olsson, L. (2010). Heat of adsorption for NH_3, NO_2 and NO on Cu-Beta zeolite using microcalorimeter for NH_3 SCR applications. Catalysis Today, 151, 237-243.

190 Rodríguez-González, L., Rodríguez-Castellón, E., Jiménez-López, A. and Simon, U. (2008). Correlation of TPD and impedance measurements on the desorption of NH_3 from zeolite H-ZSM-5. Solid State Ionics, 179, 1968-1973.

191 Sharma, S. B., Meyers, B. L., Chen, D. T., Miller, J. and Dumesic, J. A. (1993). Characterization of catalyst acidity by microcalorimetry and temperature-programmed desorption. Applied Catalysis A: General, 102, 253-265.

192 Auroux, A. (1997). Acidity characterization by microcalorimetry and relationship with reactivity. Topics in Catalysis, 4, 71-89.

193 Hidalgo, C. V., Itoh, H., Hattori, T., Niwa, M. and Murakami, Y. (1984). Measurement of the acidity of various zeolites by temperature-programmed desorption of ammonia. Journal of Catalysis, 85, 362-369.

194 Sazama, P., Wichterlova, B., Dedecek, J., Tvaruzkova, Z., Musilova, Z., Palumbo, L., Sklenak, S. and Gonsiorova, O. (2011). FTIR and 27Al MAS NMR analysis of the effect of framework Al- and Si-defects in micro- and micro-mesoporous H-ZSM-5 on conversion of methanol to hydrocarbons. Microporous and Mesoporous Materials, 143, 87-96.

195 Kapustin, G. I., Brueva, T. R., Klyachko, A. L., Beran, S. and Wichterlova, B. (1988). Determination of the number and acid strength of acid sites in zeolites by ammonia adsorption: Comparison of calorimetry and temperature-programmed desorption of ammonia. Applied Catalysis, 42, 239-246.

196 Sugawara, K., Nobukawa, T., Yoshida, M., Sato, Y., Okumura, K., Tomishige, K. and Kunimori, K. (2007). The importance of Fe loading on the N_2O reduction with NH_3 over Fe-MFI: Effect of acid site formation on Fe species. Applied Catalysis B: Environmental, 69, 154-163.

197 Brandenberger, S., Kröcher, O., Tissler, A. and Althoff, R. (2010). Estimation of the fractions of different nuclear iron species in uniformly metal-exchanged Fe-ZSM-5 samples based on a Poisson distribution. Applied Catalysis A: General, 373, 168-175.

198 Lanzani, G.,Laasonen, K. (2010). NH_3 adsorption and dissociation on a nanosized iron cluster. International Journal of Hydrogen Energy, 35, 6571-6577.

199 Ates, A. (2007). Characteristics of Fe-exchanged natural zeolites for the decomposition of N_2O and its selective catalytic reduction with NH_3. Applied Catalysis B: Environmental, 76, 282-290.

200 Wahba, M. and Kemball, C. (1953). Heats of adsorption of ammonia and hydrogen on metal films. Transactions of the Faraday Society, 49, 1351-1360.

201 Dumesic, J. A.,Trevino, A. A. (1989). Kinetic simulation of ammonia synthesis catalysis. Journal of Catalysis, 116, 119-129.

202 Connell, G. and Dumesic, J. A. (1987). The generation of Brønsted and Lewis acid sites on the surface of silica by addition of dopant cations. Journal of Catalysis, 105, 285-298.

203 John, W. (1967). The nature of active sites on zeolites: I. The decationated Y zeolite. Journal of Catalysis, 9, 225-236.

204 Forni, L., Vatti, F. P. and Ortoleva, E. (1995). Temperature-programmed desorption-diffusion of ammonia in molecular sieves V. ZSM-5 zeolite. Microporous Materials, 3, 367-375.

205 Yu, Y., Xiong, G., Li, C. and Xiao, F.S. (2001). Characterization of aluminosilicate zeolites by UV Raman spectroscopy. Microporous Mesoporous Materials, 46, 23-34.

206 Mihailova, B., Valtchev, V., Mintova, S., Faust, A.C., Petkov N. and Bein, T. (2005). Interlayer stacking disorder in zeolite beta family: a Raman spectroscopic study. Physical Chemistry Chemical Physics, 7, 2756-2763.

207 Gao, Z. X., Kim, H. S., Sun, Q., Stair, P. C. and Sachtler, W. M. H. (2001) UV−Raman Characterization of Iron Peroxo Adsorbates on Fe/MFI Catalyst with High Activity for NO_x Reduction. Journal of Physical Chemistry B, 105, 6186-6190.

208 Sun, K., Fan, F., Xia, H., Feng, Z., Li, W. X. and Li, C. (2008) Framework Fe Ions in Fe-ZSM-5 Zeolite Studied by UV Resonance Raman Spectroscopy and Density Functional Theory Calculations. Journal of Physical Chemistry C, 112, 16036-16041.

209 Jia, C., Massiani, P. and Barthomeuf, D. (1993) Characterization by infrared and nuclear magnetic resonance spectroscopies of calcined beta zeolite. Journal of Chemical Society, Faraday Transactions, 89, 3659-3665.

210 Vimont, A., Thibault-Starzyk, F. and Lavalley, J. C. (1999) Infrared Spectroscopic Study of the Acidobasic Properties of Beta Zeolite. Journal of Physical Chemistry B, 104, 286-291.

211 Stach, H., Jänchen, J. and Lohse, U. (1992) Relationship between acid strength and framework aluminium content in dealuminated faujasites. Catalysis Letters, 13, 389-393.

212 Jansen, J. C., Creyghton, E. J., Njo, S. L., van Koningsveld, H. and van Bekkum, H. (1997) On the remarkable behaviour of zeolite Beta in acid catalysis. Catalysis Today, 38, 205-212.

213 Kumar, S., Sinha, A. K., Hegde, S. G. and Sivasanker, S. (2000) Influence of mild dealumination on physicochemical, acidic and catalytic properties of H-ZSM-5. Journal of Molecular Catalysis A: Chemical 154, 115-120.

214 Berrier, E., Ovsitser, O., Kondratenko, E. V., Schwidder, M., Grünert, W. and Brückner, A. (2007) Temperature-dependent N_2O decomposition over Fe-ZSM-5: Identification of sites with different activity. Journal of Catalysis, 249, 67-78.

215 Doronkin, D. E., Stakheev, A. Y., Kucherov, A. V., Tolkachev, N. N., Kustova, M., Høj, M., Baeva, G. N., Bragina, G. O., Gabrielsson, P., Gekas, I. and Dahl, S. (2009) Nature of Active Sites of Fe-Beta Catalyst for NO_x-SCR by NH_3. Topics in Catalysis, 52, 1728-1733.

216 Høj, M., Beier, M. J., Grunwaldt, J. D. and Dahl, S. (2009) The role of monomeric iron during the selective catalytic reduction of NO$_x$ by NH$_3$ over Fe-BEA zeolite catalysts. Applied Catalysis B: Environmental, 93, 166-176.

217 Pérez-Ramírez, J., Groen, J. C., Brückner, A., Kumar, M. S., Bentrup, U., Debbagh, M. N. and Villaescusa, L. A. (2005) Evolution of isomorphously substituted iron zeolites during activation: comparison of Fe-beta and Fe-ZSM-5. Journal of Catalysis, 232, 318-334.

218 Tosheva, L., Mihailova, B., Valtchev, V. and Sterte, J. (2001) Zeolite beta spheres. Microporous and Mesoporous Materials, 48, 31-37.

219 Hensen, E. J. M., Zhu, Q., Hendrix, M. M. R. M., Overweg, A. R., Kooyman, P. J., Sychev, M. V. and van Santen, R. A. (2004) Effect of high-temperature treatment on Fe/ZSM-5 prepared by chemical vapor deposition of FeCl$_3$: I. Physicochemical characterization. Journal of Catalysis, 221, 560-574.

220 Sun, Z., Yuan, H., Liu, Z., Han, B. and Zhang, X. (2005) A Highly Efficient Chemical Sensor Material for H$_2$S: α-Fe$_2$O$_3$ Nanotubes Fabricated Using Carbon Nanotube Templates. Advanced Materials, 17, 2993-2997.

221 Vimont, A., Thibault-Starzyk, F. and Daturi, M. (2010) Analysing and understanding the active site by IR spectroscopy. Chemical Society Reviews, 39, 4928-4950

222 Hegde, S. G., Kumar, R., Bhat, R. N. and Ratnasamy, P. (1989) Characterization of the acidity of zeolite Beta by FTi.r. spectroscopy and t.p.d. of NH$_3$. Zeolites, 9, 231-237.

223 Camiloti, A. M., Jahn, S. L., Velasco, N. D., Moura, L. F. and Cardoso, D. (1999) Acidity of Beta zeolite determined by TPD of ammonia and ethylbenzene disproportionation. Applied Catalysis A: General, 182, 107-113.

224 Barthel, N., Finiels, A., Moreau, C., Jacquot, R. and Spagnol, M. (2001) Kinetic study and reaction mechanism of the hydroxyalkylation of aromatic compounds over H-BEA zeolites. Journal of Molecular Catalysis A: Chemical, 169, 163-169.

225 Maier, S. M., Jentys, A. and Lercher, J. A. (2011) Steaming of Zeolite BEA and Its Effect on Acidity: A Comparative NMR and IR Spectroscopic Study. Journal of Physical Chemistry C, 115, 8005-8013.

226 Zhang, X., Shen, Q., He, C., Ma, C., Cheng, J. and Hao, Z. (2012) N$_2$O catalytic reduction by NH$_3$ over Fe-zeolites: Effective removal and active site. Catalysis Communications, 18, 151-155.

227 Lónyi, F. and Valyon, J. (2011) A TPD and IR study of the surface species formed from ammonia on zeolite H-ZSM-5, H-mordenite and H-beta. Thermochimica Acta, 373, 53-57.

228 Penzien, J., Abraham, A., van Bokhoven, J. A., Jentys, A., Müller, T. E., Sievers, C. and Lercher, J. A. (2004) Generation and Characterization of Well-Defined Zn^{2+} Lewis Acid Sites in Ion Exchanged Zeolite BEA. Journal of Physical Chemistry. B, 108, 4116-4126.

229 Bodoardo, S., Chiappetta, R., Onida, B., Figueras, F. and Garrone, E. (1998) Ammonia interaction and reaction with Al-pillared montmorillonite: an IR study. Microporous and Mesoporous Materials, 20, 187-196.

230 . Zhang, W., Burckle, E. C. and Smirniotis, P. G. (1999) Synthesis and Toluene Adsorption/Desorption Property of Beta Zeolite Coated on Cordierite Honeycomb by an In Situ Crystallization Method. Microporous and Mesoporous Materials, 33, 173-185.

231 Ward, J. W. (1967) The nature of active sites on zeolites: I. The decationated Y zeolite. Journal of Catalysis, 9, 225-236.

232 Cheng, K., Kang, J., Huang, S., You, Z., Zhang, Q., Ding, J., Hua, W., Lou, Y., Deng, W. and Wang, Y. (2012) Mesoporous Beta Zeolite-Supported Ruthenium Nanoparticles for Selective Conversion of Synthesis Gas to C5-C11 Isoparaffins. ACS Catalysis, 2, 441-449.

233 Zecchina, A., Marchese, L., Bordiga, S., Pazè, C. and Gianotti, E. (1997) Vibrational Spectroscopy of NH_4^+ Ions in Zeolitic Materials: An IR Study. Journal of Physical Chemistry B, 101, 10128-10135.

234 Lónyi, F. andValyon, J. (2001) On the interpretation of the NH_3-TPD patterns of H-ZSM-5 and H-mordenite. Microporous and Mesoporous Materials, 47, 293-301.

235 Sanchez-Escribano, V., Montanari, T. and Busca, G. (2005) Low temperature selective catalytic reduction of NO_x by ammonia over H-ZSM-5: an IR study. Applied Catalysis B: Environmental, 58, 19-23.

236 Sing, K. S. W., Everett, D. H., Haul, R. A. W., Moscou, L., Pierotti, R. A., Rouquérol, J. and Siemieniewska, T. (1985) Reporting physisorption data for gas/solid systems with special reference to the determination of surface area and porosity. Pure andApplied Chemistry, 57, 603-619.

237 Dragoi, B., Gervasini, A., Dumitriu, E. and Auroux, A. (2004) Calorimetric determination of the acidic character of amorphous and crystalline aluminosilicates. Thermochimica Acta, 420, 127-134.

238 Auroux, A., Huang, M. and Kaliaguine, S. (1995) Crystallinity Dependence of Lewis Acidity and Lewis Basicity in Na Zeolites. Journal of Physical Chemistry, 99, 9952-9959.

239 Tewari, G. D., Khandelwal, D. P., Bist, H. D. and Tayal, V. P. (1983) Evans holes in the infrared spectra of some transition metal formate dihydrates. Canadian Journal of Chemistry, 61, 2745-2748.

240 . Zhang, Y., Su, Q., Wang, Z., Yang, Y., Xin, Y., Han, D., Yang, X., Wang, H., Gao, X. and Zhang, Z. (2008) Synthesis and Toluene Adsorption/Desorption Property of Beta Zeolite Coated on Cordierite Honeycomb by an In Situ Crystallization Method. Chemical Engineering Technology, 31, 1856-1862.

241 Wang, H. and Xin, W. (2001) Surface Acidity of H-Beta and Its Catalytic Activity for Alkylation of Benzene with Propylene. Catalysis Letters, 76, 225-229.

242 El-Malki, E. M., van Santen, R. A. and Sachtler, W. M. H. (1999) Introduction of Zn, Ga, and Fe into HZSM-5 Cavities by Sublimation: Identification of Acid Sites. Journal of Physical Chemistry B, 103, 4611-4622.

243 Connell, G. and Dumesic, J. A. (1987) The generation of Brønsted and Lewis acid sites on the surface of silica by addition of dopant cations. Journal of Catalysis, 105, 285-298.

244 Fripiat, J. J., Van der Meersche, C., Touillaux, R. and Jelli, A. (1970) Study of protonic transfers in the ammonia-silica gel system by infrared and pulsed proton magnetic resonance spectroscopy and by conductivity measurements. Journal of Physical Chemistry, 74, 382-393.

245 Bolis, V., Barbaglia, A., Broyer, M., Busco, C., Civalleri, B. and Ugliengo, P. (2004) Thermodynamic Study of Water Adsorption in High-Silica Zeolites. Origins Life Evolution Biosphere, 34, 69-77.

246 Kusunoki, I. (1974) Sticking coefficient curves expected for multilayer adsorption Journal of Physical Chemistry, 78, 748-751.

247 Kefirov, R, Ivanova, E., Hadjiivanov K., Dzwigaj S. and Che, M. (2008) FTIR Characterization of Fe^{3+}–OH Groups in Fe–H–BEA Zeolite: Interaction with CO and NO. Catalysis Letters, 125, 209-214.

248 Hadjiivanov, K., Saussey, J., Freysz, J.L. and Lavalley, J.C. (1998) FT-IR study of $NO+O_2$ co-adsorption on H-ZSM-5: re-assignment of the 2133 cm^{-1} band to NO^+ species. Catalysis Letters, 52, 103-108.

249 Sedlmair, C., Gil, B., Seshan K., Jentys A. and Lercher, J.A. (2003) An in situ IR study of the NO_x adsorption/reduction mechanism on modified Y zeolites. Physical Chemistry Chemical Physics, 5, 1897-1905.

250 Perdana, I., Creaser, D., Öhrman, O. and Hedlund, J. (2005) NO_x adsorption over a wide temperature range on Na-ZSM-5 films. Journal of Catalysis, 234, 219-229.

251 Szanyi, J. and Paffett, M.T. (1996) The Adsorption of NO and Reaction of NO with O_2 on H-, NaH-, CuH-, and Cu-ZSM-5: An *in Situ* FTIR Investigation. Journal of Catalysis, 164, 232-245.

252 Brosius, R., Bazin, P., Thibault-Starzyk, F. and Martens, J.A. (2005) Operando FTIR study of reaction pathways of selective catalytic reduction of NO_x with decane in the presence of water on iron-exchanged MFI-type zeolite. Journal of Catalysis, 234, 191-198.

253 Lobree, L.J., Hwang, I.C., Reimer, J.A. and Bell, A.T. (1999) An in situ infrared study of NO reduction by C3H8 over Fe-ZSM5. Catalysis Letters, 63, 233-240.

254 Nova, I., Ciardelli, C., Tronconi, E., Chatterjee, D. and Bandl-Konrad, B. (2006) NH_3–NO/NO_2 chemistry over V-based catalysts and its role in the mechanism of the Fast SCR reaction. Catalysis Today, 114, 3-12.

255 Goodman, A.L., Underwood, G.M. and Grassian, V.H. (1999) Heterogeneous Reaction of NO_2: Characterization of Gas-Phase and Adsorbed Products from the Reaction, $2NO_{2(g)} + H_2O_{(a)} \rightarrow HONO_{(g)} + HNO_{3(a)}$ on Hydrated Silica Particles. Journal of Physical Chemistry A, 103, 7217-7223.

256 Apostolescu, N., Schröder, T. and Kureti, S. (2004) Study on the mechanism of the reaction of NO_2 with aluminium oxide. Applied Catalysis B: Environmental, 51, 43-50.

257 Wang, Z.M., Arai, T. and Kumagai, M. (2001) Cooperative and Competitive Adsorption Mechanism of NO_2, NO, and H_2O on H-Type Mordenite. Industrial & Engineering Chemistry Research, 40, 1864-1871.

258 Mignon, P., Pidko, E.A., Van Santen, R.A., Geerlings, P. and Schoonheydt, R.A. (2008) Understanding the Reactivity and Basicity of Zeolites: A Periodic DFT Study of the Disproportionation of N_2O_4 on Alkali-Cation-Exchanged Zeolite Y. Chemistry - A European Journal, 14, 5168-5177.

259 Hensel, K. and Morvová, M. (1996) The Conversion of NO_x in a Corona Discharge with an Electrode Material Variation. Contributions to Plasma Physics, 36, 1, 51-61.

260 Mul, G., Pérez-Ramírez, J., Kapteijn, F. and Moulijn, J.A. (2002) NO Adsorption on Ex-Framework [Fe,X]MFI Catalysts: Novel IR Bands and Evaluation of Assignments. Catalysis Letters, 80, 129-138.

261 Ruggeri, M. P., Grossale, A., Nova, I., Tronconi, E., Jirglova and H., Sobalik, Z. (2012) FTIR in situ mechanistic study of the NH_3–NO/NO_2 "Fast SCR" reaction over a commercial Fe-ZSM-5 catalyst. Catalysis Today, 184, 107-114.

262 Dubkov, K.A., Ovanesyan, N.S., Shteinman, A.A., Starokon, E.V. and Panov, G.I. (2002) Evolution of Iron States and Formation of α-Sites upon Activation of FeZSM-5 Zeolites. Journal of Catalysis, 207, 341-352.

263 Plane, J.M.C.and Rollason, R.J. (1999) A study of the reactions of Fe and FeO with NO_2, and the structure and bond energy of FeO_2. Physical Chemistry Chemical Physics, 1, 1843-1849.

264 Panov, G.I., Starokon, E.V., Pirutko, L.V., Paukshtis, E.A. and Parmon, V.N. (2008) New reaction of anion radicals O^- with water on the surface of FeZSM-5. Journal of Catalysis 254, 110-120.

265 Ciardelli, C., Nova, I., Tronconi, E., Chatterjee, D., Bandl-Konrad, B., Weibel, M. and Krutzsch, B. (2007) Reactivity of NO/NO_2–NH_3 SCR system for diesel exhaust aftertreatment: Identification of the reaction network as a function of temperature and NO_2 feed content. Applied Catalysis B Environmental, 70, 80-90.

266 Brüggemann, T.C., Przybylski, M.D., Balaji, S.P. and Keil, F.J. (2010) Theoretical Investigation of the Mechanism of the Selective Catalytic Reduction of Nitrogen Dioxide with Ammonia on H-Form Zeolites and the Role of Nitric and Nitrous Acids as Intermediates. Journal of Physical Chemistry C, 114, 6567-6587.

267 Sinditskii, V.P., Egorshev, V.Y., Levshenkov, A.I. and Serushki, V.V. (2005) Ammonium Nitrate: Combustion Mechanism and the Role of Additives. Propellants, Explosives, Pyrotechnics, 30, 269-280.

268 Gunawan, R. and Zhang, D. (2009) Thermal stability and kinetics of decomposition of ammonium nitrate in the presence of pyrite. Journal of Hazardous Materials, 165, 751-758.

269 Humienik, M.O. (2001) On the thermal stability of some ammonium salts. Thermochimica Acta, 378, 107-112.

270 Koga, N. and Tanaka, H. (1992) Effect of sample mass on the kinetics of thermal decomposition of a solid: Part 1. Isothermal mass-loss process of molten NH_4NO_3. Thermochimica Acta, 209, 127-134.

271 Russell, T.P. and Brill, T.B. (1989) Thermal decomposition of energetic materials 31— Fast thermolysis of ammonium nitrate, ethylenediammonium dinitrate and hydrazinium nitrate and the relationship to the burning rate. Combustion and Flame, 76, 393-401.

272 Herrmann, M.J. and Engel, W. (1997) Phase Transitions and Lattice Dynamics of Ammonium Nitrate. Propellants, Explosives, Pyrotechnics, 22, 143-147.

273 Li, M., Yeom, Y., Weitz, E. and Sachtler, W.M.H. (2006) An acid catalyzed step in the catalytic reduction of NO_x to N_2. Catalysis Letters, 112, 129-132.

274 Ribeiro, F. (2012). Identification of the active site in Cu/SSZ-13 catalysts for Selective Catalytic Reduction of NO_x by NH_3 by combining Operando X-ray Absorption Spectroscopy and DFT Modeling. CLEERS Workshop 2012, Detroit, USA.

275 Ribeiro, F. (2013). Investigations of Ammonia SCR on Cu-Chabazite. CLEERS Workshop 2013, Detroit, USA.

276 Tuschel, D.D., Mikhonin, A.V., Lemoff, B.E. and Asher, S.A. (2010) Deep Ultraviolet Resonance Raman Excitation Enables Explosives Detection. Applied Spectroscopy, 64, 425-432.

277 Li, P. and Tezel, F.H. (2007) Adsorption separation of N_2, O_2, CO_2 and CH_4 gases by β-zeolite. Microporous and Mesoporous Materials, 98, 94-101.

278 Iwasaki, M. and Shinjoha, H. (2010) Analysis of the adsorption state and desorption kinetics of NO_2 over Fe–zeolite catalyst by FT-IR and temperature-programmed desorption. Physical Chemistry Chemical Physics, 12, 2365-2372.

279 Savara, A., Sachtler, W.M.H. and Weitz, E. (2009) TPD of NO_2^- and NO_3^- from Na-Y: The relative stabilities of nitrates and nitrites in low temperature $DeNO_x$ catalysis. Applied Catalysis B: Envirnomental, 90, 120-125.

280 Ruggeri, M.P., Nova, I. and Tronconi, E. (2012) Is NO oxidation to NO_2 the rate determining step of the Standard SCR reaction? CAPOC 9 conference, Brussels, Belgium.